The Pennsylvania State University
The Graduate School
Eberly College of Science

UNIVERSAL FEW-BODY PHYSICS IN A THREE-COMPONENT FERMI GAS

A Dissertation in
Physics
by
Jason Reid Williams

Submitted in Partial Fulfillment
of the Requirements
for the Degree of

Doctor of Philosophy

December 2010

The dissertation of Jason R. Williams was reviewed and approved* by the following:

Kenneth M. O'Hara
Assistant Professor of Physics
Downsbrough Career Development Professorship
Dissertation Advisor, Chair of Committee

David S. Weiss
Professor of Physics

Peter E. Schiffer
Associate Vice President for Research
Director of Strategic Initiatives
Professor of Physics

Qiang Du
Verne M. Willaman Professor of Mathematics
Professor of Materials Sciences

Jayanth R. Banavar
Professor of Physics
Department Head

*Signatures are on file in the Graduate School.

Abstract

This dissertation reports on experimental studies of universal three-body physics in an ultracold Fermi gas. The sample consists of lithium-6 atoms occupying an incoherent mixture of the three lowest energy hyperfine spin states in thermal equilibrium. Using an externally applied magnetic field, three overlapping Feshbach resonances among the various two-body scattering channels were used to tune the s-wave interactions. In the range of magnetic fields from 0 to 1500 Gauss, the three s-wave scattering lengths were widely tunable from the non-interacting limit to deeply within the universal regime where the behavior of the gas is independent of the microscopic details of the inter-particle interactions. We measured the stability of the gas over the ranges of magnetic fields from 0 to 690 Gauss and 834 to 1500 Gauss where all pairwise interactions are attractive and find that the three-body recombination rate constant in these regions varies by over eight orders of magnitude. Further, we observe resonant loss features in the low field region near 130 and 500 Gauss, and a narrow feature in the high field region at 895 Gauss.

Recent calculations indicate that these loss features arise from a series of universal three-body bound states (Efimov trimers) near threshold. Our determinations of the three-body parameters in these regimes are used to perform the first complete calculation of the spectrum of Efimov states in any Fermi system. Further, we have realized degeneracy of a three spin-state Fermi gas in the high-field limit where all three inter-particle scattering lengths converge, exhibiting universal quantum physics in the SU(3) symmetric regime. Finally, we preformed a numerical simulation of a novel cooling scheme, demonstrating the feasibility of producing multi-component Fermi gasses with temperatures on the order of 10^{-3} of the Fermi temperature in a combined three-dimensional optical lattice and Laguerre-Gaussian trapping potential. These investigations will guide future experiments aimed at achieving three component (color) superfluidity and exotic magnetic ordering in three-state Fermi gases which have no solid-state analog.

Table of Contents

List of Figures

List of Tables

Acknowledgments

I would like to extend my deepest gratitude to all of the people who have made my graduate experience at The Pennsylvania State University positive and successful. Principally, I would like to thank Ken O'Hara who has been a wonderful graduate research adviser. Ken is an inspired experimentalist who ran the lab with a positive and academic attitude, which in-turn translated to the lab providing an ideal learning environment.

While in the O'Hara Lab, I had the opportunity to collaborate with a host of talented researchers. I appreciate the knowledge and enthusiasm that our former postdoc John Huckans brought to the lab. John helped pull us through seemingly insurmountable problems with the vacuum and atom trapping lifetimes to yield our first publishable results. I have also had the privilege of working closely with Ronald Stites, Eric Hazlett, and Yi Zhang. Without their hard work, late nights, and inspired technical abilities, it's inconceivable that the work detailed in this thesis could have been completed. I am happy to leave the experiment in their capable hands.

I would also like to thank David Weiss and Kurt Gibble. The knowledge they imparted, particularly during the informal discussions at our weekly AMO journal club meetings, has been invaluable. Additionally, I am thankful to the members of my thesis committee; Dave Weiss, Peter Schiffer, and Qiang Du for their review of and input in the thesis.

Our understanding of the few-body system has been greatly enhanced through discussions and collaboration with numerous specialists in collision theory, most notably Eric Braaten, Daekyoung Kang, Jose D'Incao, and Brett Esry. We are particularly indebted to Eric and Daekyoung for providing the numerical code to fit our three-body loss measurements.

Finally, I would like to thank my family for more reasons than I can express. My mother, Sharon Anaya, has provided a reservoir of love and support that I often couldn't have thrived without. I also am thankful to my children. Elora is a sweetheart, whose contagious enthusiasm always manages to bring me back to

earth. Sagan's unique combination of attentiveness and imagination often captivate me while always putting a smile on my face. Cole, who is generally happy and generous, always manages to bring joy into the room. To my wife Harmony, I owe everything. She has been my constant companion for over fifteen years, during which time she has raised our family while providing me with the love, support, and acceptance to follow my dreams. Harmony has been my source of strength and the greatest friend I have ever had, and for this, I am truly grateful.

Chapter 1

Introduction

Over the last century, pioneering work in quantum physics has lead to uncounted breakthroughs in our understanding of the physical world. Quantum mechanics provides a quantitative theory of matter at atomic and subatomic scales, and can be applied to systems with many degrees of freedom through the formalism of quantum field theory. The remarkable success of quantum theory, which provides the underlying basis for many fields of physics and chemistry, can be seen in its ability to describe phenomena over a wide range of length and energy scales. These range from many-body phases in condensed matter and solid-state physics; to atomic-scale phenomena studied in quantum chemistry and atomic, molecular, and optical physics; eventually leading to a general understanding of fundamental particle physics by means of quantum electrodynamics and quantum chromodynamics.

One of the most amazing features of these disciplines is that the underlying physics is often related, leading to universal theories that can describe numerous physical systems [12, 13, 14, 15, 2]. Strongly correlated Fermi systems, for example, are defined by strong interactions between pairs of spin-up and spin-down fermions. These systems can be found in superconductors, neutron and nuclear matter [16, 17, 12, 18], quark-gluon plasmas [19], and have been recently realized in ultracold atomic Fermi gases [20, 21, 22, 23, 24, 25, 26, 27, 28, 29].

Universality generally emerges when the microscopic details of the scattering processes can be neglected. This can occur, for example, when the deBroglie wavelength is much larger than the range of pairwise interactions. In this regime,

the pairwise interactions can be fully described by the so-called scattering length a, which contains all of the information about the short-range properties of the two-body scattering potential. Even stronger[1] classes of universality occur when the scattering length greatly exceeds the range of two-body interactions or even the average interparticle spacing.

Universality is beneficial for understanding the physics of numerous interacting Fermi systems. Here, the properties of one system can be studied to learn about other universally connected nonrelativistic particles with proper rescaling of the relevant length and energy scales. Such universal connections are particularly amazing when making analogies between the behaviors of ultracold atomic Fermi gases and atomic nuclei as the energy scales vary between these systems by ~ 18 orders of magnitude.

1.1 Universal Three-Body Physics

The universal properties of bosonic or fermionic systems with short-range two-body potentials, in turn, connect to an astonishing and counterintuitive universal behavior in the three-body system, as first predicted by V. Efimov in 1970 [30]. Efimov first considered an ensemble of identical spinless particles interacting via resonant two-particle interactions. He assumed that the resonance arose from a bound state in the two-body scattering potential which is degenerate with the two-body scattering threshold ($E = 0$), causing the scattering length to diverge. In this limit, he found that an infinite number of arbitrarily-shallow three-body bound states (Efimov states) emerge, even when binding is prohibited in the two-body system.

For identical bosons in the resonant limit, the ratio of the binding energies of successive Efimov states (n) approaches a universal constant in the asymptotic limit, given by $E_T^{(n+1)}/E_T^{(n)} \to 1/515.03$. This universal ratio is independent of the mass or structure of the particles as well as of the form of their short-range interactions. In two papers published in 1971 and 1979 [31, 32], Efimov went on to prove that the three-body system has universal properties not only in the resonant

[1]Universality in these cases are stronger in the sense that fewer and fewer parameters are needed to characterize a particular physical system within the universality class.

limit, but rather throughout the universal regime in which the magnitude of the scattering length is large as compared to the characteristic range of the two-body potential.

Efimov found that the number of supported weakly-bound trimer states, which is now finite for $|a| \neq \infty$, decrease as the magnitude of the scattering length is reduced for systems exhibiting both repulsive ($a > 0$) and attractive ($a < 0$) pairwise interactions. Here too, however, the critical scattering lengths at which the binding energies of successive Efimov states disappear, through either the free-atom or atom-dimer thresholds, also scale geometrically. Efimov further predicted that the entire spectrum of three-body bound states obeyed a universal scaling so that knowledge of the binding energies of one of the Efimov trimer states at a single scattering length is all of the information required to derive the entire spectrum of universal trimer states at all scattering lengths throughout the universal regime.

Although Efimov's scenario quickly became well-established theoretically, over 36 years passed between Efimov's first predictions and the experimental confirmation of the existence of these universal trimer states. The unambiguous identification of Efimov states in nature is difficult since typical systems do not exhibit resonant two-body interactions and their scattering lengths can not be varied in general. T. Lim *et al.* proposed in 1977 that the excited state of the ^{4}He trimer is an Efimov trimer [33]. This state, however, has eluded experimental observation. The ground-state ^{4}He trimer, observed by W. Schöllkopf and J. P. Tönnies [34], can also be interpreted as an Efimov state [18], although its classification is still debated. In nuclear physics, for which the concept of Efimov physics was originally devised, a number of systems display low-energy universality associated with Efimov physics including the triton and two-neutron Halos such as ^{20}C [18]. While initial studies of bound state observables are becoming available in these systems, corrections to the universal models must be included to properly account for the finite range of the interactions.

The first unambiguous signature of the existence of Efimov states came in 2006 when T. Kraemer and co-workers observed a resonant enhancement of the loss rate from three-body recombination in an ultracold gas of attractively interacting ^{133}Cs atoms due to an Efimov trimer state coming into resonance with the free-atom scattering threshold [35]. A minima in the three-body loss rates was also observed

at positive scattering lengths due to an interference in two recombination pathways. Although this phenomena is also associated with the existence of Efimov states in the system, the two observed features were not associated with the same scattering resonance, and no universal connections between the features were expected.

Since that time, the experimental and theoretical study of Efimov physics in the field of cold atom physics has progressed rapidly. In an ultracold gas of bosonic ^{7}Li atoms, two resonant features were observed in the measured rates of three-body loss (Efimov resonances) associated with a single scattering resonance [36]. Additionally, evidence for the existence for the first two Efimov states in bosonic ^{39}K and ^{7}Li have been reported [37, 38]. In all of these studies, the various critical scattering lengths at which resonant effects emerge in the measured three-body loss rates are relatively well predicted with the universal theories based on Efimov's findings. However, it is generally expected and experimentally observed that as the magnitudes of the scattering lengths are decreased, corrections to the universal theories are required to account for the finite range of the two-body potentials.

Efimov resonances have also been observed in hetero-nuclear mixtures of ultracold bosonic ^{41}K and ^{87}Rb atoms [39]. Here, two resonant loss features were found associated with Efimov trimer states in the KRbRb and RbKK channels. The properties of Efimov states can also be determined in atom-dimer mixtures in the form of resonances in the atom-dimer inelastic scattering rates. Such resonances have been observed in the loss rates of atom-dimer mixtures of ^{133}Cs atoms [40].

These experiments explored the spectrum of Efimov trimer states that emerge in various ultracold bosonic gases whose pairwise interactions were resonantly enhanced by a single two-body scattering resonance. In general, the systems closely mirror Efimov's original model. It was the ultracold nature of these classical (i.e. non-degenerate) gases that enabled these studies. Comparison of the data with the universal models requires that the system be in the threshold regime, in which the collision energy is the smallest energy in the system, above which thermal effects rapidly decrease the visibility of the Efimov resonances. The threshold regime was reached in the previously mentioned experiments by cooling the atoms with large scattering lengths to sufficiently low temperatures. Thanks to the extensive experimental and theoretical research of these systems, the Efimov effect in bosonic systems near an isolated Feshbach resonance is now becoming well understood.

The investigation of Efimov's scenario for a system of three distinguishable, equal-mass particles becomes more complicated. Here, pairwise interactions among the various components are not necessarily equal and scattering resonances may exist which differ for each pair of particles. The few-body physics of these systems can be quite rich, however, due to the coexistence of multiple scattering lengths with mutually varying magnitudes and even signs. Examples of such cases that can exist in nature include different isotopes of the same atom that can have nearly the same mass but widely varying pairwise interaction strengths. Also, the proton and neutron have nearly the same mass, but vary in their interaction properties. A primary result of my thesis work involved studies of three-body physics in dilute, nearly-degenerate gases of fermionic lithium-6 atoms at ultracold temperatures occupying three distinct hyperfine spin states to directly explore this novel system.

1.2 Ultracold Fermi Gases

Ultracold gasses of neutral alkali atoms provide ideal model systems to simulate complicated few- and many-body quantum mechanical phenomena that can be extended to describe the physics of denser systems. These gases, which can achieve temperatures below 1 nK [41], often occupy a regime of phase-space density where quantum mechanics dictates the properties of the systems. Further, these gases are among the cleanest and most dynamically adjustable experimental systems available, where the temperature, density, and scattering length of the gases can often be varied over a wide range using simple optical and magnetic fields. As these gases are so cold that a ground-state analysis of the systems generally suffice and the atoms interact via short-range contact interactions, the systems can often be theoretically modeled exactly and complexity can be slowly added to simulate a variety of physical phenomena.

These dilute gases are generally produced by laser cooling [42] and subsequent evaporative cooling [43] in optical or magnetic trapping potentials. The degree to which quantum statistics becomes important for the understanding of an ensemble of atoms is parameterized by the phase-space density $\rho = n\lambda_{dB}^3$, where n is the density of the gas and $\lambda_{dB} = \sqrt{2\pi\hbar^2/(mk_BT)}$ is the thermal de Broglie wavelength for the atoms with mass m and temperature T. For a system of identical particles,

as ρ becomes on the order of unity the thermal de Broglie wavelength becomes comparable to the average interparticle spacing and the wavepackets of adjacent particles begin to overlap. In this quantum degenerate regime, the symmetry of the many-body wave function must be considered and a classical description of the gas is no longer possible.

For identical particles of integer spin (bosons), the many-body wave function must be symmetric with respect to exchange of the constituent particles. The ground state of this system has remarkable properties, resulting in a macroscopic occupation of the lowest accessible energy state. This form of matter, which was first predicted by Satyendra Nath Bose and Albert Einstein in 1924-1925, is called a Bose-Einstein condensate (BEC) and is characterized by a superfluid phase with zero entropy. The realization of a Bose-Einstein condensed gas of weakly interacting alkali atoms [44, 45, 46], seventy years after the theoretical prediction of the BEC phase, therefore enabled a host of new studies of quantum systems using dilute ultracold atomic gases.

On the other side of the spectrum, the many-body wavefunction for identical particles with half-integer spin (fermions) must be antisymmetric under exchange. The phase-space density distribution of these particles must therefore obey the famous Pauli-Exclusion principle, in which simultaneous occupation of a quantum state is prohibited. For an ensemble of N identical and non-interacting fermions, the many-particle system can be described in terms of single-particle energy states where, at zero temperature, the particles fill the N lowest energy quantum states up to the so-called Fermi energy while all higher energy states are empty.

Whereas bosons undergo a dramatic phase transition to a condensed phase which marks the onset of degeneracy, the transition between a classical (thermal) and quantum (degenerate) fermionic system is continuous. From a theoretical point of view, the simulation of quantum Fermi systems with ultracold Fermi gases is quite interesting, however, as all of the material elementary particles, including quarks, electrons, muons, taus and neutrinos, obey Fermi statistics. Further, in the presence of even arbitrarily small attractive interactions the atoms can undergo a phase transition to a superfluid state by forming Cooper pairs, similar to the well-known superconducting transition of the electron gas in certain metals at low temperatures as described by the Bardeen-Cooper-Schrieffer theory [47, 48].

Ultracold Fermi gases can provide a robust and highly dynamic model system to explore the phenomena of superfluidity and studies of these gases may be useful for simulating the frictionless flow exhibited by electrons in a variety of solid-state systems.

Much of the utility of using ultracold gases as model system for studying quantum fermionic phenomena lies in the fact that all of the scattering events involving angular momentum are frozen out, as the kinetic energy of particles is insufficient to overcome the height of the centrifugal barrier for even p-wave scattering. In this regime, the collisions are generally sufficiently low-energy that the de Broglie wavelength (λ_{dB}) is much larger than the characteristic range of the two-body potential. The atoms undergoing pairwise collisions therefore cannot resolve the microscopic properties of the potential and s-wave scattering dominates the physics of the interparticle interactions.

In a sample of identical fermions, however, s-wave scattering is prohibited by symmetry. Therefore, mixtures of at least two distinguishable components (e.g., a gas occupying at least two distinct internal states) are required for the atoms to interact. For this same reason, three-body interactions are generally prohibited in two-component Fermi gases, requiring a third component to study phenomena associated with three mutually-interacting bodies. Another fortunate feature of ultracold multi-component Fermi gases of neutral alkali atoms is that the s-wave scattering lengths may be varied by means of magnetically tuned Feshbach resonances [9]. These resonances are attributed to the existence of weakly bound dimer states in the two-body potentials coming into resonance with the scattering threshold.

In this respect, fermionic ^{6}Li gases occupying the lowest hyperfine ground states are an exceptional choice for studies of interacting multi-component Fermi gases over a wide range of interaction strengths. Very broad Feshbach resonances occur in these systems, which are magnetically accessible at moderately-high magnetic field values, to arbitrarily tune the strengths and signs of their s-wave scattering length to realize physical systems characterized by either attractive or repulsive interactions. Additionally, in the range of fields near the resonance where the scattering length is tuned to large positive values (exhibiting repulsive interactions), a weakly bound dimer state exists. The molecular state can then be populated by

collisions among the particles to study bosonic phenomena in degenerate molecular Fermi gases.

1.3 Progress with 2-State Fermi Gases

The first experiment to create a quantum degenerate gas of fermionic atoms was conducted by D. Jin's group in 1999 [49]. They showed that a magnetically trapped sample of ^{40}K atoms occupying two different internal states could be cooled to degeneracy using the same techniques that lead to the realization of Bose-Einstein condensation in the previous studies with ultracold bosonic gases, namely laser and evaporative cooling. Shortly thereafter, highly-degenerate gases were also realized by means of sympathetic cooling with bosons in a magnetic trap [50, 51, 52], and direct evaporative cooling of two-component ^{6}Li gases in an optical dipole trap [53, 54]. In the later technique, the degenerate gas was confined in a conservative optical potential which allowed for the use of an external magnetic field to tune the interactions by means of a Feshbach resonance. In so doing, the first realization of a strongly interacting degenerate Fermi gas was reported by J. Thomas' group in 2002 [20].

Accessing the magnetically tuned Feshbach resonance enabled a range of studies associated with strongly interacting Fermi gases exhibiting large attractive or repulsive pairwise interactions. At field values where the scattering lengths are large and positive, a gas of bosonic molecules can form. The molecular gas will eventually condense at sufficiently low temperatures to form a molecular BEC, as demonstrated by three groups in 2003 [55, 23, 56]. On the negative scattering length side of the resonance, no weakly-bound dimer states exist and the ground-state of the gas, which exhibits attractive pairwise interactions, is described by a Bardeen-Cooper-Schrieffer (BCS) superfluid phase. It is now well understood that the pairing mechanisms in both limits (BEC and BCS) are smoothly connected by a crossover through the resonance [21, 57, 58, 59].

Indeed, the demonstrated stability of two-component Fermi gases against two- and three-body loss and the possibility of tuning the pairwise interactions to realize quantum fermionic and bosonic phenomena by use of magnetically tuned Feshbach resonances has made these systems the standard for exploring so-called

BEC-BCS crossover physics. Notably, in 2004 Fermi condensates were observed by pair projection measurements using fast magnetic field sweeps [59, 57], and collective mode measurements have demonstrated superfluid transition behaviors in the damping behaviors of the gases [60, 21, 61, 62]. Additionally, radio-frequency and photo-emission spectroscopy has been used to explore the elementary excitation spectrum in the gases, revealing a pairing gap near the transition and inferring information about the sizes of the pairs [63, 64, 28, 65]. Finally, the observation of a vortex lattice in a rotating strongly interacting Fermi gas on both sides of the resonance is direct evidence for high temperature superfluidity in these systems [59].

A number of experiments have also studied the universality of strongly- interacting Fermi gases in the vicinity of a Feshbach resonance. At the peak of the resonance the gas is in the unitarity regime, where the s-wave scattering length diverges to $\pm\infty$. Here, there exists a universality that connects the unitary Fermi gas to that of an ideal Fermi gas, whose energies scale by a universal constant β [66, 67]. Detailed measurements have also been made of the hydrodynamic expansion of normal [20] and rotating [14, 68] strongly interacting Fermi gases, which also arises in a quark-gluon plasma [69, 19], as a consequence of very low viscosity hydrodynamics characteristic of a nearly perfect fluid. Recent measurements of the amplitude of the high momentum tail of the momentum distributions, called the contact, for Fermi gases in the BEC-BCS crossover have also proven useful for verifying such universal relations as the adiabatic sweep theorem and the generalized virial theorem [70] for strongly interacting Fermi systems.

Finally, the properties of two-component Fermi gases loaded into cubic optical lattice potentials (optical dipole traps made of standing wave laser light to create a regular lattice potential) have been recently explored. These lattice-confined systems are promising for simulating the low-temperature phase diagram of the Fermi Hubbard model [71] which predicts that, at sufficiently low temperatures, such phenomena as quantum magnetism and possibly even d-wave superfluid phases should emerge [72, 73, 74]. These experiments have revealed direct observation of the Fermi surface filling the first Brillouin zone [75], interaction-controlled transport [76], Mott and band insulating phases [77, 75, 78, 79], BCS superfluidity in a weak lattice potential [80], and anti-bunching reflecting the Pauli exclusion prin-

ciple [81]. Temperatures low enough to observe more complex quantum phases in a lattice such as Néel antiferromagnetism, strongly correlated Fermi liquids, spin liquids in frustrated geometries, or d-wave superfluidity have yet to be attained in cold-atom-based Fermi systems [82].

1.4 Three-Component Fermi Gases

Nearly all of the previous investigations of ultracold Fermi gases with tunable interactions have focused on mixtures of gases occupying two distinct internal states. The addition a third distinguishable component to the gas can drastically change the nature of the problem. Whereas the interactions of two-component samples can be fully described by a single s-wave scattering length (a), the pairwise interactions among the various components of a three-state gas are not necessarily equal, and multiple scattering resonances can exist simultaneously. Further, three-body interactions are no longer forbidden, allowing for the study of phenomena associated with the quantum mechanical three-body problem (e.g., Efimov physics) in ultracold multi-component Fermi gases .

In this thesis, I will discuss our recent experiments studying few-body interactions in dilute, ultracold gases of lithium-6 atoms occupying the three lowest-energy hyperfine spin states. This multi-component Fermi gas is unique in that three broad, overlapping Feshbach resonances exist which allow for simultaneous resonant enhancement of all three pairwise interaction strengths. Further, a zero-energy resonance at high fields causes the three pairwise interaction strengths to converge to an anomalously large value where a universal SU(3) symmetric description of the gas is appropriate. Also, the three generally unequal s-wave scattering lengths characterizing the system cross zero at fields below the Feshbach resonances, allowing for the study of very weakly-interacting three-component gases at these fields. For the majority of the fields studied, however, all three s-wave scattering lengths are unequal and exceed the characteristic range of the two-body potentials, so that the gas is generally in the threshold regime and exhibits universal behaviors.

A variety of interesting new phenomena can now be studied with these three-component systems. With the inclusion of three-body interactions, a spectrum

of Efimov states may now be supported [1, 83]. Theoretical investigations of Efimov's scenario for a system of three distinguishable equal-mass particles, however, becomes more complicated. Prior to our studies, the universal theories derived to calculate the influence of Efimov states on the three-body loss rates of an ultracold gas concentrated on systems described by a single resonantly enhanced scattering length. It was therefore not obvious how the universality of Efimov's scenario would translate for the ultracold system of three distinguishable particles studied in our experiments.

It is also interesting to consider the low-temperature properties of the three-component Fermi system in a regime where superfluid phases are expected for multiple pairs of components in the gas. It's not obvious to what extent such effects as pairing competition between multiple paired states and trion formation will have on the ground state of the gas [84, 85, 86, 87, 88, 89].

Excitement in this system is inspired by its close connection to strongly interacting quark matter. If the pairwise interactions are all attractive and of equal magnitude, the SU(3) symmetric gas is expected to exhibit a novel *atomic color superfluid* phase analogous to color superconductivity in quantum chromodynamics (QCD). Further, if the ratio of the interaction energy to the kinetic energy can be increased (e.g., in an optical lattice), the system is well described by a SU(3) symmetric Hubbard Hamiltonian. Here, a quantum phase transition to a Fermi liquid of trimers may be applicable for quantum simulation of the color superfluid to Baryon phase transition conjectured in QCD [90, 91, 92].

Future studies of the above phenomena, however, critically depend on the magnitude of the two- and three-body loss rates, particularly when two or more scattering lengths are resonantly enhanced. Two- and three-body loss and heating processes can impose stringent limits on the maximum achievable phase space density, in turn defining the degree to which quantum phenomena can arise in the systems. Further, the unambiguous observation of three-body loss resonances associated with Efimov trimer states requires negligible two-body loss [35].

Our early experiments were therefore dedicated to exploring few-body physics in ultracold gases of ^{6}Li atoms occupying the three lowest-energy hyperfine spin states. The primary observable in our experiments was the magnetic field dependence of the stability of the gas with respect to three-body loss. The measurements

were taken over a wide range of interaction strengths to answer such questions as "What is the stability of the gas against three-body decay in both the weakly- and strongly-interacting regimes?" and "How does the Efimov effect translate for non-identical particles characterized by multiple scattering resonances?". Our measurements are also applied to establish the feasibility of using this multi-component gas as a quantum simulator of iconic models in condensed matter and quantum field theory. These measurements are therefore an important first step for future studies of universality and exotic many-body phenomena in multi-component Fermi systems.

1.5 Thesis Outline

This dissertation reviews the general setup of Professor Ken O'Hara's Lab and the first set of experiments preformed to study the few-body physics of ultracold multi-component Fermi gases of ^{6}Li atoms with resonantly enhanced interactions. The thesis is organized as follows:

Chapter 2 provides a general overview of the properties of ultracold gases of ^{6}Li atoms occupying the three lowest-energy hyperfine spin states. The chapter begins with a brief description of the ground-state hyperfine structure of the atoms. The low-energy two-body scattering properties and inelastic loss rates of the gas are then considered, leading to a discussion of magnetically tuned Feshbach resonances in ground-state ^{6}Li atoms. Finally, the universal properties of ^{6}Li gases with resonantly enhanced interactions is discussed.

Chapter 3 summarizes the universal theory which describes the quantum mechanical three-body problem for particles with resonantly enhances pairwise interactions. We start by considering the simplified three-body system of identical bosons in hyperspherical coordinates to derive the universal form of the three-body potentials. The basics of Efimov's theories are then reviewed for understanding of the general properties of the Efimov trimer states. Additionally, the theoretical predictions for the variation of the three-body loss rates associated with the existence of the universal trimer state are reviewed as these rates are direct experimental observables useful in calculating the spectrum of Efimov trimer states for a given system. The extension of these universal theories to our system where three

distinguishable particles interact with three unique but resonantly enhanced scattering lengths is then briefly discussed. Finally, the effects of the finite temperature of the gas on measurements of the Efimov features are considered as pertaining to our experiments.

Chapter 4 provides an overview of the experimental apparatus used to create and probe degenerate and/or ultracold two- and three-component gases of fermionic ^{6}Li atoms over a range of magnetic bias fields spanning 0 to 1500 Gauss. Strict control over the ultra-high vacuum, magnetic, and optical environments experienced by the atoms are required to enable our experiments. The various components installed to cool a ^{6}Li Fermi gas from 465 ℃ to ultracold temperatures ranging from $\sim$ 2 μK to 30 nK, and prepare and probe equally populated incoherent mixtures of multi-component Fermi gases in thermal equilibrium for our few-body studies of these ultracold systems is discussed in detail.

Chapter 5 discussed the techniques used in our experiments both to produce degenerate and nearly-degenerate ultracold Fermi gases of ^{6}Li atoms occupying the three lowest-energy hyperfine states and to extract information about the gases using low-intensity absorption imaging techniques. Evaporative cooling is used to initially prepare two-component gases at ultracold temperatures which, at certain magnetic fields, leads to a long-lived molecular BEC as the gas is cooled to degeneracy. Manipulation of the internal atomic states using radio-frequency pulses and magnetic field gradients creates the incoherent three-state mixtures. Further, at high fields, spectroscopically resolved absorption imaging of the three atomic states can be used to extract information about the density, temperature, and degeneracy of each component of the gas. Finally, we discuss our method of adiabatically relaxing the gas into conservative large-volume trapping potentials to achieve extremely low temperatures and densities, enabling our studies in regimes characterized by strong pairwise interactions and high rates of three-body loss.

Chapter 6 reports on our first measurements of the stability of the gas to three-body loss along with the measurement of the three-body recombination rate coefficients for the three-state Fermi gas over a wide range of magnetic fields. We observed high stability when at least two of the three s-wave scattering lengths were small, rapid loss in the vicinity of the three Feshbach resonances, and two unexpected resonant loss features at fields below the Feshbach resonances, which

were later described by the existence of an Efimov trimer state at these fields. Recent analytic interpretations of the low-field three-body loss rates to characterize the nature of the Efimov state and the three-body loss rates in this system are discussed at the end of the chapter.

Chapter 7 reviews our recent experiments exploring the magnetic field dependent three-body recombination rates for a three-state Fermi gas of ^{6}Li atoms in the high field, strongly universal regime where all three pairwise interactions are large and attractive, with the goal of mapping out the spectrum of Efimov features near the scattering resonances. We observed enhanced three-body recombination attributable to an excited Efimov trimer state near the three-atom scattering threshold. Additionally, we demonstrate quantum degeneracy of a three-component Fermi gas in the high-field limit, where the multi-component Fermi gas becomes SU(3) symmetric. The end of the chapter discusses the implications of this research in terms of the theoretical study it has enabled and the various features that have been recently observed in three-component ^{6}Li gases in the high-field regime.

Chapter 8 briefly discusses many-body physics in two- and three-component Fermi gases. Various novel many-body phenomena have been theoretically predicted to emerge when a third spin component is added to the system. Our previous measurements of the stability of the three-component ^{6}Li gas in the high-field regime is used to determine the feasibility of experimentally studying some of this new physics using ultracold ^{6}Li gases occupying the three states discussed in this thesis. Then, a brief review of the physics of multi-component Fermi gases loaded into three-dimensional (3D) optical lattice potentials is discussed. For two-component Fermi gases, the lattice has been shown to enhance the critical temperature for BCS superfluid pairing, and quantum magnetic ordering is expected to emerge at low temperatures for repulsively interacting particles. At sufficiently low temperatures, lattice-confined three-component Fermi gases may exhibit multi-component superfluid phases in the high-field SU(3) symmetric regime and novel phases at lower fields which cannot be explained by the paradigm models in condensed matter theory. Finally, a theoretical investigation of a cooling method that we developed to filter high entropy-density atoms from a 3D optical lattice potential is discussed. We found that by using this method, a sample of fermionic atoms

can be prepared in the lattice potential at unprecedented low temperatures and uniform densities.

Chapter 9 concludes the dissertation by reviewing the achievements of this Ph.D. project and provides an outlook for future studies with ultracold multi - component Fermi gases.

Chapter 2

Fermi Gases

In our experiments, a three-component Fermi gas is comprised of ultracold ^{6}Li atoms in the three lowest-energy hyperfine spin states. At ultracold temperatures, the pairwise interactions among these particles can be simply described in terms of a single parameter, the s-wave scattering length a. By applying an external magnetic field, these s-wave scattering lengths can be tuned over a wide range due to a collisional scattering resonance known as a Feshbach Resonance. In the vicinity of this resonant feature, the s-wave scattering lengths may be tuned to the universal regime where the behavior of the gas is independent of the microscopic details of the inter-particle interactions. The ability to control the pairwise interactions among ultracold atoms to access the universal regime plays a crucial role in all experiments with strongly interacting Fermi gases.

^{6}Li has the remarkable property that three broad, overlapping Feshbach resonances exist among atoms occupying the three lowest-energy spin states, enabling studies of universal three-body physics where multiple attractive and/or repulsive pairwise interactions among particle can simultaneously affect the ground-state of the system with widely varying magnitude. Further, inelastic two-body loss of the atoms is negligible in the presence of a magnetic field due to both the Pauli exclusion principle, which inhibits collisions among identical fermions; and spin polarization of the valence electron, where hyperfine-changing transitions are highly suppressed. This chapter concentrates on the two-body interactions among ^{6}Li atoms in the three lowest-energy spin states to demonstrate that this is an ideal system for exploring universal three-body physics with ultracold Fermi gases.

2.1 ^{6}Li Hyperfine States

The majority of ultracold atomic physics experiments utilize the unique properties of alkali metal atoms, where the single unpaired valence electron yields a relatively simple atomic structure and spectra. The fermionic isotope ^{6}Li studied in our experiments is a light alkali metal atom with atomic number three and nuclear spin of one. We are primarily interested in the properties of the ground ($1s^2 2s^1$) and excited electronic states ($1s^2 2p^1$) of this isotope, given by the spectroscopic notation 2^2S and 2^2P respectively. The transition between these states are represented by the broad spectroscopic D-line.

The fine structure splitting of the D-line arises from the spin-orbit interaction for the unpaired valence electron moving in the electric field of the nucleus. This interaction is a magnetic dipole interaction between the intrinsic angular momentum $\mathbf{S}$ and the orbital angular momentum $\mathbf{L}$, which couple to the total angular momentum $\mathbf{J} = \mathbf{L} + \mathbf{S}$. The ground state of ^{6}Li is singular in the $|J, m_J\rangle$ basis with $S = 1/2$, $L = 0$, $J = 1/2$ expressed in spectroscopic notation as $2^2S_{1/2}$. The excited state, on the other hand, yields two J values ($S = 1/2$, $L = 1$, $J = 1/2$, $3/2$). This interaction term gives rise to the splitting of the spectroscopic D-line into the D_1 and D_2 lines corresponding to the $2^2S_{1/2} \leftrightarrow 2^2P_{1/2}$ and $2^2S_{1/2} \leftrightarrow 2^2P_{3/2}$ transitions respectively.

Further splitting of the spectroscopic D_1 and D_2 lines emerges due to the interaction energy of the nucleus, which has a non-spherical charge distribution and an intrinsic spin, with the electric and magnetic field of the valence electron. In ^{6}Li, the nuclear Hamiltonian includes electric monopole, magnetic dipole, and electric quadrupole interaction terms. The electric monopole interaction represents the electric interaction of the electron with the spherical part of the nuclear charge distribution, leading to an overall shift of all of the energy levels. The higher order terms, collectively known as the hyperfine interaction terms, lead to further splitting of the ground and excited states. The hyperfine Hamiltonian must therefore account for the nuclear angular momentum $\mathbf{I}$, with eigenstates that are represented in terms of the total atomic angular momentum $\mathbf{F}$, where $\mathbf{F} = \mathbf{J} + \mathbf{I}$.

An energy level diagram displaying the fine and hyperfine structure of the 2^2S and 2^2P lines is shown in Figure 2.1. The reported hyperfine splitting for the

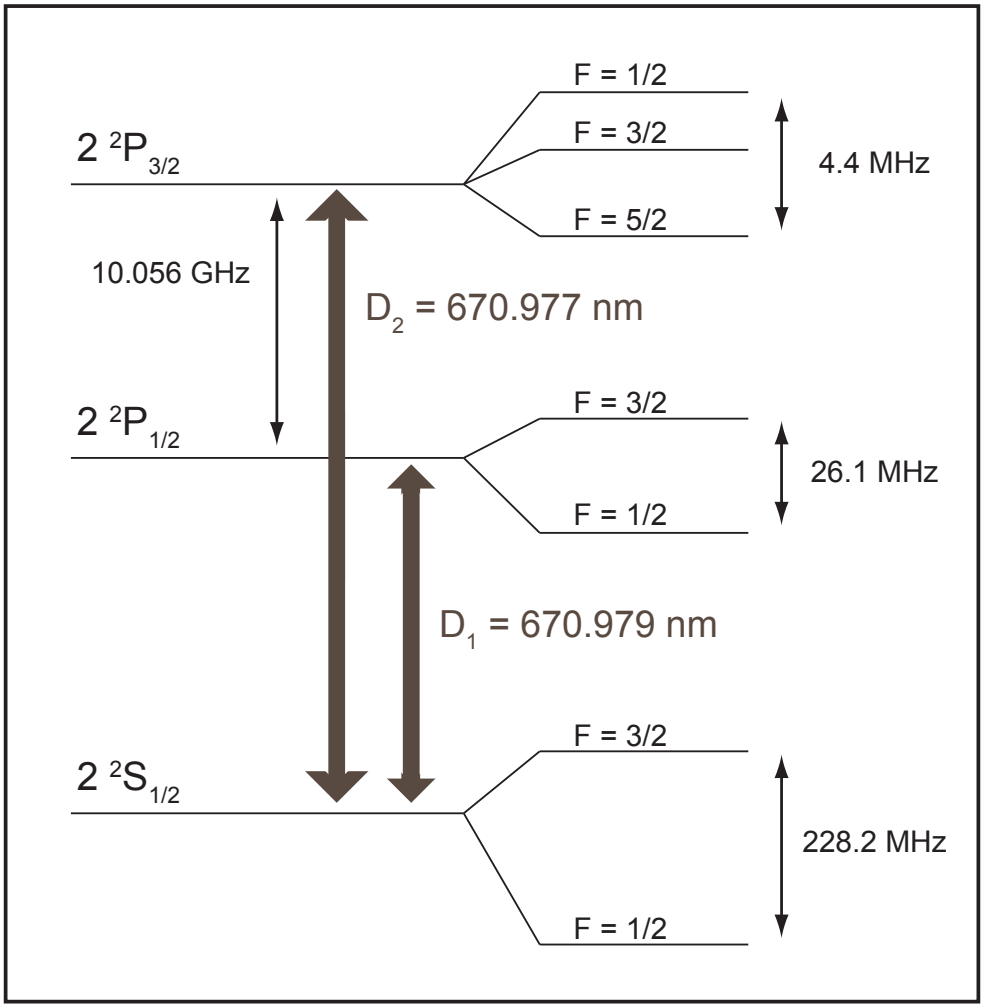

Figure 2.1. Energy level diagram of the fine and hyperfine structure of the 2^2S ground and 2^2P excited states of ^{6}Li. The energy level splittings are not to scale.

ground ($2^2S_{1/2}$) and excited ($2^2P_{1/2}$, $2^2P_{3/2}$) energy levels were measured in [93]. Further details on the atomic structure of ^{6}Li including an extensive analysis of the physical and optical properties of bulk and atomic ^{6}Li for application to atomic cooling and trapping experiments is given in Appendix A of [11]. This energy level structure essentially details the relevant spectroscopic transitions between the ground and 2P excited states in ^{6}Li in the absence of external fields.

Property	Symbol	Value
Total Electronic g-Factor	g_J ($2^2S_{1/2}$)	-2.0023010
	g_J ($2^2P_{1/2}$)	-0.6668
	g_J ($2^2P_{3/2}$)	-1.335
Nuclear Spin g-Factor	g_I	0.0004476540
Magnetic Dipole Constant (MHz)	$A_{2^2S_{1/2}}/h$	152.1368407
	$A_{2^2P_{1/2}}/h$	17.375
	$A_{2^2P_{3/2}}/h$	-1.155
Electric Quadrupole Constant (MHz)	$B_{2^2P_{3/2}}/h$	-0.10

Table 2.1. g-factors and Hyperfine constants for the 2^2S ground and 2^2P excited electronic states of ^{6}Li

2.1.1 Hyperfine States in a Magnetic Field

The majority of our experimental applications are preformed in the presence of a significant magnetic field (**B**). Even for magnetic fields as small as a few Gauss, the Zeeman interaction energy (E_{ZE}) is no longer small as compared to the hyperfine splitting (E_{hf}) for the 2^2S ground and 2^2P excited states of ^{6}Li. In this case, **F** is no longer a good quantum number and the total magnetic and hyperfine interactions must be considered in the $|\ J\ m_J,\ I\ m_I\rangle$ basis. The combined Hamiltonian which must be solved for the eigenenergies of the system in a static magnetic field is given by [94]

$$\begin{aligned} H_{int} &= H_{hf} + H_{ZE}, \\ H_{hf} &= A_J\ \mathbf{I}\cdot\mathbf{J} + \frac{B_J[3(\mathbf{I}\cdot\mathbf{J})^2 + 3/2(\mathbf{I}\cdot\mathbf{J}) - I(I+1)J(J+1)]}{2I(2I-1)\ J(2J-1)} \\ H_{ZE} &= -\mu_B(g_J\mathbf{J} + g_I\mathbf{I})\cdot\mathbf{B} \end{aligned} \tag{2.1}$$

where A_J and B_J are the magnetic dipole and electric quadrupole hyperfine constants for an atom in state J, and μ_B is the Bohr Magneton. These quantities along with the relevant g-factors for the two lowest-energy electronic levels of ^{6}Li are listed in Table 2.1.

For the electron in the $2^2S_{1/2}$ ground state (L = 0), the angular wavefunction is spherically symmetric and does not support the nuclear electric quadrupole interaction. The combined Hamiltonian can therefore be diagonalized yielding six eigenstates $|1\rangle$ - $|6\rangle$, expressed in terms of superpositions of the product states $|m_s,\ m_I\rangle$ [95]

$$\begin{aligned}
|1\rangle &= \sin\ \Theta_+\ |1/2\ 0\rangle - \cos\ \Theta_+\ |-1/2\ 1\rangle \\
|2\rangle &= \sin\ \Theta_-\ |1/2\ -1\rangle - \cos\ \Theta_-\ |-1/2\ 0\rangle \\
|3\rangle &= |-1/2\ -1\rangle \\
|4\rangle &= \cos\ \Theta_-\ |1/2\ -1\rangle + \sin\ \Theta_-\ |-1/2\ 0\rangle \\
|5\rangle &= \cos\ \Theta_+\ |1/2\ 0\rangle + \sin\ \Theta_+\ |-1/2\ 1\rangle \\
|6\rangle &= |1/2\ 1\rangle
\end{aligned} \tag{2.2}$$

where the states are numbered in order of increasing energy. The coefficients are defined as

$$\begin{aligned}
\sin\ \Theta_\pm &= \frac{1}{\sqrt{1+(Z^\pm+R^\pm)^2/2}} \\
\cos\ \Theta_\pm &= \sqrt{1-\sin^2\ \Theta_\pm} \\
Z^\pm &= \frac{\mu_B B}{A_{2^2S_{1/2}}}(-g_J(2^2S_{1/2})+g_I) \pm \frac{1}{2} \\
R^\pm &= \sqrt{(Z^\pm)^2+2}
\end{aligned} \tag{2.3}$$

The corresponding eigenenergies of the ground state levels $|n\rangle$, given in units of frequency (E/h where h is Planck's constant), are shown in Figure 2.2 as a function of applied magnetic field in units of Gauss (1 Gauss = 10^{-4} Tesla). Note that at zero field, the good angular momentum quantum numbers for the 2^2S ground state are $F = 1/2$ and $F = 3/2$. As the magnetic field is applied, the degeneracy of the $|F,\ m_F\rangle$ states are quickly lifted, resolving into the six calculated eigenstates. In the high field limit, known as the *Paschen-Bach regime* ($\mu_\mathrm{B}\ \mathrm{B} \gg A_{2^2S_{1/2}}$), the product states $|m_S\ m_I\rangle$ become good approximations to the true eigenstates of the Hamiltonian. The eigenstates then separate into spectroscopic triplets of the high-magnetic-field seeking states $|m_S = -1/2,\ m_I = 0, \pm 1\rangle$ and low- magnetic-field

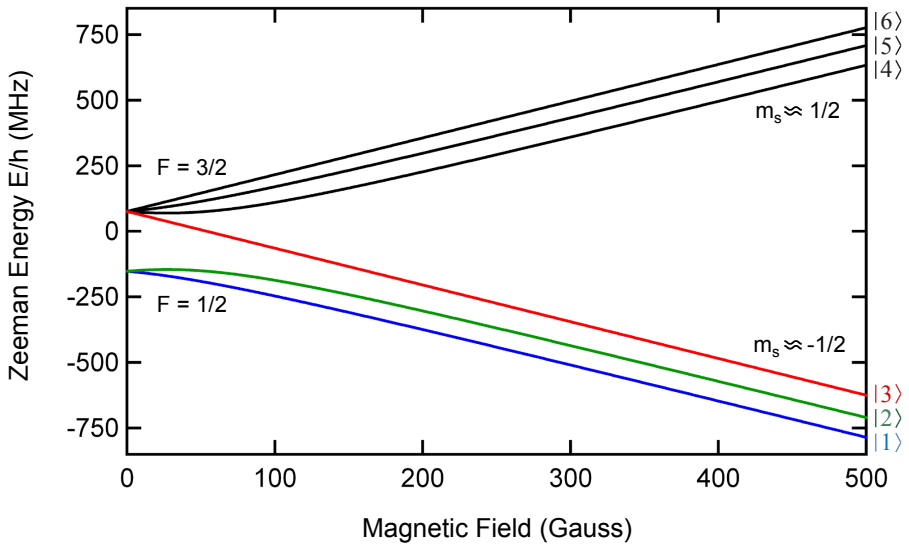

Figure 2.2. Magnetic-field dependence of the $2^2S_{1/2}$ ground state of ^{6}Li

seeking states $|m_S = 1/2,\ m_I = 0, \pm 1\rangle$.

Numerical results for the tuning of the $2^2P_{3/2}$ Zeeman states in a uniform magnetic field are shown in Appendix A, Figure A.2. The mathematica code from [11] numerically diagonalizes the interaction Hamiltonian, Equation 2.2, to determine how the eigenenergies of these atomic levels tune in a magnetic field. As shown in the figure, these states quickly enter the Paschen-Bach regime due to the small hyperfine splitting, and rapidly converge to the spectroscopic triplet states, described in the product basis $|J,\ m_J\rangle|I,\ m_I\rangle$, where the interaction energy is simply given by

$$E_{int} = \frac{\mu_B}{\hbar}(g_J m_J + g_I m_I)B + \frac{h}{2}A_{hf} m_I. \tag{2.4}$$

In the limit of high magnetic field, the energy splitting between the eigenstates for a given $|J, m_J\rangle$ triplet state asymptotes to the value of the hyperfine splitting for both the ground and excited electronic levels. This limiting behavior allows us to preform state-selective operations within the ground high-field seeking states over a wide range of magnetic fields with minimal sensitivity to the applied magnetic fields. In the following, I will discuss the low-energy scattering properties of a gas of ground-state fermionic ^{6}Li atoms to demonstrate the unique properties which emerge for this system under the influence of an applied magnetic field.

2.2 S-Wave Elastic Collisions

Two neutral alkali atoms scattering off each other interact primarily via a short-ranged electrostatic molecular potential V($\mathbf{R}$) in which the interaction depends only on the relative distance between the particles ($\mathbf{R}$= $\mathbf{r}_1$ - $\mathbf{r}_2$). In the center of mass frame of the two particles, the collisional problem reduces to the study of the scattering of a single particle by the spherically symmetric potential V($\mathbf{r}$). At large distances, V($\mathbf{r}$) is approximated by the *van der Waals* potential for neutral atoms with a $J = 1/2$ ground state which falls off as

$$V(r) \simeq -\frac{C_6}{r^6}. \tag{2.5}$$

At smaller distances, on the order of an atomic dimension, the atoms experience a strong Pauli repulsion as the electron orbitals overlap, which increases rapidly as $\mathbf{r} \to 0$. The net action of both the attractive long-range force and the repulsive short-range force produces a potential well that may support many bound molecular states. For low-energy collisions, the asymptotic behavior of the interaction potential is fixed by the van der Waals coefficient (C_6) which defines the characteristic length scale at which the kinetic energy of the relative motion of two atoms with reduced mass M equals their interaction energy.[96]

$$l_{vdw} = (2MC_6/\hbar^2)^{1/4} \tag{2.6}$$

For alkali-metal atoms, l_{vdw} can be much larger than the atomic scale, typically on the order of several nanometers, due to the strong polarizability of these atoms.

To describe the essential properties of the scattering states of ultracold atoms, a quantum mechanical treatment is necessary [97, 98, 99, 100, 101, 102]. In this formalism, an incident particle can be represented as a plane wave with momentum $\hbar k_i$. Scattering of this wave from the interaction region results in some of the wave amplitude leaving in the form of a spherical outgoing wave with momentum $\hbar k_f$. The final asymptotic wave function of the particle (ignoring normalization factors) is given by

$$\Psi(\mathbf{r}) = e^{i\mathbf{k}_i \cdot \mathbf{r}} + f(\mathbf{k}_f,\ \mathbf{k}_i)\frac{e^{ik_f r}}{r}. \tag{2.7}$$

In this expression, only the scattering amplitude $f(\mathbf{k}_f,\ \mathbf{k}_i)$ depends on the potential $\mathrm{V}(\mathbf{r})$. It can be shown that the differential scattering cross section can be calculated from the scattering amplitude from the following [97]

$$\frac{d\sigma}{d\Omega} = \frac{k_f}{k_i}|f(\mathbf{k}_f,\ \mathbf{k}_i)|^2. \tag{2.8}$$

For the case of elastic scattering from a central potential, the scattered wave function can be expanded in terms of *partial waves* (wave functions associated with states of well-defined angular momentum). In this basis, the scattering amplitude can be expressed in terms of the Legendre polynomials $\mathrm{P}_l(\mathrm{x})$ in the orbital angular momentum basis $|l\rangle$.

$$f(k,\ \theta) = \frac{1}{k}\sum_{l=0}^{\infty}(2l+1)e^{i\delta_l(k)}\sin[\delta_l(k)]P_l(\cos\theta) \tag{2.9}$$

where $\cos(\theta) = \hat{k}_f \cdot \hat{k}_i$ is the scattering angle of the particle and $\delta_l(k)$ is the acquired phase shift associated with the l^{th} partial wave. Finally, the total cross section can be derived from the imaginary part of the forward scattering amplitude using the *Optical Theorem* [102]

$$\begin{aligned} \sigma(k) &= \frac{4\pi}{k}\Im(f\{k,0\}) & (2.10)\\ &= \frac{4\pi}{k^2}\sum_{l=0}^{\infty}(2l+1)\sin^2[\delta_l(k)]. & (2.11) \end{aligned}$$

It is interesting to note that the *S-matrix* elements for the scattering event, which describe the overlap of the initial state (Ψ_i^+) with the time reversal of the final state (Ψ_f^-), are directly related to the acquired phase shift as [103]

$$\begin{aligned} \langle f|S|I\rangle &= \langle\Psi_f^-|\Psi_i^+\rangle & (2.12)\\ S_l(k) &= e^{2i\delta_l(k)}. & (2.13) \end{aligned}$$

In this partial wave basis, both the S-matrix and the total cross section are functions of the channel momentum k and the angular momentum l. We shall see that this basis is ideal for studying collisions in the limit of low energy, where high

angular momentum contributions are suppressed so that only a few partial-waves need to be considered.

The previous results generally considered the elastic scattering of a particle from a central potential V(**r**), which can be directly applied to the case of collisions among distinguishable particles. When considering scattering among identical particles, the above results must be slightly altered to account for the proper symmetry of the wavefunctions. It is impossible to distinguish between the final states for two identical particles when each scatter by an angle of θ or when they are backscattered by an angle of $\pi-\theta$. The differential cross section which accounts for this symmetry is given by

$$\frac{d\sigma}{d\Omega}_{id} = |f(k,\theta) \pm f(k,\pi-\theta)|^2. \tag{2.14}$$

Here $0 < \theta < \pi/2$ is the angle between the incident and scattered particles and the sign $(+/-)$ applies for bosons and fermions respectively. Aside from increasing the total scattering length by a factor of two due to quantum statistics, the extra term in Equation 2.14 varies the spectrum of available partial wave interactions. This can be seen from the angular dependence contained in the Legendre polynomials in Equation 2.9, which are related by $\cos(\pi-\theta) = -\cos(\theta)$, $P_l(\pi-\theta) = (-1)^l P_l(\theta)$. Therefore, the sum in Equation 2.11 only runs over even (odd) integers of l for identical bosons (fermions), so that only these partial waves contribute to the scattering amplitudes for identical particles.

The partial waves describe effective unidimensional scattering potentials which, for $l > 0$, have long-range centrifugal barriers ($V_{eff}(r) = V(r) + l(l+1)/r^2$). Much of the utility of using ultracold gases lies in the fact that the energy of this barrier can be much larger than the kinetic energy of the colliding atoms. For ^{6}Li atoms, the angular momentum barrier for the van der Waals potential is greater than $k_B * 6.5$ mK for all partial wave scattering channels above $l = 0$ [104]. In the low temperature limit ($k \to 0$), all partial-wave cross sections except for the s-wave ($l = 0$) contribution vanish as E^{-2l} [103], where $E = \hbar^2 k^2/(2M_r)$ is the kinetic energy of the incident particle. Thus, for the ultracold temperatures relevant to this thesis ($T \leq 2\ \mu K$), all but the s-wave scattering amplitudes can be neglected. Considering the previous discussion of collisions among indistinguishable particles, it

is found that s-wave interactions are therefore forbidden among identical fermions. Interactions among spin-polarized fermions at ultracold temperatures are highly suppressed [105] and for this reason, we use mixtures of atoms in different internal spin states throughout most of our experiments.

To determine the ultracold collisional cross section, it is convenient to expand the s-wave phase shift in terms of k^2 [106, 101].

$$k\cot(\delta_0(k)) = -\frac{1}{a} + \frac{1}{2}r_e k^2 + \cdots \tag{2.15}$$

$$a = -\lim_{k\to 0}\frac{\tan\delta_0}{k} \tag{2.16}$$

where a is the s-wave scattering length and r_e is the effective range describing the distance over which the distorted wave differs from a free wave. The limiting behavior of the total scattering cross section at zero-energy is given by

$$\lim_{k\to 0}\sigma = \frac{(C)\ 4\pi a^2}{1+k^2a^2}. \tag{2.17}$$

The constant C depends on the nature of the interacting particles, where $C = 1$ for scattering between distinguishable particles and $C = 2$ or 0 for identical bosons and fermions respectively.

The physical interpretation of the s-wave scattering length is given in [101]. In the low-energy limit, the s-wave scattering length is defined as the distance between the center of the scattering potential and zero-crossing of the asymptotic radial wavefunction on the r axis. The value of a therefore represents how much the particle wavefunction is modified by the scattering potential. Further, the sign of the scattering length defines whether the wavefunction is repelled from or attracted to the origin, where positive (negative) scattering lengths correspond to repulsive (attractive) interactions between the particles.

For finite energies ($k \neq 0$), so long as the collisions are sufficiently low-energy that the de Broglie wavelength (λ_{dB}) is much larger than the characteristic range of interactions ($\lambda_{dB} \gg r_e$), the atoms undergoing pairwise collisions cannot resolve the microscopic properties of the potential and the scattering length dominates the description of the interaction. For weak interactions, the s-wave scattering length is much smaller than the both the de Broglie wavelength of the colliding

atoms and the average inter-particle separation ($a \ll k^{-1},\ n^{1/3}$). In this limit, the low-energy scattering amplitude $f \to -a$ and cross section $\sigma \to (C)\ 4\pi a^2$ can be fully described by the s-wave scattering length.

In this limit, the interaction potential can be treated as an effective contact interaction using the Born approximation [95, 107]

$$V(\mathbf{r}) = g\delta(\mathbf{r}) = \frac{4\pi\hbar^2 a}{M_r}\delta(\mathbf{r}). \tag{2.18}$$

This approximation is generally valid for ultracold collisions in the dilute limit, where both the de Broglie wavelength and the inter-particle spacing $n^{-1/3}$ greatly exceed the characteristic range of the potential.

2.3 Inelastic Collisions

In the previous discussion, purely elastic two-body collisions were considered. Since ^{6}Li atoms have internal degrees of freedom, there is the additional possibility for inelastic internal-state-changing collisions that may lead to heating and loss of our confined atoms. It is therefore necessary to consider the possible inelastic processes that can occur for a multi-component Fermi gas as these loss-mechanisms will determine the dominant physical processes that we can observe.

For a N-body problem where there exists only one possible scattering state (channel), the phase shift $\delta(k)$ must be real due to the unitarity of the S-matrix, which states that particle flux must be conserved. When the atoms undergoing a collision have internal structure, allowing for more than one possible interaction potential, a coupled-channel treatment of scattering may be necessary. Transitions to other channels can occur in such a case and the particle flux of a single channel is no longer necessarily conserved. For simplicity, I will denote the entrance channel as $|i\rangle$ and all other coupled channel states as $|j\rangle$. The phase shift associated with a particular channel $\delta(k)$ will therefore be complex where

$$S_i = e^{2i(\delta_{ii}+i\delta_{ji})} = e^{-2\delta_{ji}}e^{2i\delta_{ii}}. \tag{2.19}$$

The real part of the complex phase δ_{ii} gives the phase shift associated with

elastic scattering. The imaginary part δ_{ji} makes $|S| \neq 1$, which implies the inelastic gain or loss of particle flux depending on the sign. In the low-energy limit, the rate for inelastic transitions is given by

$$\lim_{k_i \to 0} R_{i \to j} = G_{i \to j} n_i \tag{2.20}$$

$$G_{i \to j} = \frac{\pi \hbar}{M_r k_i} |S_{ji}|^2 \tag{2.21}$$

where $G_{i \to j}$ is the inelastic decay rate constant, n_i is the density of the atoms in the entrance channel and k_i is the wavevector of the atoms before the collision.

In this section, I will briefly discuss the relevant inelastic two-body processes that can occur among ultracold atoms occupying the three lowest-energy spin states in ^{6}Li ($|1\rangle$, $|2\rangle$, $|3\rangle$). For an extensive discussion of these processes, refer to [95]. Due to energy and momentum conservation, two-body interactions cannot drive transitions between free atoms and bound molecular states. Therefore, we only need to consider hyperfine-changing collisions here. Three-body interactions, which constitute the primary observable in our experiments, will be discussed in detail in Chapter 3.

In the asymptotic limit, the eigenstates of two colliding ^{6}Li atoms in our system are the states $|1\rangle$, $|2\rangle$, or $|3\rangle$. When the two fermions collide, they approach each other in an antisymmetric combination $|\{\alpha,\ \beta\}-\rangle$, where α and β are one of the eigenstates. For s-wave interactions, this means that for interactions to exist, the total spin wave functions χ must be antisymmetric.

$$|\{\chi_1,\ \chi_2\}-\rangle = \frac{1}{\sqrt{2}}(|\chi_1\rangle|\chi_2\rangle - |\chi_2\rangle|\chi_1\rangle) \tag{2.22}$$

The two-body collision therefore consists of colliding particles which approach each other in an entrance channel $|i\rangle = |\{\alpha,\ \beta\}-\rangle$ and recede from each other in one or more exit channels $|j\rangle = |\{\alpha',\ \beta'\}-\rangle$. For two ground state alkali atoms, the interaction potential is given by the sum of a central electrostatic interaction potential $V^c(\mathbf{r})$ and a magnetic dipole-dipole interaction potential $V^d(\mathbf{r})$. The dipole-dipole interaction is much weaker than the electrostatic interaction and therefore has been neglected in the previous discussion of the low-energy elastic scattering properties of the gas. When the inelastic collision rate due to $V^c(\mathbf{r})$

vanishes, however, $V^d(\mathbf{r})$ must be considered as it gives the dominant inelastic rate constant.

As discussed previously, s-wave collisions among particles in the same spin state are strictly forbidden, which can also be seen from Equation 2.22 $|\{\alpha,\ \alpha\}-\rangle = 0$. Therefore, only three entrance channels must be considered in an ultracold gas of ^{6}Li atoms occupying the $|1\rangle,\ |2\rangle,\ |3\rangle$ ground states ($|\{2,\ 1\}-\rangle,\ |\{3,\ 1\}-\rangle$ and $|\{3,\ 2\}-\rangle$). The stability of a gas of ultracold ^{6}Li atoms only occupying the two lowest-energy hyperfine states $|1\rangle$ and $|2\rangle$ to inelastic loss has been discussed in detail [95]. This mixture has been the workhorse of the ultracold ^{6}Li experiments to date attributed both to the existence of a the broad Feshbach resonance in this channel and because this mixture is virtually impervious to inelastic collisions in the low-temperature limit. In the following, I will show that the same mechanisms inhibit the inelastic two-body collisions for all of the entrance channels relevant to our experiments.

2.3.1 Spin-Exchange Collisions

For collisions among ground state neutral alkali atoms, depending on whether the valence electron from each atom couple to form a singlet spin state ($S = S_1 + S_2 = 0$), or a triplet spin state ($S = S_1 + S_2 = 1$), the atoms will approach along either a singlet $V_s(\mathbf{r})$ or triplet molecular potential $V_t(\mathbf{r})$. For our ultracold ^{6}Li gases, the single potential approximation is not justified because the spin of the valence electron is coupled to the spin of the nucleus through the hyperfine interaction. The valence electrons from two colliding atoms are therefore coupled into a superposition of the triplet and singlet states, and the collisions cannot be described simply by scattering from either potential.

Interactions by means of the central (singlet and triplet) potential is given by $V^c(\mathbf{r}) = V_s(\mathbf{r})P^s + V_t(\mathbf{r})P^t$ where P^s and P^t denote projection operators onto the singlet and triplet total-electron-spin subspaces [108]. A central potential cannot change the orbital angular momentum and hence total angular momentum conservation requires that the total spin angular momentum is also conserved in the collision. Therefore, $V^c(\mathbf{r})$ only couples channels with the same $M_F = m_{f1} + m_{f2}$ where m_{fn} is the spin projection of atom n in the F-basis. The

entrance channel $|\{2,\ 1\}-\rangle$, were $M_F = 0$, is therefore coupled to four other channels: $|\{2,\ 1\}-\rangle \rightarrow |\{4,\ 5\}-\rangle$, $|\{6,\ 3\}-\rangle$, $|\{5,\ 2\}-\rangle$, and $|\{4,\ 1\}-\rangle$. All of these states have much higher energy than the $|\{2,\ 1\}-\rangle$ mixture, making the reactions endothermic. A thermal energy of at least 10 milliKelvin would be required to make any of these spin-exchange transitions and therefore, for the ultracold collisions considered here these higher-lying channels are closed.

The only available spin-exchange collision in the $|1\rangle$, $|2\rangle$, $|3\rangle$ mixture is the $|\{3,\ 1\}-\rangle \rightarrow |\{4,\ 2\}-\rangle$ reaction, where all other processes are either energetically forbidden or require higher partial-wave scattering, which is forbidden at ultracold temperatures. In the absence of a magnetic field, these channels will be energetically degenerate, leading to a finite inelastic spin-exchange rate constant $G^c_{31\rightarrow 42}$. As soon as a magnetic field is applied however, the degeneracy is lifted and the $|\{4,\ 2\}-\rangle$ channel will become closed for field values where the required energy for the $|\{3,\ 1\}-\rangle \rightarrow |\{4,\ 2\}-\rangle$ reaction exceeds the available thermal energy of the atoms. In this limit, all of the inelastic spin-exchange collisions in the high-field-seeking ground states are fully suppressed, and the dipole-dipole interaction provides the dominant mechanism for inelastic two-body reactions.

2.3.2 Dipolar Relaxation Collisions

The magnetic dipolar interaction potential $V^d(\mathbf{r})$ predominantly arises from the electron-electron magnetic dipole interaction. Although electron-nucleon, and nucleon-nucleon magnetic dipole interactions exist, the nuclear magnetic moment μ_n is several orders of magnitude smaller than the Bohr magneton μ_e. The corresponding dipolar decay rate constants are smaller by a factor of $(\mu_n/\mu_e)^2 \simeq 2\times 10^{-5}$ [109] and are therefore neglected here. The magnetic dipole-dipole interaction can therefore be written in terms of the electron spin operators $\mathbf{S}_1$ and $\mathbf{S}_2$ as

$$V^d(\mathbf{r}) = \frac{\mu_0(2\mu_B)^2}{4\pi r^3}[\mathbf{S}_1\cdot\mathbf{S}_2 - 3(\mathbf{S}_1\cdot\hat{\mathbf{r}})(\mathbf{S}_2\cdot\hat{\mathbf{r}})]. \tag{2.23}$$

where μ_0 is the permeability of free space.

This interaction transforms as spherical tensors of rank two in both coordinate

and spin space, which can be written in the form [108]

$$V^d(\mathbf{r}) = -\left(\frac{24}{5\pi}\right)^{1/2} \frac{\mu_0 \mu_B^2}{r^3} \sum_{\mu=-2}^{2} Y^*_{2\mu}(\hat{\mathbf{r}}) \Sigma_{2,\mu} \tag{2.24}$$

where $Y_{lm}(\hat{\mathbf{r}})$ is a spherical harmonic and $\Sigma_{2,\mu}$ is a spherical tensor of rank two made up from the two spin operators with components

$$\Sigma_{2,0} = -\sqrt{\frac{3}{2}}(S_{1z}S_{2z} - \mathbf{S}_1 \cdot \mathbf{S}_2/3) \tag{2.25}$$

$$\Sigma_{2,\pm 1} = \pm\frac{1}{2}(S_{1z}S_{2\pm} + S_{1\pm}S_{2z}) \tag{2.26}$$

$$\Sigma_{2,\pm 2} = -\frac{1}{2}S_{1\pm}S_{2\pm} \tag{2.27}$$

This interaction can induce transitions in which the orbital angular momentum quantum number changes by 0 or ± 2, and the total electron spin projection of the atoms changes by 0, ± 1, or ± 2. Two atoms colliding in a s-wave entrance channel can therefore be scattered to a d-wave state, where the angular momentum is provided by the electron spins.

To understand what channels can be coupled by $V^d(\mathbf{r})$, it is instructive to refer to Equations 2.3, in which the eigenstates of the $2^2S_{1/2}$ ground state of ^{6}Li are expressed in the $|m_S,\ m_I\rangle$ basis. Here we are considering the possible exothermic inelastic collisions that might occur among atoms in a mixture of the high-field seeking states in the range of magnetic fields above $\sim$ 10 Gauss, in which the eigenstates $|1\rangle \rightarrow |6\rangle$ are well resolved.

For the lowest-energy entrance channel, $|\{2,\ 1\}-\rangle \rightarrow |1\rangle_1, |1\rangle_2$ is the only available exothermic reaction. In this case, however, the initial state has an antisymmetric spin wave function requiring a symmetric spatial wave function, whereas the final state has a symmetric spin wave function requiring an antisymmetric spatial wave function. As discussed previously, the s-wave entrance channel wave function can only couple to s-wave and d-wave (symmetric) exit channel wave functions for inelastic dipolar collisions. Therefore, the magnetic dipole-dipole interaction must preserve the total spin symmetry of the system. The lowest-energy entrance channel is therefore fully immune to hyperfine changing inelastic collisions at ultracold temperatures.

This is not necessarily the case for collisions among all of the relevant entrance channels. In fact, there are three exothermic hyperfine changing collisions that are allowed for atomic gases of ^{6}Li atoms occupying the three lowest-energy spin states: the single spin flip transitions $|\{3,\ 1\}-\rangle \rightarrow |\{2,\ 1\}-\rangle$ and $|\{3,\ 2\}-\rangle \rightarrow |\{3,\ 1\}-\rangle$, and a two spin-flip process $|\{3,\ 2\}-\rangle \rightarrow |\{2,\ 1\}-\rangle$. These decay channels lead to finite inelastic magnetic dipole-dipole rate constants for each transition $G^d_{31\rightarrow 21}$, $G^d_{32\rightarrow 31}$, and $G^d_{32\rightarrow 21}$.

The decay rates for transitions from the initial state $|\{\alpha,\ \beta\}-\rangle$ to a final state $|\{\alpha',\ \beta'\}-\rangle$ are essentially given by Fermi's golden rule [110]. For the case of alkali-atoms interacting at $T = 0$, the inelastic dipolar rates due to these couplings are approximated by [108]

$$G^d_{\alpha,\ \beta\rightarrow\alpha',\ \beta'} \propto v'_{\alpha',\ \beta'} \sum_{\mu} |\langle \alpha',\ \beta'|\Sigma_{2,\mu}|\alpha,\ \beta\rangle|^2 \tag{2.28}$$

where $v'_{\alpha',\ \beta'} = \sqrt{2(\epsilon_\alpha + \epsilon_\beta - \epsilon_{\alpha'} - \epsilon_{\beta'})/M_r}$ is the relative velocity gained in the exothermic reaction from the initial state with energy $\epsilon_i = \epsilon_\alpha + \epsilon_\beta$ to the final state with energy $\epsilon_f = \epsilon_{\alpha'} + \epsilon_{\beta'}$.

Experimental and theoretical investigations of the stability of an ultracold gas of ^{6}Li atom in a $|3\rangle - |1\rangle$ mixture at a bias field $B = 8.3$ Gauss have determined the low-field decay rate constant for the $|\{3,\ 1\}-\rangle$ entrance channel to be $G_{31\rightarrow 21} \ll 2\times 10^{-14}$ cm^3/sec [111]. For a gas with a density of $n = 10^{12}$/cm^3, this corresponds to an inelastic dipolar collision rate of $R_{31\rightarrow 21} \ll 0.02$/sec. From Equation 2.28, it can be assumed that at low fields, $G^d_{31\rightarrow 21} \sim G^d_{32\rightarrow 21} > G^d_{32\rightarrow 31}$, where the single spin flip process from state $|3\rangle \rightarrow |2\rangle$ are dominant over the $|2\rangle \rightarrow |1\rangle$ transitions attributed to the greater energy released in this reaction.

At high magnetic fields, the matrix terms in Equation 2.28 becomes suppressed, attributed to the spin polarization of the valence electron. The magnetic field dependence of the spin-flip transitions are scaled by the coefficients $\sin\Theta_\pm$ and $\cos\Theta_\pm$, given in Equation 2.4 where

$$\lim_{B\rightarrow\infty} \sin\Theta_\pm = \frac{\mathrm{A}_{2^2\mathrm{S}_{1/2}}}{\sqrt{2}\mu_B B} \qquad \lim_{B\rightarrow\infty} \cos\Theta_\pm \rightarrow 1. \tag{2.29}$$

For all of the dipolar transitions that we are considering, at high magnetic fields

$G^d_{i\to j} \propto (\sin\Theta_\pm)^2$, suppressing the total inelastic dipolar rate constants G^d by approximately *two orders of magnitude* at an applied magnetic field value of 1000 Gauss. Therefore at the relevant densities and timescales for our experiments ($n < 10^{12}/\mathrm{cm}^3$, $t \sim 10$ sec) the effects of inelastic two-body hyperfine-changing processes are negligible.

2.4 Scattering Resonances

Resonant scattering in atomic and molecular systems has been a subject of intense investigation since the earliest days of quantum physics. A resonance occurs when the s-wave scattering phase changes by π over a relatively narrow range of energy. For collisions among neutral atoms, resonant phenomena is generally attributed to the presence of a molecular state that is coupled to the scattering state of the colliding atoms. Such resonances may be due to a vibrational level either at the dissociation energy or trapped behind a repulsive barrier of a single molecular potential (*shape resonance*), or by coupling to a bound state which has a different symmetry and potential than that of the colliding atoms (*Feshbach resonance*). From low-energy scattering theory, it is known that the presence of a molecular level which is barely above (below) the energy of the scattering continuum leads to a large negative (positive) scattering length that increase in magnitude as the energy of the bound level approaches the continuum and diverges when these two levels are degenerate [101].

To understand the physical origins of Feshbach resonances, consider the interactions among ground-state, high-field seeking, neutral alkali atoms in the presence of a large externally applied magnetic field. The atoms predominantly approach along the triplet molecular potential (entrance channel), where the singlet state is Zeeman shifted to a higher energy that greatly exceeds the available kinetic energy of the ultracold atoms. Here, the transitions to the continuum of the singlet potential are forbidden (closed channel). This potential is important for the physics discussed however, because it may support bound molecular states near the threshold of the entrance channel.

The ability to tune the interactions in such a system lies in the fact that the scattering states have different magnetic moments ($\Delta\mu$), allowing for the energy

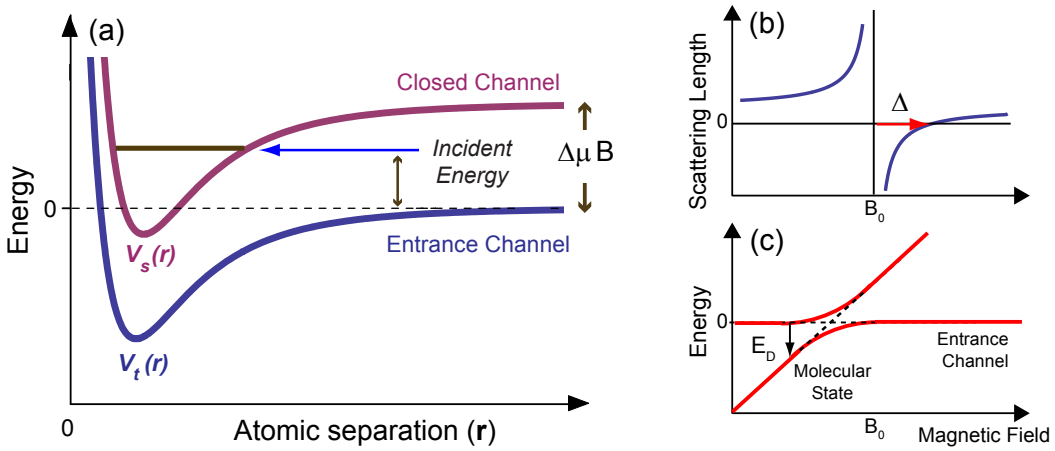

Figure 2.3. (a) A Feshbach resonance occurs when a bound molecular state in a closed channel energetically coincides with the collision energy of the particles in the entrance channel. (b) By varying the applied magnetic field in the vicinity of the resonance location at B_0, the s-wave scattering length can be widely varied to large positive and negative values, diverging at the resonance location. (c) As the molecular level is energetically tuned through the scattering continuum, coupling of the entrance and closed channels dresses the scattering and molecular states. This causes an avoided crossing which adiabatically connect these levels as the magnetic field is varied.

difference between the scattering state in the open channel and the molecular state in the closed channel to be tuned with respect to each other using an externally applied magnetic field, as shown in Figure 2.3(a). When these states energetically approach each other even a weak coupling, given by the hyperfine interaction for our ground-state ^{6}Li atoms, can lead to strong mixing between the two channels. Although, for elastic collisions, the atoms enter and leave the interaction in the same channel state, the coupling allows the atoms to occupy a virtual molecular state for a finite time, altering the scattering phase shift and allowing the scattering length to become resonantly enhanced. This phenomenon is called a magnetically tuned Feshbach resonance and allows the interactions to be externally tuned to yield arbitrarily large positive and negative scattering lengths.

The enhancement of the two-body interactions that arise from the coupling of a discrete state to the continuum was first studied by H. Feshbach and U. Fano in the framework of nuclear [112] and atomic physics [113] respectively. The response of the s-wave scattering length a as a function of the applied magnetic field B for a magnetically tuned Feshbach resonance can be described, in the absence of

inelastic loss, by a simple expression [114].

$$a(B) = a_{bg}\left(1 - \frac{\Delta}{B - B_0}\right) \tag{2.30}$$

This expression, which is plotted in Figure 2.3(b), demonstrates that the Feshbach resonance occurs at a magnetic field B_0 when the scattering length diverges $a \to \pm\infty$. The width of the resonance is denoted by Δ, which also gives the zero crossing of the scattering length at $B = B_0 + \Delta$. For magnetic fields far detuned from the resonance position, the scattering length is well approximated by the background scattering length a_{bg}. It is important to note that both a_{bg} and Δ can be either positive or negative. More details on the applications of Feshbach resonances to ultracold atom experiments can be found in a recent review article [9]

2.4.1 Resonant Scattering in ^{6}Li

The three lowest-energy spin states of ^{6}Li studied in this thesis have the amazing property that both shape and Feshbach resonances allow for resonantly enhanced pairwise interactions in the presence of reasonably large magnetic field. Shielding of the repulsive force between the ^{6}Li nuclei in the singlet state leads to a relatively deep singlet potential which supports 38 vibrational bound states and exhibits a s-wave singlet scattering length of $a^s = +45.16\ a_0$ [19, 115], where $a_0 \approx 0.5\mathring{A}$ is the Bohr radius. The triplet potential, on the other hand, is much shallower due to the vanishing probability density for the valence electrons between the nuclei. This potential supports 9 bound states and exhibits a zero-energy resonance where the energy of the virtual $\nu = 10$ vibrational state is within 0.03% of the dissociation energy of $V_t(\mathbf{r})$ [95], leading to an anomalously large triplet s-wave scattering length $a^t = -2140\ a_0$ [115].

At sufficiently high magnetic fields ($B > 100$ Gauss), atoms in the three lowest-energy spin states ($|1\rangle$, $|2\rangle$, $|3\rangle$) become predominantly electron spin polarized, with $m_S = -1/2$ in the $|m_S,\ m_I\rangle$ basis. Pairwise interactions between the atoms in these states are described by three s-wave scattering lengths a_{12}, a_{23} and a_{13}. In the high field limit the atoms predominantly approach along the shallow triplet potential. The background s-wave scattering length for the atoms then converges

Scattering Channel	Partial Wave	B_0(Gauss)	Δ(Gauss)
$\|1\rangle$ $\|2\rangle$	s	834.1	-300
$\|2\rangle$ $\|3\rangle$	s	811.2	-222.3
$\|1\rangle$ $\|3\rangle$	s	690.4	-122.3
$\|1\rangle$ $\|2\rangle$	s	543.25	0.1
$\|1\rangle$ $\|1\rangle$	p	159.14	na
$\|1\rangle$ $\|2\rangle$	p	185.09	na
$\|2\rangle$ $\|2\rangle$	p	214.94	na

Table 2.2. Properties of the observed s- and p-wave Feshbach resonances for ^{6}Li in the three lowest-energy spin states, taken from Reference [9]

to $a_{\alpha\beta} \rightarrow a^t$ where α, β represent atoms in any of the high-field seeking states. This limiting behavior opens the exciting possibility of studying strongly interacting three-component Fermi gases in the SU(3) symmetric regime where all of the pairwise interactions are effectively identical.

Below 1000 Gauss, a molecular state in the highest vibrational level of the singlet potential comes into resonance with the entrance channel. This bound state is split into multiple hyperfine states with $F = 0$, $m_F = 0$ and $F = 2$, $m_F = \pm 2, \pm 1, 0$ due to the coupling between the $I = 1$ nuclear spins of each atom. Therefore, each binary mixture exhibits Feshbach resonances with the amazing property that there exists three broad s-wave resonances which all overlap [115]. This allows for simultaneous resonant enhancement of the three pairwise interaction strengths and coexisting attractive and repulsive interactions to study a wide range of strongly-interacting phenomena. Figure 2.4 shows the magnetic field dependence of the scattering lengths a_{12}, a_{23} and a_{13} in units of the Bohr radius a_0, from a coupled channel calculation by P. Julienne at NIST, [116], based on precise measurement of the interaction parameters [115].

In addition to the broad Feshbach resonances, a number of other two-body resonant features are also present below 1000 Gauss. In the $|1\rangle - |2\rangle$ scattering channel, an extremely narrow Feshbach resonance exists with a width of only ~ 100 mG [117]. Further, p-wave resonances, associated with p-wave rotational levels of the $\nu = 38$ bound state of the singlet potential, have been observed in the $|1\rangle - |1\rangle$, $|1\rangle - |2\rangle$, and $|2\rangle - |2\rangle$ scattering channels [118, 119]. An overview of the Feshbach

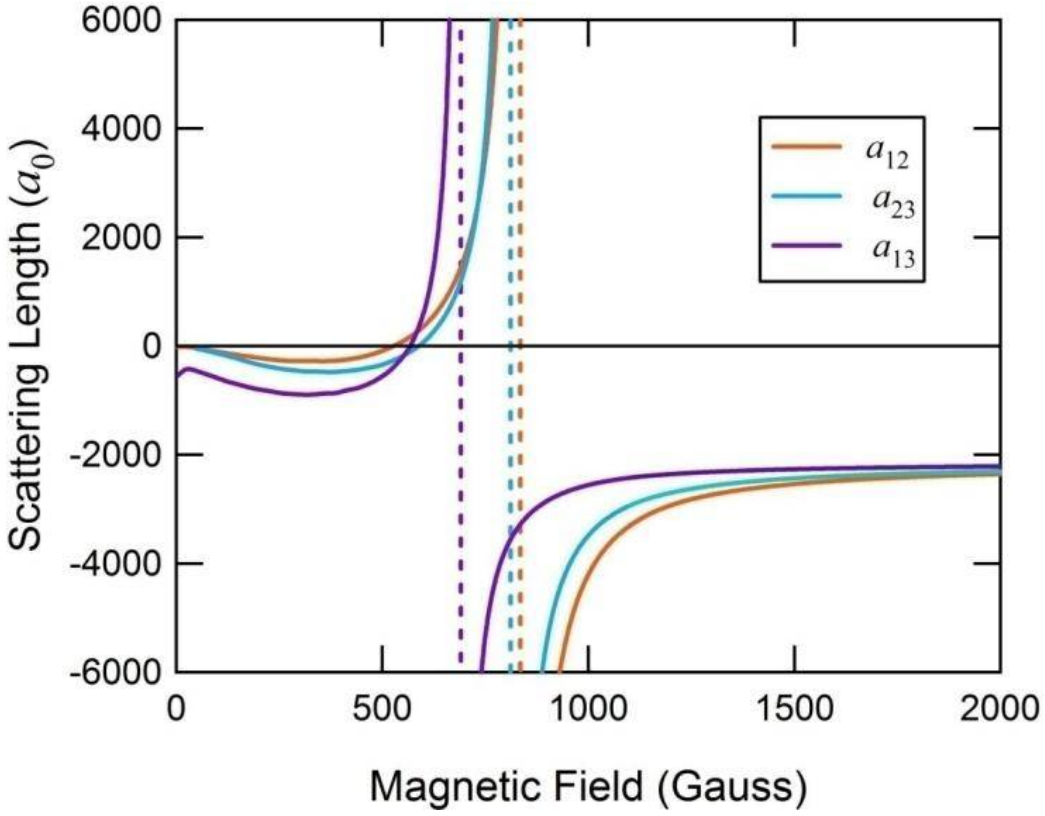

Figure 2.4. Variation of the scattering length with respect to applied magnetic field for the three lowest-energy spin states of ^{6}Li

resonances observed in ^{6}Li is given in Table 2.2.

2.5 Universality

Universality is a fundamental concept in physics. It illustrates the ability to describe the long-rang behaviors of various systems with expressions that only depend on a small set of universal constants. In other words, universal physical systems behave identically under certain limits regardless of their microscopic properties. Universality is prevalent in the physics of ultracold atomic gases where resonant enhancement of the pairwise interactions allows the low-temperature scattering properties to be solely described by the s-wave scattering length a. In fact, the quantum simulation of condensed matter, nuclear, and particle physics phenomena with ultracold atoms is dependent on the universal behaviors of these gases.

In our experiments, the characteristic range of interactions r_0 is given by the van der Waals length scale, discussed in section 2.2, where $l_{vdw} = 62.5\ a_0$ for ^{6}Li. When $a \gg l_{vdw}$, the scattering length dominates over the microscopic properties of the interaction potential. This constitutes the *universal* regime in which the two-body properties of the gas depend only on the scattering length (We will see in Chapter 3 that an additional three-body parameter κ_* is required to describe the three-body properties of the system). In this regime the pairwise interactions are dominated by the value of the scattering length, where first-order corrections to the universal theory scale with powers of l_{vdw}/a [1].

In the vicinity of a Feshbach resonance, where the scattering state in the open channel and the molecular state in the closed channel are strongly coupled, the scattering length can be very large. For *entrance-channel dominated resonances*, the system exhibits universal properties over a large fraction of the resonance width, typically associated with relatively broad resonances ($\Delta > 1$ Gauss). In contrast, narrow resonances are typically *closed-channel dominated resonances*, where a small fraction of the resonance width is in the universal regime. One of the most interesting aspects of Feshbach resonances is that in the universal regime, for positive values of a, a dressed molecular state exists with a binding energy given by

$$E_D = \frac{\hbar^2}{2Ma^2}. \tag{2.31}$$

In this regime, the details of the interaction become irrelevant and all of the properties of the dimer are characterized by the scattering length a. The molecular wave function of this universal dimer extends over a much larger range than the interaction potential, falling off exponentially in the asymptotic limit as $\exp(-r/a)$ [120]. The regime where the extent of a bound quantum object is much larger than the classical system is also referred to as the *quantum halo regime*.

In two limiting cases, the universal predictions become exact.

- *The scaling limit*: a is fixed and $r_0 \to 0$,
- *The unitarity limit*: r_0 is fixed and $a \to \pm\infty$.

The scaling limit is a powerful approximation, often referred to as the *zero range limit*, to calculate the properties of universal systems. In this approximation, the

point-like pseudo-potential approximation for the two-body potential in Equation 2.18 is exact and the scattering length is the only relevant length scale in the problem. This method is often used in renormalization group calculations to predict the universal behaviors of observables in strongly interacting systems [1]. In the two-body sector, the scaling limit is associated with a *continuous scaling symmetry* which is a trivial consequence of the fact that the scattering length is the only length scale remaining in the problem. Here, the scattering length (a), position ($\mathbf{r}$), and time (t) variables are all rescaled by the appropriate powers of a positive number (λ)

$$a \to \lambda a, \qquad \mathbf{r} \to \lambda \mathbf{r}, \qquad t \to \lambda^2 t. \tag{2.32}$$

Under this symmetry, the two-body observables such as binding energies of the universal dimer and scattering cross sections simply scale with the appropriate powers of λ as suggested by dimensional analysis. For real atoms, this symmetry is only an approximation and *scaling violations* emerge which break the symmetry, giving first-order corrections on the order of $r_0/|a|$ [1].

The unitarity limit can be reached experimentally as the interactions diverge attributable to resonant enhancement of the scattering length ($B \to B_0$ for Feshbach resonances). In this case, the low-energy collisional cross section is limited by the size of the de Broglie wavelength and the k^2a^2 term in the denominator of equation 2.17 dominates, yielding a maximum temperature-dependent cross section given by

$$\lim_{a \to \pm\infty} \sigma = \frac{(C)\ 4\pi}{k^2}. \tag{2.33}$$

Fermi gases in this limit are known as unitary Fermi gases where the scattering properties of these gases are completely dependent on the wave vector of the thermal energy and the inter-particle spacing is the only remaining length scale.

In this regime, there exists a universality that connects the unitary Fermi gas to that of an ideal Fermi gas. In a uniform strongly interacting Fermi gas, the ground-state energy is a universal fraction of the energy of a noninteracting gas at the same density, denoted by $1 + \beta$ [20, 11] where β is the universal constant that cannot be calculated analytically. The state of the art measurements for this universal constant yield $\beta \simeq -0.6$ [66], measured by the group of J. Thomas at Duke University using an ultracold gas of ^{6}Li atoms in the two lowest-energy spin

states near the broad Feshbach resonance at 834 Gauss [26]. They have also made detailed measurements of the hydrodynamic expansion of normal [20] and rotating [14, 68] strongly interacting Fermi gases, which also arises in a quark-gluon plasma [69, 19], as a consequence of very low viscosity hydrodynamics characteristic of a nearly perfect fluid. These few examples demonstrate the power of using ultracold two-component Fermi gases in the universal regime as quantum simulators for a variety of phenomena in strongly interacting Fermi gases over a wide range of length and energy scales [26]. In the following chapter, I will discuss the universal theory of three-body interactions, which have become accessible in our experiments with the inclusion of a third spin component to our ultracold Fermi gas.

Chapter 3

Universal Three-Body Physics

In the 1970s, Vitali Efimov published a series of ground-breaking papers, effectively solving the quantum mechanical three-body problem for low-energy particles with resonantly enhanced s-wave interactions [30, 31, 121, 32]. His investigations found that a non-relativistic system of three identical bosons, with sufficiently strong interactions, can support a spectrum of three-body bound states whose number increase to ∞ as the scattering length is tuned to resonance. Further, these so-called Efimov trimer states exhibit universal behaviors as a consequence of a discrete scaling symmetry in the zero-range limit.

This chapter begins by summarizing the textbook results for the quantum mechanical three-body problem as pertaining to identical bosons. Much of the information given here is based on a recent review article discussing universality in few-body systems by E. Braaten and H. W. Hammer [1]. We start by considering the three-body system in hyperspherical coordinates and the various simplifying assumptions that effectively reduce the Hamiltonian to an uncoupled set of radial Schrödinger equations in terms of three-body hyperspherical potentials. With the three-body potentials in hand, the universal properties of the Efimov trimer states are then explored. Evidence for the existence of the Efimov states can be indirectly observed in the form of resonant enhancement or suppression of the three-body recombination rate in ultracold atomic gases. Recent theoretical advancements predicting the locations and widths of these resonant features will be discussed for the case of identical bosons to provide a general overview of the various features that arise with the inclusion of universal trimer states.

The application of the above theory to our case is discussed in the last two sections. Here, three distinguishable particles interact with three unique, resonantly-enhanced scattering lengths. Recent analytical approximations are discussed to demonstrate the new features that are expected to arise in our system. Further, the methodology for numerically solving for the rate constants using a generalization of the Skorniakov and Ter-Martirosian (STM) equations is reviewed as this method has been directly applied to analyze our data. Finally, the effects of the finite temperature of the gas on the observed Efimov features are discussed. This review is not designed to cover the entire scope of the rapidly evolving field of universal few-body physics, but instead concentrates on the variety of phenomena that arise when three-body interactions are included by means of adding a third spin-state to ultra-cold gases of fermionic atoms.

3.1 Three-Body Interactions

Although the quantum mechanical three-body problem has been investigated since nearly the beginning of quantum mechanics [122], it is still generally considered an unsolved problem. Consider even the simple case of three atoms of equal mass m at located at positions $\mathbf{r}_i$, interacting via a central potential $V(\mathbf{r}_1, \mathbf{r}_2, \mathbf{r}_3)$. The Schrödinger equation for this system is given by

$$\left[-\frac{\hbar^2}{2m} \sum_{i=1}^{3} \bigtriangledown_i^2 + V(\mathbf{r}_1, \mathbf{r}_2, \mathbf{r}_3) \right] \Psi(\mathbf{r}_1, \mathbf{r}_2, \mathbf{r}_3) = E \ \Psi(\mathbf{r}_1, \mathbf{r}_2, \mathbf{r}_3) \tag{3.1}$$

where $\Psi(\mathbf{r}_1, \mathbf{r}_2, \mathbf{r}_3)$ is the three-atom wavefunction. After transforming to the center-of-mass frame, six degrees of freedom still remain. Here, spherically symmetric pairwise interactions between the atoms imply total angular momentum conservation, but this only provides three constraints of motion. This leaves a three-dimensional partial second order non-linear differential equation for which no general solution exists. Here I briefly describe hyperspherical coordinate space and the simplifying assumptions which allow for an analytic solution to the quantum mechanical three-body problem for the case of three resonantly interacting identical bosons when only pairwise interactions are considered. For a thorough review of this formalism, refer to References [123, 1].

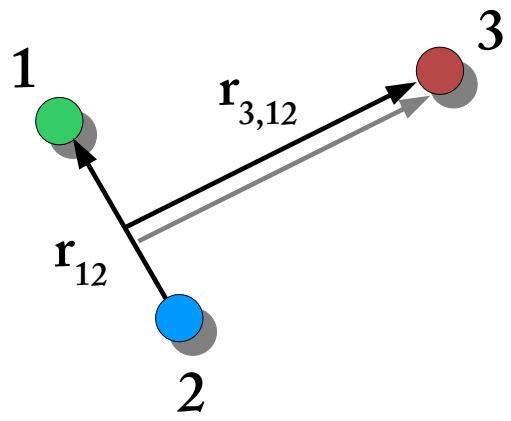

Figure 3.1. Hyperspherical coordinate system for three particles

3.1.1 Hyperspherical Coordinates

The universal quantum-mechanical three-body problem can be most easily understood by formulating it in terms of *hyperspherical coordinates*. This coordinate system is expressed as of a set of Jacobi coordinates consisting of vectors representing the separation between atom pairs $\mathbf{r}_{ij} = \mathbf{r}_i - \mathbf{r}_j$ and a vector representing the separation of the third atom from the center-of-mass of the atom pair $\mathbf{r}_{k,ij} = \mathbf{r}_k - \frac{1}{2}(\mathbf{r}_i + \mathbf{r}_j)$ as illustrated in Figure 3.1.

In this formalism it is useful to consider the *hyperradius* R and the *Delves hyperangle* α_k [124], defined as

$$R^2 = \frac{1}{3}(r_{12}^2 + r_{23}^2 + r_{13}^2) = \frac{1}{2}r_{ij}^2 + \frac{2}{3}r_{k,ij}^2 \tag{3.2}$$

$$\alpha_k = \arctan\left(\frac{\sqrt{3}r_{ij}}{2r_{k,ij}}\right) \tag{3.3}$$

where (i, j, k) is a permutation of the particle numbers (1,2,3). The hyperangle α_k varies from 0, when atom k is far from atoms i and j, to $\pi/2$, when atom k is near the center-of-mass of the other two atoms. Further, the hyperradius R, which represents the root-mean-square separation of the three atoms, is only small if all three atoms are mutually in close proximity.

In the center-of-mass frame, six variables are necessary to describe the three-body Schrödinger equation. The hyperspherical coordinates used are the hyperradius R, one of the hyperangles α_k, and the unit vectors $\hat{r}_{ij}$ and $\hat{r}_{k,ij}$. The five

dimensionless variables $(\alpha_k, \hat{r}_{ij}, \hat{r}_{k,ij})$, referred to as the hyperangular variables, are collectively denoted as Ω. In terms of hyperspherical coordinates, the Schrödinger equation in the center-of-mass frame reduces to

$$\left[T_R + T_{\alpha_k} + \frac{\Lambda_{k,ij}^2}{2mR^2} + V(R,\Omega)\right]\Psi = E\ \Psi, \tag{3.4}$$

where T_R is the hyperradial kinetic energy operator, T_{α_k} is the kinetic energy operator associated with the hyperangle α_k, and $\Lambda_{k,ij}$ is a generalized angular momentum operator which contains the conventional angular momentum operators associated with the vectors $\mathbf{r}_{ij}$ and $\mathbf{r}_{k,ij}$. More details on this derivation can be found in Reference [1].

3.1.2 Faddeev Equations

Up to this point, the analysis of the three-body problem has been exact for a general three-body system. One assumption that greatly simplifies the physics considers only configurations where a two-body cluster is well separated from the third atom. The resulting *Faddeev equations* are a set of equations equivalent to the three-body Schrödinger equation in Equation 3.4 that makes use of this simplification. Along with the restrictions associated with low-energy collisions at ultracold temperatures, the three-body problem can be reduced to a set of integro-differential equations in terms of only the hyperradius R.

We first assume that the three-body interaction potential can be expressed as

$$V(\mathbf{r}_1, \mathbf{r}_2, \mathbf{r}_3) = V(r_{12}) + V(r_{23}) + V(r_{13}). \tag{3.5}$$

where the terms $V(r_{ij})$ are two-body potentials depending only on the separation between atom pairs. This assumption is well justified for short-range potentials which decrease as a power of r^{-n}, for $n \geq 3$ [125]. In this case, the three-body terms at short distances can be expressed at low energies as a sum of two-body potential terms to reproduce their universal effects. The total wavefunction of the system is then expressed in terms of three different sets of coordinates of the form

$$\Psi(\mathbf{r}_1, \mathbf{r}_2, \mathbf{r}_3) = \Psi^{(1)}(\mathbf{r}_{23}, \mathbf{r}_{1,23}) + \Psi^{(2)}(\mathbf{r}_{31}, \mathbf{r}_{2,31}) + \Psi^{(3)}(\mathbf{r}_{12}, \mathbf{r}_{3,12}), \tag{3.6}$$

which are solutions to the three-body Schrödinger equation. These wavefunctions are generated by the following set of Faddeev equations [126].

$$\left(T_R + T_{\alpha_k} + \frac{\Lambda^2_{k,ij}}{2mR^2}\right)\Psi^{(k)} + V(\mathbf{r}_{ij})(\Psi^{(k)} + \Psi^{(i)} + \Psi^{(j)}) = E\ \Psi^{(k)} \tag{3.7}$$

At this point, it is useful to transform the Faddeev wavefunction $\Psi^{(k)}$ into hyperspherical coordinates. This can be most easily achieved by expanding the wavefunction in terms of spherical harmonics for the unit vectors $\hat{r}_{ij}$ and $\hat{r}_{k,ij}$ and considering only the zero orbital angular momentum terms for each component [1]. The assumption of neglecting subsystem angular momentum is well justified for three-body interactions in our ultracold atomic gases. The Schrödinger wavefunction in Equation 3.6 for three identical particles then reduces to

$$\Psi(\mathbf{r}_1, \mathbf{r}_2, \mathbf{r}_3) = \Psi(R, \alpha_1) + \Psi(R, \alpha_2) + \Psi(R, \alpha_3). \tag{3.8}$$

In hyperspherical coordinates, the Faddeev equations then reduce to a particularly simple set of equations given by

$$(T_R + T_{\alpha_k} - E)\Psi(R, \alpha_k) + V(\sqrt{2}R\sin\alpha_k) \times[\Psi(R, \alpha_1) + \Psi(R, \alpha_2) + \Psi(R, \alpha_3)] = 0 \tag{3.9}$$

The three Faddeev equations in hyperspherical coordinates can be reduced to a single equation by using the fact that the hyperangles α_i, α_j, and α_k are not independent. Implementing a set of rotations that express the hyperangles α_2 and α_3, in terms of $\alpha_1 = \alpha$ and integrating over the angular variables $\hat{r}_{23}$ and $\hat{r}_{1,23}$, the resulting integro-differential equation for $\Psi(R, \alpha)$ is given by [125]

$$(T_R + T_\alpha - E)\Psi(R, \alpha) = -V(\sqrt{2}R\sin(\alpha)) \times \left[\Psi(R, \alpha) + \frac{2}{\sin(2\phi)}\int_{|\phi-\alpha|}^{\pi/2-|\pi/2-\phi-\alpha|} \frac{\sin(2\alpha')}{\sin(2\alpha)}\Psi(R, \alpha')\, d\alpha'\right] \tag{3.10}$$

The angle ϕ depends only on the masses of the particles, equal to $\pi/3$ when they are all equal. This equation is referred to as the *low-energy Faddeev equation*.

The solution of Equation 3.10 is simplified by using a hyperspherical expansion [1]. Here, the Faddeev wavefunction $\Psi(R,\alpha)$ is expanded in a complete set of functions in terms of the hyperangle α

$$\Psi(R,\alpha) = \frac{1}{R^{5/2}\sin 2\alpha}\sum_n f_n(R)\Phi_n(R,\alpha). \tag{3.11}$$

The functions $\Phi(R,\alpha)$ must vanish at $\alpha = 0,\ \pi/2$ due to the divergence of the prefactor. Using this expansion, the low-energy Faddeev equation can be manipulated to obtain a coupled set of eigenvalue equations for the hyperradial wave functions $f_n(R)$ given by

$$\begin{aligned}\left[\frac{\hbar^2}{2m}\left(-\frac{\partial^2}{\partial R^2}+\frac{15}{4R^2}\right)+V_n(R)\right]f_n(R) \\ +\sum_m\left[2P_{nm}(R)\frac{\partial}{\partial R}+Q_{nm}(R)\right]f_m(R) = E\ f_n(R),\end{aligned} \tag{3.12}$$

where the potentials $P_{nm}(R)$ and $Q_{nm}(R)$ induce coupling between different hyperradial channels [1].

The channel potentials for the hyperradial variable R are given in terms of channel eigenvalues $\lambda_n(R)$ as

$$V_n(R) = [\lambda_n(R)-4]\frac{\hbar^2}{2mR^2}. \tag{3.13}$$

Here, the hyperradial dependence of the channel potentials $V_n(R)$ is fully contained in the form of the channel eigenvalues. In the following, I will describe the simplifying assumptions used to describe the channel potentials in hyperspherical coordinate space in terms of effective $1/R^2$ potentials capable of supporting a series of universal bound trimer states.

3.1.3 Hyperspherical Channel Potentials

In the *adiabatic hyperspherical approximation*, the eigenvalues $\lambda_n(R)$ are assumed to be independent of R. Here, the coupling potentials $P_{nm}(R)$ and $Q_{nm}(R)$ vanish and Equation 3.12 decouples to form a set of radial Schrödinger equations for each hyperspherical potential. This assumption, which is valid in the two limiting

ranges of the hyperradius $R \ll |a|$ and $R \gg |a|$ [1], greatly simplifies the analysis of the Faddeev equations, which can now be solved numerically for the values of the channel eigenvalues $\lambda_n(0)$.

The hyperradius R is separated into distinct regions when the scattering length is much larger than the characteristic range of interactions $|a| \gg l$, based on the form of the hyperradial wavefunction in these regions. For identical bosons, the regions are separated as [127]

- the *short-distance region* $\mathrm{R} \leq l$,
- the *scale-invariant region* $l \ll \mathrm{R} \leq |a|$,
- the *long-distance region* $\mathrm{R} \sim |a|$,
- the *asymptotic region* $\mathrm{R} \gg |a|$.

In the scaling limit ($l \to 0$) the short-distance region goes to zero and the low-energy Faddeev equation can be reduced to an exact transcendental equation, first derived by Efimov in 1970 [30]. Here, the channel eigenvalues $\lambda_n(R)$ can be solved for numerically to determine the hyperradial dependence of the hyperspherical channel potentials.

The lowest three channel potentials for both positive (solid line) and negative (dashed line) scattering length as functions of $R/|a|$ are shown in Figure 3.2 [127]. It is interesting to note that for both positive and negative a, the lowest hyperspherical potential is attractive whereas all other channel potentials are repulsive for all R. It is the attractive $V_0(R) \propto 1/R^2$ potential that allows for the universal three-body bound states, giving rise to the Efimov effect. As $R \to \infty$, nearly all of the hyperspherical potentials asymptote to the 3-atom threshold. The only exception occurs for the $V_0(R)$ potential for $a > 0$, which asymptotes to the binding energy of the universal dimer $E_D = -\hbar^2/ma^2$, discussed in Section 2.5, plus a free atom. As $R/|a| \to 0$, the hyperspherical potentials asymptote to $1/R^2$ potentials whose coefficients depend on the channel eigenvalues $\lambda_n(0)$. The limiting value of the lowest eigenvalue is [1]

$$\lambda_0(R) \to -s_0^2 \left(1 + 1.897\frac{R}{a}\right), \tag{3.14}$$

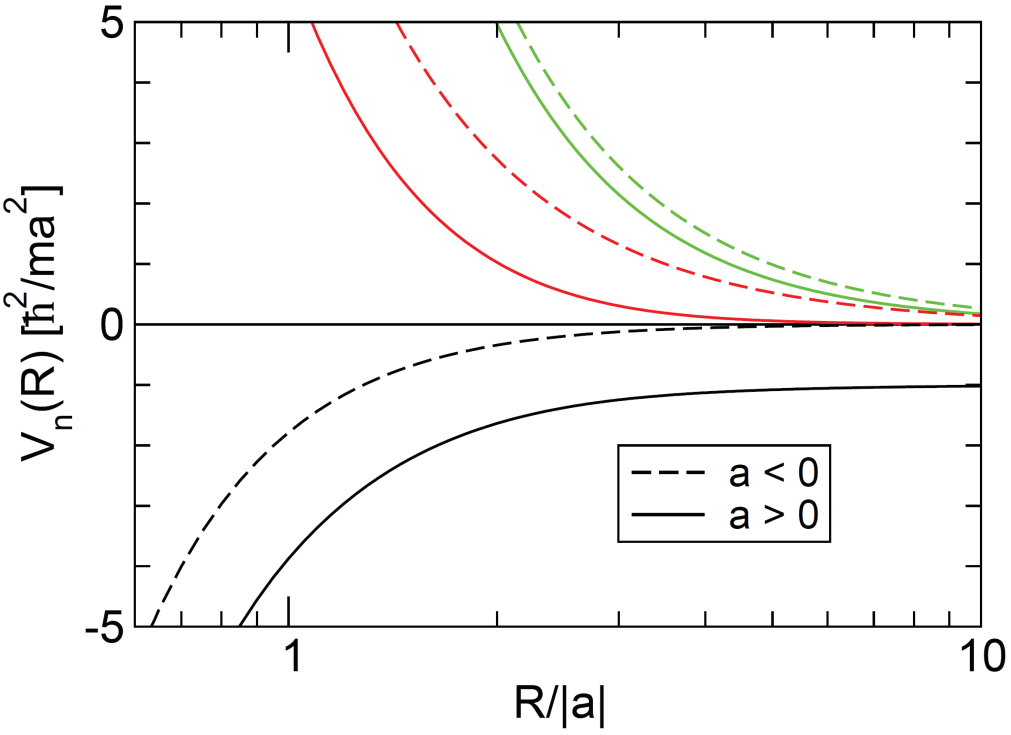

Figure 3.2. The three lowest-energy hyperspherical channel potentials for attractive (dashed) and repulsive (solid) pairwise interactions, $V_0(R)$ is denoted in black. Figure taken from Reference [1].

where $s_0 = 1.00624$ is calculated numerically from the transcendental equation.

3.1.4 Efimov States in the Resonant Limit

In the resonant limit, where $|a| \to \infty$, the channel eigenvalue $\lambda_0(R) = -s_0^2$ is a constant and the adiabatic hyperspherical approximation is applicable for all finite values of R. In this limit, the eigenvalue equation given by Equation 3.12 for the lowest channel hyperradial wave function $f_0(R)$ reduces to

$$\frac{\hbar^2}{2m}\left[-\frac{\partial^2}{\partial R^2} - \frac{s_0^2 + 1/4}{R^2}\right] f_0(R) = E\ f_0(R). \tag{3.15}$$

This is an analogous equation to the radial Schrödinger equation for a particle in a $1/R^2$ potential. The hyperradial potential can support three-body bound states with binding energies $E_T^{(n)} = (\hbar\kappa^{(n)})^2/m$, where $\kappa^{(n)}$ are the wave numbers

of these trimer states. As discussed in the following, Efimov showed that for three identical bosons, the calculation of the binding energies for all of the Efimov states $E_T^{(n)}$ could be reduced to the calculation of a single universal function ξ which depends on the energy and scattering lengths of the particles.

It should be stressed that Equation 3.15 is not valid in the short-distance region, as it ignores the microscopic properties of the scattering potential and the $1/R^2$ potential is too singular as $R \to 0$ to allow for a well behaved analytic solution. In the scale invariant region ($l \ll R \ll |a|$), the hyperradial wave function $f_0(R)$ is represented by an incoming hyperradial wave and an outgoing hyperradial wave which is reflected off the short distance region $R \sim l$ [1]. The eigenvalue equation can then be solved by matching the short- and long-range hyperradial wavefunctions and their logarithmic derivatives. Efimov showed that at unitarity this solution yields an infinite series of three-body bound states (Efimov trimers) whose binding energies are given by

$$E_T^{(n)} = \left(e^{-2\pi/s_0}\right)^{n-n_*} \frac{\hbar^2 \kappa_*^2}{m}, \qquad \text{as } n \to \infty,\ a = \pm\infty \tag{3.16}$$

where κ_* is the wave number associated with the state $n = n_*$. More details related to matching of the boundary conditions and the derivation of this energy spectrum can be found in [127, 1].

The beauty of Efimov's solution lies in the fact that the entire spectrum of universal trimer states in the resonant limit can be calculated once the single three-body parameter (κ_*) is determined. This parameter encapsulates all of the information pertaining to the short-range three-body interactions, analogous to the scattering length in the two-body problem.

Generally the three-body parameter cannot be determined from knowledge of the two-body potentials alone and must be determined experimentally for each atomic species due to the short-range, non-additive, purely three-body interaction that exist in these triatomic systems [128]. Note that there are an infinite number of arbitrarily shallow Efimov states in the resonant limit with an accumulation point at the three-atom scattering threshold. Further, the binding energies of the spectrum of Efimov states obeys log-periodic scaling with subsequent states emerging at multiplicative factors of $e^{2\pi/s_0} \sim 515.03$ as the binding energy is

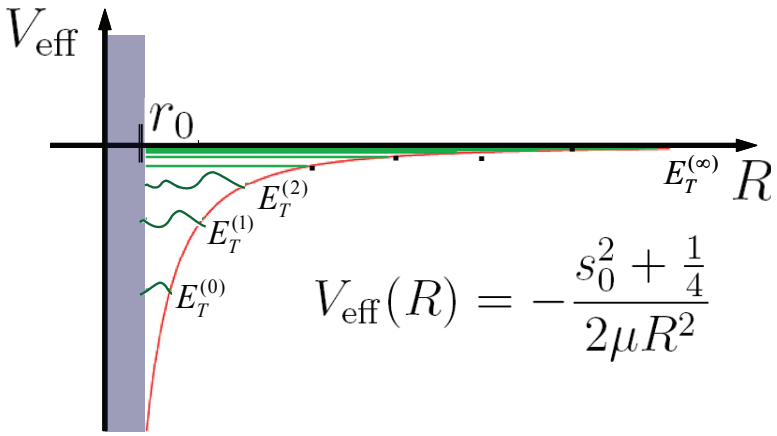

Figure 3.3. A representation of the lowest hyperspherical potential in the resonant limit $a = \pm\infty$ and the spectrum of Efimov trimer states $E_T^{(n)}$ are shown. The log-periodic scaling of the binding energies has been reduced from ~ 515 to 2 for clarity.

decreased.

The previous discussion is only exact for resonant interactions in the scaling limit ($l \to 0$). In real systems, there is always a finite characteristic range of interactions, which must be accounted for. Since the eigenvalue equation 3.15 is no longer valid for $R < l$, the three-body spectrum is bounded from below where the deepest Efimov state has a binding energy

$$E_T^{(0)} \sim \frac{\hbar^2}{ml^2}. \tag{3.17}$$

For Efimov states near this cutoff, there are power-law scaling violations with leading order corrections to the binding energies on the order of $\kappa_*^{(n)} l$ [129]. These corrections decrease rapidly as the binding energy of the Efimov states goes to zero at the three-atom scattering threshold.

3.1.5 Universal Scaling at Finite Scattering Length

In the two-body problem in the scaling limit, the continuous scaling symmetry given by Equation 2.32 is a consequence of the fact that the scattering length is the only relevant length scale. In the three-body sector in the scaling limit, Efimov showed that *logarithmic scaling violations* occur due to the boundary conditions

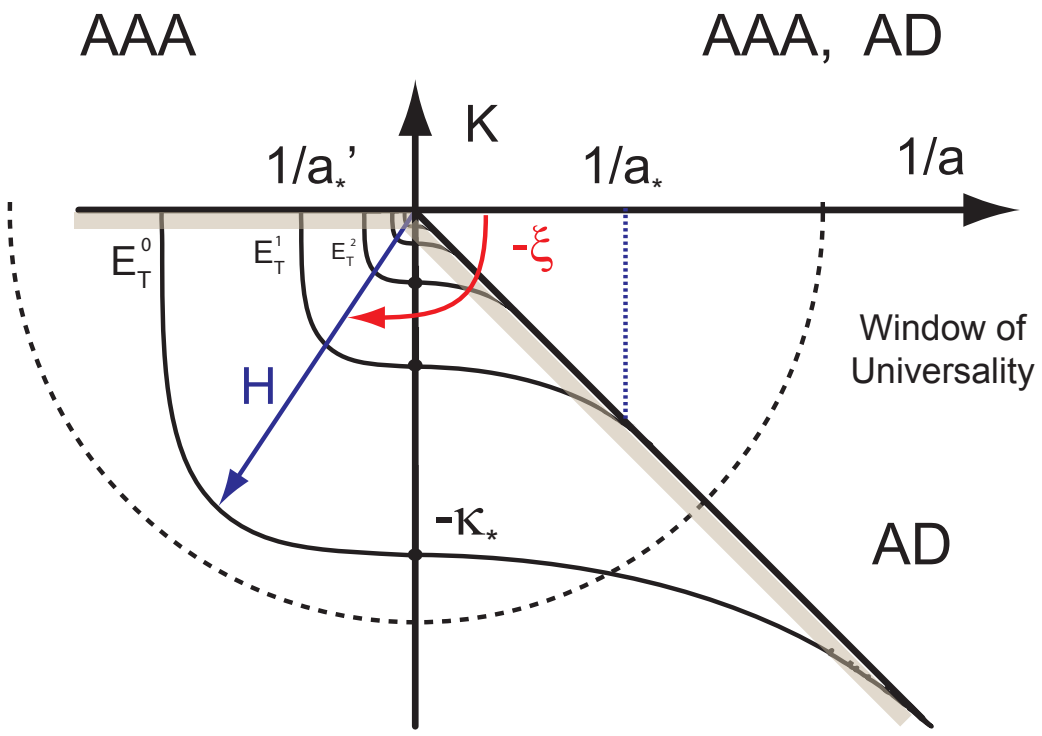

Figure 3.4. The spectrum of Efimov trimers (E_T) on the $a^{-1} - K$ plane. Here, the discrete scaling factor was reduced from 22.7 to 2.2, allowing a greater range of a^{-1} and K to be shown. The grey lines indicate the threshold for the 3-atom scattering states AAA and atom-dimer scattering states AD. Outside of the window of universality, either the scattering length is smaller than l, or the on-resonance binding energies of the trimers exceed E_T^0, given by Eq. 3.17. The characteristic shape of the trimer binding energies were taken from [1].

imposed on the short- and long-range hyperradial wavefunctions. Remarkably, these scaling violations have a log-periodic form so that a *discrete scaling symmetry*, a discrete subgroup of the continuous scaling symmetry, remains exact. Examples of this symmetry include

$$\kappa_* \to \kappa_*, \qquad a \to \lambda_0^n a, \qquad \mathbf{r} \to \lambda_0^n \mathbf{r}, \qquad t \to \lambda_0^n t \tag{3.18}$$

where n is an integer and $\lambda_0 = e^{\pi/s_0} \approx 22.7$. Under this symmetry, observables such as the binding energy and cross sections scale with integer powers of λ_0. In fact, it is this symmetry which gives the log-periodic form of the trimer binding energies in the resonant limit, given in Equation 3.16.

While an infinite number of bound Efimov trimers exist in the resonant limit, at

finite values of the scattering length only a finite number of bound states exist. This is evident in the fact that no Efimov states exist outside of the universal regime, where the scattering length is on the order of or smaller than the characteristic range of interactions l.

The characteristic shape of the binding energy for the Efimov trimers with respect to the inverse of the scattering length $1/a$ and the wave number variable ($K = \text{sign}(E)\sqrt{m|E|/\hbar^2}$) is shown in Figure 3.4 [1]. On the positive side of the resonance ($a > 0$), the diagonal line represents the energy of the shallow two-body bound state with binding energy $E_D = -\hbar^2/(ma^2)$. The grey region represents the atom-dimer dissociation threshold for the three-body system. For negative scattering lengths, no universal two-body bound states exist and the three-body dissociation threshold occurs at zero energy as indicated. The Efimov trimers are represented by the solid curves below threshold. Although only a few are shown, on resonance ($1/a \to 0$) there are infinitely many branches of Efimov trimers which intercept the vertical axis at $K = -(e^{-\pi/s_0})^{n-n_*}\kappa_*$.

As the magnitude of the scattering length is decreased from infinity to $a < 0$, the effective hyperradial potential increases at large distances ($R \approx |a|$). As a result, the energy of the most loosely bound Efimov trimers are "pushed up" until, at a critical value of the scattering length ($a_*^{\prime(n)}$), the Efimov trimer states $E_T^{(n)}$ are dissociated at the three-body scattering threshold. For $a > 0$, on the other hand, the effective potential decreases as the magnitude of the scattering length is decreased from infinity. Here, the effective potential converges to the dimer binding energy ($V_0(R) \to E_D$) for large hyperradii. At critical scattering lengths $a_*^{(n)}$, the Efimov trimer states $E_T^{(n)}$ converge with the atom-dimer threshold and dissociate to form a free atom and weakly-bound dimer.

Efimov derived powerful constraints on the three-body observables that he called the *radial law* [32]. He showed that when expressed in terms of the polar variables H and ξ defined by $1/a = H\cos(\xi)$ and $K = H\sin(\xi)$, shown in Figure 3.4, the binding energies for all of the Efimov states can be calculated from a single universal function in terms of ξ. The energy of the n^{th} trimer state in the universal limit is parameterized as

$$E_T + \frac{\hbar^2}{ma^2} = \left(e^{-2\pi/s_0}\right)^{n-n_*} \exp[\Delta(\xi)/s_0]\frac{\hbar^2\kappa_*^2}{m} \tag{3.19}$$

where $\Delta(\xi)$ is a universal function of the polar angle $\xi \in [-\pi, \ -\pi/4]$, given by $\tan(\xi) = -\sqrt{(mE_T/\hbar^2)}a$. The form of the universal function $\Delta(\xi)$ can be found by either solving the Schrödinger or Faddeev equations numerically for short-ranged model potentials [130], or by using effective field theory calculations (EFT)[1]. In so doing, the critical scattering lengths a'_* and a_* where the Efimov trimer comes into resonance with the three-body and atom-dimer scattering thresholds are calculated using a zero-range model ($l \to 0$) as [1, 131]

$$a'_* = -1.50763\kappa_*^{-1}, \qquad a_* = 0.0707645\kappa_*^{-1}. \tag{3.20}$$

As can be seen from Equation 3.19, the shapes of the Efimov trimers with respect to the scattering length are identical to within a multiplicative factor. This is a direct consequence of the discrete scaling symmetry for the three-body system in the universal regime, and corresponds to multiplying the three-body parameter by the discrete scaling constant ($\kappa_*^{(n)} = \kappa_*\lambda_0^n$). Therefore, the critical scattering lengths a'_* and a_*, which are directly dependent on $1/\kappa_*^{(n)}$, occur at values that differ by multiplicative factors of λ_0. In the scaling limit, the entire spectrum of Efimov states for identical bosons depend on only the scattering length a, which is generally known, and a single three-body parameter κ_*.

If there are no deeply bound molecular states in any of the two-body channels, the Efimov states are sharp states with the spectrum given at unitarity by Equation 3.16. If such deeply bound dimers exist, their inclusive effects can be incorporated by analytically continuing the three-body parameter κ_* to a complex value, expressed in the form $\kappa_*\exp(i\eta_*/s_0)$, where η_* is the inelasticity parameter, and both κ_* and η_* are positive real numbers. Substituting this expression into Equation 3.16 yields the binding energies and widths of the Efimov trimers at unitarity with non-zero decay given by [8]

$$E_T^{(n)} = \left(e^{-2\pi/s_0}\right)^{n-n_*} \frac{\hbar^2\kappa_*^2\cos(2\eta_*/s_0)}{m}, \qquad \text{as } n \to \infty, \ a = \pm\infty \tag{3.21}$$

$$\Gamma_T^{(n)} = \left(e^{-2\pi/s_0}\right)^{n-n_*} \frac{2\hbar^2\kappa_*^2\sin(2\eta_*/s_0)}{m}. \tag{3.22}$$

In the following, I will discuss the available observables and the theoretical formalism that has developed over the last decade to enable the experimental mea-

surement of the three-body parameters κ_* and η_* for strongly interacting ultracold gases of identical bosons.

3.2 Experimental Observables

For a system of three arbitrary atoms, labeled A, B, and C, the various processes that are likely to display resonant phenomena associated with Efimov physics are [132]

$$\begin{aligned}
A+B+C &\rightarrow AB^*+C && \text{Three}-\text{body recombination} && (3.23)\\
&\rightarrow AB+C && && (3.24)\\
AB^*+C &\rightarrow AB^*+C && \text{Elastic scattering} && (3.25)\\
&\rightarrow AB+C && \text{Vibrational relaxation} && (3.26)\\
&\rightarrow AC^*+B && \text{Reactive scattering} && (3.27)\\
&\rightarrow AC+B. && && (3.28)
\end{aligned}$$

Here, AB (AB^*) represents a deeply bound (universal) dimer state. In our experiments, we are primarily interested in the three-body recombination rate for three distinguishable atoms in a thermal gas. For ultracold atoms, the third atom recedes from the dimer with an energy roughly equal to the binding energy of the dimer. Since the molecular binding energies of the deeply bound dimers are generally much greater than the depth of the trapping potential, these three-body recombination events are evident in atom loss from the trap.

The rate equations for the number densities n_i of the atoms A, B, and C in the presence of three-body loss is given by

$$\frac{dn_i}{dt} = -K_3\, n_A\, n_B\, n_C. \tag{3.29}$$

The three-body recombination rate constant K_3 can be separated into K_3^{deep} for recombination into the deep dimers AB and $K_3^{shallow}$ for recombination into the shallow (universal) dimer states AB^*. If all of the pairwise scattering lengths are negative, no universal dimer states exist, and $K_3^{shallow}$ is zero.

In ultracold gas experiments, the spectrum of Efimov states in the universal

regime are manifest in the experimentally measurable three body recombination rates. In fact the first conclusive evidence for the existence of Efimov trimer states was observed by R. Grimm's group at the University of Innsbruck in 2006 [35]. Using a gas of ultracold, non-degenerate bosonic ^{133}Cs atoms, they detected a resonant enhancement of the three-body loss at negative scattering lengths and a loss minima at positive a, corresponding to resonant effects associated with Efimov trimer states. These measurements, along with the corresponding theoretical predictions for the variation of K_3 associated with the trimer states [133], provided the first conclusive evidence of the validity of Efimov's theory.

To get a general overview of these experimentally observable resonance features, it is useful to first consider the case of three identical bosons with resonantly enhanced interactions. Here, the cross-sections for all rates and possible processes can be calculated from the scattering matrix elements S_{fi} for scattering from an entrance channel i to the exit channel f. The S-matrix elements were discussed for two-body elastic and inelastic collisions in Chapter 2. In the three-body sector, Efimov's radial law gives simple relations based on probability conservation which enable the calculation of the S-matrix elements [31, 121, 32]. Various analytical results for the two- and three-body recombination rate constants for identical Bosons and the manifestation of Efimov physics in these observations is discussed in the following sections.

3.2.1 Atom-Dimer Scattering

In Chapter 2 we showed that the differential scattering cross section for two-body collisions can be expressed in terms of the scattering length. Here we consider collisions between a free atom and a universal dimer near the atom-dimer threshold. The functional form of the elastic atom-dimer cross section σ_{AD} was first deduced by Efimov. Discrete scaling symmetry implies in this case that the ratio of the atom-dimer scattering length to the scattering length for two free atoms a_{AD}/a must be a log-periodic function of $a\kappa_*$ with a period π/s_0 [1]. The exact form of the atom-dimer scattering length, with the added effects of loss attributed to decay to deeply bound dimer states, takes the form [1]

$$a_{AD} = a(1.46 + 2.15\cot[s_0\ln(a/a_*) + i\eta_*]), \tag{3.30}$$

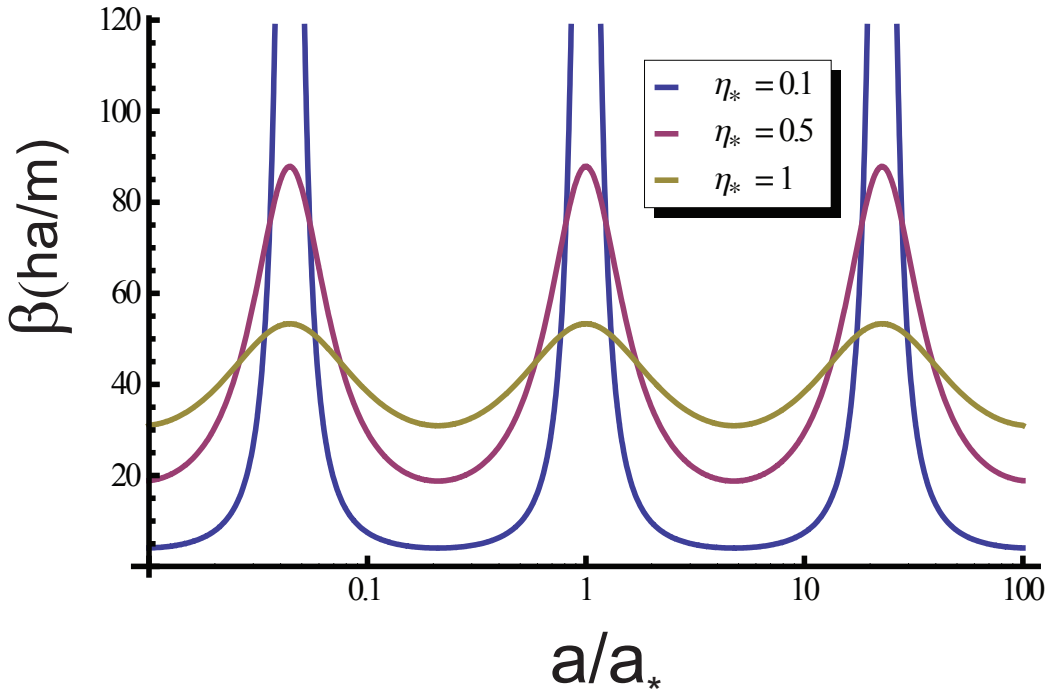

Figure 3.5. Dimer relaxation rate constant (β in units of $\hbar a/m$) as a function of a/a_* for various values of the inelasticity parameter η_*.

where a_* is one of the locations where an Efimov state crosses the atom-dimer threshold given in Equation 3.20. Further, this equation demonstrates that as $\eta_* \to 0$, a_{AD} vanishes if a has one of the values $0.38a_*(e^{\pi/s_0})^n$. The existence of the deeply bound molecular states opens up an inelastic loss channel in which an atom and universal dimer undergo a low energy collision to form an atom and a deeply bound molecular state. In general, every decay event releases enough energy to result in loss of both the atom and the dimer from the trap. The decrease of the number density of atoms and shallow dimmers is then given by

$$\frac{d}{dt}n_A = \frac{d}{dt}n_D = -\beta n_A n_D, \tag{3.31}$$

where β is the relaxation rate event constant, first calculated in Ref. [133] as

$$\beta = \frac{20.3\sinh(2\eta_*)}{\sin^2[s_0\ln(a/a_*)] + \sinh^2(\eta_*)}\frac{\hbar a}{m}, \tag{3.32}$$

and m is the mass of one of the particles. The coefficient of $\hbar a/m$ is shown in Figure 3.5 as a function of a/a_* for several values of the inelasticity parameter η_*. Resonant enhancement of β occurs at scattering lengths coinciding with an Efimov trimer crossing the atom-dimer threshold. As can be seen, increasing the magnitude of the inelasticity parameter η_*, associated with dimer decay to deeply bound molecular states, reduces the dimer relaxation rate constant at the resonance positions and broadens the width of the resonance. This "washing out" of the resonances associated with Efimov physics in the presence of large inelastic loss is a general feature in both the two- and three-body recombination measurements.

3.2.2 Three-Body Recombination of Identical Bosons

In Efimov's derivation of the radial law, he assumed that decay into the deeply bound dimer states was negligible. Using Efimov's relations in the hyperspherical framework, Nielsen and Maceck [134] and Esry *et al.* [135] derived the approximate functional form of the three-body recombination rate into the shallow universal dimer, given as

$$K_3^{shallow} \simeq C_{max}(\sin^2[s_0 \ln(a\kappa_*) + \gamma])\frac{\hbar a^4}{m}, \qquad (a > 0) \tag{3.33}$$

The constant C_{max} and the phase γ were first calculated using effective field theory [136]. This approximate expression, which is correct to within an error of $\sim 1\%$, demonstrates the amazing feature that the coefficient of $\hbar a^4/m$ oscillates between zero and C_{max} as a function of a. The oscillatory loss behavior comes about from an interference effect between two decay pathways, as illustrated in Figure 3.6 (a). The 3-body recombination process involves an avoided crossing between the 3-atom scattering state on the lowest hyperspherical potential in the entrance channel and the highest s-wave two-body scattering state on the exit channel [135]. Coupling between these two channels occurs in the long-distance region $R \sim 3a$. As shown, the incoming 3-atom scattering state can decay by two distinct paths, depending on whether the scattering state decays while R is increasing or decreasing. The scattering wavefunction, which is a superposition of waves traveling both paths, will then exhibit interference between the scattering states reflecting off the short-distance region of the potentials dependent on the scatter-

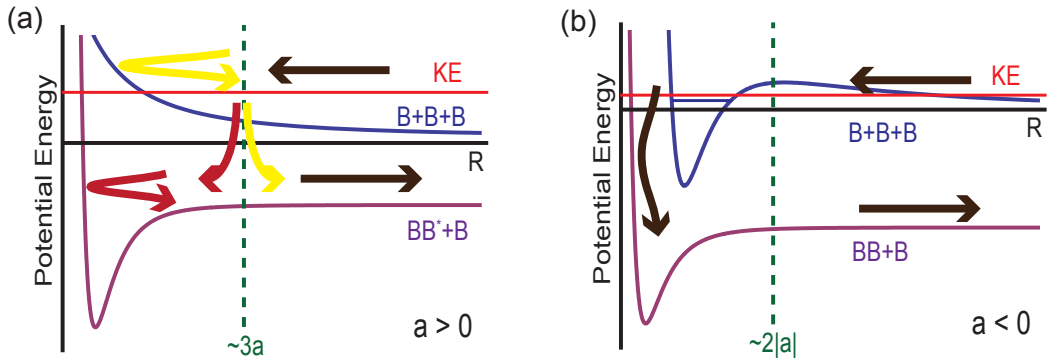

Figure 3.6. The lowest two adiabatic hyperspherical potential curves (purple and blue) for (a) $a > 0$ and (b) $a < 0$. (a) For positive scattering lengths, three-body decay to the universal dimer state and a free atom occurs in the long-distance region where an interference between two distinct decay paths (yellow and red) leads to the oscillatory behavior of K_3. (b) For $a < 0$, resonant tunneling through a repulsive barrier to a bound trimer state results in enhanced decay to deeply bound molecular states in the short-distance region. An analogous figure was published in a recent review of universal few-body physics by C. Greene [2].

ing length a. Using Equation 3.33, it is found that the recombination zeroes are located at $a"_* = 0.32(e^{\pi/s_0})^n \kappa_*^{-1}$. Note that these zeroes exhibit the log-periodic dependence $a"_*^{(n+1)}/a"_*^{(n)} \simeq 22.7$. This phenomena was first derived in References [135, 134], where the behavior was described in terms of *Landau-Zeener-Stückelberg oscillations* [137].

If we include the effects of deeply bound dimmers into the analysis, three-body decay now includes loss to both the shallow dimer state $K_3^{shallow}$ and to the deeply bound molecular states K_3^{deep}. The approximate expression for these decay rate constants for $a > 0$ are given by [1]

$$K_3^{shallow} \simeq C_{max} e^{-2\eta_*} \left(\sin^2[s_0 \ln(a/a"_*)] + \sinh^2(\eta_*)\right) \frac{\hbar a^4}{m} \tag{3.34}$$

$$K_3^{deep} \simeq D_{max} \left(1 - e^{-4\eta_*}\right), \frac{\hbar a^4}{m} \qquad (a > 0) \tag{3.35}$$

where D_{max} is a numerical constant [133]. For identical bosons with positive scattering lengths, the total three body recombination rate constant with respect to $(a\kappa_*)^{-1}$ for various inelasticity parameters η_* is shown in the right-hand panel of Figure 3.7. Decay to the deeply bound molecular states significantly reduces the

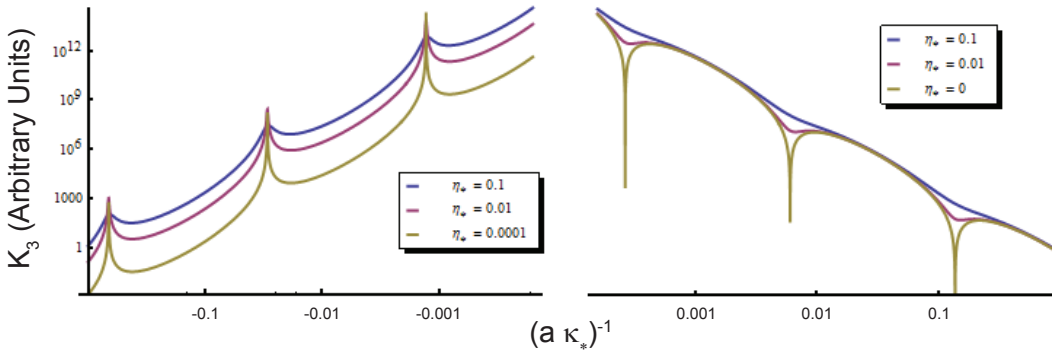

Figure 3.7. Log-Log plot of K_3 scaling with $(a\kappa_*)^{-1}$ for negative (left panel) and positive (right panel) values of a. The rate coefficient is in arbitrary units, demonstrating the general a^4 scaling behavior and the influence of Efimov states for systems of identical bosons. Decay to deeply bound molecular states, parameterized by η_*, reduces the visibility and broadens the Efimov resonances.

visibility of the Stückelberg oscillations. Further, the finite width of the Efimov trimers associated with this loss broadens the resonances, further "washing out" the resonant features.

For identical bosons at negative scattering lengths, no universal dimer exists and the only three-body loss channels are to the formation of deeply bound molecular states. Resonant enhancement of K_3 in this case is observed when the Efimov trimer state cross the free-atom threshold. The three-body decay process for $a < 0$ is depicted in Figure 3.6 (b). The lowest hyperspherical potential exhibits a barrier in the region ($R \sim 2|a|$) for these repulsively interacting particles [138, 135], At sufficiently low energy, the scattering state must tunnel through this barrier to access the short-distance region and decay to the deeply bound molecular potential shown. Transmission through the barrier is enhanced when the energy of an Efimov trimer state trapped behind the barrier comes into resonance with the incident energy (KE) of the particles. The 3-body recombination rate therefore exhibits resonant peaks at scattering lengths associated with the Efimov trimers crossing threshold.

The analytic expression for the three-body recombination rate is given by [133]

$$K_3^{deep} = C'_{max} \frac{\sinh(2\eta_*)}{\sin^2[s_0 \ln(a/a'_*)] + \sinh^2(\eta_*)} \frac{\hbar a^4}{m}, \qquad (a < 0) \qquad (3.36)$$

where a'_* is given in Equation 3.20. The total three body recombination rate constant with respect to $(a\kappa_*)^{-1}$ for various inelasticity parameters η_* is shown in the left-hand panel of Figure 3.7. As with the resonant features on the positive scattering length side of unitarity, as η_* increases the resonant loss peaks (Efimov resonances) become washed-out making their experimental detection and characterization of the three-body parameters more difficult. These relatively simple expressions for β and K_3 are correct only for a system of identical particles, but they are useful guides to provide a general overview of the features that are expected to emerge associated with the existence of Efimov states near threshold. The following section briefly discusses the extension of this universal three-body theory to a system of non-identical particles with multiple scattering lengths applicable to our ultracold Fermi gas.

3.3 Efimov Physics in Fermi Gases

Extension of Efimov's theory for a general 3-body system in which the three particles have identical masses and large but unequal scattering lengths was first discussed by Amado and Noble [139] and by Efimov [140, 121]. This problem is of fundamental interest, approximating such low-energy systems as multiple strongly-interacting isotopes of heavy atoms and nuclear matter consisting of interacting protons and neutrons. The general case of 3-body systems with unequal masses has also been considered in detail [139, 140, 121, 141], exhibiting a mass-ratio dependent scaling factor λ_0, but this broad subject is beyond the scope of this thesis.

It is not obvious at first glance whether Efimov trimer states exist for a system of fermions or distinguishable particles, let alone how the universal relations and scaling symmetries translate to such systems. These questions are answered by determining the channel eigenvalue $\lambda_0(R)$ for the lowest hyperspherical potential in the scaling limit, analogous to Eq. 3.14. The Efimov effect occurs so long as $\lambda_0(R)$ is negative at $R = 0$. Further, the value of $\lambda_0(0) = -s_0^2$ provides the discrete scaling factor as DSF $= e^{\pi/s_0}$. The various results for this general case are summarized in the review article [1] and presented here in Table 3.1. Note that so long as all three particles are resonantly interacting, the Efimov effect occurs with

Identical Fermi Pairs	Large a_{ij}	Efimov Effect	DSF
0	3	Yes	22.7
0	2	Yes	1986.1
1	2	No	-
0, 1, 3	0, 1	No	-

Table 3.1. Classification of equal-mass systems exhibiting the Efimov effect and the corresponding discrete scaling factors.

the same discrete scaling factor (DSF $\simeq$ 22.7) regardless of the imbalance of the scattering lengths. For systems where less than three distinguishable Fermi states exist, however, the Efimov effect does not occur. Even when the scattering lengths are widely varying, the entire spectrum of Efimov trimers and resonances are still universally connected, and can be described by the three-body parameters κ_* and η_* indicating the binding energies and widths of the trimer states respectively.

In general, solving for the dependence of the binding energies and threshold crossings of the Efimov trimers on the individual scattering lengths is a technically difficult problem. Consider the three-component Fermi gas in our system where three broad Feshbach resonances individually tune the various scattering lengths. Here, the spectrum of Efimov trimers are not simply described in terms of Efimov's radial, shown in Figure 3.4, as three individual scattering lengths now characterize the system and the locations of the three scattering resonances do not coincide. Further, it is now possible to achieve mutual attractive and repulsive pairwise interactions among the various single-particle states, possibly leading to new resonant features that can be detected in the measurement of K_3.

3.3.1 Analytic Approximations for K_3

Analytic approximations for the three-body collisional properties of ultracold gases near overlapping Feshbach resonances were recently derived for collections of identical bosons and distinguishable particles by J. D'Incao and B. Esry [142]. Their analysis effectively solves for the inelastic three-body rates using the hyperspherical formalism with model two-body molecular potentials [138]. They demonstrate that the entire spectrum of resonant features in the recombination rate can be

described with interference minima (M) and resonant enhancement terms (P) associated with the Stückelberg interferences and resonant tunneling through the effective three-body potential barriers described previously. These terms are of the form

$$M_{s_0}^{s_0^*}\left(\frac{x}{y},\frac{z}{u}\right) \propto \sin^2\left[s_0\ln\left(\left|\frac{x}{y}\right|\right)+s_0^*\ln\left(\left|\frac{z}{u}\right|\right)+\Phi\right]+\sinh^2(\eta_*) \quad (3.37)$$

$$P_{s_0}^{s_0^*}\left(\frac{x}{y},\frac{z}{u}\right) \propto \frac{\sinh(2\eta_*)}{\sin^2\left[s_0\ln\left(\left|\frac{x}{y}\right|\right)+s_0^*\ln\left(\left|\frac{z}{u}\right|\right)+\Phi\right]+\sinh^2(\eta_*)}. \quad (3.38)$$

In these expressions, Φ and η_* are the unknown three-body parameters which must be determined empirically. The variables $x,\ y,\ z$, and u each represent either a single pairwise scattering length (a_{ij}) or the characteristic range of interactions (r_0). $s_0 = 1.00624$ and $s_0^* = 0.41370$ are the scaling constants associated with the discrete scaling factors 22.7 and 1986.1 respectively. For strongly interacting identical bosons, s_0 is set to zero, and the expressions for M_{s_0} and P_{s_0} are identical to Equations 3.34 and 3.36 respectively.

These expressions demonstrate the complexity of analyzing general, strongly-interacting three-body systems, which is essentially built into the form of the three-body hyperradial potential $V_0(R)$. Consider the case where all the interactions are repulsive $a_{ij} < 0$ and $|a_{12}| \gg |a_{23}| \gg |a_{13}|$. In both the short-distance and asymptotic regions, $V_0(R)$ and the hyperradial wave functions are insensitive to the particular values of the scattering lengths. Two scale-invariant regions now exist: region (a) $|a_{12}| \gg |a_{23}| \gg |a_{13}| \geq R \gg |l|$, in which all three atom pairs resonantly interact in much the same way as if all three scattering lengths were infinite, leading to a $s_0 = 1.00624$ scaling; and region (b) $|a_{12}| \gg |a_{23}| \geq R \gg |a_{13}| \gg |l|$ where only two pairs of particles are resonantly interacting, leading to a $s_0^* = 0.41370$ scaling of $V_0(R)$ [143] For all larger values of R, the atoms are too far separated to support the weakly-bound Efimov trimers. Esry and D'Incao showed that in contrast to identical bosons with a single isolated resonance, for which interference minima occur in K_3 for $a > 0$ and resonant enhancement of K_3 for $a < 0$, minima and peaks in K_3 occur ubiquitously near overlapping resonances and, in some cases, these resonances can simultaneously tune K_3 in the same scattering process.

3.3.2 Integral Equations for Calculating K_3

E. Braaten and co-workers have demonstrated a method of calculating K_3 for a three-component Fermi gas at threshold with resonant interactions by numerically solving a generalization of the Skorniakov-Ter-Martirosian (STM) equations. Using this formalism, they were able to fit the measured three-body recombination rate data for three-component ^{6}Li Fermi gases in the low-field regime (122 Gauss $< B <$ 485 Gauss) taken by our group [144] and that of S. Jochim's group in Heidelberg [145], where all of the pairwise scattering lengths were negative. The fit enabled them to extract the low-field three-body parameters and make a strong claim that the resonant loss features observed in the this region were attributed to Efimov physics [146].

Subsequently, using recent K_3 measurements by our group in the high-field region $B > 840$ Gauss [147], they were able to numerically fit our data to extract the high-field three-body parameters and map out the entire spectrum of Efimov features throughout the universal regime spanning the three overlapping Feshbach resonances [8]. This spectrum has been valuable in analyzing our data and designing future experiments to test the universal properties of our ultracold gas. In the following I will briefly describe the basis of their theory.

In the low-temperature limit, the optical theorem can be used to express the rate constant K_3 in terms of the forward *T-matrix* elements for 3-atom elastic scattering in the limit where the momenta of the three atoms goes to zero,

$$K_3 = 2\Im(T(0,0,0;0,0,0)). \tag{3.39}$$

The T-matrix elements can, in turn, be expressed in terms of the atom-dimer scattering amplitudes $A_{ij}(p,q;E)$ where i and j are the initial and final states, and the scattering occurs from relative-momentum state p between the incident atom-diatom pair to relative-momentum state q between the scattered atom-dimer system at energy E. Considering only s-wave interactions, the rate constant K_3 is given by [8]

$$K_3 = \frac{32\pi^2}{m}\sum_{i,j} a_i a_j \Im(A_{ij}(0,0;0)). \tag{3.40}$$

In this notation, $a_i = a_{jk}$, the sums i,j are over the labels (1,2,3), and the imag-

inary component of the atom-dimer scattering amplitude in the limit of zero momenta is denoted by $\Im(A_{ij}(0,0;0))$. This formalism can also be applied to determine the exclusive decay rates to one of the shallow universal dimers as

$$K_3^{ij} = \frac{512\pi^2\hbar}{3\sqrt{3}ma_k^2}\left|\sum_l a_l(A_{lk}(0,2/(\sqrt{3}a_k);0)\right|^2 \tag{3.41}$$

where again k is the complimentary spin to ij and the dimer and recoiling atom both have momentum $2/\left(\sqrt{3}a_k\right)$.

For two-body, $l = 0$ potentials in the zero-range limit, the momentum-space Faddeev equations for the atom-dimer scattering amplitudes reduce to the integral equations derived by Skorniakov and Ter-Martirosian [129]. The nine scattering amplitudes in Equation 3.40 satisfy coupled integral equations that are generalizations of the *STM equations* [8] which, assuming the initial relative momentum and total energy are set to zero, are given by

$$A_{ij}(0,p;0) = \frac{1-\delta_{ij}}{p^2} + \frac{2}{\pi}\sum_k(1-\delta_{kj})\int_0^\Lambda dq\, Q(p,q;0)D_k(3q^2/4)A_{ik}(0,q;0) \tag{3.42}$$

where

$$Q(p,q;E) = \frac{q}{2p}\log\frac{p^2+pq+q^2-mE}{p^2-pq+q^2-mE}, \tag{3.43}$$

$$D_k(p^2) = \left[-1/a_k + \sqrt{p^2-i\epsilon}\right]^{-1}. \tag{3.44}$$

Here Λ is an ultraviolet cutoff that must be large compared to p, $1/|a_1|$, $1/|a_2|$, and $1/|a_3|$. Note that the solutions to the integral equations 3.42 depend log-periodically on Λ with the discrete scaling factor $\lambda_0 \simeq 22.7$ such that Λ only differs from the three-body parameter κ_* by a numerical constant. Analogously, extension of these generalized STM equations to account for deeply bound dimer states involves extending the cutoff parameter to the complex plane as $\Lambda\exp(i\eta_*/s_0)$, and extending the path of integration in the variable q to run both along the real axis from 0 to Λ and then along the complex plane from Λ to $\Lambda\exp(i\eta_*/s_0)$. In so doing, the rate for decay to deeply bound dimer states K_3^{deep} becomes non-zero.

The T-matrix elements in Equations 3.40 can be further reduced to three cou-

pled integral equations for the three linear combinations $\sum_i a_i A_{ij}(0,p;0)$. The solutions to these equations for the real part of $A_{ij}(0,p;0)$ are singular as $p \to 0$ [148]. Therefore, the rate constant K_3 is finally simplified by subtracting the singular terms, proportional to $1/p^2$, $1/p$, and $\ln(p)$, as $\Im(A_{ij}(0,p;0))$ is extrapolated to $p = 0$ [8]. The final set of three, coupled integral STM equations are then solved numerically to extract the three-body parameters κ_* and η_* from the variation of the rate constant with respect to the scattering lengths $K_3(a_{12}, a_{23}, a_{13})$.

This powerful method has been adapted for a variety of applications including solving for the spectrum of Efimov states for our three-component Fermi gases [146, 8] as well as probing the influence of finite range corrections [149] and finite temperature effects [150] on the universal spectrum of Efimov trimer states and resonant three-body recombination features. If this theory is applied to the simplified case of distinguishable particles with identical, resonantly-enhanced scattering lengths ($a_{12} = a_{23} = a_{13} \gg l$), the analytic expressions for the recombination rates of identical bosons (Equations 3.34 and 3.36) are recovered. The three-body recombination rates are therefore sensitive only to the magnitude and sign of the scattering lengths in the universal regime, and insensitive to the statistics of the particles.

3.4 Efimov Physics at Finite Temperatures

In principle, an infinite series of Efimov resonances should become observable in systems of identical bosons as the scattering length is tuned toward $\pm\infty$ from above or below the resonance. In practice however, this is obviously not the case at finite temperatures, where the scattering lengths themselves are unitarity limited to on the order of the size of the deBroglie wavelength, as discussed in Section 2.5. In fact there are three primary thermal effects that limit the visibility of the Efimov resonances: *unitarity*, *thermal averaging*, and *higher partial waves*. A detailed review of the effects of temperature on the three-body rates K_3 can be found in Reference [151]

The universal expressions given for the three-body scattering observables K_3 are only valid in the threshold regime $k|a| \leq 1$, where the collision energy is the

smallest energy scale in the system. This requirement is not assured even with our ultracold gases due to the extremely low energy scales set by the binding energy of the universal dimer ($E_D = \hbar^2/(ma^2)$) for positive scattering lengths and the height of the repulsive barrier in the lowest hyperspherical potential for negative scattering lengths [135]. For identical bosons with large negative scattering lengths, the height of the barrier in the adiabatic three-body potential is given by [151].

$$U_{max} = 0.158\hbar^2/(ma^2) \tag{3.45}$$

For thermal energies much lower than this barrier height, the measured rate coefficient is independent of the energy and can be compared to the calculated recombination rates at threshold. Thermal averaging, or averaging of the energy-dependent rate coefficients for an ensemble at temperature T, only becomes important for energies on the border of the threshold regime. Its effects generally reduce the visibility of the resonant features in the recombination rate.

The effects of unitarity and higher partial waves can be understood by examining the three-body recombination rate defined in terms of the S-matrix [151]

$$K_3 = \frac{1}{2}\sum_{J,\pi}\sum_{i.f}\frac{32N!(2J+1)\pi^2}{Mk^4}|S_{fi}^{J\pi}|^2 \tag{3.46}$$

where N is the number of identical particles, and J and π are the total angular momentum and the overall parity respectively. $k = \sqrt{2ME/\hbar^2}$ is the hyperradial wave number in terms of the energy E and the three-body reduced mass $M = m/\sqrt{3}$, and i and f label the initial and final scattering channels. In our experiments, K_3 is defined as the rate coefficient for the number of atoms lost per spin state attributed to three-body interactions. This term differs from the event rate at which triplets of atoms collide, defined in Reference [151], simply by the included factor of 1/2 in the above expression. At threshold, the $J^\pi = 0^+$ contribution dominates with the 2^+ term suppressed as $K_3 \propto E^2a^8$ [152]. As the scattering length is increased with a non-zero collision energy, the unit recombination probability limit ($|S|^2 = 1$) is at some point reached.

Accounting for thermal averaging, which reduces the maximum detectable value of K_3 by a factor of two, for a gas at temperature T the maximum value of K_3 is

then given by

$$K_3^{max} = \frac{32\pi^2\hbar}{4Mk^4} = \frac{\sqrt{108}\pi^2\hbar^5}{m^3(k_BT)^2}. \tag{3.47}$$

D'Incao and co-workers showed that, whereas K_3 reached the unitarity limit for $a > 0$ outside the threshold regime, for $a < 0$ the rate saturates at a value nearly a factor of 10 below the unitarity limit. Subsequently, they define a critical scattering length

$$a_c = \hbar/\sqrt{mk_BT} \tag{3.48}$$

above which the visibility of the maxima and minima in the rate coefficients K_3 are significantly affected by the finite temperature of the gas. Essentially, both thermal averaging and unitarity primarily restrict the number of resonant features observable. The truncation of these features at finite energies, however can also shift the apparent location and width of the resonant peaks unless these effects are included in the analysis of the data. Treatment of the thermal effects in our data will be discussed in greater detail in Chapter 6.

Chapter 4

Experimental Apparatus

The creation and detection of ultracold many-component Fermi gases requires strict control over the ultra-high vacuum, magnetic, and optical environments experienced by the atoms. This chapter describes the experimental apparatus used to create and probe degenerate and/or three-component gases of fermionic lithium-6 atoms spanning a range of magnetic bias fields of 0 to 1500 Gauss. I began working in Professor O'Hara's lab in the spring of 2005. At that time, the only installed components of the experiment were the optics tables. Approximately one year later, we first observed trapping of ^{6}Li atoms in a Magneto-Optical Trap, and in September 2007, we achieved degeneracy of a two-component Fermi gas of ^{6}Li atoms. Over the six years that I have been with the lab, our experimental system has undergone numerous upgrades. In this thesis I will concentrate on describing the most recent experimental system, only reviewing older iterations of the apparatus that were directly relevant to our experimental results.

This chapter is organized as follows: In the first section, the vacuum system is discussed including the design of our apparatus and the various components required to maintain ultra-low vacuum in the experimental chamber to assure that our trapped atomic gas is long lived. The oven region is then discussed, which creates a high flux, collimated atomic beam that provides the source for our atomic gas. The second and third sections detail the design and control of our laser system and the various electromagnets installed to cool, image, and manipulate the atoms during various stages of the experiment.

The atoms are initially cooled from the atomic beam of ^{6}Li atoms at a tem-

perature of 465 ℃ using a zero-crossing Zeeman slower, as described in Section 4. Eventually, the slowed atoms drift into the experimental chamber where they become trapped and are cooled to a temperature $T \sim 200\mu$K using a Magneto-Optical Trap. The theory and implementation of this cooling scheme is described in Section 5. From the Magneto-Optical Trap, some of the atoms are loaded into a conservative trapping potential provided by the Gaussian profile of high power ($\sim$ 100 Watts), far red-detuned laser beams. These so-called optical dipole traps are used extensively in our experiments to provide an adjustable confinement for the atoms, in which the gas is eventually evaporatively cooled to degeneracy. We have also implemented large-volume dipole traps capable of adiabatically cooling the gas to achieve extremely low temperature and density samples. The design, implementation, and control of our laser-trapping systems is discussed in detail in Section 6.

Section 7 discusses our method of extracting information about the density and momentum profile of the gas using standard absorption imaging techniques. In Section 8, we discuss the design of our radio frequency antennas and the system of electronics used to apply radio-frequency magnetic fields to manipulate the internal states of our atoms. Finally, the computer-based control system is discussed in Section 9, designed to provide highly precise and temporally controlled signals to command the various components in our experimental apparatus. Essentially all of these systems were designed and installed over the last six years that I have been with the lab. Thanks in large part to the ingenuity and hard work of Ken O'Hara and his group, the current apparatus is robust and highly dynamic, ideal for studying few- and many-body physics in multi-component Fermi gases.

4.1 Vacuum System

The entire vacuum system is approximately 55" long and consists of three regions: the oven, the Zeeman slower, and the experimental chamber. (see Figure 4.1) The oven (1) and the Zeeman slower (2) are designed to collimate an atomic beam from a vapor of ^{6}Li atoms heated to approximately 465 ℃ and initially slow and cool the beam for subsequent cooling and trapping in the experimental region. This process necessitates maintaining high vacuum in the oven region to minimize

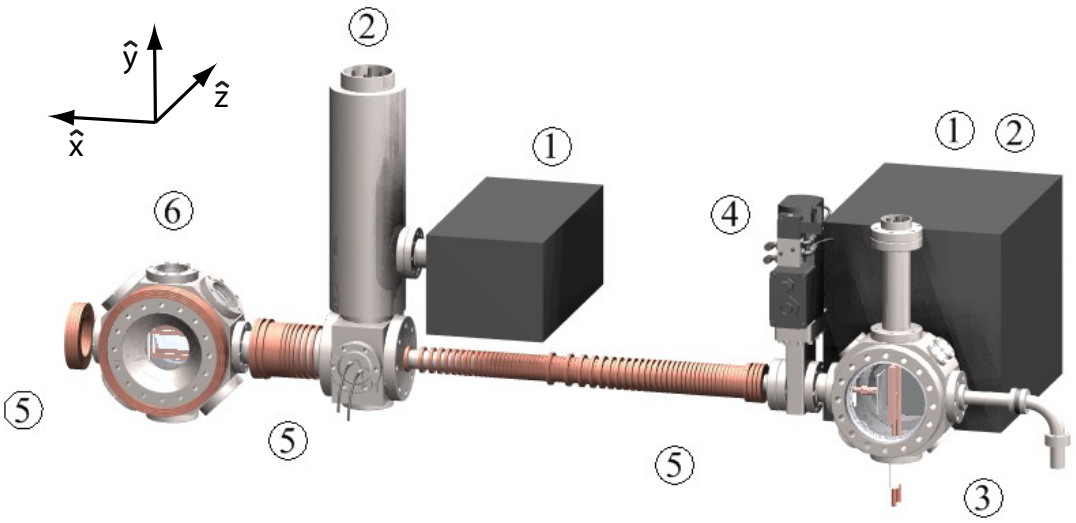

Figure 4.1. Overview of the entire vacuum system. The image has been slightly rotated along the $\hat{x}$-$\hat{y}$ plane.

attenuation of the atomic beam and chemical reactions of the Lithium source with background gases. Further, an ultra-high vacuum in the experimental region must be maintained throughout the experimental process to minimize heating and loss of magnetically and optically trapped atoms from background gas collisions.

The primary pumping sources in our apparatus are Ion Pumps, Titanium Sublimation Pumps, and Non-Evaporable Getters. These pumps are ideal for use in ultracold atomic gas experiments due to their cleanliness, ability to pump a variety of gases, and vibration free operation.

Ion pumps utilize ionization of background gases and acceleration of these ions in a strong electric field towards a solid chemically active cathode to pump atoms and molecules out of the system [153]. Our ion pumps (VacIon Plus StarCell) are triode types with a Titanium cathode, and are specially designed for pumping large amounts of Noble gases and hydrogen, with operating pressures between 10^{-2} and 10^{-11} Torr.

Titanium Sublimation Pumps (TSP) are used to supplement the pumping action of our ion pumps. Titanium is highly reactive and can be applied to large areas of the vacuum system, can be more effective in removing certain reactive elements, and can help combat the regurgitation effects of ion pumps. The TSP consists of titanium filaments through which a high current is passed (47 Amps for 7 minutes), sublimating a thin layer of titanium atoms onto the walls of the vacuum system. Reactive background gases form stable compounds when they come into contact with the titanium layer, effectively removing them from the system. For highly reactive gases (eg. H_2), this yields pumping rates as large as 10 l/(s cm^2) times the surface area of the sublimation layer. Over time, the titanium layer becomes saturated, and a new layer of titanium must be sublimated to maintain the pumping efficiency.

Non-Evaporable Getters (NEG) are supplemental pumps that work on much the same principal as the TSP. Our getters, manufactured by SAES getters, are composed of a thin layer of st707 powder on Constantan (amagnetic) strips. These getter strips can be cut and applied to any region of the vacuum system, and are shipped with a protective passivation layer which is removed during bake-out of the vacuum system. St707 is a TiZrV alloy that is highly efficient for absorbing reactive molecules (O_2, H_2O, N_2, CO, CO_2, H_2). After activation, the getters can have a pumping rate as high as a few 0.1 l/(s cm^2) for H_2. Over time, however, the getters develop a film of reacted materials requiring reactivation to maintain their pumping efficiency.

The TSP and ion pumps are used in conjunction to achieve maximum pumping for both reactive and Noble gases. We use a combination ion/TSP pump (Vacion Plus 150 Star-Cell ion pump, 125 l/s for N, with integrated TSP cartridge and heaters) to maintain vacuum in the oven region, along with an ion pump (Vacion Plus 75 Starcell, 65 l/s for N) and TSP (Varian) connected to a 4" diameter, 12" tall chamber between the Zeeman slower and the experimental chamber to maintain UHV in these regions. These pumps are shown in Figure 4.1. Further, NEG strips are applied to both the walls of the drift tube for the Zeeman slower and wherever possible in the experimental chamber itself. The NEGs were then activated during the 2–3 day initial bake-out of the vacuum system (400 ℃ in the

Zeeman slower and oven regions, 200 ℃ for the experimental chamber). Finally, an all-metal gate valve (MDC, GV-1500M-P) is positioned between the oven region and the Zeeman slower, allowing us to bring the pressure in the oven region up to atmosphere for service or to replenish the lithium source while maintaining an ultra-high vacuum throughout the rest of the system.

The experimental chamber consists an 8" Multi-CF Spherical Octagon from Kimball Physics (MCF800-SO2000800). The use of this chamber is highly advantageous in that it has large optical access and high conductance to the pumping regions to maintain the UHV environment. Further, in contrast to glass cells, the windows can all be antireflection (AR) coated on both sides and the eight 2-3/4" Conflat (CF) ports have integrated grooves to allow mounting of components within the chamber itself (i.e. the RF coils shown in Figures 4.1 and 4.6). The Octagon is mounted to the Zeeman slower on one of the CF ports, and capped with 2-3/4" viewports on the other 7. On the faces of the Octagon are a pair of recessed viewports. The glass faces of the viewports, which are AR coated for 671nm and 1064nm light, are each located only 1" from the center of the chamber. These large viewports provide nearly 90 degrees of optical access along the axis of the chamber and contain multiple mounting surfaces for high current electromagnets, which have been useful for externally applying large bias and gradient fields to the atoms.

Differential pumping was required between the oven region and the Zeeman slower to achieve ultra-high vacuum in the experimental chamber. The pressure differential is maintained by separating these regions with a 4" long, 0.25" outer diameter (OD), 0.19" inner diameter (ID) copper rod that limits the conductance of background gases between the oven and high-vacuum regions. The conductance is a measure of the number of atoms or molecules passing through a region of the vacuum system per second. As particles collide with the walls of the tube, they hit, stick, and desorb in a cosine distribution, limiting their transmission flux [154]. Therefore, smaller ratios of tube diameter to tube length lead to smaller conductances.

For a tube with a diameter (D) and length (L), measured in inches, the conductance (C) of air at room temperature and the resultant pressure differential

across a tube are given by [154, 153]

$$C = 78\frac{D^3}{L}ls^{-1} \quad (4.1)$$

$$\frac{P_1}{P_2} = \frac{C}{S+C} \quad (4.2)$$

where P_1 (P_2) are the steady-state pressures in the high (low) vacuum regions and S is the speed of the pump in the high vacuum region. The pressure drop across our differential pumping tube (C = 0.133 ls^{-1}, $P_1/P_2 \simeq 500^{-1}$) should allow us to maintain a pressure on the order of 10^{-11} Torr in the experimental region, regardless of the higher vacuum in the oven region ($5.4*10^{-9}$ Torr for the hot oven or $6*10^{-10}$ Torr when the oven is in the cold state).

The background gas pressure in the experimental region sets an upper bound for the lifetime of our ultracold trapped gases. Heating and loss of the trapped gas is attributed to elastic collisions between the ultracold atoms and the background gas atoms and molecules nominally at room temperature ($T = 300$ K). For a residual background gas of lithium atoms at a pressure P = 10^{-11} Torr, the loss rate for our sample, which is directly proportional to the pressure, is $\Gamma_c = 0.0028$ s^{-1}, which should cause the atoms to decay exponentially with a time constant of $\tau_c = 1/\Gamma_c = 355$ sec [155]. This time constant far exceeds any of the characteristic timescales in our experiments and such loss should therefore be negligible.

4.1.1 ^{6}Li Oven

The oven region consists of the heated lithium chamber and nozzle, along with the shutter and collimators used to produce a high-flux, pulsed atomic beam. The lithium chamber and the nozzle sections are housed in 2" diameter aluminum cylinders which are machined to maximize their thermal contact with the stainless steel components. These aluminum housings, which are heated with regulated band heaters and imbedded with multiple thermocouples for temperature feedback, have a large thermal mass and are designed to provide a highly uniform and reproducible thermal environment for the lithium chamber and nozzle regions.

The lithium chamber is a 3/4" OD × 1-1/2" tall half-nipple with a 1-1/3" CF flange from MDC Vacuum. Approximately 2 grams of solid lithium is loaded into

the chamber which, during operation, is heated to 435 ℃. At this temperature, liquid lithium fills the bottom 1/3 of the chamber (^{6}Li melting point = 180.7 ℃). The rest of the chamber is filled with lithium gas at a vapor pressure of 3.6×10^{-4} Torr [11]. The chamber is oriented vertically and connected to a 90° CF elbow fitting (MDC vacuum 403000). A nozzle is then attached to the end of this fitting to limit the conductance of the atomic vapor into the rest of the system.

The gasket connecting the lithium chamber to the CF elbow fitting is prone to failure in lithium ovens [156] due to the daily temperature cycling of these regions and the highly reactive nature of lithium. We therefore use nickel gaskets between these regions because nickel is both more immune to failure from repeated temperature cycling and is less reactive in a corrosive environment. Regardless, we still experienced a failure of the nickel gasket in our first iteration of the oven, where we used heater tape to heat the oven instead of band heaters. The failure occurred in the form of a green deposit (likely a lithium-salt [156]) surrounding the nickel gasket which caused a short in the heater tape. It is conceivable that, due to imperfect winding of the heater tape, a temperature minima was at the location of the gasket where lithium gas would condense and wet the gasket material. With the more uniform thermal environment provided by the band heaters and aluminum housing, we have run the lithium oven for over two years with no noticeable degradation in the atomic beam.

In our original design, the nozzle consisted of a glass capillary array, composed of an array of 100 micron diameter tubes approximately 2 mm in length, to provide a large flux collimated lithium beam. These arrays are rated to withstand temperatures above 450 ℃ and are often used for gas flow collimation and differential pressure barriers. We found however, that the lithium vapor reacted with the glass in the array at temperatures on the order of 460 ℃ and when we removed the array after a period of operation, the array had turned black and was etched over a large volume of the material.

Our current nozzle is based on a design which was developed for a dual-species lithium/sodium apparatus [156]. It is machined from a double-sided 1-1/3" Conflat Flange Blank from MDC vacuum and contains a 1/4" diameter, 0.15" long aperture radially centered on the flange. To inhibit condensation of lithium vapor onto the nozzle, it is heated to a temperature of 465 ℃ during operation, and held at 350 ℃

when the oven heater is off. This assures that the atoms in the lithium vapor will condense back in the lower temperature oven region, whose temperature defines the vapor pressure of the atomic gas. The number density of atoms in the vapor, as calculated from the ideal gas law, is approximately $n_0 = P/k_bT = 4.7 * 10^{12}$ cm^{-3}. At this temperature, the flux of atoms from the lithium reservoir Φ and the number of atoms diffusing through the nozzle per second $\dot{N}$ are [157]

$$\Phi = n_0\bar{v}/4 = 1.89 \times 10^{17}/(cm^2 s) \quad (4.3)$$

$$\dot{N} = \Phi A_S = 6 \times 10^{16}/s, \quad (4.4)$$

where $\bar{v} = \sqrt{8k_BT/(\pi m)} = 1610\ m/s$ is the average velocity of the atoms in the vapor and A_S is the area of the nozzle-aperture.

At the end of the nozzle, a thin-walled stainless steel tube separates the high temperature sections of the oven from the rest of the vacuum system. This tube is machined from a 3/4" OD × 3" long nipple from MDC Vacuum. The thickness of the tube wall is reduced to approximately 0.01" over a length of 0.825" to significantly limit its thermal conductance (G = .0052 W/K). This allows for a thermal gradient along the tube while maintaining the tensile strength to support the nozzle and lithium chamber. By wrapping the high-temperature sections with multiple layers of flexible fiberglass for thermal insulation and simple air cooling of the low-temperature sections of the oven region, we maintain temperatures of 465 ℃ (435 ℃) in the nozzle (lithium chamber), and a temperature of 60 ℃ at the end of the thin-wall drift tube.

The low temperature sections of the oven consist of the oven chamber, which houses the collimators and shutter for the atomic beam, and the vacuum pumps to maintain vacuum in this region (see Figure 4.1). The oven chamber is a 6" spherical square (Kimball Physics, MCF600-SS200408), connected to the combination ion pump/TSP on one of the 6" CF flanges and capped with a glass viewport on the other. Radially, it has four 2-3/4" CF flanges and four pairs of 1-1/3" CF flanges which are used to connect various parts of the vacuum system, a vacuum gauge, and an electrical feedthrough for the shutter.

The first element that the high-temperature atoms encounter after effusing through the nozzle is a 1.4" X 3" X 1/4" copper cold plate with a 1/4" aperture

centered on the atomic beam. The copper plate is centered in the oven chamber and maintained at room temperature with two 1/4" diameter copper rods. These rods are part of a high-current CF feedthrough which is mounted on the bottom flange of the oven chamber. The cold plate acts as a collimator for the beam to protect our shutter from excessive buildup of solid lithium along with providing a low-temperature condensation region to capture the majority of the atoms from the atomic beam and maintain a high vacuum in the oven region. We have the ability to further cool this plate to liquid-nitrogen temperatures to enhance the condensation rate of lithium atoms onto this plate and further improve our vacuum in this region. The vacuum in the oven region raises by only a factor of ten with the inclusion of the atomic beam, however, and further cooling of this plate has not been necessary.

The atomic beam entering the Zeeman slowing region is collimated by the combination of the high-temperature nozzle (1/4" aperture diameter) and the end of the differential pumping tube (.19" aperture diameter), discussed in Section 4.1 which are separated by approximately 11". The resultant collimated atomic beam enters the high-vacuum region with a solid-angle of 40 mrad. The intensity of the atomic beam can be determined from the number of atoms leaving the oven per second in spherical coordinates with respect to the directions given by θ, ϕ and v [158].

$$d\dot{N}_{v,\theta,\phi} = \frac{n_0 A_S}{\pi^{3/2}\bar{v}^3} v e^{-v^2/\bar{v}^2} \cos(\theta) v^2 \sin(\theta) dv d\theta d\phi. \tag{4.5}$$

Integrating this equation over the solid-angle of the beam for all velocity classes yields an intensity of $\dot{N} = 8.6 \times 10^{10}$ atoms/s with an average velocity along the axis of the Zeeman slower $\bar{v}_x \simeq 1600$ m/s and transverse to the slower $\bar{v}_r \simeq 30$ m/s.

During an experimental sequence, lithium atoms are initially slowed and trapped in the experimental region from the atomic beam. After the atoms are collected in the trap, if the atomic beam is left on continuously, the atoms in the beam will elastically collide with the trapped atoms causing loss in the same manner as through collisions with background gases. This loss mechanism can be inhibited by shunting the atomic beam after the loading stage. To this end, we have installed a ultra-high vacuum (UHV) compatible shutter (UNIBLITZ, Ls6T2

with encapsulated coil), centered on the atomic beam and thermally connected to the cold plate to relieve the thermal load on the shutter mechanics caused by repeated cycling. The Teflon-coated shutter blade fully blocks the aperture when engaged with 100 Hz (continuous) and 400 Hz (pulsed) cycling frequencies.

We quickly found that shuttering of this atomic beam is mandatory for achieving long lifetimes and minimal heating of our trapped atoms during the experimental sequence. Aside from heating and loss of the trapped atoms due to scattering from the hot atomic beam, the lifetime of the trapped gas reduced to a few seconds when the duty cycle of the atomic beam was greater than 10%. Likely, the atoms from our high-flux atomic beam which were not cooled to within the capture velocity of our optical and magnetic trapping potentials remained for a significant time in the experimental region before migrating to our ion and TSP pumps, thereby increasing the vacuum pressure in the experimental chamber. The combination of longer delay times between experiments and maintaining a 1 second load time of the atomic beam has allowed us to accumulate large samples of trapped atoms with lifetimes exceeding 30 seconds.

4.2 Laser System

The initial stages to slow and cool the effusive atomic beam from 738 K to $\sim 200\ \mu$K and trap the atomic samples in the experimental chamber are derived from the radiation pressure that atoms experience in a near-resonant light field. Here I describe the system of lasers, optics, feedback electronics, and frequency references necessary to cool and image the ^{6}Li gas for our experiments. An overview of our cooling/imaging laser system to produce multiple light sources with wavelengths nominally centered on the D_2 transition of lithium at ~ 671 nm, is shown in Figure 4.4. Two primary requirements for this laser system are that the laser linewidths must be much narrower than the natural linewidth of the transitions ($\Gamma = 5.87$ MHz for the D_2 line) and the laser system must be stabilized to the atomic transition throughout the experiment. Further both the frequency and intensity of the lasers are designed to be dynamically adjustable, allowing for multiple cooling stages and providing imaging frequencies for multiple Zeeman sublevels over a large range of magnetic field, which is instrumental to our experiments.

Before the spring of 2009, the light for the cooling and imaging lasers was derived from a Coherent 899-21 ring-dye laser. The liquid gain medium, Ld-688 dye in a concentration of 1.17 grams per liter of solvent (2-Phenoxyethanol, 98%), was pumped with nominally 6 Watts of 532 nm laser light from a solid-state laser (Verdi V18 from Coherent Inc). The dye laser was frequency stabilized to an internal reference cavity which in turn was locked to the D_2 transition in ^{6}Li using the fluorescence from a transversely pumped ^{6}Li collimated atomic beam. Although the Coherent 899 provided up to 1 Watt of power at 670.977 nm, which was sufficient to cool $\sim 10^8$ atoms to below 0.3 mK in a Magneto-Optical Trap (MOT) (see Section 4.5), the Dye laser had an unacceptably large linewidth (~ 4 MHz) and long-term power and pointing instabilities which severely affected the shot-to-shot stability ($\sim 50\%$) of our data.

Recently, we have made significant upgrades to both our cooling/imaging lasers and our magnet system. The source for our laser light is now derived from two tunable, grating stabilized diode lasers (Toptica DL100). As the power output from these sources is relatively low (~ 10 mW) and hundreds of mW of power is required for Zeeman slowing the atomic beam and trapping the atoms in a MOT, the light from each of these lasers are amplified to approximately 500 mW by tapered amplifiers (Toptica TA-0670-05000). The solid-state design and mechanical stability of the these laser systems has greatly improved both the linewidth and stability of our optical system where, after the system has been run for a short time, the experimental shot-to-shot stability is now less than 10% and the optical power and directionality are effectively stable.

4.2.1 Laser Lock to Iodine

Previous frequency references for ultracold lithium experiments used either the Doppler minimized fluorescence from a collimated lithium beam [25] or sub-Doppler saturated absorption spectroscopy in a high-temperature lithium cell [159, 160, 161]. The lithium beam has limited application because saturated-absorption spectroscopy is difficult in these setups and the signals are homogenously broadened by the finite transit-time of the atoms through the probe beam. Lithium cells, on the other hand, can be used for saturated absorption spectroscopy but they re-

quire high temperatures to maintain a sufficient vapor pressure and difficulties arise with lithium condensing on the windows.

We have recently upgraded the laser locking system from using a collimated ^{6}Li beam to using sub-Doppler saturated absorption spectroscopy [162] of molecular iodine. Much of this work was carried out by Yi Zhang over the Summer of 2009, but theoretical investigations to fully characterize the system are still under way. For our first step, we mapped out the spectrum of hyperfine lines in the R(142)5-6 rovibronic transition of the $B0_u^+ \leftarrow X0_g^+$ electronic system in $^{127}I_2$ [163]. This rovibronic line, whose observation has not been previously documented, is particularly useful because it is centered approximately 1 GHz to the red of the D_2 transition in ^{6}Li and we found that the hyperfine lines have sufficient line strengths to provide high-resolution feedback for locking of the spectroscopy laser.

To measure the hyperfine components of this line, we used standard sub-Doppler saturated absorption spectroscopy techniques. Our spectroscopy setup is shown in Figure 4.2. Saturated absorption spectroscopy is based on velocity-selective absorption of resonant light. In a vapor cell, particles move randomly in all directions with a Boltzmann velocity distribution along each axis. Standard absorption spectroscopy samples this velocity distribution, where atoms moving with a velocity v have a Doppler shifted resonance frequency

$$\nu_0' = \nu_0 \left(1 + \frac{v}{c}\right). \tag{4.6}$$

The sign has been chosen for a laser beam propagating along the positive axis so that atoms traveling along the laser beam have resonance frequencies blue shifted to higher frequencies, and atoms traveling counter to the laser beam are red shifted. This leads to spectral widths on the order of GHz for molecular iodine at room temperature.

By counter-propagating two spectroscopy laser beams through the cell with frequencies varying by a small amount $\Delta\nu$, only atoms in a single axial velocity class are simultaneously resonant with both lasers, given by

$$v_{res} = \frac{c\Delta\nu}{2\nu_0} \tag{4.7}$$

Saturated absorption spectroscopy uses a pump-probe technique to measure this

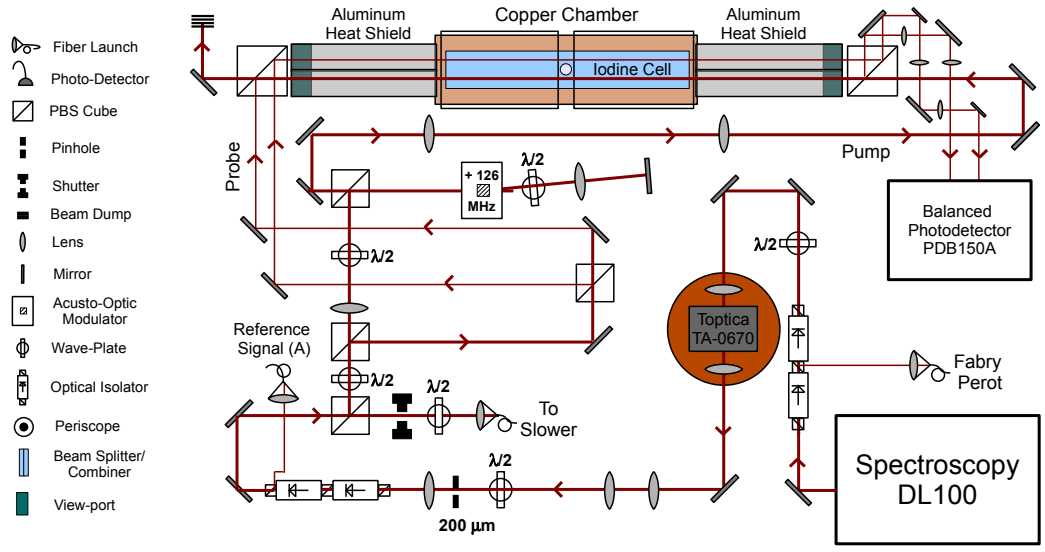

Figure 4.2. Optical layout for sub-Doppler absorption spectroscopy and frequency locking the spectroscopy laser to molecular iodine in a temperature controlled vapor cell.

velocity-selective spectra. Here, an intense pump beam depletes the atomic population in the lower state that can be excited by the probe beam at the velocity class v_{res}.

In our setup, the pump beam consists of approximately 60 mW of light from the spectroscopy laser which is double-passed through an acousto-optic modulator (AOM) to up-shift the frequency of the light by approximately 252 MHz and amplitude modulate the beam at 100 kHz. The $\sim$ 10 mW probe beam is at the frequency of the spectroscopy laser. A second identical probe beam is displaced from the pump beam as it propagates through the cell to sample the Doppler profile of the iodine spectra. The saturated absorption signal from the probe beams, which is detected on a balanced photodetector system (Thorlabs PDB150A) is then monitored with a Lock-in amplifier. The Lock-in looks for fluctuations in the absorption signal at the frequency of and in phase with the modulation introduced by the AOM, removing the Doppler background.

A "cold-finger" on the iodine cell is held nominally at room-temperature to define the vapor pressure in the cell (7.56 mTorr at 260 K). The body of the iodine cell, on the other hand, is housed in a copper chamber and heated with regulated

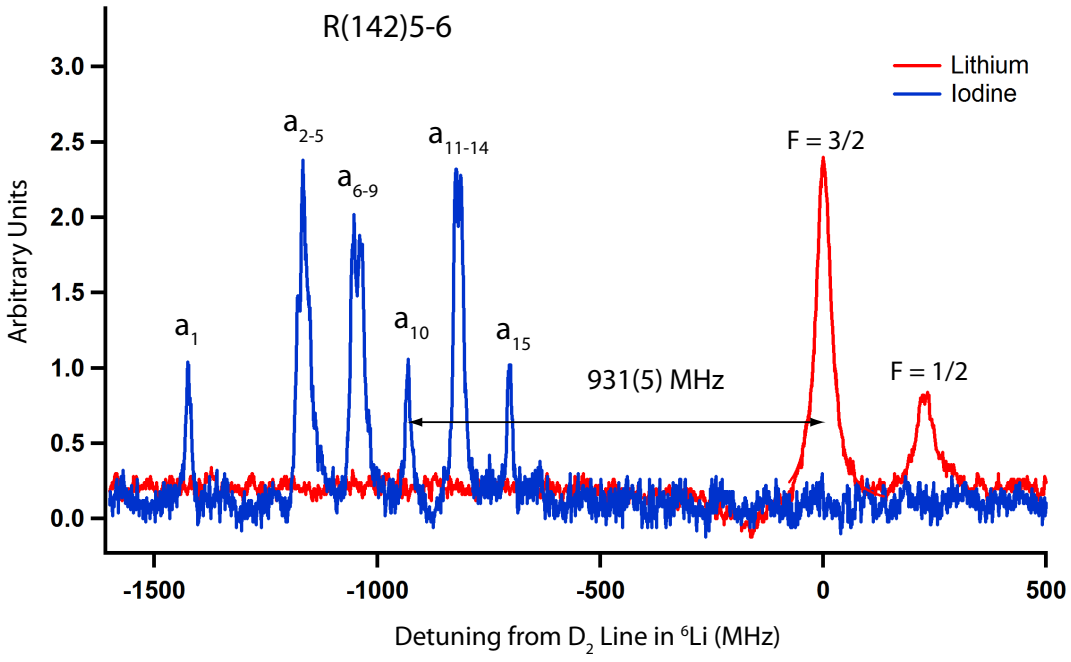

Figure 4.3. Hyperfine-resolved absorption spectra of the R(142)5-6 rovibronic transition $^{127}I_2$ compared to the D_2 transition lines in ^{6}Li. The line strengths for the $^{127}I_2$ and ^{6}Li spectra are in arbitrary units, not on the same scale.

band heaters to $\sim$ 200 ℃ to enhance the population of atoms in the excited rovibrational levels. Further, aluminum cylinders are attached to the view ports of the chamber and capped with AR coated windows to provide a thermal gradient from the heated chamber, minimizing air currents which perturb the optical beams.

Simultaneous measurement of the saturated absorption spectra of the R(142)5-6 rovibronic line in $^{127}I_2$ and the D_2 line from a collimated ^{6}Li beam are shown in Figure 4.3. Although the sub-Doppler spectra for the iodine line follows the 1-4-4-1-4-1 hyperfine structure for the even rotational quantum numbers [164], our resolution is not sufficient to resolve the multiplets. We decided to use the a_{10} singlet hyperfine line, which is frequency downshifted from the ^{6}Li resonance by 931(5) MHz with a linewidth on the order of 1 MHz, as the frequency reference for our 670 nm laser system.

By frequency modulating the $\sim$ 126 MHz AOM shift on the pump beam by $\pm$ 2 MHz at a rate of 100 kHz, the lock-in amplifier outputs an error signal proportional to the frequency offset of the spectroscopy laser from the a_{10} hyperfine line in Iodine. As the probe and pump frequencies are separated by 2×126 MHz, the

zero-crossing of the error signal occurs when the spectroscopy laser is 814(5) MHz to the red of the D_2 transition in ^{6}Li. This error signal is shaped by a home-built PID board [165] to shape the signal for feedback to the piezo actuator of the DL100 laser, thereby locking the frequency of the spectroscopy laser. The remaining light from this laser ($\sim$ 100 mW), is coupled through a single-mode, polarization maintaining fiber to be used for Doppler cooling of the atomic beam along the Zeeman slower. To minimize the noise in this frequency locking scheme the entire optical setup shown in Figure 4.2 is housed on a 2' $\times$ 3' optical table which is raised above the floating optical table by four 2" $\times$ 2" $\times$ 3" Absorbathane cubes, reducing the resonance frequency of the table to 7.5 Hz. Further, the table is housed in a Styrofoam box to provide acoustic shielding from the rest of the room. With these improvements, we lock the spectroscopy beam to the a_{10} hyperfine line with a signal noise on the order of 200 kHz.

4.2.2 Experimental Laser System

Whereas the frequency of the spectroscopy laser is effectively static, the experimental laser system, shown in Figure 4.4 is designed to be highly dynamic, providing light for both the frequency-dependent magneto-optical cooling in the experimental region as well as light for imaging the atomic gas, whose resonance frequency is highly dependent on both the magnetic field applied to the atoms and the atomic state under investigation. To achieve such high precision tunability over a wide frequency range, the experimental laser is phase-frequency locked to a programmable frequency offset of the spectroscopy laser using an optical phase-locked loop (OPPL) designed for use with grating stabilized diode lasers [166]. In this system, the rate at which the relative phase between the spectroscopy (master) laser and the experimental (slave) laser changes is locked to a fixed value, which is defined by an external waveform generator. Figure 4.5 gives an overview of the OPPL design.

A series of AOMs frequency shift a small fraction of the light from both the locked spectroscopy laser and the experimental laser to optimize the frequency-locking range of the OPPL, as shown in Figure 4.4. These beams are then combined on a high speed, differential output photodiode with integrated preamp

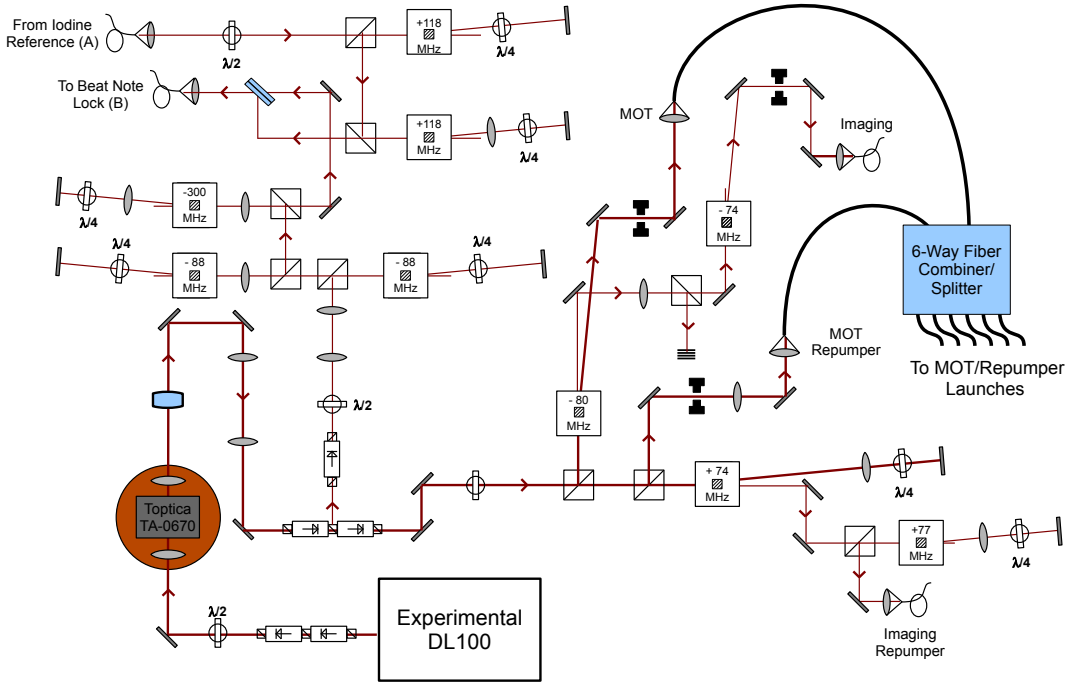

Figure 4.4. Optical layout for producing cooling and imaging light near the D_2 transition in ^{6}Li. The symbols are defined in Figure 4.2.

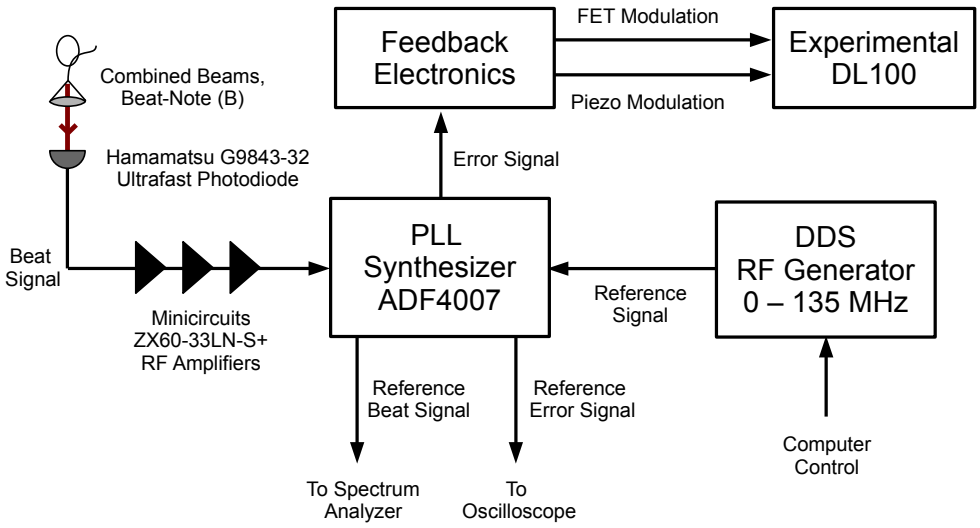

Figure 4.5. OPPL design to offset lock the experimental laser to the spectroscopy laser.

(Hamamatsu G9843-32). A high frequency divider/PLL synthesizer (Analog Devices ADF4007) divides the frequency of the detected beat-note signal between the lasers by a factor of 16 and compares this signal to a reference frequency provided by a home-built Direct Digital Synthesizer (DDS). The DDS system, based on the design by Dr. Todd P. Meyrath and Dr. Florian Schreck [167], can produce Radio Frequency (RF) signals between DC and 135 MHz and is interfaced with a microprocessor for dynamic computer control. The error signal produced by the ADF4007 is sent through feedback electronics, as described in [166], to provide feedback to the FET and the piezo actuator of the experimental DL100 diode laser. Fast recovery of the feedback lock and suppression of saturation of the error signal are provided by feed-forward of the piezo actuator as the experimental laser is switched to new frequencies. The experimental laser is therefore continuously phase-frequency locked to the spectroscopy laser, which in turn is locked to the iodine hyperfine line discussed in the previous section, and is tunable between $\sim$ 50 MHz and -2.1 GHZ from the D_2 line of lithium with a linewidth below 1 MHz and switching speeds on the order of 1 ms.

4.3 Magnet System

Much of the technology we use to cool dilute neutral gases to degeneracy and induce resonant enhancement of pairwise interactions in our samples is based on the Zeeman shift of the atomic hyperfine levels under the influence of an applied bias or gradient magnetic field. As described in Chapter 2, the low-energy interaction properties of ^{6}Li atoms in the three lowest-energy hyperfine spin states is quite rich in the range of applied magnetic fields between 0 and 2000 Gauss due to the presence of multiple s- and p-wave Feshbach resonances between these three states and the effective convergence of the scattering-lengths for the three high-field seeking states for fields above $\sim$ 1500 Gauss. Additionally, gradient magnetic fields can be used to both directly apply forces on the atoms and to alter the resonant frequencies of the atoms in the presence of near-resonant light attributed to the spatially-dependent Zeeman shift.

To this end, we have installed multiple sets of electromagnets about the experimental chamber, as shown in Figure 4.6. The primary and booster coils, axially

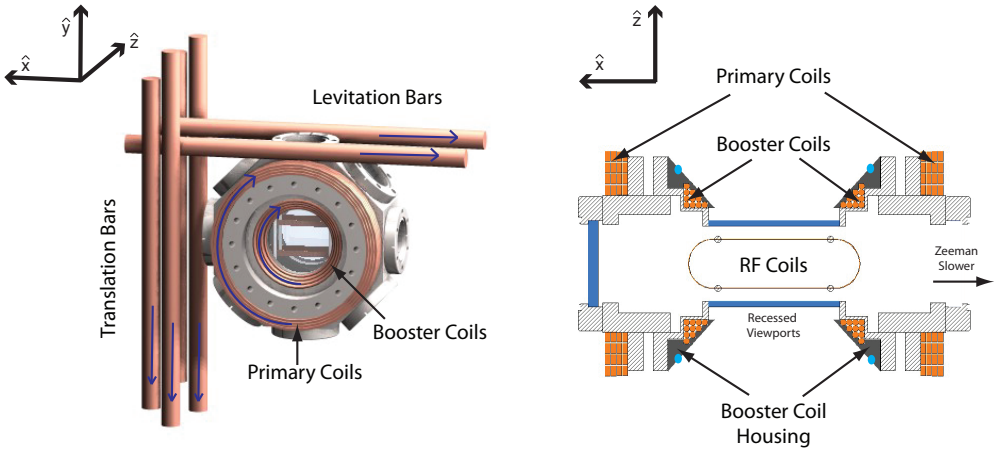

Figure 4.6. Overview of the current-carrying bars and coils used to manipulate the atoms in the experimental chamber. The blue arrows indicate the direction of current flow.

centered on the experimental chamber, are designed to provide a large bias field and/or field gradients at the center of the experimental chamber. The primary coils in particular are the workhorse of our experiment, providing both the quadrupole field for our Magneto-Optical Trap and the uniform bias field for tuning interatomic interactions. The four current carrying bars external to the vacuum system provide a field at the center of the chamber along the polarization axis ($\hat{z}$) of the experiment. The gradient fields perpendicular to this axis can exert forces on the atoms to stabilize against gravity and correct for stray forces at the center of the experimental chamber. Our experiments required flowing large currents through the magnets (up to 1000 Amps) with a high level of stability and temporal control. In this section, I describe the design and electronic control of our magnet system to address these issues.

4.3.1 Primary Coils

Our primary coils are among the most stable and dynamically adjustable devices in our labs. These coils are attached directly to the outside of the 8" viewports on the experimental chamber, and separated by 3.75", thereby approximately satisfying the Helmholtz condition when identical currents are passed through the coils. Each coil consists of 16 turns of shielded copper wire ($(3/16")^2$ cross-sectional area with a $(1/16")^2$ hollow core), and the pair is sandwiched between padded Plexiglas plates

to minimize shifting due to inductive forces during rapid turnoff of the current. Swagelok connectors at the ends of the wires provide electrical connections to the power supplies and a port for water flow through the hollow core of the wires.

The primary coils are able to flow a steady-state current in excess of 600 Amps and can be run in either Helmholtz or anti-Helmholtz configuration. Independent computer control of the currents in each coil allows us to apply an arbitrary magnitude of the bias and gradient of the magnetic field along the $\hat{z}$ axis up to ~ 1000 Gauss or ~ 62 Gauss/cm at the center of the experimental chamber. For simplicity, the coils are named Chandlee (1) and Corridor (2), based on the proximity of the coils to the Chandlee building at PSU or the corridor of the lab. The power supplies for these coils (Sorensen DHP-20-660) can supply continuous currents of up to 660 Amps per coil and can be remotely computer-controlled with a 0-10 Volt reference. Internal feedback in the supplies maintains the programmed current to within 0.2% in constant current mode. However, we found that the current-switching slew-rates in this mode are on the order of a few Amps/ms due to the large filtering capacitors in the supplies.

4.3.2 Booster Coils

In addition to the primary coils, a pair of 10 turn booster coils are fit within the recessed housing of the viewports as shown in Figure 4.6. These coils have a radius of 3", are separated by 2.6", and are wired in series to enhance the bias field of the Primary coils in Helmholtz configuration. The coils were mounted to the rear surface of a water-cooled copper housing which was specially designed to secure the booster coils within the inner profile of the recessed viewports and provide sufficient coil to metal contact for heat dissipation. Further, the inner radius of the housing was machined with a conical profile such that after installation, the coils had virtually no impact on the optical access to the center of the chamber. A slit was cut radially through the copper housing and electrical isolation was installed between the copper housing and the metal of the viewport to suppress additional eddy currents during switching of these coils.

Due to insufficient heat dissipation from these coils through the water-cooled housing, we were limited to constant currents of a few hundred Amps or pulsed

currents of up to 600 Amps for a few hundred milliseconds, driven by a Sorensen DHP-15-660 power supply. The booster coils nearly touch the viewport glass, whose vacuum seals are only rated to withstand up to $\sim$ 200 ℃. Overheating of these coils could cause a catastrophic failure of our vacuum system. The coils were sufficient, however, to provide up to an additional 500 Gauss bias field at the center of the chamber for many seconds to study the two- and three-body loss properties of the ground-state ^{6}Li atoms at high fields ($B > 1000$ Gauss).

4.3.3 Current Control

Current control external to the power supplies was implemented for the Chandlee coil, Corridor coil, and the Booster coil pair to increase the slew-rates, maintain low current noise, and assure long-term stability of the field. The current is controlled with a bank of 10 Power MOSFETs (IXYS IXFN-108N20) which are mounted on a water cooled plate with thermal compound to assure good thermal contact. Each of the MOSFETs can continuously flow up to 180 Amps of current and dissipate 700 W of power. The MOSFETS are all wired in parallel to easily accommodate the maximum current provided by the power supplies and each of the gates are connected to the control voltage V_G through a 1 Ω resistor to suppress high frequency oscillation of the gate voltages, called parasitic oscillation [168] that occur during switching transients.

Servo control of the current, outlined in Figure 4.7, was designed similar to the magnetic trap current servo used in the degenerate Fermi gas apparatus in D. Jin's Lab at JILA, Boulder Co. [169] The current from the power supplies are measured with closed loop current sensors (Honeywell CSNK500M). These sensors behave like a current transducer with 5000 turns and a 50 Ω coil resistance with ± 0.5% accuracy. The output current I_S from each sensor is converted to a voltage V_S with a stable 100 Ω burden resistor R_S. Differential amplification between the signal from the current sensors and a reference signal V_R, provided here by a 0-10 V analog output from our computer control system, provides feedback to the gate of the MOSFETs.

Switching the current from Helmholtz to anti-Helmholtz configuration is based on controlling the current path with high-current Integrated Gate Bipolar Transis-

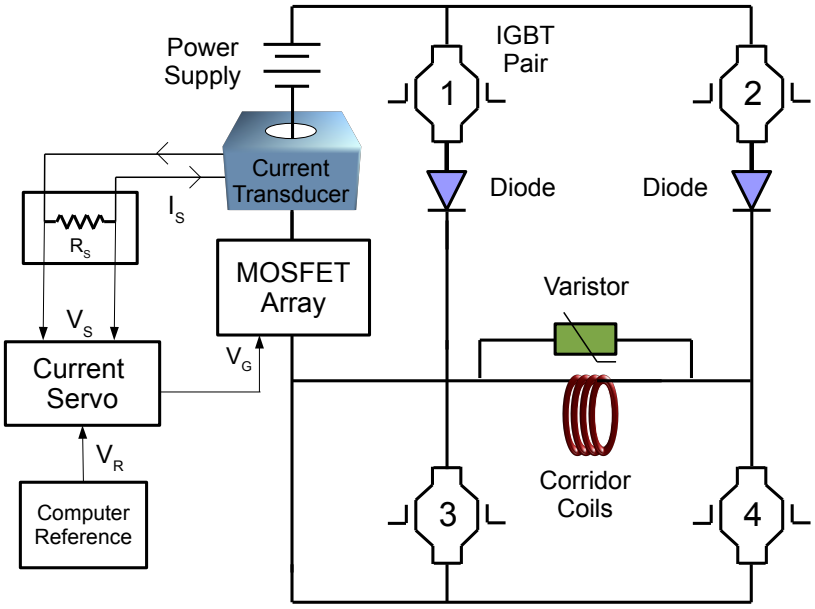

Figure 4.7. Current control electronics for the Corridor coils.

tors (IGBT Powerex, CM600HA-5F). These are effectively high current switches, which can each accommodate up to 600 Amps of current with switching times on the order of microseconds. Figure 4.7 shows a schematic of the IGBT current control system for the Corridor coil. Each of the switches shown constitutes two IGBTs in parallel. The diode and thyristor protect the power supply and IGBT modules from inductive voltage spikes due to the rapid turnoff. For the Corridor coil, depending on whether the IGBT pairs 1 & 3 or 2 & 4 are activated, the current will flow through the coils either in the same direction as or in opposition to the direction of current flow through the Chandlee coils. For the Chandlee coil, a single IGBT pair and diode is used to simply provide rapid shunting of the magnetic field. No IGBTs, diodes, or thyristors are installed for the booster coil system. Computer triggering of a logic circuit, designed by Ron Stites in our lab, controls the IGBT drivers (Powerex BG2B), allowing the coils to be shunted and switched rapidly within the same experimental procedure.

Using this current control scheme, the slew-rate is significantly enhanced, limited only by the resonance frequency of the coils, and the current is immune to long-term drifts. The bias magnetic field induced by these currents at the center of the experimental chamber was measured and calibrated using high-field RF spec-

troscopy of the ultracold lithium atoms in the two lowest hyperfine spin-states (see Section 5.2). Using this technique, the current and field stability was found to be on the order of a part in 10^3. Recent improvements include replacing the current sensor with a precision current transducer whose linearity is better than 3 ppm (DanFysik Ultrastab 867) and temperature stabilization of the burden resistors to the peak of their stability curve at 25 ℃ which, to date, has increased the stability of the magnets by approximately two orders of magnitude.

4.3.4 Gradient Fields

As discussed previously, gradient magnetic fields can exert significant forces on the atoms. For an atom in a magnetic hyperfine state M_F, in a magnetic field whose gradient is along the $\hat{z}$ axis, this force is given by

$$F = -g_F \mu_B M_F \frac{dB}{dz}. \tag{4.8}$$

For most of our experiments, atoms in the three lowest-energy hyperfine spin states are spin polarized by a large magnetic field pointing in the $\hat{z}$ direction. Atoms in these three spin states, whose quantum numbers vary only by the nuclear spin, therefore effectively feel the same force given by the $\hat{x}$, $\hat{y}$, and $\hat{z}$ gradients of the component of the magnetic field along the $\hat{z}$ direction and the magnetic moment of the electron.

Magnetic field gradients were used in our experiment to cancel stray forces and counter the force of gravity, which is highly detrimental to achieving low temperature, low density degenerate clouds because this energy scale sets the minimum trapping force necessary to hold the atoms. To counter the gravitational force on the atoms, a magnetic field pointing in the $\hat{z}$ direction with a gradient of approximately 1 Gauss/cm along the $\hat{y}$ axis was necessary. It turns out that the simple field from an infinitely long wire positioned directly above the atoms, and aligned with the $\hat{x}$ axis provides an ideal gradient profile for levitating the atoms, given by

$$B(y) = \frac{\mu_0 I \hat{z}}{2\pi y} \tag{4.9}$$

where y is the vertical distance from the axis of the wire to the atoms, μ_0 is the

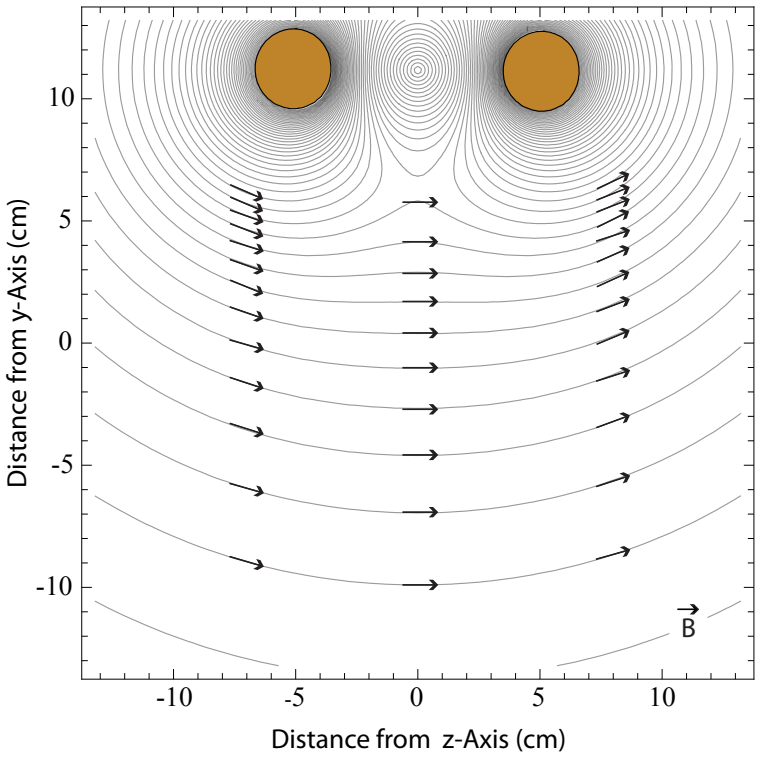

Figure 4.8. Calculated profile for the magnetic field induced by the levitation bars along the $\hat{y}$-$\hat{z}$ plane. The current-carrying bars are shown in orange and the arrows indicate the direction of the B-field.

permeability of free space, and I is the current in the wire along the $\hat{x}$ axis.

To approximate this field profile, a pair of $\sim$ 3/4" diameter current-carrying (levitation) bars at the top of the experimental chamber were installed, as shown in Figure 4.6. Additionally, two pairs of current-carrying (translation) bars were installed at the front of the experimental chamber to apply forces to the atoms along the $\hat{x}$ axis. These bar sets carry very large currents, where the levitation bar set and the first set of translation bars at the front of the chamber are wired in series and driven by a 1000 A power supply (Sorensen DHP 5-1000). Further, the second set of translation bars at the front of the chamber are independently controlled, driven by a 440 A power supply (Agilent 6690A). The direction of the currents through these bars are shown by the blue arrows in the figure. Each of the power supply are programmed by a 0-10 V analog output from the computer control system. The profile of the magnetic field from the levitation bars in the $\hat{y}$-$\hat{z}$ plane is shown in Figure 4.8, where the center of the experimental chamber is

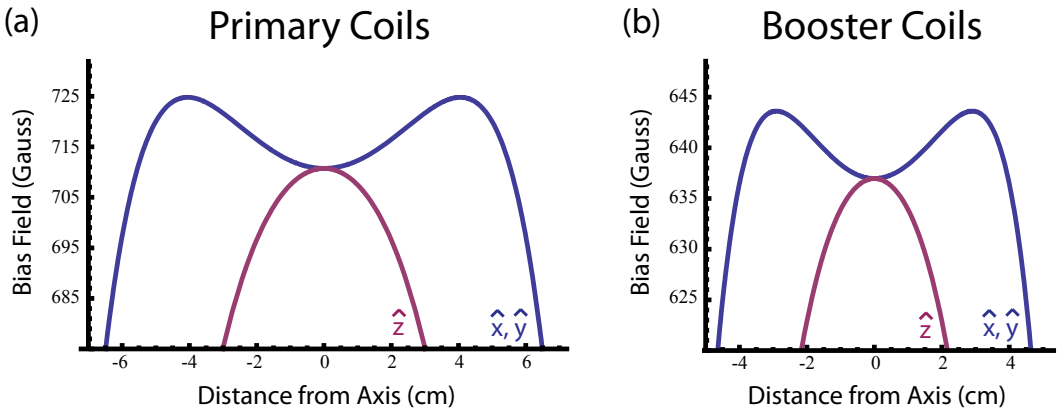

Figure 4.9. Magnetic field profile along the (blue) $\hat{x}$, $\hat{y}$ and (red) $\hat{z}$ axes for (a) the primary coils and (b) the booster coils. The fields were calculated assuming a current of 500 A for each coil set.

located at (0,0) on this plot. Using a combination of the gradient field from these bars and an induced gradient from the primary coils, we are able to cancel the force of gravity and all other translational forces exerted on the atoms to within the detectable precision of our experiments.

In discussing the bias field produced by the primary coils and the booster coils, it was assumed that the coils perfectly obeyed the Helmholtz criteria. A more realistic analysis showed that, at the center of the experimental chamber, non-negligible gradient fields from these coils can significantly affect the atoms. These gradients are caused by the finite size of the coils, slight deviations of the radius from their displacement, relative rotations of the coils, inhomogeneities of the winding, etc. The bias field is therefore modified by a weak hyperbolic parabola field distribution in the $\hat{x}$,$\hat{y}$-$\hat{z}$ plane near the center of the chamber, whose saddle-point location is highly dependent on the homogeneity and rotation of the coils. For both the primary and booster coils, the ratio of the coil radius to the displacement of the pair is greater than one, resulting in a local minima (maxima) of the field along the $\hat{x}$ and $\hat{y}$ ($\hat{z}$) axes. A representative radial and axial magnetic field profile due to the deviation of the mean radius of the primary and booster coils from the Helmholtz configuration is shown in Figure 4.9. These forces minimally perturbed the atoms in our initial atom traps, but were found to be useful in providing confining forces to the atoms along the $\hat{x}$-$\hat{y}$ plane for our later experiments. This application will be discussed in more detail in Chapter 5.

4.4 Zeeman Slower

Atoms interacting with a collimated laser beam resonant with the atomic transition undergo a scattering process where each absorbed photon transfers its momentum to the atoms. The spontaneously emitted radiation is then isotropically radiated, averaging zero net momentum after many scattering events. The net force exerted on the atoms from the unidirectional absorption of near-resonant photons is the basic mechanism behind laser cooling of atomic gases. The maximum force exerted on the atoms from these scattering events is given by $F_{max} = \hbar k\Gamma/2$, where $\hbar k$ is the momentum of the absorbed photons and Γ is the atomic spontaneous emission rate.

For light resonant with the $^2S_{1/2}$ to $^2P_{3/2}$ cycling transition in ^{6}Li this force results in a very large acceleration of the atoms ($a_{max} = 1.8 \times 10^6 m/s^2$). We utilize this scattering force to slow our high-temperature atomic beam so that the atoms can be trapped and further cooled at the center of the experimental chamber. Realistic implementation of this simple scheme must, however, account for Doppler shifting of the atomic resonance frequency which is on the order of 1.4 GHz for atoms traveling at 1 km/s. For a cooling beam resonant with these atoms, as the atoms are decelerated they will quickly fall out of resonance with the laser light and cooling will cease.

In 1982, Nobel laureate Williams Phillips and co-workers used a spatially-dependent magnetic field, provided by a tapered solenoid along the axis of an atomic beam, to shift the atomic frequency of Na atoms into resonance with a counter-propagating laser beam to account for the Doppler shift as the atoms are slowed along the drift tube. To maintain a constant deceleration of the atoms requires that the Zeeman shift obey the following condition

$$\delta\omega + \frac{\delta\mu B(z)}{\hbar} = kv \tag{4.10}$$

Where $\delta\omega$ is the detuning of the laser from the zero-field atomic resonance, $\delta\mu = (g'_F M'_F - g_F M_F)\mu_B$ is the difference of the atomic magnetic moment between the ground and excited states and k is the wave vector of the light. More details on the design and implementation of Zeeman slowers can be found in References [170, 171].

In our system, we use a zero-crossing Zeeman slower, which means that the bias field crosses zero and changes direction along the solenoid. The calculated magnetic field profile along our slower is shown in the subset of Figure 4.10. This design allows for lower current requirements, adjustability of the field between the different sections, and a significantly detuned slower beam to minimally perturb the atoms collected at the center of the experimental chamber. The solenoid consists of two spatially inhomogeneous coils of water-cooled wire, specially wound around the drift tubes to provide the required magnetic-field profile shown. At the end of the experimental chamber, a coil consisting of 16 turns of water-cooled wire provides a counter magnetic field to zero the field at the center of the experimental chamber.

All three of the slower coils are electrically connected in series, powered by a computer-controlled power supply (Sorensen DCS8-125E). Slight adjustments of the location of the zero-crossing along the axis of the Zeeman slower is provided by an adjustable stainless-steel current shunt. The field from the slower coils at the center of the experimental chamber is adjusted with the axial distance of the final coil from the chamber. Details about the specific slower parameters are given in Table 4.4. Although stray magnetic fields have been minimized by running the wires which carry the supply and return current along the same path, the effect of the slower field on the location of the atoms during magneto-optical trapping is visibly noticeable, but does not seem to affect the loading efficiency of the MOT (see Section 4.5).

To cool the atoms, ~ 100 mW of light from the spectroscopy laser system is sent through a polarization maintaining fiber to the optics table supporting the vacuum system. The optical layout for the slower beam is shown in Figure 4.10. The slower light, which is approximately 814 MHz red detuned from the D_2 transition, is converted to right circularly polarized light with a $\lambda/4$ wave plate before it is counter-propagated with the atoms. The beam has a diameter of approximately 15 mm at the entrance window of the experimental chamber and is focused onto the nozzle of the atomic oven. The $|F' = 5/2\rangle \leftrightarrow |F = 3/2,\ m_F\rangle$ cooling transitions for the atoms near the beginning of the slower region are shown in Appendix A. At the zero-crossing of the slower field, the light is on resonance with atoms which were slowed to approximately 540 m/s. Here, the intensity of the light is ~ 12

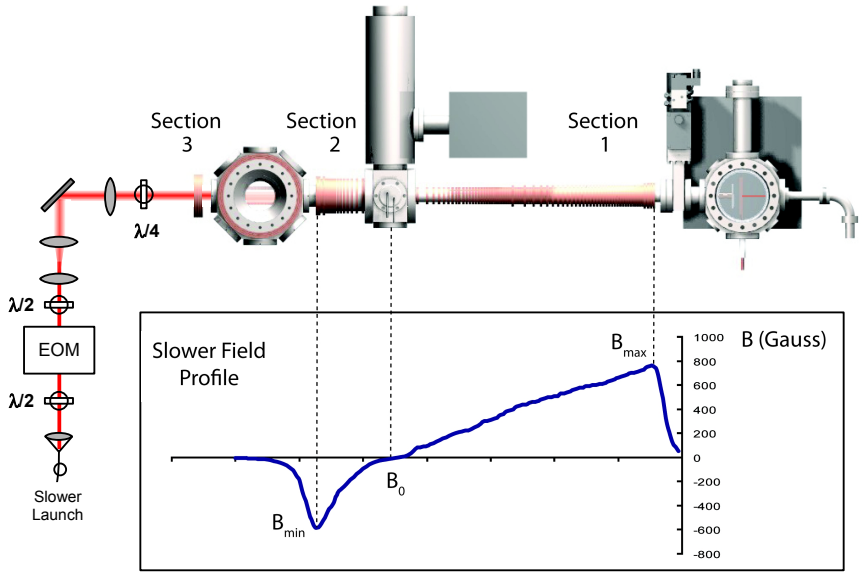

Figure 4.10. System of optics and magnetic coils used in our zero-crossing Zeeman slower. The insert shows the profile of the $\hat{x}$ magnetic field provided by the slower solenoids (1) and (2).

times the saturation intensity of the atoms (I_{Sat}).

At low bias fields near this zero-crossing, the cooling transitions are no longer closed due to mixing of the nuclear and angular momentum quantum numbers in the hyperfine states. This is particularly predominant in the D_2 transition of ^{6}Li, where the hyperfine spacing of the $^2P_{3/2}$ manifold is smaller than the natural linewidth of the cycling transition Γ. Atoms cycling on this transition can decay back the $^2S_{1/2}$ $|F = 1/2\rangle$ dark states, where they are far-detuned from the cooling light and the cooling cycle will cease. To maintain population in the cycling transition for all fields, an electro-optic modulator (New Focus 4001) frequency modulates the slower beam, creating side-band frequencies at 228 MHz. Atoms are optically pumped from the dark states with the blue sideband and can subsequently scatter light from the slower beam throughout the entire length of the slower.

The bias field is rapidly extinguished as the atoms enter the experimental chamber and scattering from the slower beam, which is now approximately 814 MHz red detuned from the D_2 transition, is suppressed. These atoms, which have an average velocity of approximately 30 m/s along the slower axis, will drift toward the cen-

Slower Property	Value
Section 1 Length (current)	20" (128 A)
Section 2 Length (current)	4" (115.4 A)
Section 3 Turns (current)	16 (115.4 A)
Maximum B-Field (B_{max})	$\sim$ 775 Gauss
Minimum B-Field (B_{min})	$\sim$ -600 Gauss
Total Electric power	680 W
Laser Power	100 mW
Laser Detuning	-814(5) MHz
Maximum Capture Velocity	$\sim$ 1100 m/s

Table 4.1. Properties of the current-carrying coils and light for the Zeeman slower

ter of the vacuum chamber where they will be trapped using the magneto-optical trapping scheme that I will describe in the next section.

4.5 Magneto-Optical Trap

As the atoms leave the Zeeman slower, they are still far too energetic to be captured by the optical dipole trap used to cool the atoms to ultracold temperatures. The atomic beam is therefore precooled in a Magneto-Optical Trap at the center of the experimental chamber. This trap combines a magnetic quadrupole field and three mutually-orthogonal pairs of $\sigma^+ - \sigma^-$ counter-propagating laser beams pointing towards the center of the quadrupole field, as shown in Figure 4.11 (a), to provide compression of both the spatial and momentum distribution of the atoms.

The six beams alone, which are all derived from the same laser and slightly red-detuned from the atomic transition, form a so-called *optical molasses* [172, 170]. Atoms moving along the axis of one of the beam pairs are Doppler shifted into resonance with the counter-propagating beam. Since the velocity of the atoms can always be described in terms of their components along the three mutually-orthogonal beam pairs, at the intersection of the beams the atoms experience a three-dimensional viscous damping force which leads to a significant reduction of the momentum distribution (and hence the temperature) of the atomic gas. This laser cooling technique was first demonstrated by Nobel laureate Steven Chu and colleagues at Bell Laboratories in 1985 [173].

As the atoms are cooled in the optical molasses, random fluctuations of both the photon absorption rate and the angular distribution of the spontaneously emitted photons lead to a random walk of the atoms in momentum space. In the steady-state, the net effect of optical cooling in three-dimensions balancing the diffusive heating caused by the random momentum kicks, assuming $I \ll I_{sat}$, yields an equilibrium temperature of the atoms given by

$$k_B T = \frac{\hbar\Gamma}{4}\frac{1+(2\delta/\Gamma)^2}{-2\delta/\Gamma}, \tag{4.11}$$

where Γ is the atomic natural linewidth and $\delta = \omega - \omega_0$ is the detuning of the lasers from the cooling transition. The minimum equilibrium temperature T_D at $\delta = -\Gamma/2$ is the *Doppler cooling limit*. For ^{6}Li atoms cooling on the D_2 cycling transition, $T_D = 142\mu K$.

The drawback of this cooling technique is that it provides no spatial confinement, allowing the atoms to random-walk out of the active volume of the beams. Further, the capture velocity of the molasses is generally quite low [170], limiting the efficiency of the Zeeman slower. The addition of a quadrupole magnetic field and the correct choice of $\sigma^{\pm}$ laser polarizations Zeeman shifts the cooling transition frequencies of the atoms closer to resonance with the photons that are moving towards the center of the trap, producing a three-dimensional restoring force to confine the atoms. Nearly all of the ultracold atomic gas systems use these Magneto-Optical Traps as an initial cooling stage due to their relatively large capture velocities and volumes, capable of trapping room temperature atomic vapors for the heavy alkalis. For more details on laser cooling and trapping techniques, please refer to References [170, 42].

In our setup, the quadrupole field is provided by running 85 Amps of current through the primary coils in the anti-Helmholtz configuration. This produces a linear gradient at the center of the chamber of 5 Gauss/cm in the radial and 10 Gauss/cm along the axis of the chamber. In addition to the primary coils, we have installed three sets of coils in Helmholtz configuration about the experimental chamber, which are useful in canceling out stray fields and moving the location of the zero-point of the gradient field in three-dimensions. Independent control of this external bias field has been quite useful in moving the center of the MOT,

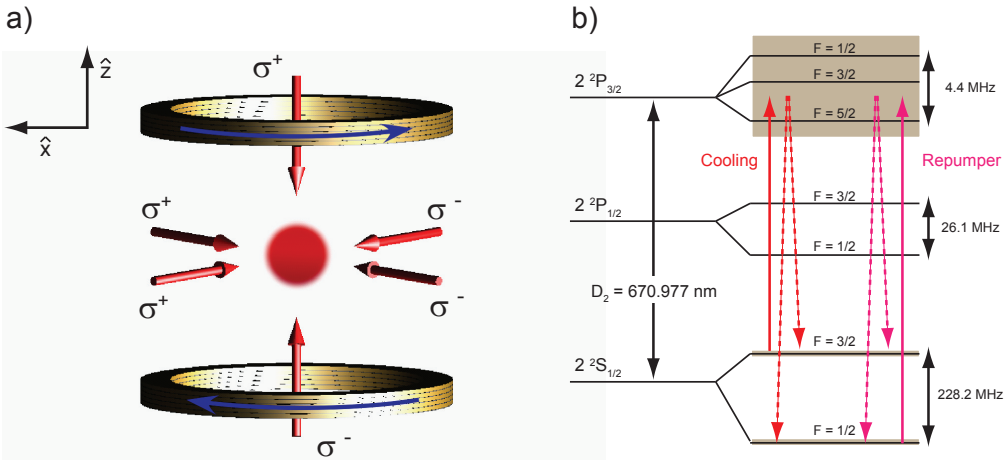

Figure 4.11. (a) Orientations and polarizations of the MOT and repumper beams for laser cooling the atoms in a gradient field, provided by the current through the Primary coils (blue arrows). (b) Energy level diagram of ^{6}Li. The solid (dashed) arrows indicate the cooling and repumping transitions (spontaneous emission transitions). The natural linewidth of the D_2 transition is indicated in grey.

which is nominally centered on the zero-point of the gradient field, to optimally load the atoms into subsequent trapping potentials.

The cooling transition used is the $^2S_{1/2}\ |F = 3/2\rangle$ to $^2P_{3/2}$ transition of the D_2 line of ^{6}Li. As discussed in Section 4.4, at the low magnetic fields provided by the anti-Helmholtz coils, the cooling transition is not closed. To maintain population in the cooling transition, the MOT cooling beams are combined with MOT repumper light that is resonant with the $^2S_{1/2}\ |F = 1/2\rangle$ to $^2P_{3/2}$ transition. An energy-level diagram of the MOT cooling and repumper transitions is shown in Figure 4.11 (b).

The MOT beams, which are produced by the experimental laser system shown in Figure 4.4, are launched into polarization-maintaining fibers from the experimental laser table and combined on a 2×6, temperature stabilized, splice-free coupler tree (Canadian Instrumentation & Research Ltd). This apparatus uses arrays of evanescent wave couplers to combine two fiber-coupled laser beams (MOT cooling and MOT repumper), and splits the combined light into six equal power beams which are output coupled to six polarization-maintaining fibers to provide light for each MOT beam. Each of the combined MOT cooling/repumper beams are launched from these fibers using home-built fiber launches, shown in Figures 4.14 and 4.19, to collimate the beams and shift their polarizations from linear to

circular using $\lambda/4$ wave plates. The six ~ 40 mm diameter beam are then directed through the viewports of the experimental chamber using adjustable gold mirrors to intersect nominally at the center of the gradient field as shown in Figure 4.11 (a).

Dual-stage cooling is implemented to optimize the loading and cooling efficiency of the MOT. In the first stage, the MOT is loaded from the Zeeman slowed atomic beam. Each MOT beam has approximately 27 mW of MOT cooling and 4 mW of MOT repumper power, where both the cooling and repumper light are ~ 30 MHz (5Γ) red detuned from resonance. For our oven temperatures of 435 ℃, we can achieve $\sim 10^8$ atoms/second loading rates. This allows us to load the MOT within 1 second, significantly reducing the experimental cycle time and the duty cycle of the atomic beam to maintain UHV vacuum in the experimental chamber. The lifetime of the atoms in the MOT is greater than 10 seconds, indicating a low background gas pressure.

The MOT now traps approximately 10^8 atoms at a temperature on the order of a mK. This temperature is significantly larger than the Doppler recoil limit due to the necessary detuning of the beams to minimize light-assisted collisions [174], which ultimately limit the steady-state density and number of atoms in the MOT. A picture of the fluorescence from the atomic gas while trapped in the MOT is shown in Figure 4.12. The image of the atoms at the center of the experimental chamber, taken through a recessed viewports, is seen in the left-hand panel.

In the second cooling stage the frequency of the MOT cooling and repumper beams are shifted to ~ 5 MHz (1Γ) red detuned from resonance, while significantly reducing their intensities (1.4 mW cooling, 2.3 mW repumper power). Cooling of the atoms in this compression stage for 7 ms is sufficient to bring the atoms into equilibrium with minimal atoms loss. At the end of the compression stage, the gas is at a temperature of ~ 200 μK, with a peak density of 2×10^{10} atoms/cm^3 and a phase-space-density on the order of 2.5×10^{-6}.

Finally, to suppress inelastic spin-exchange collisions between atoms in the $^2\mathrm{S}_{1/2}$ $|F = 1/2\rangle$ and $|F = 3/2\rangle$ states, described in Chapter 2, the MOT cooling beams were rapidly extinguished and the gas was illuminated with only the MOT repumper light for 200 μs to optically pump the atoms into the $|F = 1/2\rangle$ ground state. All of the experimental parameters for the Zeeman slower, MOT, MOT

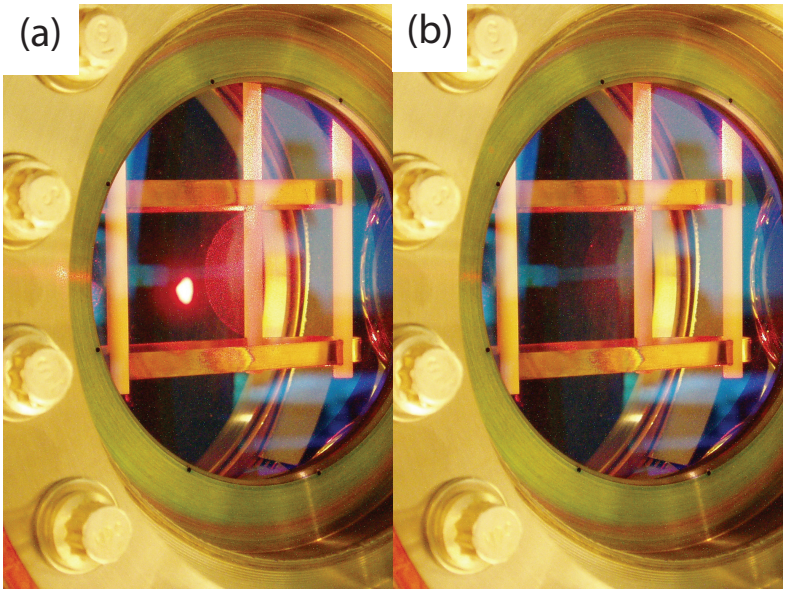

Figure 4.12. (a) Fluorescence from the MOT inside the experimental chamber. (b) The chamber with the atomic beam shuttered is shown for reference

compression, and optical pumping stages described previously were experimentally determined to provide optimum transfer into the optical trapping potentials described in the next section.

4.6 Optical Dipole Traps

Our experiments studying the universal physics of many-component Fermi gases required, in the end, that we produce extremely cold, nearly degenerate Fermi gases occupying the three lowest-energy hyperfine spin states whose interactions are tunable by a large magnetic field pointing along the $\hat{z}$ quantization axis. The dipole force from a gradient light field provides an optimum potential to satisfy these requirements. The atoms experience a conservative force in the optical dipole trap which is effectively insensitive to both the atomic hyperfine state of the trapped atoms, for linearly polarized light, and to applied magnetic fields. Such optical trapping potentials are readily available from the Gaussian profile of far off-resonance laser beams and have been used extensively to trap and evaporatively cool Fermionic atoms to degeneracy with extraordinarily low heating and trap loss rates [53, 147, 175]

4.6.1 Far-Off-Resonance Dipole Traps

The origin of the optical dipole force is derived from the dispersive interaction of the induced atomic dipole moment $\mathbf{p}$ with the intensity gradient of a light field. For an atom of polarizability α in the presence of an electric field E, the dipolar potential U_{dip} is given by

$$U_{dip} = -\frac{1}{2}\alpha \mathbf{E}^2. \tag{4.12}$$

A rigorous analysis for the dipolar trapping potential and light scattering rate Γ_{sc} for two-level neutral atoms in the limit of large detunings of the light $(\omega_0 - \omega)$ and negligible saturation $(I \ll I_{sat})$ yields [176]

$$U_{dip}(\mathbf{r}) = -\frac{3\pi c^2}{2\omega_0^3}\left(\frac{\Gamma}{\omega_0 - \omega} + \frac{\Gamma}{\omega_0 + \omega}\right) I(\mathbf{r}) \tag{4.13}$$

$$\Gamma_{sc}(\mathbf{r}) = -\frac{3\pi c^2}{2\hbar\omega_0^3}\left(\frac{\omega}{\omega_0}\right)\left(\frac{\Gamma}{\omega_0 - \omega} + \frac{\Gamma}{\omega_0 + \omega}\right)^2 I(\mathbf{r}), \tag{4.14}$$

where c is the speed of light, Γ is the damping rate, which corresponds to the spontaneous decay rate of the excited level, and $I(\mathbf{r})$ is the intensity profile of the beam. In general, the rotating-wave approximation is valid in which the counter-rotating term $(\omega_0 + \omega)$ in the above equations are neglected, yielding expressions for the dipole trapping potential U_{dip} and scattering rates Γ_{sc} proportional to $I(\mathbf{r})/(\omega_0 - \omega)$ and $I(\mathbf{r})/(\omega_0 - \omega)^2$ respectively. Using high intensity beams whose frequencies are far detuned to the red of the atomic transition can produce large trapping forces on the atoms with minimal heating from off-resonant scattering of the trapping light.

The multi-level structure of atoms and molecules can greatly complicate the analysis of the dipole force. Even in this case, however, the atoms can act as an effective two-level system so long as the trapping laser is far detuned from all of the transition frequencies. For the case of neutral ^{6}Li, which has both Fine and Hyperfine structure in the $2^2\mathrm{S} \leftrightarrow 2^2\mathrm{P}$ transition, the detuning of a far-red-detuned trapping laser δ is defined with respect to the center of the D-line doublet. In such a far-off resonance dipole trap (FORT), the detuning of the laser, which is generally on the order of hundreds of THz, greatly exceeds the Fine structure splitting of the $2^2\mathrm{P}$ levels ($\delta_{FS} = 10.1$ GHz) and hence also the Hyperfine splitting

in the $^2S_{1/2}$ ($\delta_{HF} = 228.2$ MHz), $^2P_{1/2}$ ($\delta'_{HF} = 26.1$ MHz) and $^2P_{3/2}$ states ($\delta''_{HF} = 4.5$ MHZ). The potential formed by the FORT beam provides an effectively state-independent trapping mechanism with second order corrections on the order of (δ_{FS}/δ) [176]. The ability to confine an arbitrary mixture of ground-state atoms along with minimal heating from light scattering and a magnetic-field insensitive trapping profile makes this an ideal trapping potential for our experiments.

For a single focused Gaussian laser beam at wavelength λ, the intensity profile is given by

$$I(\mathbf{r},\mathbf{z}) = \frac{I_o}{1+(z/z_0)^2}\exp\left[\frac{-2r^2}{w_0^2}\right], \tag{4.15}$$

where $I_0 = 2P/(\pi w_0^2)$ is the peak intensity of the laser beam with power P, $1/e^2$ intensity radius at the focus (waist w_0), and Rayleigh range ($z_0 = \pi w_0^2/\lambda$). Inserting this expression into Equation 4.13 for the trapping potential yields

$$U_{dip}(\mathbf{r},\mathbf{z}) = -\frac{U_o}{1+(z/z_0)^2}\exp\left[\frac{-2r^2}{w_0^2}\right]. \tag{4.16}$$

Here, U_0 is the maximum depth of the trapping potential. This trap depth is often expressed in terms of the recoil energy ($E_R = \hbar^2k^2/(2m)$) that the atoms of mass m gain from a single scattering event from the FORT light with wavevector k.

Ultracold atoms are generally confined near the center of the trapping potential ($r \ll w_0$). In this regime, the trapping potential is well approximated by a harmonic profile, as can be seen from the Taylor expansion of Equation 4.16

$$U_{dip}(\mathbf{r},\mathbf{z}) \simeq -U_o\left(1-\frac{z^2}{z_0^2}-2\frac{r^2}{w_0^2}\right)+\ldots \tag{4.17}$$

The first term is simply an offset representing the overall trap depth. The second and third terms on the right hand side of the equation are compared with the harmonic oscillator potential for a particle with mass m to yield the trapping frequencies along the axial (ω_z) and radial (ω_r) directions for a single-beam FORT trap, given by

$$\omega_z = \sqrt{\frac{2U_0}{mz_0^2}} \qquad\qquad \omega_r = \sqrt{\frac{4U_0}{mw_0^2}}. \tag{4.18}$$

The aspect ratio of the trapped gas (ω_r/ω_z) can be quite large unless the FORT

beam is highly focused. Highly elongated cigar-shaped traps result in very small axial trapping frequencies, and relatively low densities. Narrow-waist beams, on the other hand, severely limit the volume of the trap and high numerical aperture lenses are required, limiting the accessible viewports to transmit the trapping beam to the atoms. Further, we have found that our high power beam can easily exceed the damage threshold of the AR coated windows (100 kW/cm^2) when tightly focusing the beams to the center of the chamber. For many of our applications, we therefore use a crossed-beam configuration where two trapping lasers are focused on the atoms at a relative angle θ. The resultant trapping frequencies for two beams crossed in the $\hat{x}$-$\hat{z}$ plane are given by [177]

$$\omega_z = \sqrt{\frac{4U_0}{m}\left(\frac{\sin^2(\theta/2)}{w_0^2}+\frac{\cos^2(\theta/2)}{2z_0^2}\right)} \tag{4.19}$$

$$\omega_x = \sqrt{\frac{4U_0}{m}\left(\frac{\cos^2(\theta/2)}{w_0^2}+\frac{\sin^2(\theta/2)}{2z_0^2}\right)} \tag{4.20}$$

$$\omega_y = \sqrt{\frac{4U_0}{mw_0^2}}, \tag{4.21}$$

where U_0 is now twice the trap depth given by a single beam. This crossed-beam configuration allows us to arbitrarily design the trap depth, volume, and aspect ratio with the beam parameters power (P), crossing angle (θ), and waist (w_0).

In our experiments, the trapping lasers are derived from a single-transverse mode, 110 Watt, linearly polarized Yb Fiber laser (IPG photonics, YLR-100-LP). This laser has a central wavelength of 1064.27 nm, multi-longitudinal mode with an emission bandwidth of 2.517 nm. At this wavelength, the laser is far red detuned with respect to the D_2 transition in ^{6}Li ($\delta_{FS}/\delta = 6 \times 10^{-5}$). The fiber laser is collimated with an output beam diameter of 5 mm ($M^2 \sim 1.05$), and is highly stable with long-term power stability on the order of $\pm 1\%$.

The beam from this 110 Watt laser was used extensively to produce multiple optical trapping potentials for our atoms. Particular attention was paid to the position and intensity fluctuations of the trapping beams as this noise can cause parametric heating of the atoms [178]. The intensity-noise induced parametric heating time constant with respect to the trapping frequencies $v_{trap} = \omega_{trap}/(2\pi)$

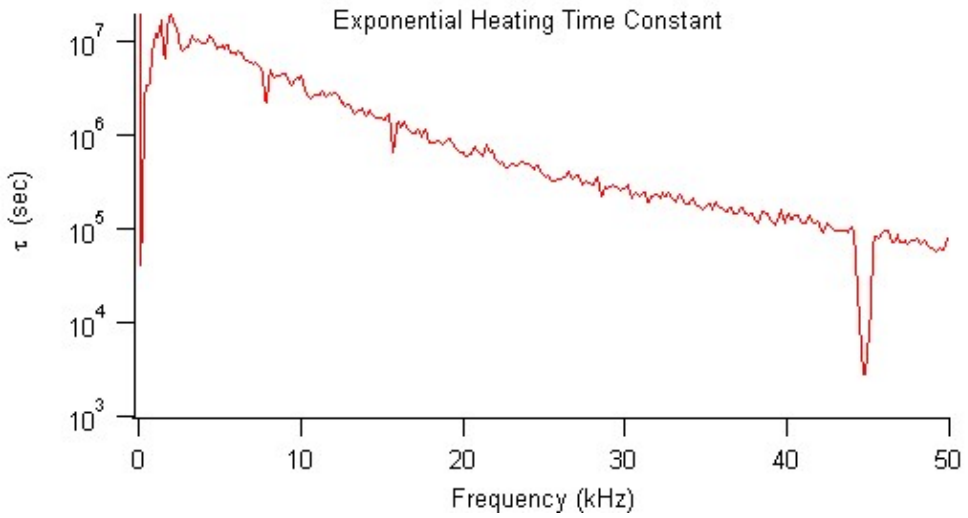

Figure 4.13. Exponential heating time constant τ with respect to trapping frequency v_{trap} attributed to intensity fluctuations of the 110 Watt IPG fiber laser

of a given trap is shown in Figure 4.13. This time constant, which describes the exponential rate at which the average energy of the gas increases ($\langle \dot{E} \rangle = \tau \langle E \rangle$) was calculated from the measured one-sided power spectrum of the relative intensity noise $S_K(\omega)$ from the laser using the relations derived in [178]. In the following sections, I will explain the geometry of our trapping potentials and the real-world complications that arise when using these multimode lasers as stable, conservative trapping potentials.

4.6.2 Real-World Complications

Our first set up for the primary FORT trap, which was loaded with atoms directly from the MOT, involved a crossed-beam geometry where the beam from the IPG multimode laser was split into two equal power beams on a polarizing beam splitter (PBS). The beams were separately focused to intersect with parallel linear polarizations at an angle of 90° at the center of the vacuum chamber. We were disappointed to see that the lifetime of the atoms in this configuration was extremely short $\sim$ 30 ms with an exponential decay profile indicating a single-body loss mechanism. Checking the intensity and position noise power spectra of the beam, the vacuum pressure in the experimental chamber, possible near-resonant light scattering sources, and thermal lensing effects on our AOM and PBS cubes

assured us that the heating and loss from the usual suspects was sufficiently small to expect much longer lifetimes ($\sim$ 4 seconds), and hence the loss mechanism was a bit of a mystery.

It turns out that a number of other groups have had similar problems trapping ^{6}Li atoms with the IPG multi-longitudinal-mode fiber lasers in the crossed-beam configuration [179, 180]. When we converted from the crossed-beam configuration to a single-beam trap, the lifetime of the gas was recovered to approximately 4 s, which was limited by collisions with background ^{6}Li vapor from our high-flux atomic beam at the time. The heating mechanism is therefore driven by the multi-frequency nature of the laser which, based on the length of the fiber laser cavity (estimated by IPG Photonics) the longitudinal mode spacing should be 7 ± 1 MHz over the $\sim$ 2.5 nm spectral width of the laser.

Discussions with David Weiss lead us to a likely explanation for the heating mechanism, which seems to corroborate with our findings and those of Rudi Grimm's group at the University of Innsbruck [179]. It is likely that the loss is caused by the various frequency components of the multi-mode laser beams driving two-photon Raman transitions between the bound states of the trapping potential and the continuum states, where the photons driving the transitions have different wave vectors dependent on the relative angle between the two beams. Another way of looking at this problem is to consider the spatial interference profile of the two lasers. For collinearly polarized beams, the various frequency components of the laser beams intersecting at a relative angle θ will create moving optical lattices with a period approximately given by $d_L \simeq \lambda/(2\sin\frac{\theta}{2})$ and phase velocity $v_L \simeq d_L \Delta\nu$, where $\Delta\nu$ is the frequency difference between two laser modes. The atoms can Bragg-scatter off of the various moving lattice potentials, leading to heating and loss of the atomic gas.

We tested this hypothesis using two methods: (1) using crossed linear polarizations for the trapping beams in the crossed-beam configuration and (2) stroboscopically alternating the crossed beams very rapidly ($\sim$ 100 kHz) such that the beams were never on simultaneously (the atoms experience a time-averaged-potential if the modulation frequency is much greater than the oscillation frequency for atoms in the trap). Both methods inhibit interference between the trapping beams, prohibiting the formation of the moving optical lattice potentials. Using

both methods, the lifetime of the gas was increased to the background-gas limited lifetime of 4 s, strongly supporting the explanation of the loss mechanism discussed above. Improvements in the MOT loading cycle has recently increased this lifetime to greater than 30 seconds.

4.6.3 Primary FORT Trap

In setting up our primary crossed-beam dipole trap, we followed the design implemented in R. Grimm's lab, where two co-propagating beams with orthogonal polarizations are intersected at a small relative angle ($\sim$12°). Figure 4.14 shows a layout of the optical system to produce the primary dipole trap. The fiber laser emits up to 110 Watts of light in collimated beam from the end of a flexible fiber output. The end of the fiber output is mounted in an aluminum housing, attached directly on the optics table to suppress position fluctuations of the emitted light and protect the collimating lens from dust. The beam is then passed through an AOM (NEOS 23080-3-1.06) which controls the relative power between the first-order diffracted beam (primary trapping beams) and the zeroth order beam, used for the large volume trapping potentials discussed in Section 4.6.5.

After passing through the AOM, the primary trapping beam is shaped by an adjustable telescope and passed through a $\lambda/2$ wave plate to a thin film polarizer. The s-polarized light is reflected vertically off the polarizer towards the bottom viewport of the experimental chamber while the remaining p-polarized component passes through the polarizer and is absorbed by a razor-blade stack (not shown). The s-polarized beam is then focused onto the center of the experimental chamber and collimated as it exits the top viewport with two identical lenses at the top and bottom of the vacuum chamber, separated by $2F$, where $F = 4$" is the focal length of the lenses. This beam is then routed around the experimental chamber, passed through another $\lambda/2$ wave plate and linear polarizer at the bottom of the chamber, and again directed through the bottom $F = 4$" lens such that this highly-polarized beam is focused on the center of the vacuum chamber.

The initial and second pass beams nearly co-propagate in the vertical direction ($\hat{y}$), with mutually orthogonal polarizations, and intersect at a relative angle of $\sim 11^\circ$ at the center of the MOT. Further, the beams are elliptical with calculated

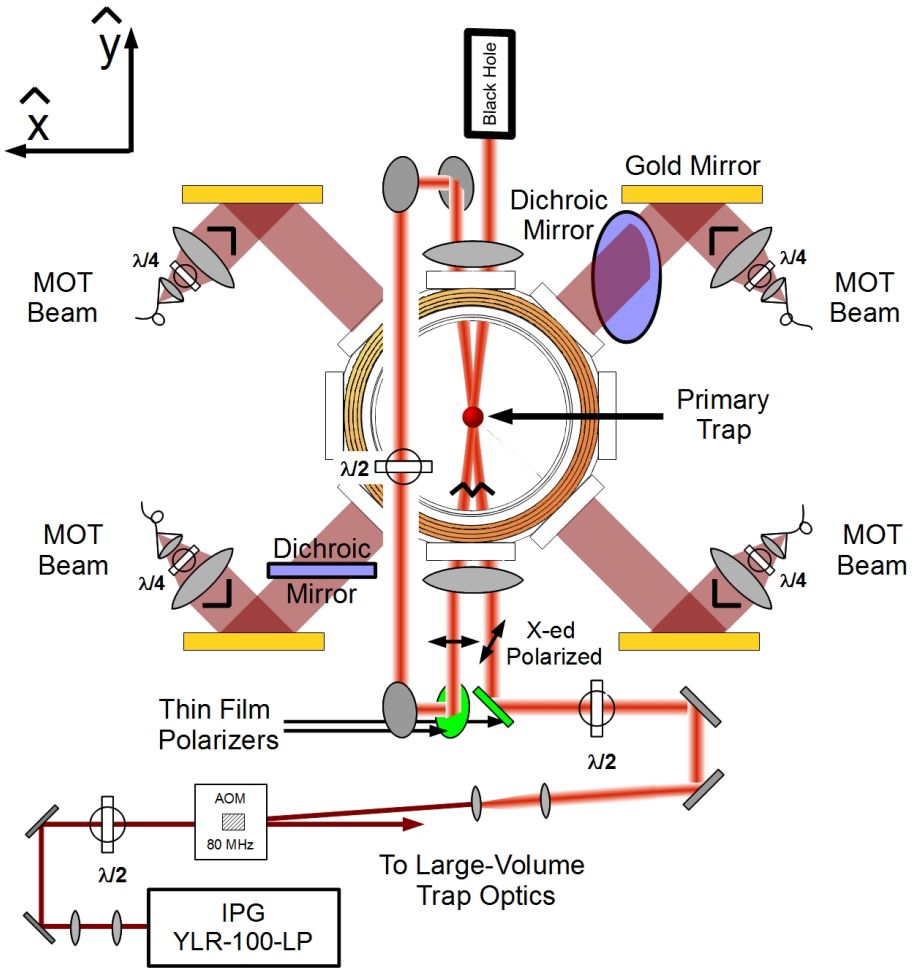

Figure 4.14. Optical design for the Primary Dipole trapping beams. The Corridor coils are shown here.

e^{-2} waist radii of $\sim$ 30 μm and $\sim$ 100 μm at the point of intersection. The ellipticity is likely attributed to an astigmatism in the beams introduced either from the laser, the AOM, or the optical components prior to the first pass through the vacuum chamber. Finally, the second-pass beam is collimated by the top lens and absorbed by a high-power laser beam dump (Blue Sky Research, Black Hole-500).

At maximum power of the trapping beams ($\sim$ 80 W for each beam), the large depth ($U_0 \sim k_B \times 1\ mK$ per beam) and relatively small aspect ratio ($\omega_r/\omega_z \simeq 10$) of this trap is designed to optimally load atoms from the MOT. To this end, the crossed dipole trap at full power is turned on 100 ms before the end of the MOT

loading stage. Optical scattering and elastic collisions during the MOT and MOT compression stages allow up to $\sim 5 \times 10^6$ atoms to be loaded into the conservative potential of the primary crossed dipole trap. At this point, the trapped atomic gas is comprised of atoms in the two lowest-energy hyperfine spin states at a temperature of approximately 200 μK.

The geometry of the primary trap is set throughout our experiments. Strict control over the power in the beams was therefore required to access various regimes of temperature, density, and phase-space densities of the atoms. Stable control of the laser power over a wide dynamic range was therefore built in to our design of the RF power delivered to the AOM. A crystal oscillator signal at 80 MHz, which is amplified to a maximum of $\sim$ 37 dBm (5 Watts), provides the RF power to drive the AOM. The intensity of this signal is attenuated by a variable voltage controlled attenuator (Mini-Circuits ZX73-2500) which, in-turn, is controlled by an arbitrary waveform generator (Agilent 33220A). Computer-controlled programming of the signal generator allows us to vary the intensity of the RF signal with a signal shape fully defined by the computer control software. In conjunction with the intrinsic stability of the AOM, the intensity of the beams can be arbitrarily controlled in a stable and reproducible manner to vary the power in each of the primary trapping beams ranging from $\sim$ 80 Watts to effectively zero.

To minimize the position dependent heating of the atoms, the optics for this trap are mounted on 1/2" steel posts as close to the optics table as possible. Further, the optics above the experimental chamber are supported by an optical breadboard above the system to minimize the oscillation amplitude of these components. The combined heating and loss rates for our atoms in the two lowest-energy spin states at low trap depths, neglecting evaporative loss, limits the lifetime of the atoms to $\sim$ 30 seconds, which is much longer than any other timescale in our experiments.

4.6.4 Calibrating the Dipole Trap

Calibration of the trapping frequencies of the Primary trap was conducted using two methods. The first method, called parametric heating, is based on the resonant heating of atoms in a harmonic potential when the intensity of the trap

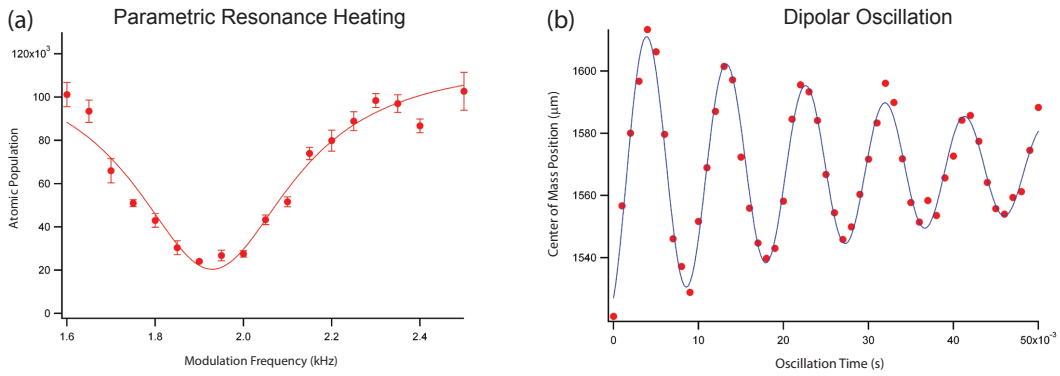

Figure 4.15. Measurement of the trapping frequencies for the primary trap (a) using parametric heating and (b) mapping the induced dipolar oscillation of the gas.

is modulated at twice the trapping frequency ($v_{mod} = 2v_{trap}$) or any of the sub-harmonic frequencies [181]. The second method measures the frequency of an induced collective dipole oscillation of the atoms in the harmonic trap.

In a simple picture, parametric heating occurs when the atoms experience a "kick" from the trapping potential at each of their classical turning points. On resonance, this leads to an exponential heating of the atoms. For our experiments, we modulated the amplitude of the RF driving the AOM intensity for a set time, and measured the atom loss from the gas with respect to the frequency of the modulation using standard absorption imaging after a time of flight (see Section 4.7). A representative parametric heating measurement of one of the radial trapping frequencies of the primary trap, with a power of nominally 3 Watts in each beam, is shown in Figure 4.15 (a).

For very weak trapping potentials and generally along the axis of the crossed-beam trap it is simpler to measure the collective dipole oscillation of the sample to calibrate the trapping frequencies. Applying a magnetic field gradient along one of the experimental axes will shift the center-of-mass of the atoms with respect to the trap. By rapidly shunting the gradient, the gas collectively oscillates with a frequency equal to v_{trap}. The frequency of this oscillation is then "mapped out" by varying the hold time during which the atoms oscillate before recording the center of mass position of the atoms using either in-situ absorption imaging or imaging after a short time of flight as described in Section 4.7.

The broad utility of this method comes from the fact that two-body interac-

tions are not affected by the dipole mode of the harmonically confined gas because the motion of the center of mass is perfectly decoupled from the internal degrees of freedom of the system [182]. Therefore, the frequency of the dipole mode characterizes any system confined in a harmonic potential, regardless of the interactions and statistics of the gas. A measurement of the induced dipole oscillation of the atomic gas along the axis of the crossed-beam trap with a power of nominally 3 Watts in each beam is shown in Figure 4.15 (b). The decay of the oscillation is likely attributed to anharmonic deviations of the gaussian trapping potential.

4.6.5 Large Volume Traps

In our recent experiments, we were measuring three-body phenomena over a range of magnetic fields where the inter-atomic scattering lengths were unitarity limited for gases at temperatures above ~ 30 nK. To this end, we have installed two large-volume (LV) dipole traps which can access much smaller trapping frequencies while maintaining large trap depths to accommodate large sample sizes. By adiabatically loading an ultracold sample of atoms from the primary dipole trap into one of these large-volume traps, we were able to achieve much lower atomic temperatures and densities.

A schematic of the optical layout for these traps is presented in Figures 4.16 and 4.17. The light for the LV traps is derived from the zero-order beam which passes through the AOM for the primary crossed-dipole trap, providing up to 110 Watts of power when the crossed-beam dipole trap is extinguished. The power from this beam can be divided among three paths. In path (A), the light intersects the atoms aligned with one of the radial MOT beams using a Dichroic mirror which reflects the 1064 nm light and passes the 671 nm MOT beam. The trapping laser is focused along the $\hat{z}$ direction using a cylindrical lens to produce a highly elliptical beam, strongly confining the atoms along the $\hat{z}$ axis, with weak radial confinement along the $\hat{x} - \hat{y}$ plane and negligible confinement along the axis of the beam. In path (B), the light is directed co-propagating with that of path (A), but now the beam is circular, providing identical radial trapping frequencies in the absence of gradient fields. Path (C) produces a beam propagating along the $\hat{x} - \hat{z}$ plane to provide confinement along the axis of the beams (A) or (B).

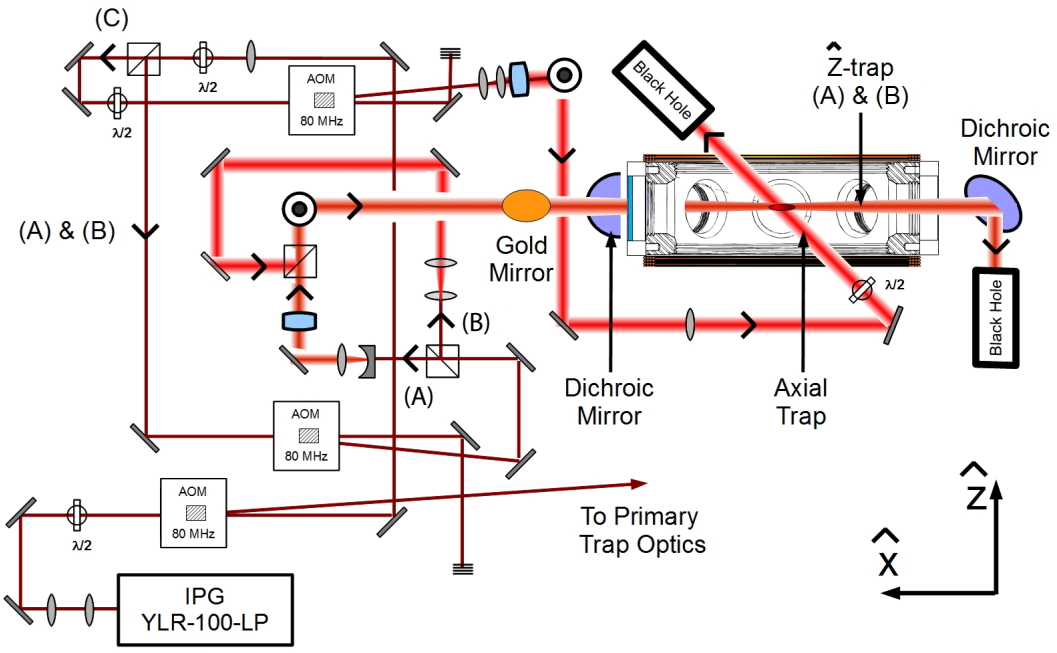

Figure 4.16. Birds-eye view of the optical setup for the large-volume trapping beams (A), (B), and (C)

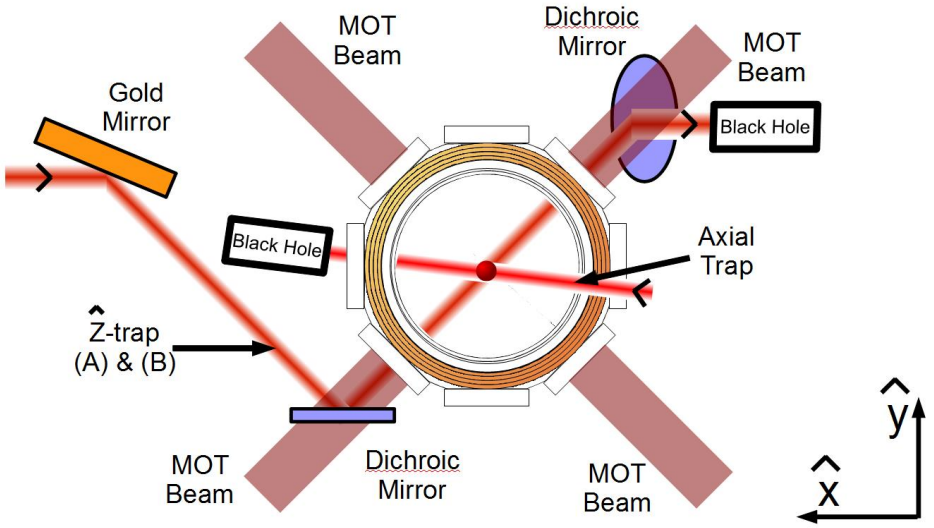

Figure 4.17. Horizontal view of the optical setup for the large-volume trapping beams. The Corridor coils are shown.

LV Beam	minimum waist (w_{min})	ellipticity (w_{min}/w_{max})	P_{max}
$\hat{z}$ Trap (A)	127 μm	0.05	$\sim$ 50 W
$\hat{z}$ Trap (B)	2.5 mm	1	$\sim$ 50 W
Axial Trap (C)	430 μm	0.8	$\sim$ 50 W

Table 4.2. Waists, ellipticities, and maximum available laser powers for the various large-volume trapping beams

The gradient of the Primary and Booster magnetic coils, described in Section 4.3.4, was quite useful for achieving ultra-low densities and temperatures in our experiments. These gradients provide sufficient restoring force along the $\hat{x} - \hat{y}$ plane to confine our ultracold atoms in the $\hat{z}$ traps (A) and (B) alone. The axial confinement beam (C) was therefore used only to increase the density of the atoms. For each path, the light is sent through a series of optics to shape the beam and AOMs to control their intensities. The RF powers for the AOMs are provided by stable 80 MHz reference frequencies from our DDS systems. This reference is amplified by home-built RF amplifiers, which can be amplitude controlled by an external 0-10 V signal, provided by our computer control system.

The trapping frequencies of these potentials were calibrated by measuring the dipole oscillation frequencies as described previously, and the large volume of these traps and very low atomic temperatures allowed both in the trap (*in situ*) imaging of the atoms and imaging after a significant time of flight, thereby allowing us to obtain information about both the position and momentum distribution of the atomic gas. Details of the various laser beams used in our LV traps can be found in Table 4.2. The loading and utility of these traps in our experiments will be discussed in greater detail in Chapter 5

4.7 Data Acquisition

Physical information about the atomic gas is primarily extracted in our experiments from pictures taken of the atomic cloud using standard absorption imaging techniques. As the atoms are illuminated with resonant light, the intensity of the light that interacts with the atomic cloud is depleted via resonant scattering. The shadow of the atoms is then imaged on the surface of a sensitive charge-coupled

device (CCD) camera to provide information about the two-dimensional density distribution of the atomic ensemble in the radial directions of the probe beam, as illustrated in Figure 4.18.

Whereas imaging atoms directly within the trap leads to *in situ* measurement of the density distribution of the atoms, by allowing the atoms to ballistically expand for a variable time (time of flight), we can also gain information about the momentum distribution of the initial trapped atomic cloud (see Section 5.3). These techniques provide the experimental observable to determine most of the relevant properties of our samples including the total atom number, number of atoms in each spin state, temperature, density, and degeneracy of the gas, etc.

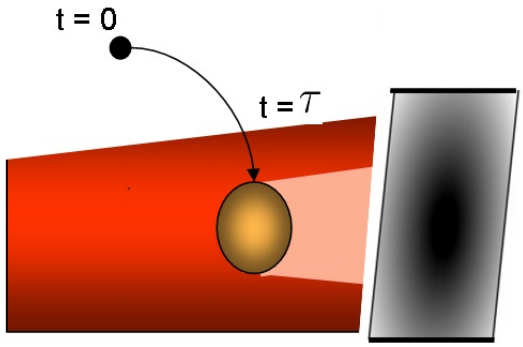

Figure 4.18. Absorption Imaging after a time-of-flight τ.

4.7.1 Absorption Imaging

A light beam with the initial spatial intensity profile $I_0(x, y)$, propagating along the $\hat{z}$ axis through a cloud of atoms is attenuated according to

$$I(x, y) = I_0(x, y)e^{-D(x,y)}, \tag{4.22}$$

where $D(x, y)$ is the optical density. For a probe beam nearly resonant with a single atomic transition with saturation intensity I_{sat}, detuning Δ, and natural linewidth of the transition Γ, the optical density is given by

$$D(x, y) = D_0(x, y)\frac{1}{1 + \frac{I}{I_{\text{sat}}} + \frac{4\Delta^2}{\Gamma^2}}, \tag{4.23}$$

$$D_0(x, y) = \sigma_0 \tilde{n}(x, y), \tag{4.24}$$

which depends on the polarization-averaged resonant scattering cross section (σ_0) and the so-called column density $\tilde{n}(x, y)$, defined as the spatial density $n(x, y, z)$ integrated over the $\hat{z}$ direction.

Three images are taken during each experimental cycle. First, a short (20 μs) absorption image pulse I_{abs} records the shadow of the atomic cloud. As the light is on-resonance with the D_2 transition, the pulse rapidly heats the atoms out of the trap, destroying the sample. Next a reference image is taken I_{ref} with an identical light pulse, 2.159 milliseconds after the atoms are "blown away" with the absorption pulse. Finally a third image is taken hundreds of ms later without any imaging light I_{bkgd} to measure the background light detected by the camera. The transmission of the light detected by the camera is then calculated as

$$T(x,y) = \frac{I_{\text{abs}}(x,y) - I_{\text{bkgd}}(x,y)}{I_{\text{res}}(x,y) - I_{\text{bkgd}}(x,y)}. \tag{4.25}$$

For on-resonance imaging ($\delta = 0$), in the low intensity limit ($I \ll I_{\text{sat}}$), the optical density is given by $D(x,y) = \sigma_0 \tilde{n}(x,y)$. In combination with the *Beer-Lambert Law*, which states $T(x,y) = e^{-D(x,y)}$, and the magnification of the imaging system (M), the processed image yields direct information about the column density distribution of the gas.

$$n(x,y) = -\frac{1}{\sigma_0 \mathrm{M}^2} \ln[T(x,y)] \tag{4.26}$$

The density distribution is the primary observable in our experiment, used in conjunction with the known experimental parameters, to measure the intrinsic properties of the gas.

4.7.2 Imaging Optics and CCD Camera

The optical layout of our imaging system is shown in Figure 4.19. The imaging light, derived from the experimental laser, is initially passed through an AOM to rapidly turn on/off the light and define the offset frequency of the probe from the MOT cooling light. The addition of a computer-controlled shutter is used to shunt the light throughout the majority of the experimental cycle, further suppressing heating attributed to near-resonant light leakage to the atoms. The light is then spatially filtered and transferred to the experimental chamber by a single mode, polarization maintaining fiber. This probe beam is expanded to a waist of 1 cm, so that the intensity ($I \sim 0.1$ $\mathrm{I_{sat}}$) is constant across the atomic gas, and reflected

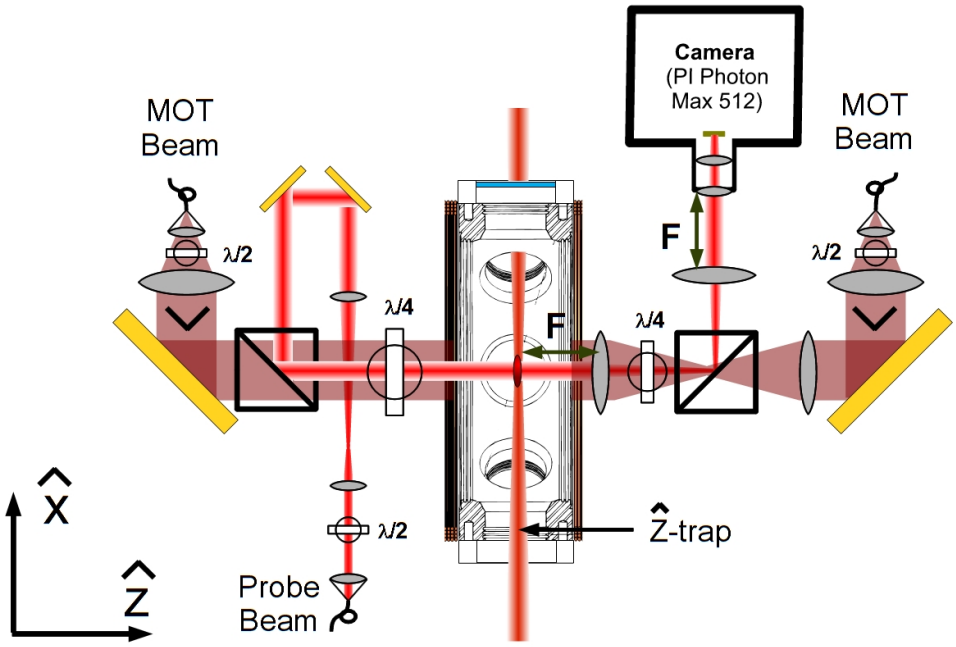

Figure 4.19. Optical design of the absorption imaging system to measure the 2D density distribution of the atomic gas.

off of a polarization-maintaining beam splitting cube (PBS) to assure vertical polarization (the same cube passes one of the horizontal MOT beams as horizontally polarized light). Subsequently, the beam is passed through a $\lambda/4$ waveplate to produce a σ^- circularly polarized beam propagating along the $\hat{z}$ quantization axis, and radially centered on the atomic gas. At the exit port of the experimental chamber, an identical $\lambda/4$ waveplate and PBS cube separates the probe from the MOT beam paths. The shadow of the atoms is focused onto the camera system (consisting of the CCD chip and a $\sim 1.32\times$ expanding telescope) with two identical lenses using standard 1F-2F-1F imaging.

The images are captured and digitized with a back illuminated, frame transfer electron-multiplying CCD camera (Princeton Instruments, Photon Max 512). The CCD chip has a 512 $\times$ 512 array of pixels, with a 16 μm $\times$ 16 μm area for each pixel. The camera has two acquisition modes, *fast kinematic readout* using an on-chip multiplication gain amplifier or a *long integration* mode using a traditional amplifier. We generally utilize the fast kinematics mode, which offers microsecond time resolution between frames. By enabling this mode, the CCD chip is vertically divided into two regions, where the camera only allows one of the regions to be ex-

posed. After exposure, the photoelectron charges in the exposed region are rapidly transferred to the unexposed region, freeing the camera to take a second picture. This allows two individual images to be stored in the CCD array. The digitized signals for the two images are finally read and processed by the data-acquisition computer system to determine the optical density of the gas. An example processed absorption image of the atoms in the primary dipole trap, directly after the MOT is extinguished, is shown in Figure 4.20. An image processing procedure written in the Igor data analysis software then analyzed the processed images and extracted the physical properties of the atomic gas.

Absorption imaging in the absence of an applied magnetic field (zero-field imaging) is predominantly used in our experiment to measure the characteristics of the MOT. Here, our atoms are imaged with light resonant on the $^2S_{1/2}$ $|F = 1/2\rangle \rightarrow^2 P_{3/2}$ transition. Again, this transition is not closed at zero-field requiring an imaging repumper beam, resonant with the $^2S_{1/2}$ $|F = 3/2\rangle \rightarrow^2 P_{3/2}$ transition, to optically pump the atoms back to the $|F = 1/2\rangle$ ground state and sustain the atomic population resonant with the imaging transition. The repumper beam intersects the atoms along the experimental -$\hat{x}$ axis during the imaging pulse (not shown in Figure 4.19). Specific details regarding zero-field imaging of ^{6}Li atoms on the D_2 transition was discussed in detail in Reference [11].

The total magnification of the imaging system was determined from the free-fall trajectory of ultracold atoms in the absence of perturbing magnetic fields. By mapping out this trajectory using zero-field absorption imaging, comparison between the detected acceleration of the atoms to the actual acceleration under gravity was used to calibrate the magnification of the imaging system (M = 1.55). This measurement was conducted using the "old" system, where the light for cooling and imaging the atoms was derived from the Coherent-899 Ring Dye laser (see Section 4.2). The uncertainty in this measurement, along with the $\sim$ 2 MHz linewidth of the probe laser, lead to uncertainties of the total atom calibration on the order of 30%.

In Chapter 2, I described the effects of a large magnetic field on the hyperfine spin states of the 2^2S and 2^2P levels of ^{6}Li. For large magnetic fields (above $\sim$ 100 Gauss), each of the hyperfine states are effectively spin polarized in the $|J\ m_J,\ I\ M_I\rangle$ basis. Absorption imaging in a high magnetic field can therefore be

treated as an optical dipole transition between nearly perfect two-level systems [26]. In this basis, the selection rules for the electric dipole transition define that the total orbital angular momentum can change by: $\Delta J, \Delta m_J = \pm 1, 0$, whereas the nuclear spin is not affected by this transition. Using σ^- imaging light propagating along the quantization axis of the magnetic field, the $|1/2 \ -1/2, \ 1 \ \pm 1, 0\rangle \leftrightarrow |3/2 \ -3/2, \ 1 \ \pm 1, 0\rangle$ transitions can be accessed, providing a closed cycling transition for each ground-hyperfine state separately and negating the utility of the repumper beam used at zero-field.

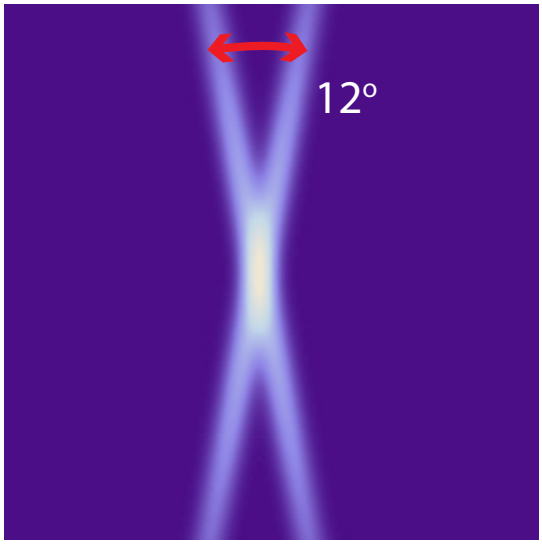

Figure 4.20. Absorption image of the atomic gas in the primary dipole trap. The scale is set to display the atoms remaining in the wings of the individual trapping beams.

Using the offset of the phase-frequency lock of the experimental laser, described in Section 4.2.2, the imaging probe can be frequency tuned over ~ 2 GHz to access the field- and state-dependent resonance frequencies of the 2^2S Zeeman sublevels. At high magnetic field, the $m_J = 1/2$ state is separated from the $m_J = -1/2$ by on the order of GHz, which is much larger than the natural linewidth of the D_2 line. Further, for monochromatic absorption imaging, the numbered states of interest in this experiment ($|1\rangle$, $|2\rangle$, $|3\rangle$) are spectroscopically resolvable, with hyperfine energy spacings between states on the order of 80 MHz. Absorption imaging in the presence of a large magnetic field (high-field imaging) is therefore a useful tool, allowing for state-selective operations (imaging and removal) to be performed on the numbered states $|n\rangle$, and was utilized for the majority of our experimental measurements.

4.8 RF System

Radio frequency (RF) fields are the primary tool we use to manipulate the internal state of our atoms. Over the range of magnetic fields applicable to our experiments,

the three lowest-energy hyperfine ground states of ^{6}Li vary by roughly 50 - 120 MHz. By applying resonant pulses, it is possible to selectively drive transitions among the hyperfine states to prepare our samples. We use RF pulses in various stages of our experiments, both to prepare balanced two-state mixtures for evaporation as well as to transfer populations between states $|1\rangle \leftrightarrow |2\rangle$ and states $|2\rangle \leftrightarrow |3\rangle$ to create balanced three-state mixtures. RF spectroscopy is also a useful tool that we use to probe the properties of the system under study. In this section, the design of our RF antennas and the system of electronics to produce an oscillating magnetic field at the atoms is discussed. Details about the spectral content of our pulses and their use to create incoherent three-state mixtures is discussed in more detail in Chapter 5.

Two RF surface coils were installed within the experimental chamber. The coils, which were designed in our lab by Ron Stites, each consist of a single copper strip 0.25" wide and 0.01" thick. These wires were shaped into a nearly enclosed "race-track" shaped loops approximately 3.5" long and 1" wide, with both coils supported on ceramic rods such that the loops are vertically separated by 1" and centered about the location of the atomic gas. Here, the distances from the atoms to the RF antennas are much smaller than the wavelength of the radiation. In this near-field limit, the RF effectively acts as an oscillating magnetic field oriented along the $\hat{y}$ axis. The design of our RF antennas is shown most prominently in Figure 4.21.

For each loop, both of the ends were silver-soldered directly to the center connectors of two UHV compatible coaxial wires (MDC Vacuum Products, In-Vacuum Insulate Wire), and the shields were soldered together close to the connectors to minimize the area of the RF loops. The other ends of the four coaxial wires were connected to BNC vacuum feedthroughs (MDC Vacuum Products) to provide electrical access outside of the vacuum system.

At first, we had serious concerns about placing the coils inside our experimental chamber. Although designed for a UHV environment, the effect of outgassing from the coil pair, which effectively surrounded our atoms, was not clear. Also, heating of the coils, which carry pulses of up to 50 Watts for hundreds of milliseconds, in an evacuated environment was a serious concern. It was also worried that the stainless steel chamber would affect the performance of the loops, where the conductive

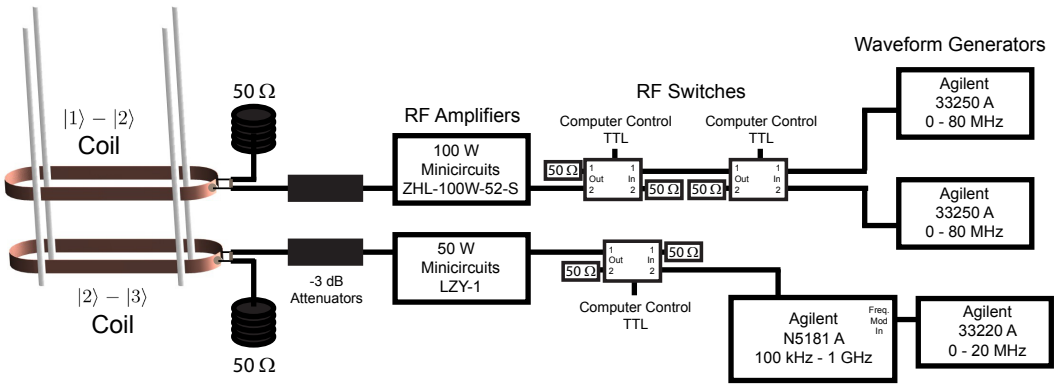

Figure 4.21. Schematic of the RF power drive system.

chamber reduces the magnetic flux return path and therefore the magnetic field experienced by the atoms. We have had no problems with the coils since their installation in 2005 and it turns out that none of these factors are serious detriments to the performance of our system.

A schematic of our various electronics dedicated to applying RF magnetic fields to the atoms is shown in Figure 4.21. In general, one of the coils was dedicated to driving $|1\rangle \leftrightarrow |2\rangle$ transitions whereas the other coil drove $|2\rangle \leftrightarrow |3\rangle$ transitions throughout an experimental sequence. For the $|1\rangle \leftrightarrow |2\rangle$ RF coil, the signals were provided by one of two arbitrary waveform generators (Agilent 33250 A). The Agilents provided frequency modulated RF signals with central frequencies resonant with the $|1\rangle \leftrightarrow |2\rangle$ transition at different parts of the experimental routine. One Agilent was centered on-resonance at the evaporation magnetic field, used to equalize the populations for optimum evaporative cooling, while the other Agilent was centered on-resonance for the field at which the three-state mixture is created. For the $|2\rangle \leftrightarrow |3\rangle$ RF coil, the signal for creating the three-state mixture is provided by a single arbitrary waveform generator (Agilent N5181 A), which can provide signals at frequencies above 80 MHz. These high frequencies are necessary to make the $|2\rangle \leftrightarrow |3\rangle$ transitions for nearly all of the fields of interest. A low-frequency waveform generator (Agilent 33220A) is used to drive the amplitude of the frequency modulation of this signal about the center frequency. Single-tone signals from the Agilents were also used for RF spectroscopy to observe Rabi-flopping of the atomic populations. The ability to choose which signal is amplified and sent through the RF coils along with control over the timing of the pulses is

provided by multiple computer controlled RF switches.

During the pulse, the signals are initially amplified to either 50 or 100 Watts using Minicircuits RF amplifiers. The signals are then each attenuated by 3 dB before passing through the coil and getting absorbed by a 50 Ω load on the exit port of the coils. The attenuators are installed to protect the amplifier from the reflected power not absorbed by the load. Although the coils are nominally impedance matched to the amplifier by the 50 Ω loads, a slight mismatch can reflect Watts of power back to damage the amplifier. The attenuators assure that the reflected power is reduced from the incident by 6 dB for further protection.

The use of multiple RF coils makes it particularly simple to apply two incoherent RF fields to the atoms by simply driving both coils independently. Future experiments may use the fact that both coils can be driven coherently to significantly increasing the B-filed experienced by the atoms. Further, by placing the RF coils inside the vacuum system, the magnetic field at the atoms is optimized. We are currently capable of inducing complete population transfer among the lowest three numbered states within $\sim 50\ \mu s$ with this system, even at high magnetic fields where the transfer efficiency is reduced due to electron-spin polarization. Recent upgrades include switching the RF frequency sources from the Agilents to using our home-built DDS waveform synthesizers, allowing for computer control of the center and modulation of the frequency during the experimental runs. Additionally, a high-power/high-frequency RF amplifier (Minicircuits ZHL-30W-252+) has been installed to allow us to access transitions to the low-field seeking states $|4\rangle$, $|5\rangle$, and $|6\rangle$ for RF spectroscopy applications with our three-component Fermi gases.

4.9 Computer-Controlled Data Acquisition

Ultracold atomic gas experiments generally require that all of the optical, magnetic, and electronic devices work in a precise timing sequence. For our applications, a timing precision of about 1 μs is sufficient. Our experimental control system includes the controller computer, two high-speed analog output boards (National Instruments, PCI-6733), two programmable TTL Pulse generators (Spincore, PulseBlaster), and both commercial and in-house produced digital synthesizers.

Each PCI-6733 AO board provides eight analog outputs (± 10 V, 5 mA) with 16 bit resolution and 1 MS/s update rate. These boards are ideal for cold atom experiments, with 15V/μs slew rates, 80 μV_{rms} noise, and an internal 20 MHz clock with 24 bit counter resolution for timing I/O. Additionally, timing signals can be routed to and from the device by means of a Programmable Function Interface which allows for external clock synchronization and triggering of DC analog outputs and externally programmed waveforms stored in the devices memory buffer.

The PulseBlaster (PB) is a multichannel, programmable TTL pulse/digital word generator, capable of producing 24 precisely timed, individually controlled digital output signals. The timing controller is driven by a 100 MHz internal crystal oscillator, and can produce TTL pulses with variable length from one clock period (10 ns) to nearly two years with a cycle delay of less than 100 ns. These boards can also be externally triggered for timing synchronization and externally reset. Our two PB boards are in a master/slave configuration in our experiment to allow enhanced complexity of the timing sequence for the TTL outputs.

Our control computer (Pentium 4, 3.4 GHz processor with 1 Gb RAM) provides the timing sequence for the various components in our experiments. The entire sequence is controlled by a LabVIEW (National Instruments) timing program. The various digital outputs and analog output values can be chronologically entered into the graphical interface of the program, with variable time delays between steps, allowing complete control of the timing events for each analog and digital channel. At the beginning of each experimental run, the program generates an array with time and state information for each device, which it sends to program the various control boards and devices throughout the experiment. Additional features in this program include:

- Programmable analog voltage ramps with variable time and step sizes,
- Generation of multiple waveforms, which are sent via GPIB to programmable digital synthesizers (i.e. the Agilent 33250 A controlling the power of the primary dipole trap) which will be time-synchronized with the experiment,
- Automated loops which automatically change either the time or amplitude of experimental parameters for multiple experimental cycles.

This highly dynamic control system is quite robust and is generally useful for a wide range of cold atom experiments.

Recently, Eric Hazlett and Yi Zhang upgraded the computer control system to incorporate programming and timing synchronization of our in-house built direct-digital synthesizers (DDS), briefly discussed in Section 4.2.2. These RF synthesizers use an AD9852 DDS IC chip from Analog Devices to generate sine signals ranging from DC to 135 MHz. The DDSs are digitally interfaced with a microprocessor module (RCM3200 RabbitCore with Rabbit 3000, 44.2 MHz microprocessor), which is programmed via Ethernet with control software directly implemented in our LabVIEW experimental control program. The DDS can be commanded to generate sequences of RF pulses and frequency ramps, which are programmed into the micro controller at the beginning of the experimental run and triggered during the experimental cycle with external digital signals. The various operation modes of these devices include single-tone, frequency shift keyed (FSK), ramped FSK, frequency chirp, and binary phase shift keyed (BPSK).

We have had great success with these synthesizers by simply following the original design of Dr. Meyrath and Dr. Schreck [167]. In addition to their use as a frequency reference for the offset lock of the experimental laser and the source for our RF fields, these synthesizers are now used in conjunction with our home-built, variable RF amplifiers to drive nearly all of our AOMs, including those controlling the cooling/repumping and imaging light as well as the AOMs that control the intensity of the large-volume trapping beams. In this way, the intensity and timing of all of the light, magnetic, and RF fields in our experiments can be controlled in a reproducible and highly dynamic manner that makes this system amenable to wide range of ultracold experiments with multi-component and/or degenerate Fermi gases.

Chapter 5

A Toolbox of Methods: Preparing and Probing 3-State Fermi Gases

The methods of producing degenerate and/or ultracold Fermi gases of ^{6}Li atoms occupying the three lowest Zeeman sublevels ($|1\rangle, |2\rangle$, and $|3\rangle$) and probing their universal properties is detailed in this chapter. To this end, we initially evaporatively cool stable mixtures of atoms occupying states $|1\rangle$ and $|2\rangle$ to degeneracy. Whereas the atoms remain unbound for magnetic fields above 834 Gauss and below $\sim$ 550 Gauss, the existence of the universal dimer state between these field values enables the atoms to be cooled into a long-lived bosonic molecular gas, finally condensing into a Bose-Einstein Condensate (BEC) as the gas becomes degenerate.

The general methods and technical requirements for studying three-component Fermi gases at magnetic fields exhibiting large three-body loss is then discussed. Particular attention to the design of the conservative dipole trapping potentials and the evaporation process was required to enable our measurements. In this system, three-body decay of the gas is attributed to recombination events consisting of one free atom from each spin state, decaying via inelastic three-body collisions to form a high-energy dimer and recoiling atom. To gain quantitative information about the rates of these three-body processes, we prepared the three-state mixture using broad-band RF pulses centered on the $|1\rangle - |2\rangle$ and $|2\rangle - |3\rangle$ transition frequencies respectively. Here, we discuss our methodology for assuring that the gas is initially prepared in an equally populated mixture in thermal equilibrium. Next, we discuss how we extract information about the temperature, density, and

population of each spin component for both classical and quantum degenerate gases from the low-intensity absorption images that provide the observables in our experiments. Finally, the design and use of our large-volume traps is discussed. By adiabatically loading our ultracold gases from the primary trap into one of these large-volume, low-frequency traps, we were able to achieve unprecedentedly low temperatures and densities for the three-component samples to study Efimov physics in the strongly universal regimes.

5.1 Evaporative Cooling

In Chapter 2, it was demonstrated that the equilibrium temperature and density of an atomic gas determines the range of physics that can be studied with a given systems. Most importantly, the phase-space density of the gas determines to what level quantum effects come into play. As discussed in Section 4.5, the maximum achievable phase space density of ^{6}Li atoms in a MOT is on the order of 10^{-6}, whereas a phase-space density in excess of one is required to observe phenomena associated with Fermi degeneracy and molecular condensation. We therefore utilize the evaporative loss of the atoms from the primary trap to further cool and increase the phase-space density of the gas. This well-known scheme was instrumental to the realization of the first Bose-Einstein condensates of dilute gases of neutral atoms [44, 45, 46], and still remains the only method capable of producing dilute, degenerate gases.

Evaporative cooling describes the process where the preferential removal of the most energetic atoms from a trap causes the average energy of the atomic gas to decrease. This process requires the selective removal of atoms from the high-energy tail of the Boltzmann distribution and elastic collisions among the atoms to rethermalize the gas to a lower average energy. Continuous rethermalization assures that the population of atoms in the high-energy tail of the Boltzmann distribution is maintained to sustaining the evaporation process. In our setup, the depth of the optical dipole trap U_0 sets the scale for evaporative cooling, where only the atoms with energies in excess of this value can leave the confining potential. The efficiency of the evaproative cooling scheme is therefore defined in terms of the so called η-parameter, given as the ratio of the trap depth to the thermal energy

of the gas ($\eta = U_0/(k_B T)$), where the atom-loss rate scales as $\dot{N} \propto \exp(-\eta)$. The cooling efficiency is maximized for large values of η, requiring that each atom lost carry away much more energy than the average energy per particle. However, large η values require longer cooling times attributed to the exponential suppression of $\dot{N}$. Evaporative cooling eventually stagnates in real systems when an equilibrium is reached between the rates of cooling from evaporation and the residual loss and heating rates present in the experiment.

To further cool the atoms, forced evaporation is required. For our system, this translates to lowering the trapping potential at an exponentially decaying rate such that η effectively remains constant. Scaling laws for the number, trap depth, and phase-space density [183] reveal that maintaining $\eta \simeq 10$ provides a good compromise between the efficiency and speed of the cooling cycle. In this reference, K. O'Hara and co-workers further found that Pauli-blocking is not a major constraint of directly cooling the gas to degeneracy because, even as the phase-space density exceeds unity, the final state of the atoms evaporated from the trap remain essentially unoccupied. Therefore, the evaporation rate is only suppressed by a factor of T/T_F due to Fermi statistics.

The success of evaporative cooling hinges on elastic collisions between the atoms dominating over the inelastic loss. As described in Section 2.3, inelastic two-body decay among atoms in states $|1\rangle$ and $|2\rangle$ are effectively negligible. One-body loss attributed to background gas collisions and heating in the trap are therefore the dominant inelastic decay process. Since the lifetime of the two-component gas in the primary trap is on the order of 30 seconds, it was necessary to assure that the rethermalization rates greatly exceeded this timescale. In the classical regime, where the gas is thermal and the effects of unitarity are negligible, the elastic collision rate can be written as [53]

$$\gamma = \frac{8\pi^2 N m \bar{v}^3 a^2}{k_B T}, \tag{5.1}$$

where N is the number of interacting particles, m is the atomic mass, $\bar{v} = \bar{\omega}/(2\pi) = (\omega_x \omega_y \omega_z)^{1/3}/(2\pi)$ is the mean trapping frequency, and a is the scattering length of the particles. Taking reasonable values for our system near the end of evaporation ($\bar{v} = 100$ Hz, $N = 4 \times 10^5$, $T \simeq 700nK$, and $a = -280a_0$ [B = 330 Gauss]),

we find that the minimum collision rate is on the order of 8 Hz, exceeding the inelasticity timescale by orders of magnitude. Although not applicable for all of our experiments, evaporation at fields near the Feshbach resonance can also be utilized, where the dramatic increase of the scattering length further assures rapid thermalization of the gas.

Evaporative cooling is implemented in our experiments directly after the 100 ms loading stage when the atoms are trapped from the MOT into the primary dipole trap. At the end of the transfer, the atoms are optically pumped into states $|1\rangle$ and $|2\rangle$ to suppress inelastic loss. A magnetic field is then applied, using the primary coils in Helmholtz configuration, either at the low-field value of 330 Gauss or near the Feshbach resonance at 840 Gauss to induce large interactions among the atoms. At this point, a broadband "noisy" RF pulse whose frequency is centered on the $|1\rangle \leftrightarrow |2\rangle$ transition is applied for 100 ms. As discussed in the next section, this pulse drives transitions between the two hyperfine states for a sufficient time to assure that an incoherent 50-50 mixture of atoms in each state is prepared, optimizing the evaporative cooling efficiency.

The trap is held at its peak depth of $U_0 \sim k_B \times$ 1 mK, where k_B is the Boltzmann's constant, for another 100 ms to allow for free evaporation and assure that $\eta_0 \sim 10$, optimizing the efficiency of the subsequent forced evaporation stages. The depth of the trap is then lowered by exponentially decreasing the power of the primary trapping beams using an exponential ramp profile with a $\tau = -0.5$ second time constant and a total ramp duration of between $T = 2.5$ to 4.5 seconds. To support the atoms against gravity and cancel out forces on the atoms along the $\hat{x}$ axis, the levitation and shim fields are linearly ramped to their final values over 100 ms during the first second of the forced evaporation stage. The final trap depth determines the temperature, density, atom number, and reduced temperature of the gas, but we can regularly produce two-component degenerate Fermi gases in states $|1\rangle$ and $|2\rangle$ with $N \sim 3 \times 10^5$ atoms in both spin states at reduced temperatures $T/T_F \leq 0.3$, .

5.1.1 Molecular Bose-Einstein Condensation

At magnetic fields slightly below the Feshbach resonances, where the atoms exhibit large positive scattering lengths, the existence of the universal molecular dimer states can greatly affect the evaporative cooling dynamics, eventually leading to the formation of a molecular BEC as the gas approaches degeneracy. To understand this phenomenon, consider the evaporative cooling of a mixture of ^{6}Li atoms in states $|1\rangle$ and $|2\rangle$ at a magnetic field value of 760 Gauss. Here, the binding energy of the dimer state is $E_D \simeq k_B \times 1.6\ \mu K$, calculated from the scattering length at this field ($a_{12} \simeq 4160 a_0$) and the universal relation given in Equation 2.31. If the thermal energy of the sample drops to a value comparable to the binding energy of the dimers, the molecular state can become populated by means of three-body recombination. Although this recombination process is expected to be Pauli-suppressed in a two-component Fermi gas, D. Petrov showed both that the recombination rate into the shallow dimer near the Feshbach resonance scales as a^6, and an energy dependence of the recombination event leads to a decreasing average energy per particle, cooling the gas. No Efimov states are expected to exist, however, for equal mass fermions occupying two spin-states [182].

On the other hand, the universal dimmers are surprisingly stable because the rates for inelastic atom-dimer and dimer-dimer collisions corresponding to molecular relaxation to deeply bound states are strongly suppressed at large scattering lengths [184]. This phenomena was experimentally verified by R. Grimm's group in Innsbruck [185] and has been utilized extensively to produce stable ultracold Feshbach molecules of fermionic atoms [117, 186, 187]. As the temperature of the gas is reduced, a chemical equilibrium between the number of atoms (N_{at}) and molecules (N_{mol}) coexisting in the gas is established, given by [188]

$$\frac{N_{mol}}{N_{at}} = \rho_{at} \times \exp\left[\frac{E_D}{k_B T}\right] \tag{5.2}$$

where ρ_{at} is the phase-space density of the atomic sample. The occupation of the molecular state therefore increases as the temperature of the sample is reduced and the gas approaches degeneracy, as has been confirmed by RF spectroscopy measurements [115].

The formation and cooling of the Feshbach molecules is amazingly robust in

optical dipole traps. As described previously, once formed the molecules are effectively stable at large scattering lengths and the dimer-dimer scattering lengths remain large, equal to $0.6a$ where a is the scattering length for free atoms [189]. Further, the polarizability of the molecules is twice as large as compared to free atoms, resulting in twice the trap depth. The increased mass of the molecules, however, assures that the trapping frequencies are the same for atoms and Feshbach molecules of the same atomic species. Evaporative cooling in a regime where both atoms and molecules coexist preferentially leads to loss of the atomic population. Eventually, the gas consists almost entirely of bosonic Feshbach molecules, resulting in the emergence of a molecular BEC as the gas is cooled to degeneracy. The creation and stability of the molecular BEC phase using ultracold fermionic atoms was first demonstrated in 2003 [23, 55, 56], leading to numerous studies of BEC-BCS crossover physics [22, 21, 57, 58, 26, 70] and applications to cool and probe the properties of ultracold, strongly interacting Fermi gases.

In a harmonic confining potential, approximating the potential experienced by the ultracold gases in our optical dipole trap, the critical temperature for molecular condensation is given by [170]

$$k_B T_c \simeq 0.94\ \hbar\bar{\omega} N_{mol}^{1/3}, \tag{5.3}$$

where $\bar{\omega} = (\omega_x \omega_y \omega_z)^{1/3}$ is the mean oscillation frequency of the trap. At temperatures below T_c, the occupation of the ground state is given by

$$N_0 = N\left[1 - \left(\frac{T}{T_c}\right)^3\right], \tag{5.4}$$

where at $T = 0$, all of the atoms occupy the ground state with a single macroscopic wavefunction describing the system. In comparing the critical temperature for molecular condensation (T_c) with the Fermi energy of free atoms in the non-interacting limit (T_F), entropy conservation requires that for harmonically trapped gases, $T_c \approx 0.22 T_F$ [108]. In fact, the direct association of molecular condensates from degenerate Fermi gases by means of adiabatic B-field sweeps across Feshbach resonances has been demonstrated as a feature of BEC-BCS crossover physics [23].

Molecular BECs are produced in our experiments, inspired by the procedures

layed out by the Innsbruck and Heidelberg groups [185, 190], by evaporatively cooling the gas at an applied magnetic field of $B = 760$ Gauss. During evaporation we lower the depth of the trapping potential by a factor of approximately 670 where, at the end of the evaporation stage, the critical temperature $T_c \sim 100nK$. As the gas becomes degenerate, the macroscopically occupied ground state of the BEC leads to an inverted parabola (Thomas-Fermi) density distribution in the center of the gas, while the thermal component in the wings of the distribution can be fit with a Gaussian.

A standard method for detecting the normal $\rightarrow$ BEC phase transition is by observing the emergence of a bimodal distribution in the time of flight images associated with the BEC and thermal components of the gas. Since our molecular BECs are strongly interacting near the Feshbach resonance, the expansion of the BEC at 760 G is comparable to that of the thermal cloud. Therefore, to distinguish the two phases, directly after the atoms are released from the trap the magnetic field is ramped to $\simeq$ 600 Gauss (reducing a_{12} by over an order of magnitude) to minimize the mean-field interaction energy and allow for the formation of the bimodal distribution. The thermal gas now expands much more rapidly during the time of flight (TOF) than the BEC component, however the molecules are deeply bound at this field and cannot be imaged with absorption imaging. After approximately 20 ms TOF, at which point the gas is highly dilute, the field is again increased to 785 Gauss. The effects of the mean-field interaction on the expanded density distribution are now minimal, and imaging of the molecules in both the thermal and BEC phases is possible.

The density distribution of our gas at various cooling stages on the route to degeneracy is shown in Figure 5.1. Each image is the result of a single experimental run, where the power in the primary trapping beams was decreased from $P \simeq 80$ mW per beam in Figures (a) and (b) to $P \simeq 30$ mW per beam in Figures (g) and (h). The left-hand panels are the direct absorption images of the gas. In the right-hand panels, a one dimensional (1D) slice of the density distribution through the center of the cloud along the $\hat{x}$ axis is shown. For each image, the 1D density distributions shown in the right-hand figures was fit to extract the thermal and BEC components of the gas. The red curves represent a Gaussian fit of the wings, corresponding to the thermal component of the gas. The blue curves in these

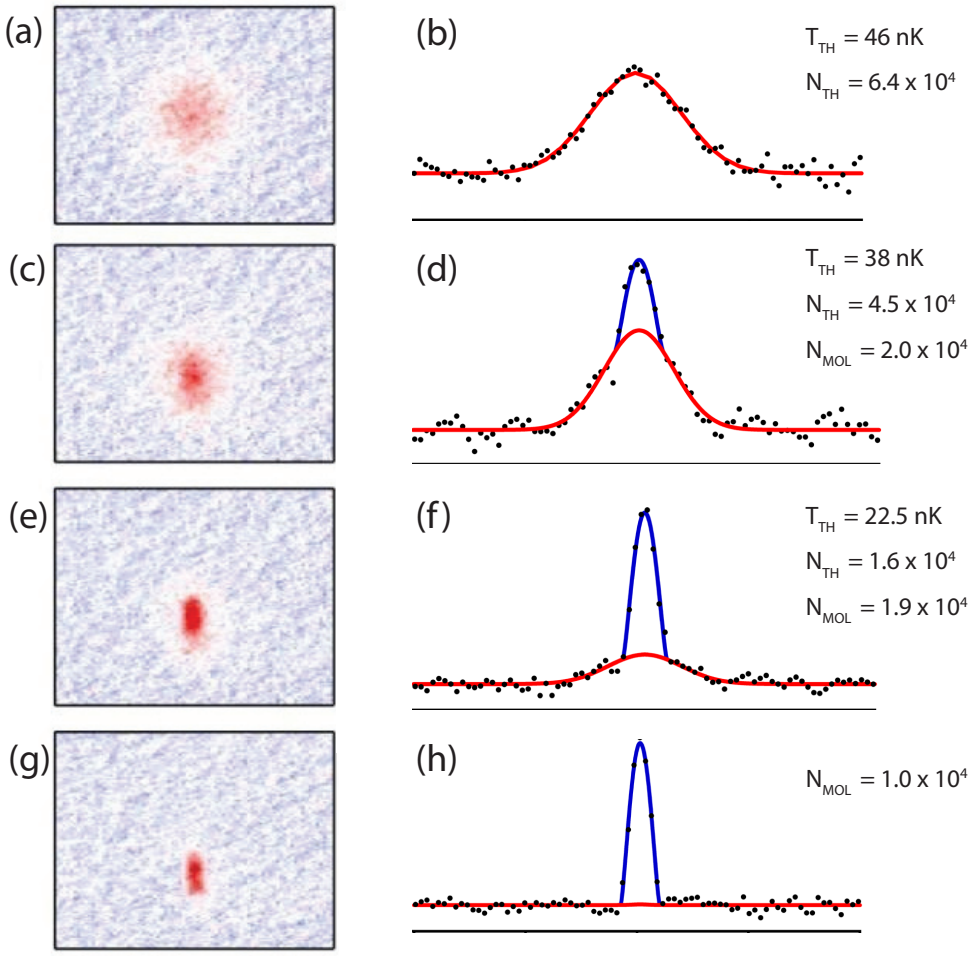

Figure 5.1. False color absorption images (left panels) and 1D density distributions (right panels) of the molecular gas after a time of flight. The depth of the trapping potential is decreased by nearly a factor of three between images (a) and (g). The bimodal distribution signaling the on-set of molecular Bose-Einstein condensation is clearly seen in panels (c)-(d) and (e)-(f). The Gaussian fit (red) represents the thermal component whereas the Thomas-Fermi fit (blue) represents the condensed component of the gas.

figures are fits using a Thomas-Fermi distribution, corresponding to the fraction of the gas in the condensed phase. In the top panels (a)-(b), the gas is purely thermal where the number and temperature of the gas is obtained from the Gaussian fit (see Sections 4.7 and 5.3). In the middle panels (c)-(d) and (e)-(f), the emergence of the bimodal distribution, signaling the onset of condensation, is clearly shown.

The number of atoms in the thermal phase and the temperature of the gas are obtained from the Gaussian fits to the wings and the occupation of the molecular

components are given from the Thomas-Fermi fits. In the bottom panel, it was not possible to extract the thermal component from the fit, signaling that a nearly pure BEC is formed at this stage. It should be noted that these figures were taken over two years ago, before we had installed the bars for the levitation and translation fields. At that time, we were only able to cool $\sim 10^4$ molecules into a nearly pure BEC. Recent advancements in our system have increased this number to $N_0 > 10^5$, demonstrating how important magnetic levitation and stable lasers/frequency references are in our experiments. Whenever possible, our two-component ^{6}Li gases are prepared in the BEC phase as a starting point for our experiments. Subsequent magnetic field ramps across the Feshbach resonance yield initial samples with $N > 10^5$ atoms per spin state at reduced temperatures of $T/T_F \leq 0.3$.

5.2 Preparing a Three-Component Fermi gas

Three-component Fermi gases are produced in our experiments by means of simultaneously applying two radio-frequency pulses whose frequencies are centered on the $|1\rangle - |2\rangle$ and $|2\rangle - |3\rangle$ transitions respectively. A magnetic field gradient provided by the levitation fields and collisions between the atoms leads to an incoherent mixture of atoms in the three lowest energy spin states. The samples are then state-selectively imaged to determine the atomic population and temperature after a variable hold time in the trap. In this section I will describe the production methodology in more detail to provide understanding of the issues involved in creating incoherent, thermally equilibrated three-component Fermi gases in our experiments.

5.2.1 RF Transitions in ^{6}Li

In a constant magnetic field, the eigenstates of our ground-state atoms, discussed in Chapter 2, are stationary. Addition of an oscillating magnetic field can induce an electromagnetic coupling between these states. Described in the framework of dressed states [174], coherent coupling can induce transitions among atomic states if the frequency of the applied radiation field is resonant with the energy difference between the states and the transitions are allowed by the selection rules.

The electromagnetic coupling from an applied RF pulse can drive magnetic dipole transitions between the Zeeman sublevels of the atoms, with selection rules $\Delta F = 0, \pm 1$, $\Delta m_F = 0, \pm 1$. For a pulse of frequency ω_{RF}, the probability for an atom to transition from state $|a\rangle$ to state $|b\rangle$ is given by the Rabi formula [191, 174]

$$P_{ba}(t) = \left(\frac{\Omega_R}{\sqrt{\Omega_R^2 + (\omega_{RF} - \omega_0)^2}} \right)^2 \sin^2 \left(\frac{\sqrt{\Omega_R^2 + (\omega_{RF} - \omega_0)^2}}{2} t \right), \tag{5.5}$$

where Ω_R is the Rabi frequency and $\omega_0 = (\mathrm{E}_b - \mathrm{E}_a)/\hbar$ is the energy difference of the states. If the RF pulse is on-resonance ($\omega_{RF} = \omega_0$), the atoms can be fully transferred between the states in a time $t = \pi/\Omega_R$, commonly referred to as the π-pulse time. For more details on RF driven atomic transitions, please refer to Reference [191].

For our three lowest-energy Zeeman sublevels, the resonant RF frequencies at large magnetic fields are typically on the order of $\omega_{RF} \sim 80$ MHz. Since the wavelength of the RF radiation is relatively long, on the order of 4 m, the momentum transferred to the atoms can be neglected as compared the energy of the externally applied trapping potentials. Further, the spontaneous decay rate for transitions among the Zeeman sublevels ($A_{ba} \propto \omega_{RF}^3$) is negligible on our experimental timescales. By applying a moderate magnetic field to define the quantization axis of the system and subjecting our atoms to a near-resonant RF field provided by our RF coils and amplifier system, we can induce transitions among the high-field seeking magnetic sublevels of the 2^2S ground state in our ^{6}Li atoms. Further, the transition can be driven with negligible heating of the atoms and, once produced, the atoms are effectively stable with respect to spontaneous decay to the absolute ground state.

Figure 5.2 shows a representative data set displaying RF induced Rabi oscillations of our atoms at a field value of $B = 930$ G. Here an initially spin-polarized gas of atoms in state $|2\rangle$ is exposed to RF radiation resonant with the $|2\rangle - |3\rangle$ transition for a variable time. The number of atoms in state $|2\rangle$ is displayed with respect to the duration of the applied RF field, demonstrating the characteristic oscillatory behavior of the population of atoms in the initial state given by

$$N_a(t) = N_a(0)(1 - P_{ba}(t)), \tag{5.6}$$

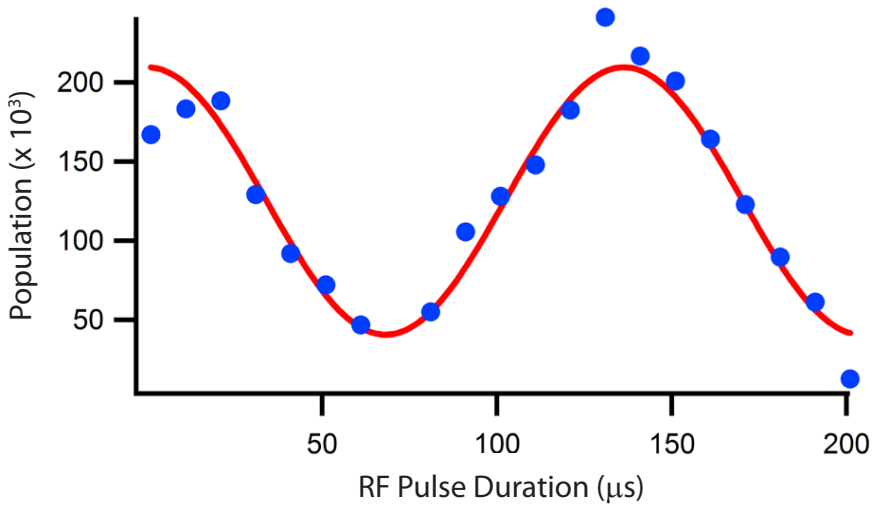

Figure 5.2. Rabi cycling of ^{6}Li atoms initially prepared in state $|2\rangle$ in the presence of a RF field near resonant with the $|2\rangle - |3\rangle$ transition frequency. The experimental data (blue dots) represent the number of atoms in state $|2\rangle$ with respect to the RF drive time. The solid (red) curve is a fit of the data to Equation 5.6.

where $N_a(0)$ is the initial population of atoms in state $|2\rangle$ and $P_{ba}(t)$ is the transition probability given in Equation 5.5. For this data, the oscillation period, peak atom number in state $|2\rangle$, and maximum transition amplitude were fit using Equation 5.6 above to determine the RF field detuning from resonance ($|\omega_{RF} - \omega_0| \simeq 2\pi \times 4$ kHz), the RF Rabi frequency ($\Omega_R \sim 2\pi \times 6$ kHz) and total atom number ($N = N_{|2\rangle}(0) \simeq 2.4 \times 10^5$). The coherence time of the atoms can also be determined from this technique by observing the decay rate of the Rabi oscillation.

With our RF power and antenna system, described in Section 4.8, we achieved Rabi frequencies over the field range 100 G $\leq B \leq$ 1500 G on the order of $\Omega_R \simeq 2\pi \times 5$ to 9 kHz, with $\pi-$pulse times of approximately 50 to 100 μs. As the transition probability is highly sensitive to the value of the homogeneous magnetic field, RF spectroscopy in the form of mapping out the resonant frequency of the atoms was used extensively in our experiments to characterize both the absolute magnetic field applied to the atoms and the amplitude noise of the magnetic fields.

5.2.2 Incoherent Three-State Mixtures

The necessity of creating samples with at least three components to study three-body physics in Fermi gases has been discussed in detail throughout this thesis. More formally, an *incoherent* three-state mixture is necessary, which is not guaranteed by simply applying resonant RF pulses to populate the various spin components. Considering the Bloch sphere representation, a resonant RF pulse does nothing but rotates the population on the Bloch sphere. For an initially spin polarized sample, so long as the decoherence mechanisms are negligible on the timescale of the pulse, all of the atoms will remain in an identical (superposition) state after the RF pulse, and therefore still cannot interact. This coherent excitation was demonstrated in the form of an absence of mean-field "clock shifts" in two-state mixtures of ^{6}Li fermions, regardless of the initial coherence of the samples. [192, 193]

Decoherence can readily occur with the inclusion of magnetic field inhomogeneities, creating a spatially dependent detuning of the atoms from the RF field. This leads to inhomogeneous phases of the atoms in the superposition state with respect to the driving field. Decoherence is further enhanced by collisions among the atoms, redistributing the phases as the atoms become distinguishable [194]. The scrambling of the particle phases causes the atoms to evolve from a coherent superposition state into a "ring state" on the Bloch sphere [193], whose average has no coherences (off-diagonal elements of the density matrix).

The magnetic field inhomogeneity in our experiments is primarily produced by the $\Delta B_y \sim 1$ Gauss/cm gradient of the levitation field. By measuring the decay rate of RF induced Rabi oscillations in a spin polarized sample, we were able to determine that the required drive time for the samples to fully decohere was in the range of 5 to 30 ms, depending on the field and trap profile in which the samples are prepared. In this measurement, decoherence was signaled by the suppression of Rabi flopping, saturating the atomic populations of the RF coupled states to a steady-state value. For driving fields on-resonance with the average of the atomic frequencies, decoherence leads to equal populations of the RF addressed states. Equal population was not assured, however, for all state-driving RF pulses. Particular attention to the stability of the transition was therefore required to assure that we produced equally-balanced three-state mixtures for our experiments.

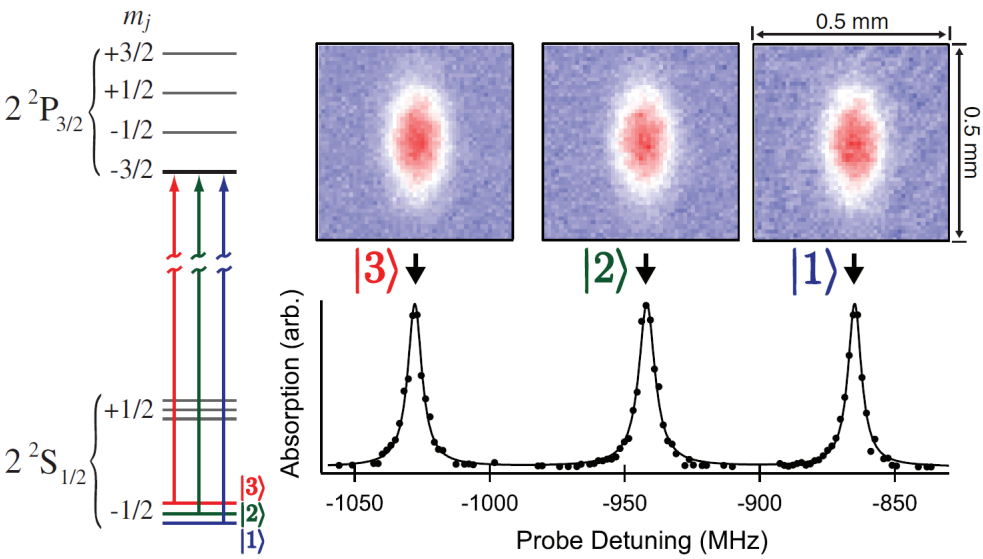

Figure 5.3. The populations in states $|1\rangle$, $|2\rangle$, and $|3\rangle$ measured by absorption imaging in the Paschen-Back regime. (Left) The hyperfine interaction in the ground state allows for spectroscopically resolvable imaging on the $m_j = -1/2 \rightarrow m_j' = -3/2$ cycling transitions. (Top right) 2-dimensional density profile of each state following a 900 μs time-of-flight. (Bottom right) The total absorption vs. probe detuning demonstrating equal populations and resolved imaging of the atoms in each spin-component.

The resonance width of the RF-driven transition is given by the relative slope of the magnetic moments, and the gradient and stability of the magnetic field. States $|1\rangle$, $|2\rangle$, and $|3\rangle$ tune almost identically in the Paschen-Bach regime for fields above 100 Gauss. The widths of the transitions are therefore quite narrow ($\sim$ 500 Hz) for pulses that are not Fourier limited. In our experiments, the RF pulses are generally $10-100$ ms in length, providing negligible Fourier broadening of the transitions. Therefore, noise and drifts in the magnetic field translate to shifts of the atomic resonance frequencies, leading to reduced efficiency of the state transfer.

To consistently produce equal-population, incoherent three-state mixtures in a manner that is immune to magnetic field gradients and drifts, we used "noisy" RF pulses to drive our transitions. Here, the on-resonance RF frequencies were modulated with a white-noise spectrum provided by an Agilent (33220A or 33250A) arbitrary waveform generator. The frequency modulation ranged in width from 10 kHz to 1 MHz ($\sim \Omega_R$ to $100\Omega_R$). Along with the decoherence mechanisms in the presence of a magnetic field gradient, the modulated RF pulse assured that

the total final populations in each of the ground states $|1\rangle$, $|2\rangle$, and $|3\rangle$ were equal [20]. The atomic populations in each of the three spin states, populated from a two state mixture by the noisy RF pulses, is shown in Figure 5.3. The images are taken at a bias field of 568 Gauss, well within the Paschen-Bach regime. In the top right panels, the on-resonance absorption images show the density distribution for each of the three states after a 900 μs time-of-flight expansion. In the bottom right panels, the total absorption signal is shown with respect to the relative detuning from the $|F = 1/2, m_F = -1/2\rangle \rightarrow |F' = 3/2, m'_F = -3/2\rangle$ zero field transition, demonstrating that the states are equally populated and spectroscopically resolvable at high fields.

5.3 Thermometry of Fermi gases

This section describes the theory and methodology of measuring the temperature of ultracold Fermi gases from the two-dimensional density distributions obtained with absorption imaging techniques. The majority of our experiments were conducted with a gas at reduced temperatures on the order of $T/T_F \sim 0.5$, where a classical treatment of the gas is appropriate. In this case, the temperature is readily extracted from a Gaussian fit to the 2D integrated density distribution, as given by absorption images of the gas. As the gas is cooled to degeneracy, the density and momentum distributions are described by a Fermi-Dirac integral function, and the simple Gaussian fit no longer applies. The methodology of directly fitting the absorption images for a degenerate gas using the integral function is at this point well established [169, 11, 28, 50]. However, the analysis requires numerical fitting routines and high resolution imaging to accurately extract the temperature. For these reasons, we primarily utilized a thermometry technique which uses a small "impurity-state" component as a classical probe to determine the degeneracy of our gases.

5.3.1 Spatial and Momentum Distributions in Harmonic Traps

We start by considering N spin-polarized (non-interacting) fermions in a harmonic potential. The single-particle Hamiltonian is given by

$$\mathrm{H}(\mathbf{r},\mathbf{p}) = \frac{1}{2m}[p_x^2 + p_y^2 + p_z^2] + \frac{m}{2}[\omega_x^2 x^2 + \omega_y^2 y^2 + \omega_z^2 z^2], \tag{5.7}$$

with density of states

$$g(\epsilon) = \frac{\epsilon}{2(\hbar\bar{\omega})^3}. \tag{5.8}$$

Here, $\bar{\omega}$ is the mean oscillation frequency of the harmonic trap. For a Fermi gas, the statistics are described by the Fermi-Dirac distribution

$$f(\epsilon) = \frac{1}{e^{\beta(\epsilon-\mu)}+1}, \tag{5.9}$$

where $\beta = (k_B T)^{-1}$, and $\mu = \mu(T,N)$ is the chemical potential of the gas which is normalized by the atom number in each spin state as

$$N = \int g(\epsilon) f(\epsilon)\, d\epsilon. \tag{5.10}$$

Direct integration of the above equation at $T = 0$ defines the Fermi energy $E_F = \mu(T = 0, N)$, which simplifies in a harmonic trap to

$$E_F = k_B T_F = (6N)^{1/3}\hbar\bar{\omega}. \tag{5.11}$$

The Fermi-Dirac occupation factor for a zero-temperature gas is unity for energies below this value and zero otherwise. The Fermi energy therefore defines the energy and temperature scales over which quantum statistics significantly affect the physics of the system. Comparison of the temperature of the cloud to the Fermi-temperature T_F is an indicator of the degeneracy of the Fermi gas, which relates to the peak phase-space density as $\rho_0 = n_0\lambda_{dB}^3 = (T/T_F)^{-3}/6$ [27].

The density distribution functions in position and momentum space for harmonically trapped Fermi gases have been calculated in multiple publications [169, 11, 28, 50] using standard statistical mechanics techniques and assuming a semi-

classical (Thomas-Fermi) approximation [195], applicable in the large N limit when many oscillator states are occupied. The 2D density and momentum distributions for harmonically trapped Fermi gases are given by [11]

$$n(x,y) = \frac{N}{b_x b_y \pi} \frac{Li_2\left[e^{\frac{U_0-\mu}{k_B T}} e^{-\left(\frac{x^2}{b_x^2}+\frac{y^2}{b_y^2}\right)}\right]}{Li_3\left[e^{\frac{U_0-\mu}{k_B T}}\right]}, \tag{5.12}$$

$$n(p_x,p_y) = \frac{N}{(2mk_BT)\pi} \frac{Li_2\left[e^{\frac{U_0-\mu}{k_B T}} e^{-\frac{p_x^2+p_y^2}{2mk_BT}}\right]}{Li_3\left[e^{\frac{U_0-\mu}{k_B T}}\right]}, \tag{5.13}$$

where the width coefficients b_i are related to the 1/e-widths (a_i) of the trapping potential of depth U_0 as $b_i = a_i\sqrt{k_BT/U_0}$ and $Li_n[z]$ are *Poly-Logarithmic* functions defined as $Li_n[z] = \sum_{k=1}^{\infty} \frac{z^k}{k^n}$. These Poly-Log functions appear often in the analysis of harmonically trapped Fermi gases. The two-dimensional distributions were given here for comparison with the 2D density distributions that we measure using absorption imaging techniques.

5.3.2 Thermometry in a Classical Gas

In the classical limit ($T \gg T_F$), the statistics of the gas are described by a Maxwell-Boltzmann distribution. In this case, the above equations for the density and momentum distributions simplify to a Gaussian form as

$$n(x,y) = \frac{N}{b_x b_y \pi} e^{-\left(\frac{x^2}{b_x^2}+\frac{y^2}{b_y^2}\right)}, \tag{5.14}$$

$$n(p_x,p_y) = \frac{N}{(2mk_BT)\pi} e^{-\frac{p_x^2+p_y^2}{2mk_BT}}, \tag{5.15}$$

where the widths (b_x and b_y) are dependent on the temperature (T) of the gas and the properties of the harmonic trap. In momentum space, the dependence on the trap parameters drop out and the Gaussian distribution is fully characterized by the atomic mass (m) and the temperature T.

To measure the temperature of the gas, we often use a method that involves releasing the atoms from the trap, and allowing the gas to freely expand for a

time-of-flight (τ). After release, the atoms will expand ballistically (assuming that the gas is not in the strongly-interacting hydrodynamic regime) so that their coordinates evolve according to

$$x = x_0 + v_x\tau = x_0 + \frac{p_x}{m}\tau, \tag{5.16}$$

where v_x (p_x) is the x-component of the atoms velocity (momentum), and similarly for the y component. After rescaling the 2D density distribution in Equation 5.14 to account for the ballistic expansion of the gas [11], referred to as *ballistic scaling*, the atomic density distribution for a classical gas after a time-of-flight is given by

$$n(x, y, \tau) = \frac{N}{c_x c_y \pi} e^{-\left(\frac{x^2}{c_x^2} + \frac{y^2}{c_y^2}\right)}, \tag{5.17}$$

where the width of the Gaussian distribution in the x direction now scales as

$$c_x = b_x\sqrt{1 + \frac{2k_B T}{m b_x^2}\tau^2} = b_x\sqrt{1 + \omega_x^2\tau^2}, \tag{5.18}$$

and similarly for the y direction. Here, ω_x is the initial trapping frequency in the $\hat{x}$ direction. For expansion times $\omega\tau \gg 1$, the trapping parameters in b_x drop out of the analysis and the temperature of the gas can be directly extracted from the Gaussian width of the expanded gas. In our system, thorough calibration of our trapping frequencies allows us to use both *in situ* imaging and time-of-flight imaging to measure the temperatures of the gas. The temperature conversions from the Gaussian width of the density profiles are given by

$$T = mc_x^2/(2k_B\tau^2), \qquad \tau \gg 1/\omega_x \tag{5.19}$$

$$T = m\omega_x^2 c_x^2/(2k_B), \qquad \tau = 0 \tag{5.20}$$

The density distributions of our gases, measured by the absorption imaging techniques discussed in Section 4.7, are fit using a 2D Gaussian fitting routine that extracts the peak density (n_0) and width (c_i) of the gas along both the $\hat{x}$ and $\hat{y}$ axes. This provides us with a check of the quality of the fit and the magnitude of perturbing forces during expansion, since the initial temperature of our thermalized

gases should be uniform in all directions. These techniques to extract the thermal properties of our classical gases have also proven useful for precision thermometry of multi-component Fermi gases in the degenerate regime. Here, we use an impurity-state thermometry technique, described in the next section, which was developed in D. Jin's Lab at JILA [27].

5.3.3 Impurity-State Thermometry

Impurity-state thermometry is a robust technique for measuring the degeneracy of multi-component Fermi gases, and is particularly well suited for probing moderately degenerate samples ($0.2 \leq T/T_F \leq 0.5$). The technique, which was first described in C. Regal's Ph.D. thesis [27], uses the facts that interactions among atoms in distinct spin states can be used to bring the various spin components of a Fermi gas into thermal equilibrium and that the Fermi energy of each component scales with the atom number in the given spin state as $E_F \propto N^{1/3}$. Therefore, if the atom number in one of the spin components is smaller, its Fermi energy is correspondingly reduced while its temperature remains consistent with that of the rest of the gas.

For a sufficiently small population in the minority spin component, the atoms in this state can in fact remain non-degenerate even when in thermal contact with multiple degenerate components, allowing for a simple Gaussian fit after a time-of-flight to deduce the temperature of gas. Subsequent measurements of the number of atoms in the degenerate components and knowledge of the parameters of the harmonic trap are all of the information required to deduce their Fermi energies and hence the degeneracy of each component in the gas. The basis of this scheme is illustrated in Figure 5.4. Here, a harmonically trapped degenerate two-component sample is in thermal equilibrium with a third minority component. The occupation of the energy states in the harmonic trap, shown on the right, demonstrates that the difference of the Fermi energies of the components ($E_{Fermi}(N_i)$) requires that the minority component be less degenerate to maintain thermal equilibrium.

As an example, consider that we cool a two-component Fermi gas of ^{6}Li atoms in states $|1\rangle$ and $|2\rangle$ with $N = 10^5$ atoms in each spin state to an absolute temperature of 180 nK, with a reduced temperature $T/T_F = 0.3$. If we now transfer a small

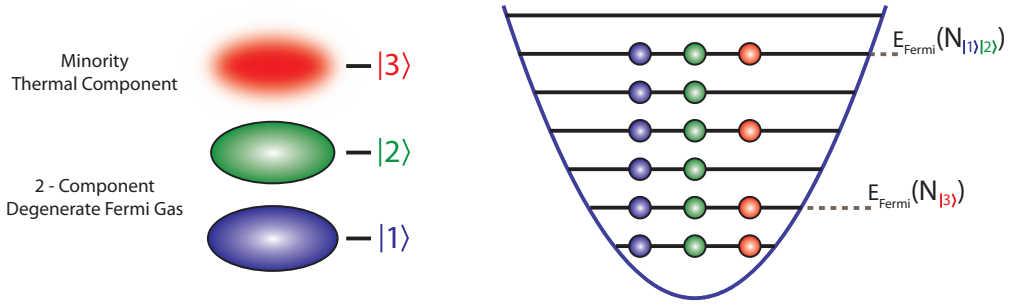

Figure 5.4. (Left) Impurity-state thermometry is a method of measuring the degeneracy of a harmonically trapped Fermi gas using a classical minority component (state $|3\rangle$ in this example), in equilibrium with the degenerate majority components (states $|1\rangle$ and $|2\rangle$ here). (Right) The reduced Fermi energy of the minority component ($\mathrm{E_{Fermi}(N_{|3\rangle})}$) combined with thermal equilibrium of the gas enables this robust thermometry technique.

amount of the population from state $|2\rangle$ to state $|3\rangle$ using a short on-resonant RF pulse, say $N' = 2 \times 10^4$, the reduced temperature of the state $|3\rangle$ atoms is increased to $T/T'_F = 0.51$. Here, a thermal analysis of the 2D density distribution is appropriate since the effects of degeneracy are negligible at these temperatures.

This thermometry method is a natural choice for our experiments at high fields, where we regularly populate these three components during the procedure. We can directly use this technique to determine the degeneracy of a two-component gas before populating the third state. Additionally, we can determine the degeneracy of a three-component gas after a variable hold time using this technique. To make this measurement, we initially create a three-component gas and hold the sample for a set time. Then, one of the spin components is removed by applying an on-resonance light pulse, which is resolved at high fields and negligibly perturbs the atoms in the other components. Finally, impurity-state thermometry is preformed by re-populating a small third component and allowing the system to come into thermal equilibrium. The technique outlined here was directly applied to demonstrate the realization of a degenerate three-component Fermi gas in the high-field SU(3) symmetric regime, as described in Section 7.2.2.

As with all thermometry methods, there are certain limitations to this technique. First, the method can only be applied if the three-state mixture is sufficiently long lived. Three-body decay itself reduces the degeneracy of the gas, reducing both the number of atoms per spin-state and possibly preferentially removing atoms from the coldest/densest regions of the gas, a phenomena referred

to as *anti-evaporative heating*. In general, we prepare our samples such that they are sufficiently long-lived to allow the system to decohere and come into thermal equilibrium while heating from three-body loss is minimal. It is also possible to remove one of the two majority components, measuring the temperature of a single spin component with the minority component, which is now effectively immune to three-body loss. Further, the gas should be weakly interacting because the effects of interactions are neglected in the analysis. These requirements are both met by either measuring the temperature in the region of the "zero-crossings" of the scattering lengths, near 550 Gauss, or by preparing highly dilute samples so that the ratio of the scattering lengths to the mean free path is small. Finally, the degeneracy of the original sample must not be strong to allow for sufficient number of atoms in the minority component for reasonable Gaussian fits of the thermal 2D density distributions.

In general, our atoms are prepared in a highly-dilute gas which is amenable to this thermometry technique. Further, our preparation scheme limits the minimum achievable temperatures to $T_{min} \sim 0.15 T_F$. Due to the generally short lifetimes of a three-component gas in the presence of strong interactions, we first cool a two-component gas and then populate the third component at the field of interest using noisy RF pulses. Therefore, the final three-component sample, with conserved energy but reduced Fermi energy, has a larger reduced temperature T/T_F by at least a factor of $N_2^{1/3}/N_3^{1/3}$. In the following, I will discuss in more detail how we load atoms into our large-volume traps to achieve extremely low temperatures and densities, allowing us to study multi-component Fermi gases in the presence of large three-body loss.

5.4 Low-Temperature/Density Atomic Gases

In Section 3.4, we discussed the temperature requirements for analyzing three-body loss data using the rates calculated at threshold. Our recent experiments were dedicated to measuring the three-body loss rates of our three-component Fermi gases in the range of magnetic fields between $834 \leq B \leq 1500$ Gauss. At these fields, slightly above the $|1\rangle - |2\rangle$ Feshbach resonance, the scattering lengths are very large ($|a| > 34\ l_{vdw}$) and negative, requiring extremely low temperature samples to

avoid unitarity limitations and thermal averaging effects on our measured rates.

Consider the three-component gas at fields above 1500 Gauss, where the scattering lengths nearly converge to $-2140a_0$. At these field, the critical temperature limit, calculated from the height of the barrier in the adiabatic three-body potential given by Equation 3.45, is $T_c = 0.158\ \hbar^2/(k_B m a^2) \simeq 1\ \mu$K. Further, the maximum three-body loss rate measurable for a gas at a temperature T, attributed to unitarity and thermal averaging, is given by K_3^{max} defined in Equation 3.47. For our ^{6}Li gases at the critical temperature, $K_3^{max}(T_c) = 7 \times 10^{-21}$ cm^6/s. The measured rates at these fields can therefore only be compared with those calculated at threshold if both the temperature of the gas and the measured three-body loss rates are significantly less than T_c and K_3^{max} respectively. In our primary trap, we regularly produce nearly-degenerate multi-component Fermi gases at temperatures on the order of $T \simeq 2\ \mu$K, which is slightly above the temperature at which thermal effects begin to significantly affect the measured loss rates.

At lower fields, in the vicinity of the Feshbach resonances, the temperature requirements can be much stricter. Consider now that the three-component gas is prepared at 875 Gauss, where the largest scattering length is $a_{12} = -12,250a_0$. Here, the critical temperature and maximum three-body decay rate are $T_c \simeq 30\ n$K and $K_3^{max}(T_c) = 7 \times 10^{-18}$ cm^6/s respectively. In the primary trap, it is currently not possible to cool a sufficient number of free fermions to such low temperatures to preform our stability measurements. Additional difficulties arise in studying such large three-body loss in our system stemming from the relatively large peak densities of our samples n_0. Since the loss rates are expected to scale as a^4 near the Feshbach resonances, a three-component sample is expected to decay rapidly at these fields in the high-density primary trap.

Considering reasonable values for our trapping parameters to hypothetically cool mixtures of free fermions with $N \sim 10^5$ atoms per spin state at a temperature of even $T = 50$ nK at this field value, the $1/e$ lifetime of the gas in a three-state mixture is found to be $\tau \leq 10$ ms for densities per spin state $n_0 \geq 10^{11}/\text{cm}^3$ and three-body loss rates $K_3 > 10^{-20}$ cm^6/s. The lifetime of the gas is therefore quite short as compared to the 100 ms duration noisy RF stage we use to create an incoherent three-state mixture in thermal equilibrium. For this reason, the primary trap was insufficient for measurements of K_3 throughout the high-field regime. We

overcame this limitation by adiabatically loading the atoms from the primary trap into one of the large-volume traps, discussed in section 4.6.5 and illustrated in Figure 5.5. In this way, the temperatures and densities of the samples are reduced by orders of magnitude, enabling the production of the three-state mixtures for our high-field recombination rate measurements.

Adiabatically changing the depth and volume of the harmonic trapping potential to vary the thermal and collisional properties of trapped atoms has played a crucial role in experiments with ultracold atomic gases. This technique has been used to increase the collision rates among particles to assist in evaporative cooling to degeneracy [196, 197], and achieve world-record breaking low temperature gases [41]. In these experiments, the volume and/or depth of the trapping potential is dynamically adjusted to alter the density and temperature of the gas. So long as the adiabaticity requirement is satisfied $d\omega_{trap}/dt \ll \omega_{trap}^2$, defining the rate at which the trapping frequencies ω_{trap} should be varied to avoid non-adiabatic transitions among vibrational states, and the shape of the potential (form of the density of states) is maintained, the phase-space density remains constant. In this case, the evolution of the temperature and density distribution for a thermal gas in an adiabatically varying harmonic trap can be determined from simple scaling laws.

We are changing both the waist and power of the lasers providing the harmonic trapping potentials as the trap is adiabatically transformed. For this analysis, it is assumed that the adiabatic theorem applies [97], which states that a physical system will remain in its instantaneous eigenstate if the perturbation is acting on the system sufficiently slowly and if there is a sufficient gap between the eigenvalue of the system and the rest of the Hamiltonian's spectrum. For our harmonically trapped gases, the eigenstates are characterized by the harmonic trapping frequencies ω which, according to Equations 4.18, are proportional to the power P and waist w of the optical trapping beams as $\omega \propto \sqrt{P}/w^2$. Adiabatic changes of the waist and power of the beams leads to the temperature scaling as $T \propto \omega \propto \sqrt{P}/w^2$. So long as the trap remains harmonic, adiabatic changes conserve the phase-space density $\rho_0 \propto n_0 T^{-3/2}$, where n_0 is the peak 3D density distribution of the gas. Therefore, as the trap is adiabatically varied, the peak density transforms as $n_0 \propto T^{3/2} \propto P^{3/4}/w^3$. Further, the collision rate and three-

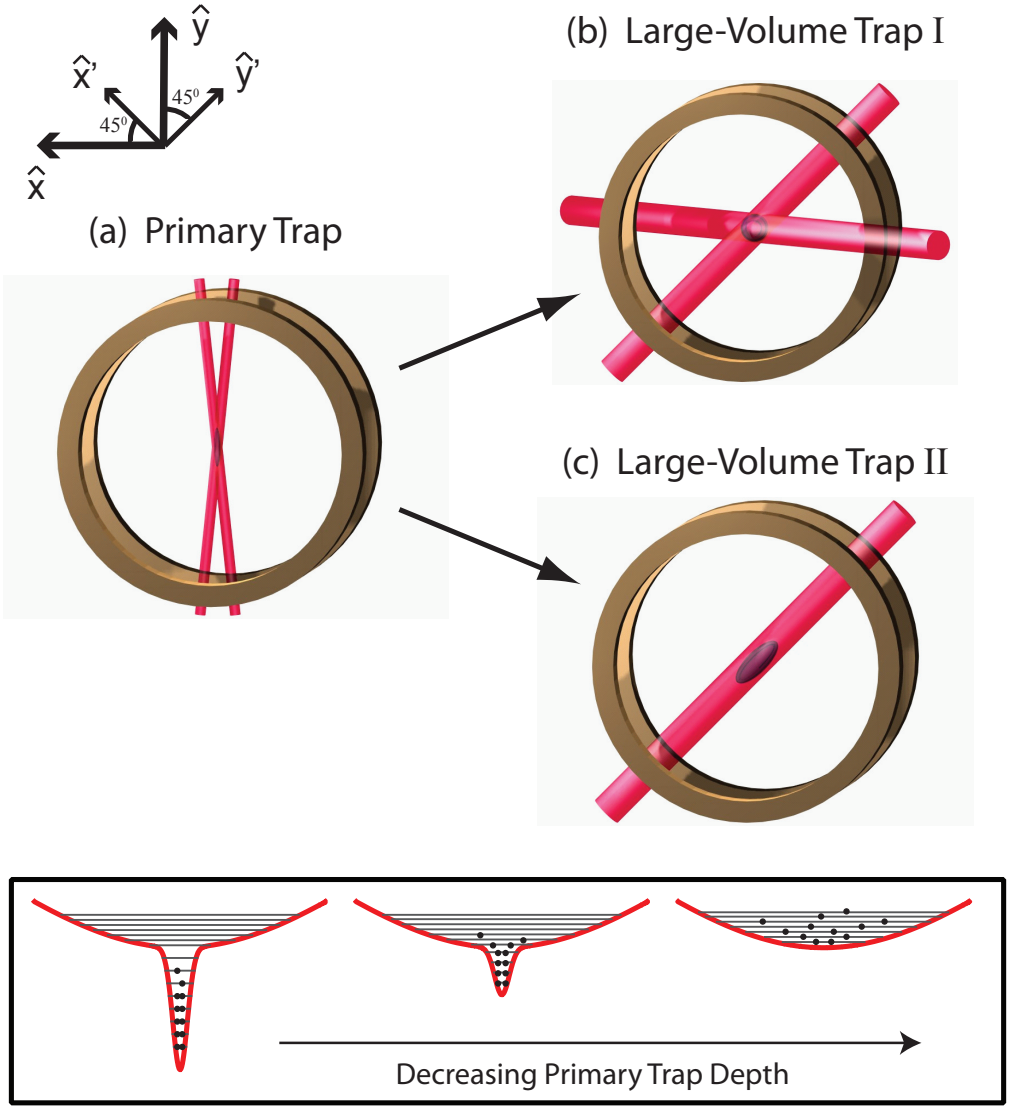

Figure 5.5. (Top) Nearly degenerate two-component ^{6}Li gases cooled in the primary dipole trap are loaded into our large-volume trap I (II) enabling us to prepare three-component samples at temperatures $T_I \leq 180$ nk ($T_I \leq 30$ nk) and densities $n_{0(I)} \simeq 5\times10^{10}$ atoms/cm^3 ($n_{0(II)} \simeq 5\times10^{9}$ atoms/cm^3). (Bottom) As the depth of the primary trap is adiabatically lowered in the presence of one of the large-volume traps, the atoms begin to occupy the lowest energy states of the large-volume trap, with greatly reduced average energy per particle and enhanced trap volume.

body recombination rates scale as $\Gamma \propto n_0 T^{1/2} \propto P^{5/4}/w^5$ and $\dot{n} \propto n^3 \propto P^{9/4}/w^9$ respectively. Therefore, by loading the atoms from the primary trap into one of the large-volume traps, it is possible to significantly decrease the temperature, density, and decay rates of our atoms to observe the properties of the gas in the presence of large three-body loss. This analysis is likely an oversimplification as it is not guaranteed that the form of the density of states is conserved when both traps are present, as illustrated by the possible variation of the vibrational energy levels in the bottom panel of Figure 5.5. No observable deviation of the reduced temperature T/T_F was observed, however, for atoms loaded into either of our large-volume traps, suggesting that the deviations of the trap profile from harmonic was negligible throughout the loading process.

In our experiments measuring the three-body loss rates at high fields, we used two different trapping geometries for the large volume trap, illustrated in panels (b) and (c) of Figure 5.5. In the first geometry (large-volume trap I), the trap is derived from the confining potential provided by the large-volume trapping beams (A) and (B), with a minor correction attributed to the confining (anti-confining) magnetic field gradients from the primary and booster magnetic coils along the $\hat{x}$ and $\hat{y}$ ($\hat{z}$) axes. The design of these trapping beams and gradient fields are discussed in detail in Sections 4.6.5 and 4.3.4 respectively. The maximum power used in each beam (A) and (B) was nominally on the order of 20 Watts during the experiment, yielding a peak depth of $U_0 \simeq 1$ μK and trapping frequencies $\omega_x = 2\pi \times 33\sqrt{1 + 1.4 \times 10^{-3}(B - 842\ G)}$Hz $\pm$ 3%, $\omega_y = 2\pi \times 21\sqrt{1 + 3.6 \times 10^{-3}(B - 842\ G)}$Hz $\pm$ 3%, and $\omega_z = 2\pi \times 94(2)$Hz. The magnetic field dependence (B) of the trapping frequencies is due to the field curvature of the booster coils, which were applied in some of our high-field data runs to supplemented the fields from the primary coils for values above 842 G.

For the second geometry (large-volume trap II), the trap is derived from the combined potentials provided by the large-volume trapping beam (C) and the magnetic field gradients from the primary magnetic coils. For this geometry, the beam was effectively collimated at the atoms, where the large waist of the confining beam ($w = 2.5$ mm) lead to negligible confinement along the axis of the beam. Confinement along the $\hat{y}'$ axis, defined to be parallel to the axis of the beam, was therefore solely provided by the harmonic gradient field from the primary coils, as

illustrated in Figure 4.9 (a). The maximum power used in beam (C) was nominally on the order of 40 Watts for this experiment, yielding a peak depth of $U_0 \simeq 10\ \mu$K and trapping frequencies $\omega_x = 2\pi \times 15(2)$Hz, $\omega_y = 2\pi \times 0.242\sqrt{B}$Hz $\pm\ 1\%$, and $\omega_z = 2\pi \times 12(1)$Hz. This trap was used to measure the three-body rate constants K_3 over a narrow range of fields (840 G $\leq B \leq$ 960 G) near the 834 G Feshbach resonance, where the loss rates of the three-component gas are orders of magnitude larger than the unitarity limited rates in the primary trap (see Section 7.2.1).

Adiabatic loading of the atoms from the primary trap into one of the large-volume potentials is illustrated in the bottom panel of Figure 5.5. As the power of the primary trapping beams is adiabatically reduced, the temperature and density of the atoms evolve to maintain the occupation distribution of the energy states (represented as grey lines in this figure). At the end of the adiabatic transfer, the atoms in the large-volume trap I (trap II) were regularly prepared in incoherent three-state mixtures at temperatures $T_I \leq 180$ nK ($T_{II} \leq 30$ nK) and initial peak densities per spin state $n_{0(I)} \simeq 5{\times}10^{10}$ atoms/cm^3 ($n_{0(II)} \simeq 5{\times}10^{9}$ atoms/cm^3). As discussed above, these temperatures and densities are sufficiently small to assure that our measurements of K_3 could be compared with zero-temperature calculations of the three-body loss rates for fields above $\simeq 875$ G.

We will show in the next few chapters how the three body parameters of our three-component gases are calculated from our three-body loss measurements. These measurements were taken both at low-fields (0 G $\leq B \leq$ 600 G) and in the high-field regime (834 G $\leq B \leq$ 1500 G). The extracted three-body parameters in these two non-universally connected regimes can, in turn, be used in conjunction with the universal theory for interacting three-body systems, discussed in Chapter 3, to predict the magnetic-field dependent stability of the gas and the spectrum of Efimov trimer states in all of the field regions where the pairwise scattering lengths are resonantly enhanced. The high field results are particularly relevant for future experiments studying many-body physics in three-component Fermi gases at fields spanning the three overlapping Feshbach resonances and in the asymptotic regime at which the particles exhibit SU(3) symmetric interactions.

Chapter 6

Experimental Findings with 3-Component Fermi Gases

In this chapter our initial experimental investigations of ultracold fermionic ^{6}Li gases occupying three mutually interacting hyperfine spin states are described. Previous to the work done by our group [144, 147] and that of S. Jochim's group in Heidelberg [145, 5, 198], a third state was utilized in both ^{40}K and ^{6}Li Fermi gases, but only as a probe for thermometry [27] and as a final state for radio frequency spectroscopy of the two-component samples [192, 115, 64]. In RF spectroscopy experiments preformed with strongly interacting ^{6}Li samples, it was found that rapid decay of atoms in the third state prohibited their detection. This rate was later measured on the $|1\rangle - |3\rangle$ Feshbach resonance at 691 Gauss to be on the order of 30 ms [28]. Such rapid inelastic decay prevents the production of three-component samples in equilibrium unless the sample is made to be very weakly interacting. Our experiments were therefore dedicated to exploring the stability of a three-component Fermi gas in thermal equilibrium over a range of interaction strengths to determine the universal few-body physics of a system of distinguishable particles with mutually enhanced pairwise interactions as well as to determine the feasibility of using this multi-component gas to study novel many-body phenomena, discussed in more detail in Chapter 7.

Our first experiments measured the collisional stability of the three-component gas and went on to measure the three-body decay rate constant over the range of fields (15 G $< B <$ 960 G). At low fields (15 G $< B <$ 527 G), all three s-wave

scattering lengths are negative and generally unequal. This region is universally disconnected from the three overlapping Feshbach resonances at higher fields due to a zero-crossing of the scattering lengths at $a_{12} \simeq 528$ G, $a_{13} \simeq 568$ G, and $a_{23} \simeq 589$ G respectively. Both regions of high stability, where the gas at reasonable densities can survive for 10s of seconds, and resonant loss peaks are observed in the low-field data. Theoretical calculations of the three-body loss rates in the low-field region found that the resonant loss peaks are associated with a ground-state Efimov trimer crossing the free-atom threshold. Recent analytic interpretations of the low-field three-body loss rates are discussed in greater detail at the end of the chapter.

6.1 Stability of 3-Component ^{6}Li Gases

Our first experiments measured the stability of our three-component gas to three-body decay. This heating and loss mechanism ultimately determines the maximum density and degeneracy of our samples, and hence the range of phenomena that we can study with our three-component gases. Although we measured the stability of the gas for magnetic fields ranging from 15 to 953 Gauss, the data above $\sim$ 600 Gauss is suspect as the measured decay may include loss events associated with two-state mixtures. Further, much of this high-field data was likely unitarity limited at the time. We therefore will focus on discussing the stability of the gas in the low-field region ($0 \leq B \leq 600$ G), where the decay can be attributed to three-body events consisting of one atom from each spin state and the loss rates are sufficiently low to assure that the interactions are in the threshold regime.

6.1.1 State Preparation

For this experiment, two-state mixtures of ^{6}Li atoms were initially evaporatively cooled in the primary dipole trap nearly to degeneracy as described in Chapter 5. Forced evaporation of the atoms occurred at a field of 330 Gauss, where $a_{12} \simeq -280a_0$. This field was chosen so that the atoms were relatively strongly interacting for efficient evaporation while assuring that the final sample consisted of free atoms. This is in contrast to evaporating near the Feshbach resonance at 834 Gauss, where the interactions can be enhanced to the unitarity limit for highly efficient

evaporation but the formation of weakly-bound molecular states, as the field is ramped below the Feshbach resonance, is unavoidable at low temperatures. The molecules associated with the a_{12} Feshbach resonance, which are weakly-bound and stable at high fields, are rapidly lost when the magnetic field is reduced to the non-universal regime because the molecules become strongly bound and the stabilizing effects discussed in Section 5.1.1 no longer apply.

This experiment was conducted before the levitation and translation bars were installed, requiring a relatively tight trap to support the atoms against gravity. After the atoms were evaporatively cooled nearly to degeneracy in the primary trap, its depth (U_0) was adiabatically increased by a factor of 4 to stabilize the gas and suppress further evaporative loss. Adiabatic recompression increased the ratio of U_0/k_BT by a factor of $\simeq 2$, but left the phase-space density unchanged. The final oscillation frequencies of the primary trap were $\omega_x = 2\pi \times 3.84$ kHz, $\omega_y = 2\pi \times 106$ Hz, and $\omega_z = 2\pi \times 965$ Hz, determined by dipole oscillation and parametric heating techniques, with a final depth per beam $U_0 \simeq 40$ μK. At this point, the total number of atoms $N \simeq 3.6 \times 10^5$ occupied a balanced two-state mixture at a temperature of $T \simeq 1.9\mu$K. The final reduced temperature $T/T_F \simeq 0.51$, is sufficiently high so that it is appropriate to treat the cloud as a thermal gas.

To create the incoherent three-state mixture, we first increase the strength of the magnetic field over 10 ms to 568 Gauss. This field is near the zero-crossing for all three scattering lengths, as shown in Figure 6.1 (b), where $a_{12} \simeq 168a_0$, $a_{23} \simeq -105a_0$, and $a_{13} \simeq 7a_0$. Here, three-body recombination is minimized but the interactions are still sufficiently strong to allow for rethermalization of the gas within ~ 20 milliseconds. We then apply a 50 ms noisy RF pulse with frequencies centered on the $|1\rangle \leftrightarrow |2\rangle$ and $|2\rangle \leftrightarrow |3\rangle$ transitions at this field, each broadened to a width of 1 MHz. The addition of a $\simeq 1$ G/cm magnetic field gradient along the $\hat{z}$ axis is provided by an imbalance of the current in the primary magnetic coils to destroy any internal state coherence in the samples. At the end of the RF pules, the sample is held for an additional 20 ms to allow the atoms to come into thermal equilibrium. The final sample consists of a balanced three-state mixture with $N \simeq 1.2 \times 10^5$ atoms in each of the high-field seeking Zeeman states. At this point, $T \simeq 1.9$ μK with a reduced temperature of $T/T_F \simeq 0.6$ and a peak density

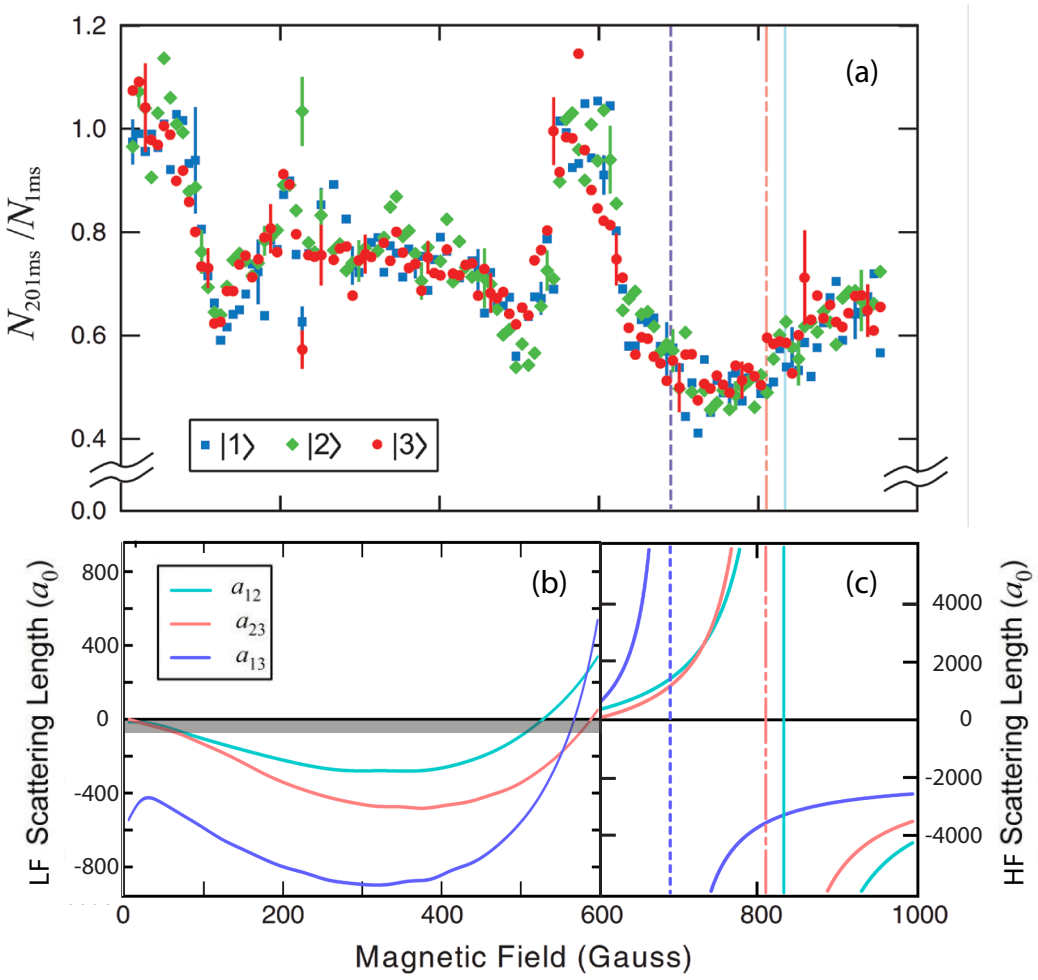

Figure 6.1. (a) Fraction of atoms remaining in each of the three spin states after a 201 ms hold time at the field of interest B_{hold}. The data is normalized to the number remaining after spending 1 ms at B_{hold}. (b) & (c) The low-field ($0 \leq B \leq 600$ G) & high-field (600 G $\leq B \leq$ 1000 G) s-wave scattering length for ^{6}Li atoms in states $|1\rangle$, $|2\rangle$, and $|3\rangle$. The scale of (b) is reduced by a factor of 6 with respect to (c), highlighting the features near zero which include the zero-crossings of the LF scattering lengths at 0 G and between 528 and 589 G. The grey region in Figure (b) represents the extent of the van der Waals length scale l_{vdw}. The purple, pink, and cyan vertical lines represent the locations of the $|1\rangle$-$|3\rangle$, $|2\rangle$-$|3\rangle$, and $|1\rangle$-$|2\rangle$ Feshbach resonances respectively.

$n_0 \simeq 5.5 \times 10^{12}$ atoms/cm^3.

6.1.2 Collisional Stability Measurement

To gain qualitative insight into the magnetic field dependence of the decay of the three-component ^{6}Li Fermi gas, we measured the fraction of the atoms in each spin state lost from the trap after being held at a particular field of interest (15 G $\leq B_{hold} \leq$ 960 G) for 200 ms. For each experimental cycle, the magnetic field was ramped from 568 G, at which the mixture was prepared, to the field of interest in 10 ms. The mixture was held constant at B_{hold} for either 1 or 201 ms, followed by a 10 ms field ramp to 953 Gauss. After an additional 20 ms hold time to allow the fields to fully stabilize, spectroscopically resolved absorption imaging was used to determine the number of atoms in a given spin state for the two hold times ($N_{1\text{ms}}$ or $N_{201\text{ms}}$). The 10 ms field ramp to 953 Gauss (where a_{12}, a_{23}, $a_{13} < 0$) ensured that any atoms which had formed weakly bound Feshbach molecules and remained trapped would be dissociated and measured. For each field value, $N_{201\text{ms}}$ is normalized by $N_{1\text{ms}}$ to correct for the fraction of atoms lost during the field sweeps, both to and from the field of interest. The raw data $N_{1\text{ms}}$ and $N_{201\text{ms}}$ for each state is presented in Appendix B, Figure B.1.

The normalized data displaying the magnetic field dependence of the fraction of atoms lost in a three-state mixture of atoms occupying states $|1\rangle$ (blue squares), $|2\rangle$ (green diamonds), and $|3\rangle$ (red circles) after a hold time of 200 ms is shown in Figure 6.1(a). The purple, pink, and cyan vertical dashed lines represent the locations of the $|1\rangle$-$|3\rangle$, $|2\rangle$-$|3\rangle$, and $|1\rangle$-$|2\rangle$ Feshbach resonances respectively. The representative error bars indicate the standard deviation in the mean, which remained relatively consistent for all of the data. During the experimental runs, the field of interest was randomly varied for each shot, and the RF and imaging frequencies were recalibrated multiple times throughout the experiment to minimize systematic errors.

To determine the influence of two- and three-body loss processes among atoms occupying only two spin states to the measurements described above, we repeated the experiment with all possible binary mixtures. For this data, the three-state mixture was first prepared as described previously. Before the field was ramped to the field of interest, however, one of the three components was removed with a resonant light pulse. Again, we make use of the fact that the Zeeman energy splitting between the states is on the order of 80 MHz at our preparation field of

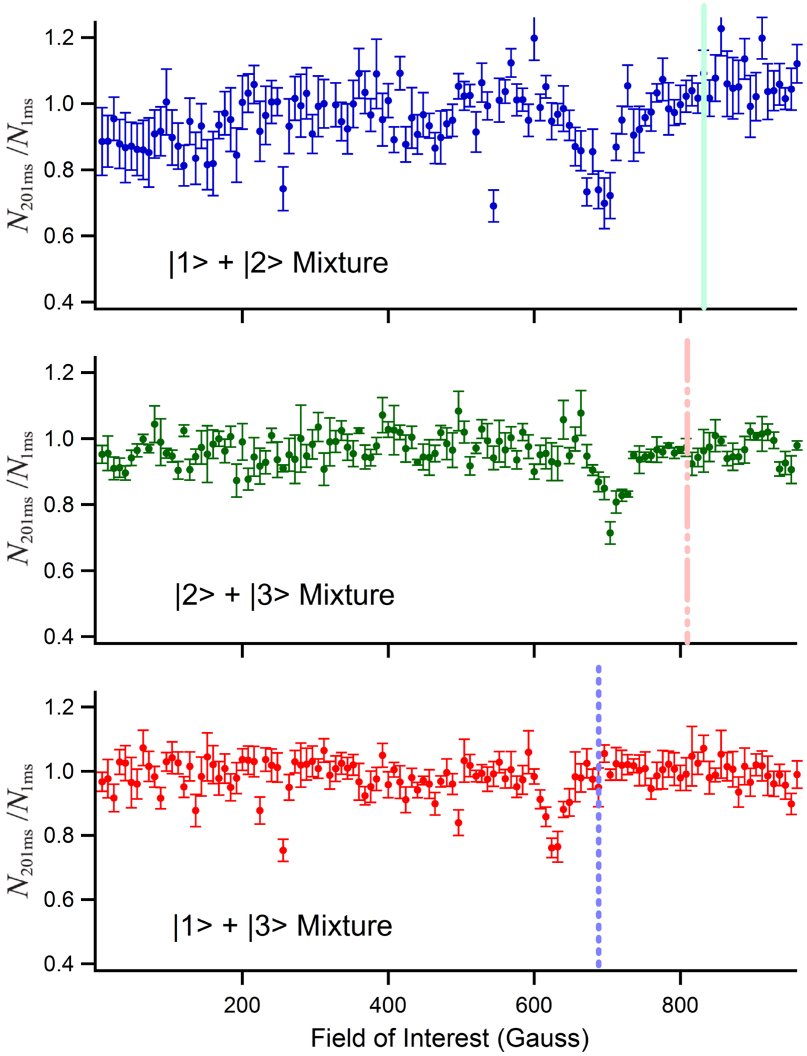

Figure 6.2. The fractional population remaining $N_{201\text{ms}}/N_{1\text{ms}}$ with respect to the field of interest for each binary mixture. Atoms in state $|1\rangle$ (blue) of a $|1\rangle$-$|2\rangle$ mixture, state $|2\rangle$ (green) of a $|2\rangle$-$|3\rangle$ mixture and state $|3\rangle$ (red) of a $|1\rangle$-$|3\rangle$ mixture are shown. The cyan, pink, and purple vertical lines represent the locations of the a_{12}, a_{23}, and a_{13} Feshbach resonances respectively.

568 G to selectively heat the atoms in one of the spin states out of the trap in a sufficiently short time $\sim 100\mu$s that the light pulse leaves the other two states effectively unperturbed. The ratio of atoms remaining after evolution times of 201 and 1 ms at the various fields of interest was then measured in an identical manner as described above.

Figure 6.2 shows the ratio $N_{201\text{ms}}/N_{1\text{ms}}$ for atoms in state $|1\rangle$ (blue) of a $|1\rangle$-

$|2\rangle$ mixture, state $|2\rangle$ (green) of a $|2\rangle$-$|3\rangle$ mixture, and state $|3\rangle$ (red) of a $|1\rangle$-$|3\rangle$ mixture respectively. We have checked the populations of the states not shown for each of the pairs over a number of points to assure that no state selective loss occurs in any of the binary mixtures. With the exception of the loss features between 600 and 750 G, each of the two-state mixtures was found to be stable. The loss features observed are attributed to three-body recombination to the weakly-bound Feshbach molecular states. Since the two-state mixtures are stable for fields $B \leq 600$ G and $B \geq 750$ G, with lifetimes limited only by heating from off-resonant light scattering from the trapping beams and one-body loss from background gas collisions, excess loss in the three state mixtures at these fields are due to three-body events involving one atom from each spin state.

In Figure 6.1(a), the dominant loss feature centered at 720 G occurs in the vicinity of the three overlapping interspecies Feshbach resonances. Significant loss due to three-body recombination is expected in this region since recombination events including one atom from each spin state are not suppresses by the exclusion principle and a significant increase in the event rate is expected when two or more scattering lengths are resonantly enhanced. When all three scattering lengths are much larger than the characteristic length scale l_{vdw}, the rates are expected to scale in some manner with the magnitude of the scattering lengths, analogous to the a^4 scaling in identical Bosonic systems (see Section 3.2).

Similarly, the high stability near zero-field and in the vicinity of the zero crossings of the Feshbach resonance, around 560 Gauss, is not surprising. Near zero field, at least two of the scattering lengths are small as compared to l_{vdw}. In this case, the system effectively consists of an interacting two-component gas, which is stable, and a "spectator" Fermi gas consisting of the third component. Near the zero-crossings, at least one of the pairwise scattering lengths was generally small. Here, three distinguishable particles can still strongly interact since the third particle acts as a mediator for the weakly interacting pair. However, all three scattering lengths are also minimized near the zero-crossings, leading to high stability against three-body loss. It is difficult to interpret the high-field data ($B \geq 600$ G) in this experiment due to the influence of three-body loss to the Feshbach molecular states and the fact that the three-body loss rates were likely unitarity limited throughout this range at the time. The general trends of highest loss near the Feshbach

resonances, high stability near the zero-crossings of the scattering lengths, and the stability of all binary mixtures for fields away from the resonance locations provides a nice quality check of the general trends of the magnetic field dependent three-body loss in the three-state mixture to what was expected based on the magnetic-field dependence of the scattering lengths shown in Figures 6.1(b) and (c).

In the low-field region, unexpected resonant loss features are observed near 127 and 504 Gauss, where the pairwise scattering lengths are not predicted to exhibit any resonances. The narrow loss feature at 127 Gauss, first reported by S. Jochim's group [145], is particularly surprising as all three scattering lengths are quite smooth in this regime with $a_{12} \simeq -140a_0 > 2\ l_{vdw}$, $a_{23} \simeq -187a_0 \sim 3\ l_{vdw}$, and $a_{13} \simeq -660a_0 > 10\ l_{vdw}$. Resonant loss is also clearly evident near 500 Gauss, exhibiting differing loss rates for the three states leading to a population imbalance. At this field, our data is in stark contrast to that published in Reference [145]. They observed no state dependent loss and the resonant feature was less visible in their qualitative data, regardless of the temperature and degeneracy of their gas [190]. We have also observed the 127 and 500 Gauss resonant features and the emergence of population imbalance only near the 500 Gauss feature at higher temperatures ($T = 4\ \mu$K) and in a different trap configuration, as discussed in Appendix B, and shown in Figure B.2. To date, the state-dependent loss mechanism is still a mystery, with possible explanations ranging from fundamental processes in which a three-body event occurs and only one or two of the reaction products are formed with enough energy to exit the trap, to simple systematic errors leading to heating and loss that have not yet been identified in our system.

At 228 Gauss, preferential loss from states $|1\rangle$ and $|3\rangle$, and suppressed loss from state $|2\rangle$ is observed. This feature is likely associated with a $|1\rangle - |3\rangle$ *p-wave* Feshbach resonance near this field. A simple calculation based on the known locations of the p-wave resonances in ^{6}Li (See Table 2.4.1) and the energy tuning of the high-field seeking Zeeman sublevels in a magnetic field [11] suggests that the $|1\rangle - |3\rangle$ p-wave resonance should occur near 223 Gauss. The $|2\rangle - |3\rangle$ and $|3\rangle - |3\rangle$ p-wave resonances are expected to occur at higher fields near 250 G and 283 G respectively. We also observed a very narrow but inconsistent loss feature at 259 G, which is not shown here. Further, the modest increase in stability observed

near 200 G did not appear in our data taken at 4 μK, see Figure B.2.

Figure 6.1(a) provides a qualitative picture of the magnetic-field dependent three-body rates that emerge with the inclusion of a third spin-state to the system. The spectrum of loss features was found to be quite rich in the low-field regime, demonstrating regions of high stability and rapid loss dependent on the magnitude of the three s-wave scattering lengths. We decided to preform a measurement of the field-dependent three-body loss rate coefficients (K_3) to quantify the stability of the gas in this field regime, along with obtaining data that can be compared with theoretical models to determine the physical basis for the anomalous loss features at 127 G and 500 G.

6.2 Measurement of Three-Body Loss

It is difficult to extract quantitative results from our previous measurements because (I) two- and three-body loss occurred during the magnetic field ramps to the field of interest and to the imaging fields, as shown in Appendix B, and (II) the temperature and density of the gas varied for different fields of interest and hold times. It is therefore difficult to apply our measurements to calculate the stability of samples with different temperatures and/or densities. Our second set of experiments measured the three-body loss rate coefficients K_3, restricted to magnetic fields where the decaying populations remained balanced. For these experiments, the magnetic field was swept to the field of interest B_{hold} in 10 ms after creation and thermal equilibrium of the three-state mixture as before. The number $N(t)$ and temperature $T(t)$ of the atoms in state $|3\rangle$ are then measured by absorption imaging at the field of interest B_{hold} for hold times ranging from 2 ms $\leq t \leq$ 4 s. In this way, the atoms are imaged at each of the fields of interest, avoiding the atom loss that may occur in a final B-field sweep, and the thermal evolution of the gas is recorded to be included in the analysis.

From the qualitative data, we saw that for fields $B \leq 600$ G and $B \geq 750$ G, two-body processes were negligible. Therefore, in our analysis we only include trap loss associated with one-body processes (i.e. collisions with background gases and heating from off-resonance light scattering) and three-body processes involving one atom from each spin state (three-body recombination events which lead to

loss of both the atom and molecule from the trap). All of the processes involving multiple atoms in the same spin state are suppressed by Pauli-blocking at these fields, and are therefore excluded from the analysis. Our analysis closely follows the model derived by R. Grimm's group for analyzing the loss rate coefficients of ultracold atomic gases, which considers the time evolution of both the number and temperature of the gas [199, 200].

6.2.1 Three-Body Loss Analysis

The differential equations which describe the one- and three-body loss of our three-component Fermi gas are given by

$$\frac{dn_i(\mathbf{r})}{dt} = -K_3 n_1(\mathbf{r}) n_2(\mathbf{r}) n_3(\mathbf{r}) - K_1 n_i(\mathbf{r}) \tag{6.1}$$

where K_3 (K_1) are the three-body (one-body) recombination rate constants and $n_i(\mathbf{r})$ denotes the density of the atoms in states $|1\rangle$, $|2\rangle$, or $|3\rangle$ for $i = 1, 2, 3$ respectively. In our case, we prepare equal populations in all three states and we are not considering loss at any magnetic fields where two-body loss is appreciable or state-selective decay is present. Therefore, the analysis is simplified because the population and density is equal for atoms in each of the states throughout the experiments ($n_i(\mathbf{r}) = n(\mathbf{r})$).

Our data is given in terms of the total atom number per spin state N and temperature T of the gas. When the three-body recombination events involve one atom from each spin state, Equation 6.1 can be simplified to yield a differential equation representing the evolution for the number of trapped atoms in each of the equally populated spin states $N(t)$ as

$$\frac{dN}{dt} = -K_1 N - K_3 \langle n^2 \rangle N. \tag{6.2}$$

Here, $\langle n^2 \rangle$ is the average value of the squared density per spin state. K_3 in this equation is the three-body rate coefficient for the number of atoms lost per spin state, defined in Equation 3.46. The one-body rate constant K_1 represents the $1/e$ lifetime of the atoms to one-body loss. Assuming a non-degenerate gas with a Gaussian density distribution in a harmonic trap, the density is normalized by

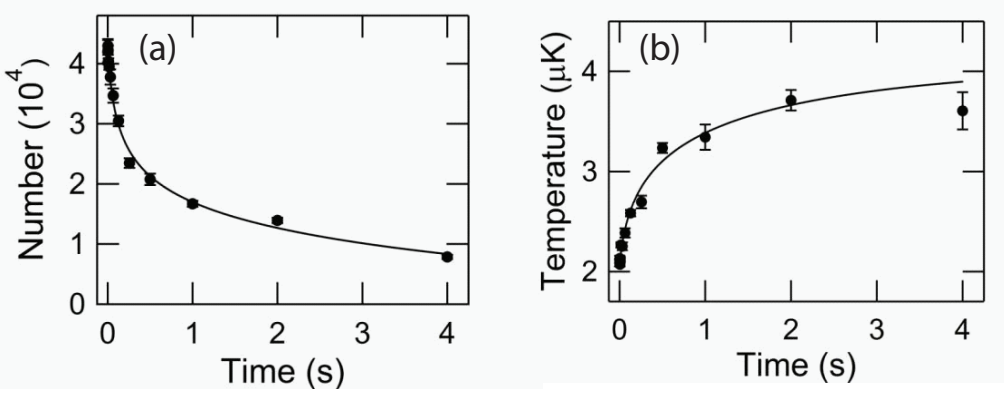

Figure 6.3. Evolution of (a) the number $N(t)$ and (b) temperature $T(t)$ for atoms in state $|3\rangle$ with respect to hold time t of the three-state mixture at a field of 302 Gauss. The solid lines are fits to the data using the routine described in the text, resulting in a three-body loss rate coefficient for this field of $K_3 = 1.19 \times 10^{-23}$ cm^6/s.

the total atom number per spin state as

$$n(\mathbf{r}) = N \left(\frac{a}{\pi}\right)^{3/2} e^{-a(x^2+y^2+z^2)}, \tag{6.3}$$

where $a = m\bar{\omega}^2/(2k_BT)$, which depends on the mean trapping frequency $\bar{\omega}$ and the temperature T of the gas. The time evolution of the atomic populations can therefore be represented in terms of the measurable quantities: total number of atoms per spin state $N(t)$, temperature of the gas $T(t)$, and the mean trapping frequencies $\bar{\omega} = (\omega_x\omega_y\omega_z)^{1/3}$ as

$$\frac{dN}{dt} = -K_1N - \gamma\frac{N^3}{T^3}, \tag{6.4}$$

where

$$\gamma = \frac{K_3}{\sqrt{27}} \left(\frac{m\bar{\omega}^2}{2\pi k_B}\right)^3. \tag{6.5}$$

In general, the time-dependence of the temperature must also be accounted for to constrain Equation 6.4 above. T. Weber and co-workers have derived a differential equation modeling the thermal evolution of the gas attributed to the two primary heating mechanisms: *anti-evaporation* and *recombination heating* [199, 200]. Equation 6.2 demonstrates that the atom-loss rates from three-body events scales with the atomic density squared. In our harmonically trapped samples, the

density is highest at the center of the trap where the particles, on-average, have the lowest energy. This results in spatially inhomogeneous three-body atom loss rates, preferentially heating the low-energy atoms from the center of the trap and leading to anti-evaporative heating of the gas. Comparing the mean potential energy of an atom undergoing a three-body recombination event ($k_BT/2$) to the average energy per particle in the gas ($3k_BT/2$), it is found that for each atom lost from anti-evaporation, an average excess of k_BT energy is left in the sample. The recombination heating mechanism accounts for the average energy that the three-body reaction products (high-energy dimer and recoiling atom) deposit as they leave the gas. An energy term k_BT_h is included in the analysis to account for this trap-dependent heating mechanism.

Relating the total heating energy ($k_B(T + T_h)$) to the energy of the trapped gas ($3Nk_BT$) yields an expression for the time evolution of the temperature of the gas in the presence of three-body decay given by

$$\frac{\dot{T}}{T} = \frac{\dot{N}}{N}\frac{k_B(T + T_h)}{3k_BT}. \tag{6.6}$$

Inserting the expression for $\dot{N}$ from Equation 6.4 into the above formula, and assuming that only the three-body loss mechanisms contribute to the heating, yields an explicit expression for the temperature evolution of the gas which is given in terms of experimental observables $N(t)$ and $T(t)$ as

$$\frac{dT}{dt} = \gamma\frac{N^2}{T^3}\frac{(T + T_h)}{3}. \tag{6.7}$$

Equations 6.4 and 6.7 form a set of coupled, nonlinear differential equations which can be numerically integrated for a given parameter set [$N(0)$, $T(0)$, K_1, K_3, and T_h] to give $N(t)$ and $T(t)$. Representative plots of the number N_i and temperature T_i evolution of atoms in state $|3\rangle$ for the set of i hold times t_i in the three-state mixture are shown in Figure 6.3. Each data point in these graphs represents the mean value of five independent measurements whose variance (σ_{N_i} and σ_{T_i} represented by the vertical error bars on each data value) are given by the uncertainty in the mean.

The best-fit parameters to simultaneously fit the measured number N_i and

temperature T_i data at each field of interest are obtained by minimizing χ^2, given by

$$\chi^2 = \sum_i \frac{(N(t) - N_i)^2}{\sigma_{N_i}^2} + \frac{(T(t) - T_i)^2}{\sigma_{T_i}^2} \tag{6.8}$$

where the sum over i includes all 12 data points taken at hold-times $t_i = 2^i$ ms, which span 2 ms $\leq t_i \leq$ 4 s. We use an iterative approach to find the best-fit values of the parameters based on the nonlinear fitting routines and numerical algorithms detailed in References [201] and [202]. The fit is preformed using the *Wolfram Mathematica* computing software as follows:

- Choose reasonable initial values for the five fitting parameters $N(0)$, $T(0)$, γ, K_1, and T_h
- For each parameter, record the χ^2 values as the parameter value is varied over $\pm 2.5\%$ in 0.5% steps while holding all other parameters constant.
- Fit the set of χ^2 values for each parameter to a parabola to find the minima, or best-fit value.
- Cycle through all parameters to determine the minimum χ^2 for each.
- Reset the initial guess parameter values equal to the stored values that minimized χ^2 and repeat the procedure until the parameter values converge.

The accuracy of the fit is most conveniently determined from the *reduced chi-squared* χ^2/ν, where ν is the number of degrees of freedom given by the number of data points minus the number of fitting parameters. From χ^2 statistics, a good fit results in $\chi^2/\nu \simeq 1$. Significant deviations from this value occur when either the assumed fitting distributions are not good representations of the data or the variances of the data are significantly under/over estimated [201]. We assumed that the Innsbruck model, given by Equations 6.4 and 6.7, was appropriate and adjusted the variance of the data to yield $\chi^2/\nu = 1$ whenever the fits significantly varied from this value.

In multi-parameter fits, the one-σ error for a given fit parameter can be estimated by determining the variation of the parameter value about its minima which increases χ^2 by one. Care must be taken in this analysis due to the possible

correlations that can exist between the parameters. In this case, the contour plot of χ^2 with respect to various parameters may be elliptical, necessitating that we consider the full range of the $\Delta\chi^2 = 1$ contour over the entire parameter space and not just the intersection of the contour with the axis of the parameter of interest [201]. To this end, for each field value we mapped out the variation of χ^2 with respect to all five of the fitting parameters. This simulation was conducted using Monte-Carlo calculations where each of the parameters were randomly selected within a range of parameter space that encompassed the $\Delta\chi^2 = 1$ contour. The $\pm 68\%$ confidence interval values are then given by the maximum and minimum values of the parameter of interest that yield an increase of χ^2 by one for any value of the other fitting parameters.

6.2.2 Low-Field Three-Body Recombination Coefficients

For each field of interest, the time evolution of the atoms in state $|3\rangle$ is measured, yielding sets of data analogous to that shown in Figure 6.3, which are then fit using our routine to extract the three-body recombination rate constant. The solid lines shown in the figure are simultaneous least-squares fits of the number and temperature data to Equations 6.4 and 6.7, demonstrating that our data is well fit by the Innsbruck model. The best-fit K_3 values over the range of magnetic fields 15 G $\leq B \leq$ 953 G is shown in Figure 6.4. Over this range, K_3 varies by over 4 orders of magnitude from 1.63×10^{-26} cm^6/s at $\sim$ 15 Gauss to 1.02×10^{-21} cm^6/s at $\sim$ 776 Gauss. Additionally, the recombination heating term T_h extracted from our fits varied from $1.5 - 4\mu$K and the one-body loss rate coefficients K_1 varied from $0.1 - 0.33$ s^{-1}, indicating relatively low but non-negligible one-body heating rates. The error bars in Figure 6.4 indicate the 68% confidence interval of our data, determined by the multi-parameter $\Delta\chi^2 = 1$ analysis described above. A systematic uncertainty in the data arising from our uncertainty in the atom number ($\pm 30\%$) and trap frequencies ($\pm 5\%$) is not included in the data. Due to the scaling of K_3 as $N^2\bar{\omega}^6$, small errors in these values can lead to large uncertainties ($\pm 70\%$) in our extracted K_3 values.

The three-body recombination rate constants closely follow the qualitative trends shown in Figure 6.1 for the collisional stability of the gas. Near 0 and

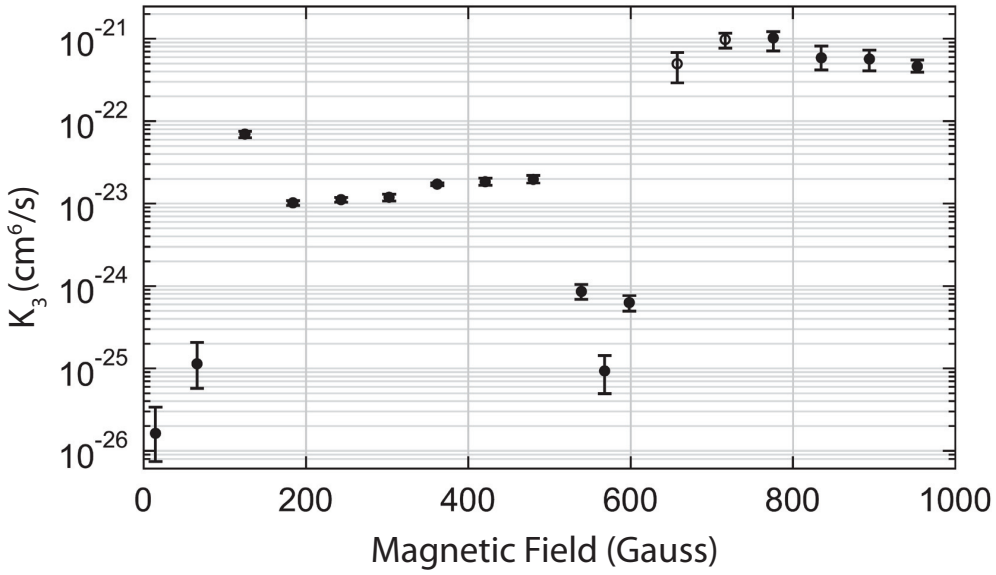

Figure 6.4. Magnetic field dependence of the three-body loss rate coefficient, K_3. The open circles represent data in the range of fields where we previously observed loss in at least one of the two-state mixtures.

568 G, the three-body recombination rates are relatively small, allowing for stable three-state Fermi gases to be created. At 568 G, the field at which we create the three-state mixture, $K_3 = 9.33 \pm 2.44 \times 10^{-26}$ cm^6/s. A gas with a density $n = 10^{12}$ cm^{-3} per spin state has a $1/e$ lifetime on the order of 10 s at this field, long compared to any of the relevant experimental timescales. Additionally, an anomalous resonant peak in K_3 is observed at $B \simeq 125$ G, which is consistent with the anomalous loss observed near this field in the qualitative data. At 504 G, corresponding to the second loss peak observed in the qualitative data, a population imbalance again emerged at longer hold times. Our model cannot account for such state-dependent loss rates and therefore we did not include a value for K_3 at this location.

In the range 600 G $< B <$ 750 G, the measured decay includes loss events that were observed in the two-state mixtures at these field values. These state-selective decay mechanisms are not included in our analysis, possibly leading to an overestimate of the reported K_3 values (represented as open circles in Figure 6.4). The temperature of the gas varied from nominally 1.9 μK to 6 μK for various hold times and field values. The maximum value of the three-body loss rate constants

at these temperatures, calculated from the absolute maximum values K_3^{max} given in Equation 3.47, ranged from $K_3^{max}(1.9\mu\text{K}) \simeq 2 \times 10^{-21}$ cm^6/s to $K_3^{max}(6\mu\text{K}) \simeq 2 \times 10^{-22}$ cm^6/s. As can be seen in Figure 6.4, all of the K_3 values measured above 600 G lie within this range and the effects of unitarity and thermal averaging on these data points cannot be ruled out. At first, we thought that the smooth decrease of the three-body rates for the three highest field values above 834 G, and the fact that the calculated K_3^{max} for these values was larger than the measured rates by at least a factor of two, signaled that the measured rates for the three highest field values were nominally correct. Later measurements taken with a colder sample (See Section 7.2.1) demonstrated, however, that these data points were under reported by over an order of magnitude attributed to the effects of unitarity.

For the low-field data ($B \leq 600$ G), the smaller pairwise interaction strengths were expected to yield reduced three-body loss in this regime. Here, the temperature of the gas varied from nominally 1.9 μK to 4 μK, leading to a maximum three-body atom loss rate of $K_3^{max}(4\mu\text{K}) \simeq 4.4 \times 10^{-22}$ cm^6/s. It is unlikely that any of our data in this region is limited by unitarity as the measured rates were lower than K_3^{max} by between a factor of six (at 125 G) and over four orders of magnitude (at 14.5 G). The extent to which the rate coefficients are significantly affected by the temperature of the gas was defined in Section 3.4 in terms of the critical scattering length a_c, given by Equation 3.48. For our temperatures, $a_c(4\ \mu\text{K}) \simeq 2680\ a_0$, nearly a factor of three times larger than the magnitudes of any of the scattering length in the low-field range. The measured low-field recombination rates are therefore independent of the energy and can be directly compared to the calculated recombination rates at threshold. The results of this experiment have been published in Physical Review Letters [144] in 2009, and our low-field K_3 results are in good agreement with those independently obtained in an earlier publication by S. Jochim's group in Heidelberg [145].

6.3 Interpretation of the Low-Field Data

The loss rates of the gas near 125 G and 500 G were anomalously large, and not explainable by any distinct features in any of the scattering lengths, therefore mer-

iting further investigation. The resonant features have been shown to be attributed to a single Efimov-like trimer state crossing the free-atom scattering threshold near these locations [3, 4, 203]. Fits to the locations and shapes of these features based on universal predictions have revealed a surprising amount of information relating to the interactions among distinguishable atoms, both in and on the verge of the universal regime. In this section, the theoretical interpretation of our three-body loss data in the range of magnetic fields from 15 to 600 Gauss is discussed in greater detail.

As discussed in Chapter 3, the zero-range approximation is only accurate so long as all of the scattering lengths ($|a_{12}|$, $|a_{23}|$, and $|a_{13}|$) are much larger than the characteristic length scale in our system, given here by the van der Waals length scale $l_{vdw} = 62.5a_0$. In the low-field region, all three scattering lengths satisfy $|a_{ij}| > 2l_{vdw}$ for magnetic field values between 122 G $< B <$ 485 G. In this universal region, all three scattering lengths are negative and relatively large (near 320 G, the smallest scattering length $a_{12} = -290a_0 = -4.6\ l_{vdw}$) and calculations of K_3 using the zero-range approximation should be reasonably accurate. The resonant loss features, whose maxima lie near 125 G and 500 G respectively are surprising, however, as they lie on the outskirts of this universal regime. Here, the effects of the finite range of the interaction is non-negligible and we were initially doubtful that the loss features could be described within the framework of Efimov physics.

In Reference [3], E. Braaten and co-workers used a generalization of the Skorniakov and Ter-Martirosian (STM) equations, discussed in Section 3.3.2, to numerically solve for the low-field rate constants in Equation 3.40. By fitting the shape of the K_3 data from the Heidelberg group [145] to their model in the region 122 G $< B <$ 485 G, and using the known magnetic field dependence of the scattering lengths [116], they were able to extract the three-body parameters describing the loss in this regime. Their results from this fit are shown in comparison to our data as the red curve in Figure 6.5. Here, the magnetic-field dependent three-body loss rates are calculated using their best-fit values of the three-body parameters: the trimer binding wave number ($\kappa_* = 76.8\ a_0^{-1}$) and the inelasticity parameter ($\eta_* = 0.11$). The blue dots in the figure are the experimentally measured values of the three-body loss rate coefficients reported by our group in Reference [144].

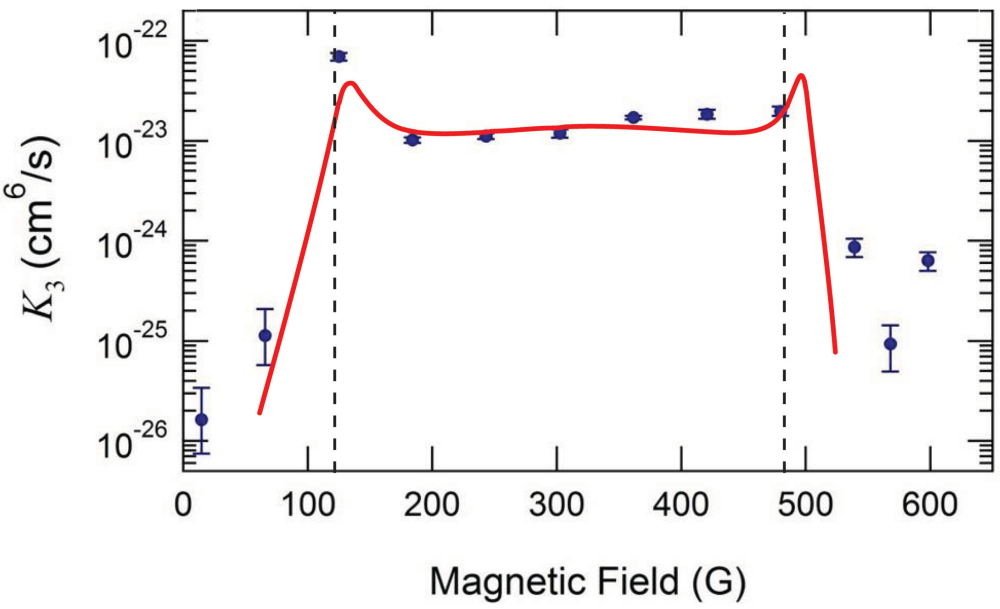

Figure 6.5. Three-body atom loss rate coefficient spanning the low-field region. Our measurements of the magnetic-field dependence of K_3 (blue dots) are compared to those calculated by E. Braaten *et al.* [3] (red curve). The universal theory predicts resonantly enhanced loss rates at ~ 125 G and 500 G attributed to an Efimov trimer state crossing the free-atom threshold at these locations. The dashed lines represent the boundaries of the universal region, outside of which at least one of the scattering lengths $a \leq 2l_{vdw}$.

The vertical lines represent the boundaries of the region in which the smallest scattering length $|a_{12}| \geq 2l_{vdw}$, outside of which, the universal theory is expected to break down due to finite range effects. The absolute normalization of the fit was determined by the three-body parameters κ_* and η_*, reflecting the universal dependence of the loss rates on the scattering lengths discussed in Section 3.2.

The fit by Braaten and co-workers is in good agreement with the shape of our narrow resonance feature near 125 G and the absolute normalization of the theoretical curve agrees with much of our data in the universal regime to within the statistical uncertainty of our K_3 measurements. A second resonant feature is predicted around 500 Gauss, near the location of the enhanced loss we previously observed in the qualitative data shown in Figure 6.1. We could not report a three-body loss coefficient at the location of the predicted peak because our data exhibited state-dependent loss rates at these fields. The three-body loss measurements published by the Heidelberg group [145] were similar to our low-field data to within a universal offset due to the systematic errors in our measurements. Their

data exhibited no sharp features in the vicinity of the resonance predicted at 500 G resonance, but instead displayed a very broad loss feature which peaked at the higher end of the universal regime.

Similar predictions of the three-body recombination rate of three-component ^{6}Li system in the low-field region have also been independently calculated by three other groups, using either a hyperspherical formalism [4], functional renormalization techniques [28], or using the analytical results derived by E. Braaten and H. W. Hammer [1] for three identical bosons, given in Equation 3.36, and assuming a reasonable form for the effective scattering length that describes the total rate for three-body collisions [5]. In all of these calculations, resonant loss features near 125 G and 500 G are predicted, attributed to an Efimov trimer state crossing the free-atom threshold near the resonance locations.

The field dependent binding energies (E_T) of the Efimov trimer state responsible for the loss peaks were calculated in References [4, 28, 8]. They found that both of the predicted resonances are actually associated with a single Efimov state crossing threshold near both 130 G and 500 G, as originally illustrated in Reference [4] and reprinted here in Figure 6.6 for reference. The binding frequency of the trimer state ($\nu_T = E_T/(2\pi\hbar)$, where $\hbar$ is Planck's constant) is predicted to increase from zero near 130 G and 500 G to a maximum of $\sim$ 10 MHz near 330 G.

The binding energy of the next deeper Efimov trimer is characterized in Reference [8]. This state is relatively uniform over the low-field regime, with a binding frequency on the order of 12 GHz. The binding frequency of this state greatly exceeds the van der Waals frequency ($\nu_{vdw} = 154$ MHz), signaling that the most weakly bound Efimov state observed in our data is also the ground-Efimov-state ($E_T^{(0)}$) and all deeper states predicted by the universal theory are simply artifacts of the zero-range approximation.

P. Naidon and M. Ueda also considered the possibility that the resonant features could be described in terms of non-Efimov trimer states, originating from other spin channels with the same total projection ($m_F = -3/2$), crossing threshold near 130 G [4]. The energy scaling of these states as a function of magnetic field are shown as the dotted lines in Figure 6.6. They found that this scenario is unlikely as the steep monotonic field dependence of these energies cannot account for the second loss feature near 500 G. From their calculations of the width (shaded blue

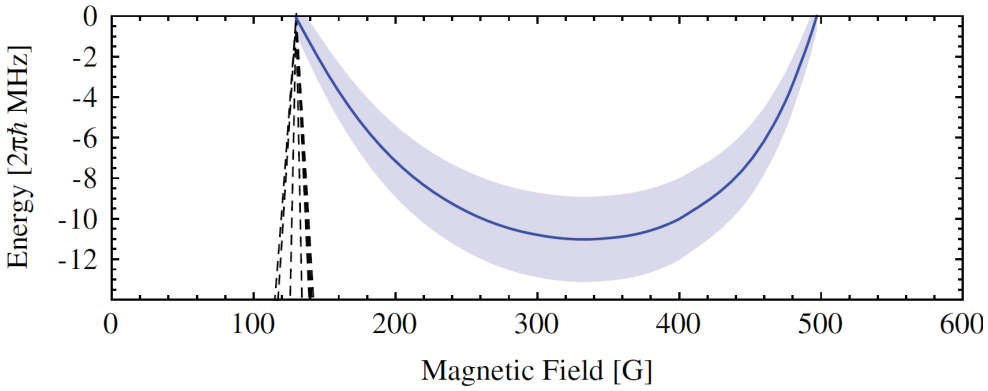

Figure 6.6. (Solid curve) The magnetic field dependent binding energies of the predicted low-field Efimov trimer state. (Shaded region) The calculated width of the Efimov state. (Dashed curves) The estimated energy scaling of possible non-Efimov trimers from all other spin channels. Figure taken from Reference [4].

region) and binding energy of the Efimov state (solid blue curve), they were also able to determine that the lifetime of the trimer is approximately 50 ns at 300 G, much shorter than any of the relevant timescales in our experiment.

In Reference [5], A. Wenz and co-workers proposed a simple analytic approximation for the three-body recombination rate in regions where all three scattering lengths are negative. In their approximation, they consider the analytical results for K_3 given in Equation 3.36, which was derived for the case when all three scattering lengths are equal. To this end, they define an effective scattering length a_m given by

$$a_m = -\sqrt[4]{\frac{1}{3}\left(a_{12}^2 a_{13}^2 + a_{12}^2 a_{23}^2 + a_{13}^2 a_{23}^2\right)}. \tag{6.9}$$

This relatively simple expression nicely reproduces many of the behaviors of universally interacting three-body systems discussed in Chapter 3. If all three scattering lengths are equal, a_m reduces to the value of the scattering lengths, reproducing the simple a^4 scaling derived for three-body recombination in this case. The effective scattering length also correctly accounts for the fact that three-body processes are suppressed when two of the three scattering lengths are small, whereas significant loss can still occur when at least two of the three scattering lengths are resonantly enhanced. This expression is not valid, however, either when one of the scattering lengths diverges, leading to a diverging three-body rate which is unphysical, or

when any of the scattering lengths cross zero. E. Braaten *et al.* considered another possible choice for the effective scattering length when all three scattering lengths are negative. Their term is expressed as the geometric mean of the three scattering lengths $a_g = -|a_{12}a_{23}a_{13}|^{1/3}$. Using their universal results to test the accuracy of the approximate expressions, they found that a_g is more accurate than a_m [8].

In Reference [5], an explanation for why the loss feature near 500 G is much broader than that predicted in References [4, 28, 3] was also provided. They showed that the observed behavior of the three-body rates could be well described using their formalism by taking into account a magnetic field variation of the trimer state lifetime. In the previous calculations, it was assumed that the three-body parameters κ_* and η_* were independent of the magnetic field so long as the scattering lengths remained in a regime where universal predictions apply. In principle, these parameters are smoothly varying functions of the magnetic field, effectively constant only in a small field range such as in the vicinity of a sufficiently narrow Feshbach resonance [133, 204].

For the lower three Zeeman levels of ^{6}Li, this variation can be significant and must be accounted for. A. Wenz and co-workers pointed out that the binding energies of the dimers responsible for the Feshbach resonances at 543 G, 690 G, 811 G, and 834 G vary strongly (by nearly a factor of 6) with magnetic field over the low-field region. The lifetime of the trimer state depends on the binging energy of the dimer because the overlap of the wavefunctions of these states increase for smaller dimer binding energies. In our loss measurements, the trimer state acts as an intermediate level, enhancing the probability for atoms to undergo three-body recombination into the dimer states. Hence, greater overlap of the wavefunctions lead to an enhanced decay probability. As the trimer lifetime is directly related to the inelasticity parameter η_* describing the widths of the resonances, this suggests that η_* should vary with the magnetic field. It is assumed in their model that the variation of η_* is dependent only on the inverse of the binding energies of the dimer states associated with the Feshbach resonances, and that all four dimer states contribute in the same way, leading to a scaling of the inelasticity parameter as

$$\eta_* = A\left(\frac{1}{E_{D,1}} + \frac{1}{E_{D,2}} + \frac{1}{E_{D,3}} + \frac{1}{E_{D,4}}\right), \tag{6.10}$$

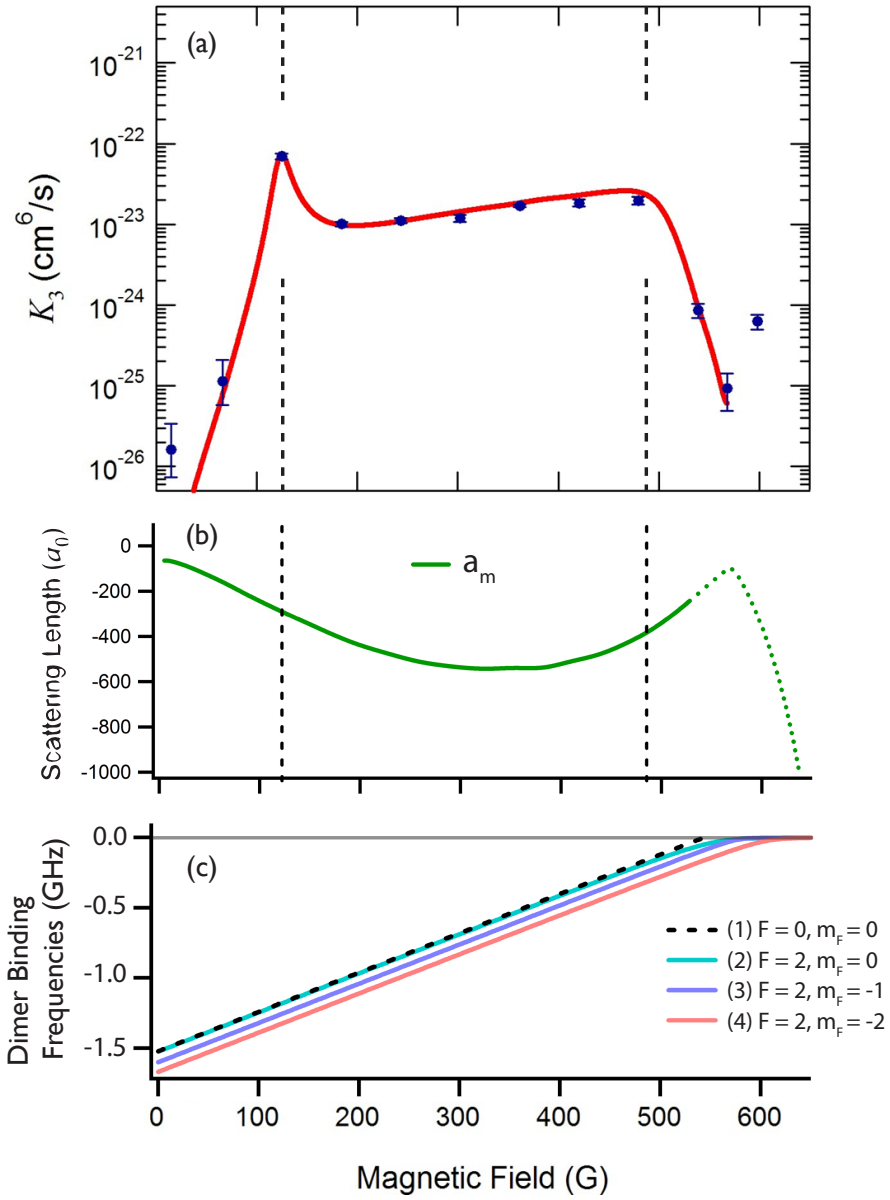

Figure 6.7. (a) Our low-field K_3 measurements (blue dots) are particularly well fit (red curve) using the model described in Reference [5]. (b) The effective scattering length a_m, calculated from Equation 6.9, is shown as the solid green curve when all $a_{ij} < 0$, and dashed outside of the range of validity when any $a_{ij} > 0$. The vertical dashed lines represent the boundaries of the universal region, outside of which at least one of the scattering lengths $a \leq 2l_{vdw}$. (c) Magnetic field dependence of the binding energies (in units of $2\pi\hbar$) of the four dimer states associated with the Feshbach resonances between 543 G and 834 G. Over the low-field universal regime, the binding energies varies by more than a factor of five.

where $E_{D,i}$ are the binding energies of the dimer states ($i = 1, 2, 3, 4$) associated with the Feshbach resonances near 543 G, 834 G, 690 G, and 811 G respectively, and A is a numerical constant [5]. The binding frequencies of the four dimer states are shown for reference in Figure 6.7(c).

A fit of our low-field three-body loss rate data using the Heidelberg model, described above, is shown in Figure 6.7(a). Here, the coefficient of the scaling relation A, along with the value of κ_* were used as the fitting parameters. Figure 6.7(b) shows the calculated effective scattering length a_m in this field regime, as defined in Equation 6.9. The effective scattering length a_m at 130 G and 510 G are equal, and a_m reaches its maximum amplitude near 330 G, qualitatively reproducing the shape of the calculated Efimov trimer binding energy shown in Figure 6.6. Above $\sim$ 527 G, at least one of the scattering lengths becomes positive and the assumptions used in deriving the effective scattering length break down until the field exceeds 834 G, above which all three scattering lengths are again negative. The binding frequencies of the four dimer states associated with the Feshbach resonances used in this calculation are shown in Figure 6.7(c). These binding frequencies, which were calculated using the model detailed in Reference [9], tune as expected with nominally two Bohr magnetons (2.8 MHz/G) for fields below the zero-crossings of the Feshbach resonances. As can be seen in the top panel of the figure, an excellent agreement with our measured three-body loss rates is obtained throughout the universal regime by fitting the data using the Heidelberg model.

Similar results have recently been obtained using a more rigorous calculation of the dependence of η_* with the magnetic field by S. Rittenhouse [205]. In this article, the three-body rates are solved for using both numerical solutions of the inelastic scattering rates, within the Wentzel-Kramers-Brillouin (WKB) approximation, using the adiabatic hyperspherical representation as well as using an analytic expression for K_3 that he derived resulting in a term analogous to that first reported in Reference [142]. It is shown in this publication that the inelasticity parameter scales with the binding energy of the dimers as $\eta_* = (1/2)\ln[1/(1 - \exp(-\beta\Delta))]$, where the parameter β encompasses the unknown short-range dependence of η_* which is independent of the dimer binding energies Δ. The fact that such good agreement can be realized between the zero-range models from References [5, 205]

and our data, without also scaling κ_* with magnetic field, suggests that even though the resonant features lie on the verge of the universal regime, the short-range physics determining the properties of the Efimov trimer state are likely independent of the magnetic field.

Our low-field measurements of the collisional stability and three-body loss rates of the lowest hyperfine spin states of ^{6}Li has revealed a great deal of information about three-body interactions in systems of distinguishable particles with unequal scattering lengths. We demonstrated that, at magnetic field values where at least two of the three scattering lengths are small, a long-lived three-component gas can be formed at high densities. The stability region around 560 G, where all three scattering lengths in this system are crossing through zero, has in fact been used to prepare weakly-interacting, quantum degenerate gases of three-component ^{6}Li atoms [190, 175].

Further, it is now generally accepted that the resonant loss features in the three-body recombination rate data near 130 and 500 G are associated with an Efimov trimer state crossing threshold near these locations. Extensive theoretical effort over the last few years to explain the low-field data, reported by the Heidelberg group [145] and our own reported results [144], now makes the observed three-body recombination rates of the gas in this field regime well described within the framework of Efimov physics. Since the two resonant loss peaks are associated with the same Efimov state crossing threshold twice, the variation of the widths of the two features has revealed that the inelasticity parameter scales with the binding energies of deeply bound molecular states. The properties of the Efimov trimer can be well described completely within a universal framework in terms of the three-body parameters κ_*, defining the spectrum of the Efimov state, and now A or β, the normalization of the inelasticity parameter, to fully predict the three-body interactions in the low-field universal regime.

Chapter 7

3-State ^{6}Li Gases at High Fields

We were interested in studying three-component Fermi gases in the high-field region ($B \geq 600$ G) for two primary reasons, (I) to determine the stability of the gas both in the vicinity of the Feshbach resonances, where superfluid two-component Fermi gases have been previously created [22]; and in the high-field limit where the gas exhibits SU(3) symmetry for application to future many-body studies with strongly-interacting gases and (II) to determine the three-body parameters in the universal regime above the ~ 560 G zero crossings, enabling the full mapping of the spectrum of Efimov trimer states and features throughout the range of fields encompassing the three overlapping Feshbach resonances. In our previous experiment, we published measurements of the three-body recombination rates for six field values in the range 600 G to 960 G. In Reference [3], E. Braaten and coworkers fit the last two data points at 894 G and 953 G using their calculations in the zero-temperature limit, predicting that an Efimov resonance should occur at fields near 1200 G. These results encouraged us to explore the high-field, strongly universal regime in more detail, where novel phenomena is expected to emerge in the vicinity of the three overlapping Feshbach resonances.

It is generally accepted that there are no universal connections of the three-body parameters across a zero-crossings of the scattering lengths [128]. This non-universal behavior is due to the magnetic-field variation of the two- and three-body potentials which define the three-body parameters in a given universal region. As the scattering lengths are tuned across a zero-crossing in a, it is assumed that the potentials have varied sufficiently that corrections to the zero-range approxima-

tions diverge ($l_{vdw}/a \to \infty$). Therefore, since the scattering lengths all cross zero between the low- and high-field regions, our previous measurements of the low-field loss rates made no predictions about the locations or widths of the Efimov resonances at fields above the zero-crossings. Independent measurements of the three-body loss rates were therefore required to extract the three-body parameters in the high-field universal regime.

This chapter describes our second set of experiments, in which we measured the three-body decay rate constants over the range of fields 834 G $< B <$ 1500 G. Here, the scattering lengths a_{12}, a_{23}, and a_{13}, shown in Figure 7.1, are all negative signaling that no universal dimer states exist. At the lower values of this range, the scattering lengths are strongly tuned by the nearby Feshbach resonances, yielding very large and widely varying interaction strengths. At the high fields, the scattering lengths all asymptote to the anomalously large triplet scattering length ($a_t = -2140a_0$), defined by the zero-energy resonance in the triplet scattering potential. Throughout the high-field regime, all three scattering lengths are significantly over an order of magnitude larger than the van der Waals length scale (l_{vdw}), well within the universal regime where theoretical calculations based on the zero-range approximation, discussed in Chapter 3, are justified.

By utilizing our various large-volume traps, we were able to measure the three-body loss rate coefficients (K_3) throughout this range of fields, observing a resonant loss feature associated with Efimov physics near 895 G as well as determining the asymptotic high-field loss rates important for future realization of many-body physics with these three-component Fermi gases in the SU(3) symmetric regime. At the end of the chapter, I will briefly discuss the implications of this research in terms of the theoretical study it has enabled, and compare our measurements with the various features that have been recently observed in three-component ^{6}Li gases.

7.1 High-Field State Preparation

For this experiment, two-component ^{6}Li gases were again evaporatively cooled in the primary dipole trap nearly to degeneracy, as described in Section 5.1. A very high evaporation efficiency can be achieved at fields close to the Feshbach reso-

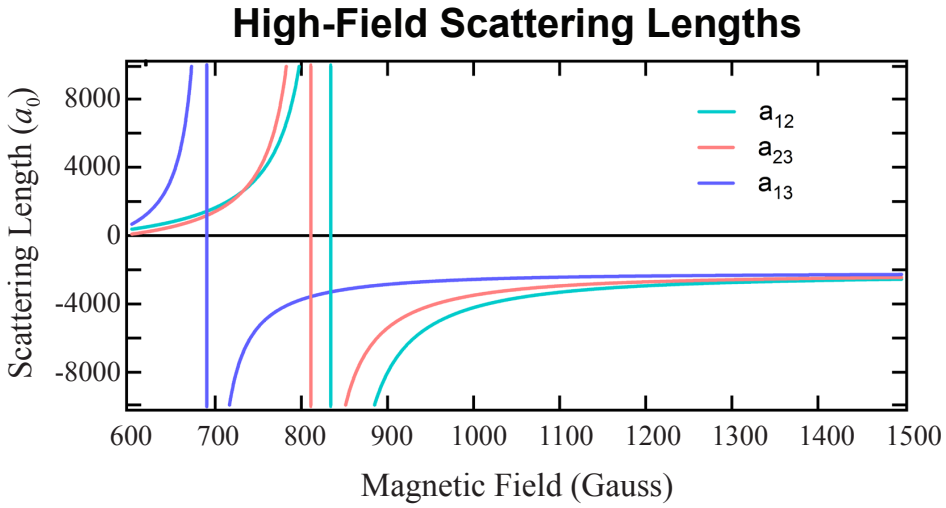

Figure 7.1. The high-field (600 G $\leq B \leq$ 1500 G) s-wave scattering lengths for ^{6}Li atoms occupying states $|1\rangle$, $|2\rangle$, and $|3\rangle$. The purple, pink, and cyan vertical lines represent the locations of the $|1\rangle$-$|3\rangle$, $|2\rangle$-$|3\rangle$, and $|1\rangle$-$|2\rangle$ Feshbach resonances at 690 G, 811 G, and 834 G respectively.

nance [206], where the s-wave elastic scattering cross-section is limited by unitarity throughout the cooling process, and the two-state mixture is effectively stable against inelastic two-body loss (see Section 2.3 and Figure 6.2). Forced evaporation of an equally balanced mixture of atoms in states $|1\rangle$ and $|2\rangle$ occurred at a field of 840 Gauss for this data set to optimize the cooling efficiency while assuring that the final gas consists of free atoms.

Preliminary measurements of the three-body loss rates for our three-state samples in the high-field regime, presented in Figure 6.4, were unitarity limited for the characteristic ~ 2 μK gases produced in the primary trap. In Section 5.4, we discussed the large-volume trapping potentials, which were specifically designed to provide a reasonably deep conservative potential to confine the ^{6}Li gas, while maintaining sufficiently low temperature samples to assure that thermal averaging and unitarity effects on the atomic lifetimes could be discounted. Further, the low densities achieved in the large-volume traps provided sufficient atomic lifetimes to prepare incoherent three-state mixtures in thermal equilibrium throughout the high-field range investigated. The atoms were directly loaded into either of the large-volume traps during the last second of the evaporation stage.

Remember that the power for the large-volume beams was derived directly from

the zero-order beam that is not deflected by the AOM controlling the primary dipole trap. As the power of the primary trapping beams is decreased for forced evaporation, the power of the large-volume trap is increased accordingly. Here, the power in the primary trap is reduced from ~ 3 W to zero while the power in the large-volume trapping beams change by less than 4%. By varying the time-constant of the primary trap decay profile and recording the equilibrium temperature of the gas, we assured that the large-volume trap was adiabatically loaded.

The stabilizing forces from the levitation and translation fields were imperative for our high-field lifetime measurements. These gradient fields served two purposes, supporting the atoms against gravity as well as translating the center of the primary and booster coil field gradients onto the atoms. Without canceling these forces, not only is the efficiency of the adiabatic transfer greatly reduced, but oscillation of the center of mass and/or breathing modes (dipolar and quadrupolar excitations) are induced as the bias magnetic fields are varied.

After the gas is adiabatically transferred into one of the large-volume traps (I or II) shown in Figure 5.5, the magnetic field is ramped to the field of interest within 10 ms. Broad-band RF fields are then applied to drive the $|1\rangle - |2\rangle$ and $|2\rangle - |3\rangle$ transitions at each field B_{hold}. Each of the RF fields are broadened to a width of 10 kHz (approximately equal to the Rabi frequency $\Omega/2\pi$). Depending on the field of interest and the large-volume trap confining the atoms, the duration of the RF fields are applied for a time ranging from 10 to 100 ms, chosen to be at least twice as long as the observed decoherence times at these fields. At the end of the RF pulse, the sample is again held for an additional 20 ms to allow the atoms to come into thermal equilibrium. The final sample, confined in either of the large-volume traps, consists of a balanced three-state mixture at a reduced temperature $T/T_F \simeq 0.5$ with $N \simeq 10^5$ atoms in each of the three high-field seeking Zeeman states.

7.2 Three-Body Loss Measurements

A very similar procedure as that described in Section 6.2 was used to determine the three-body loss rate coefficients for each field of interest 834 G $\leq B_{hold} \leq$ 1500 G. For this experiment, however, the number and temperature of the trapped

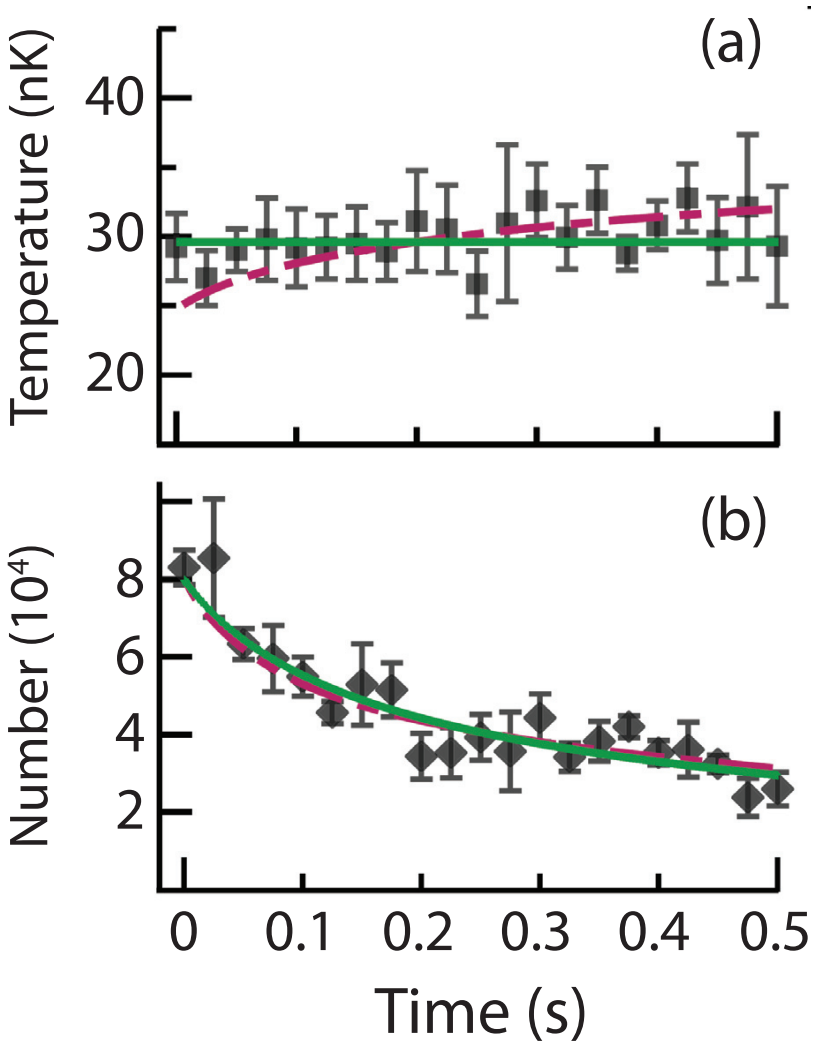

Figure 7.2. Evolution of (a) the number $N_i(t)$ and (b) temperature $T_i(t)$ for atoms in state $|3\rangle$ with respect to hold time t_i of the three-state mixture. This data was taken from *in situ* images of the atoms in the large-volume trap II at a field of 877 Gauss. The green (red) lines are fits to a model which does not include (includes) antievaporation.

atoms were measured as a function of hold time by *in situ* absorption imaging. An example data set taken at the field of interest $B_{hold} = 877$ G for the number N_i and temperature T_i evolution of the three-state mixture for the set of 21 hold times $t_i = 25 \times i$ ms in the large-volume trap II is shown for the atoms in state $|3\rangle$ in Figure 7.2. Each data point in these graphs represents the mean value of five independent measurements whose variance (σ_{N_i} and σ_{T_i}), represented by the vertical error bars on each point, are given by the uncertainty in the mean.

The magnitude of the two- and three-body loss arising in two-state mixtures is greatly suppressed at high-fields from the mechanisms discussed in Section 2.3. We tested this assumption for fields in the range 834 G $\leq B_{hold} \leq$ 1500 G by measuring the population of the remaining atoms in all possible binary mixtures confined in the large-volume trap I after a 200 ms hold time. The decay was consistent with one-body loss due to background gas collisions with a $1/e$ lifetime $1/\Gamma = 2.8$ s. The measurements confirmed that two- and three-body decay is negligible in the high-field regime when only two spin-components are involved in the collision events. Therefore, at ultracold temperatures, three-body loss events including one atom from each spin state are the dominant loss process in our three-component ^{6}Li gases for all of the high-field values and atomic densities investigated.

The Innsbruck model, given by Equations 6.4 and 6.7 for the number $N(t)$ and temperature $T(t)$ evolution of each state, was used to extract the three-body recombination rate coefficients (K_3) for the low-field data. As shown in Figure 7.2 (b), the temperature of the gas in the high-field regime remains approximately constant as the gas decays. This is consistent with the fact that the energetic atom and molecule produced in a three-body decay event have a mean free path (l_{MFP}) much larger than the characteristic size of the gas. From the measured dissociation energy of the most weakly-bound molecular state in the ^{6}Li triplet potential [207], the particles (atom and dimer) are expected to each recoil with an energy $E_R \sim k_B \times 500$ K. The mean free path of the reaction products are therefore very large for fields above 834 G ($l_{MFP} \simeq 6$ km in a sample with density $n_0 = 5 \times 10^{10}/\text{cm}^3$), and the high-energy reaction products generally exit the cloud without depositing energy. This is in stark contrast with the low-field data, where recombination into the deeply bound states associated with the Feshbach resonances can produce much lower-energy reaction products with significant probabilities of depositing energy into the gas as they exit the trap (at 500 G, decay into the most weakly-bound dimer states shown in Figure 6.7(c) leave the trap with recoil energy $E_R \sim k_B \times 7$ mK and mean free path $l_{MFP} \simeq 850$ μm for samples with densities $n_0 = 5.5 \times 10^{12}/\text{cm}^3$).

For the high-field data, the recombination heating term T_h in Equation 6.7 can therefore be neglected. Although our measurements are generally consistent with a model that includes a small rise in temperature due to the antievaproative

heating mechanism, shown by the red dashed curves in Figure 7.2 (a) and (b), lower values of χ^2 are obtained by simply fitting the evolution of the atomic population using Equation 6.4 and assuming that the temperature remains constant, as shown by the green solid curves in the figures. Since the overall temperature increase is minimal compared to the absolute temperature of the samples, ignoring the thermal evolution of the gas does not significantly change the results of the fit.

7.2.1 High-Field K_3 Data

To determine the high-field three-body loss rates (K_3), the number evolution of the atoms in state $|3\rangle$ at each field is fit with an analytic solution to Equation 6.4 using K_3, the initial atom number (N_0), and the temperature (T) as free parameters. For fields between 834 G and 1500 G, the measured values of K_3 are shown in Figure 7.3. The red circles (blue triangles) correspond to data taken in the large-volume trap I (II), giving the three-body loss rates for atoms at a temperature $T \leq 180$ nK (30 nK) with a reduced temperature of $T/T_F \simeq 0.5$ and an initial peak density in each spin state of $n_0 \simeq 5 \times 10^{10}$ (5×10^9) atoms/cm^3. The error bars give the statistical error from the fit, as discussed in Section 6.2.1, and the uncertainty in the trap frequencies added in quadrature. A systematic uncertainty of $\pm 60\%$ arising from the uncertainty in the absolute atom number ($\pm 30\%$) is not included in these error bounds.

As the field is varied, the measured values of K_3 varied by several orders of magnitude. The smooth decrease of the loss rates as the field is increased above $B \simeq 975$ G was qualitatively expected from the variation of the scattering lengths at these fields, shown in Figure 7.1. At 975 G, the rates measured in the large-volume traps I and II converge. Below this field, the divergence of K_3 for the high-temperature ($T \leq 180$ nK) and low-temperature ($T \leq 30$ nK) measurements signal the influence of thermal averaging and unitarity on the data. In addition to the smooth variation of the loss rate with magnetic field, resonant three-body loss is observed near 900 G in both data sets. This loss feature cannot be directly explained by distinct peaks in any of the scattering lengths at this field, suggesting the presence of an Efimov trimer states crossing the three-atom threshold near the resonance location.

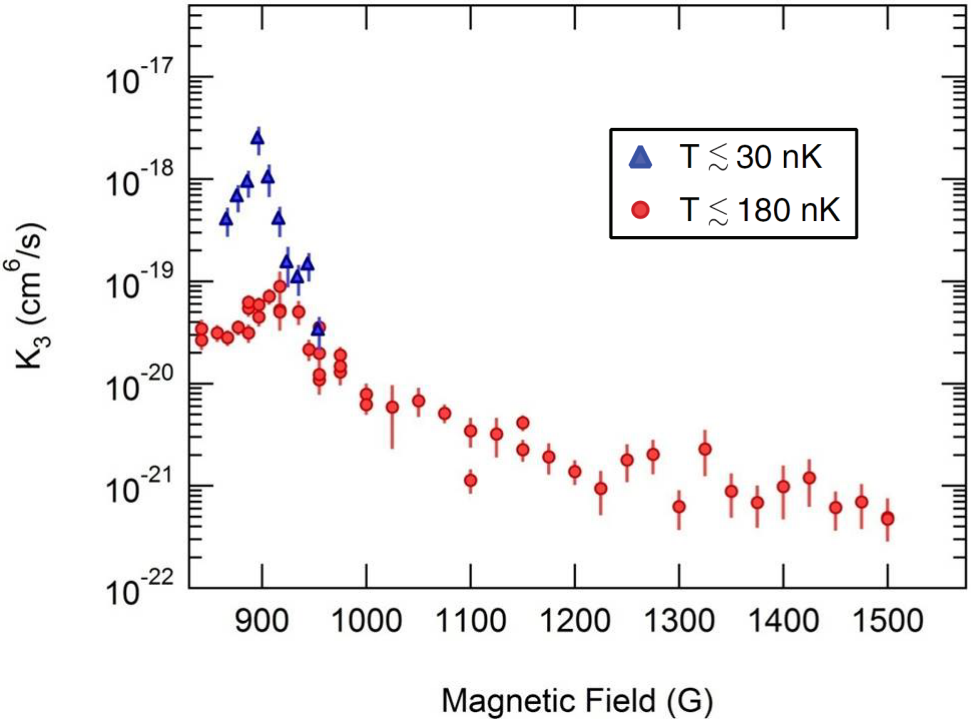

Figure 7.3. Measured three-body loss rate coefficients in the high-field regime. The red circles and blue triangles correspond to K_3 data extracted from lifetime measurements taken with the three-component ^{6}Li gases confined in the large-volume traps I and II respectively.

For fields above 834 Gauss, $|a_{12}|$, $|a_{23}|$, $|a_{13}| \gg l_{vdw}$ signaling that the system is deeply in the universal regime. The data should therefore be well described by the zero-range calculations of K_3 discussed in Chapter 3. Further, the zero-temperature approximation for calculating the field dependence of K_3 requires the temperature of the gas must both be in the threshold regime and unaffected by unitarity. From calculations of the height of the asymptotic barrier in the three-body potential and the unitarity limit for our three-component gases, given by Equations 3.45 and 3.47 respectively, it is found that our measured rates can be compared to the zero-temperature calculations for the $T \leq 180$ nK ($T \leq 30$ nK) data for fields $B > 960$ G ($B > 875$ G), and three-body loss rates $K_3^{max} \ll 2\times10^{-19}$ cm^6/s ($K_3^{max} \ll 8\times10^{-18}$ cm^6/s). The measured values for K_3 are below $K_3^{max}/10$ for the 180 nK (30 nK) data for fields above 975 G (907 G). These subsets of data should be in excellent agreement with the zero-temperature calculations of

the three-body loss rates, allowing for the first determination of the three-body parameters for this multi-component ^{6}Li gas in the strongly universal, high-field regime.

In our measurements, all three scattering lengths were unequal, requiring a numerical analysis to accurately extract the high-field three-body parameters from our measurements of the field dependence of K_3. We were able to fit the data using an iterative computer routine that was kindly provided by D. Kang and E. Braaten [6]. The code numerically solves for the three-body rates using a generalization of the STM equations [3, 8]. This is the same routine that E. Braaten and co-workers used to fit the low-field data [3], as discussed in Section 6.3. The best fit (solid line) to the subsets of the 30 nK data (907 G $\leq B \leq$ 975 G) and the 180 nK data (975 G $\leq B \leq$ 1500 G), using D. Kang and E. Braaten's code, is shown in Figure 7.4. The three-body parameters κ_* and η_* are the only free parameters in this fit. As shown in the figure, our K_3 data is well described with the numerical calculation for fields $B \geq 907$ G, yielding $\kappa_* = 6.9(2) \times 10^{-3} a_0^{-1}$ and $\eta_* = 0.016^{+0.006}_{-0.010}$, where the combined statistical and systematic uncertainty indicate 1 standard deviation.

7.2.2 Interpretation of the High-Field Data

From our high-field measurements, the calculated three-body parameters were then used to make predictions of the zero-temperature three-body loss rates for all fields above 834 G using the code provided by D. Kang and E. Braaten. These results are shown as the dotted line in Figure 7.4. This model predicts that a peak in K_3 at $B = 895^{+4}_{-5}$ G is attributed to an Efimov trimer state crossing the three-atom scattering threshold. The three-body loss rate coefficients are locally maximized at this field, where $K_3 = 4.1^{+8.5}_{-1.5} \times 10^{-17}$ cm^6/s at $T = 0$. The measured loss rates for the 30 nK data qualitatively resemble this behavior, also peaking near 895 G, though at a significantly smaller magnitude due to unitarity. The 180 nK data is further suppressed at this field, also exhibiting a shift of the peak location which is likely associated with the finite temperature of the gas.

The dashed line in Figure 7.4 shows a fit to the data using the code from D. Kang and E. Braaten and taking the unitarity limit into account. Here, the calculated rates are scaled by $1/K_3 + 1/K_3^{max}$, as suggested in Reference [7]. The

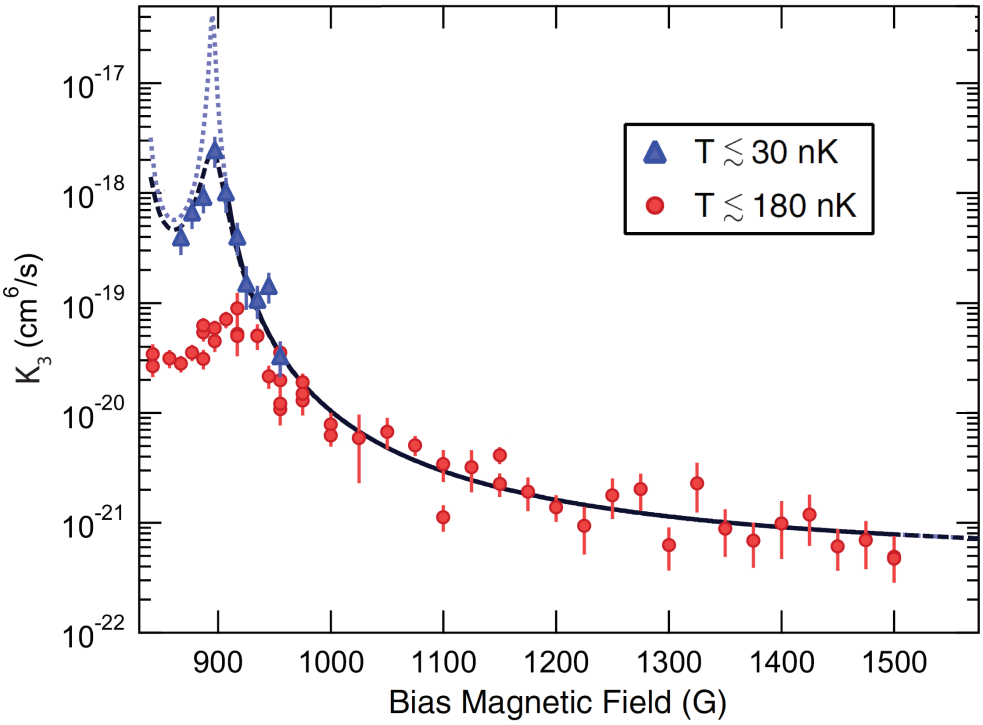

Figure 7.4. Fit of the measured three-body loss rate coefficients in the high-field regime using the numerical code provided by D. Kang and E. Braaten [6]. The fit to the measured K_3 rates for fields above 970 G (solid line) was used to extract the high-field three-body parameters. The zero-range calculations predict a resonant-loss peak at 895 G (dotted blue line), due to an excited Efimov trimer state crossing the three-atom threshold at this location. Using a model that accounts for the saturation of the loss rates from unitarity (dashed line) [7], the 30 nK data (blue triangles) is well fit in the vicinity of the Efimov resonance.

"unitarized" recombination rate therefore accounts for the observed saturation of K_3 in the thermal gas to a value $K_3^{sat} \simeq K_3^{max}/3$. This model provides a good fit to our data for all high-field values, demonstrating that the measured three-body loss rates are well described by the zero-range model in this highly universal regime, and the resonant loss feature at 895 G is explained by an Efimov trimer state crossing the free-atom threshold near this location. The measured high-field three-body recombination rates and the subsequent fit of the data to extract the three-body parameters discussed here were published by our group in Physical Review Letters [147] in 2009.

Our measurement of the three-body parameters in the high-field regime also

predict that at very high-fields, $B \gg 1500$ G the three-body loss rates saturate to $K_3 \simeq 5 \times 10^{-22}$ cm^6/s. This saturation is attributed to the convergence of the three scattering lengths to $a = -2140a_0$ at high fields. We were particularly interested in the stability of the gas in the high-field SU(3) symmetric regime for the possibility of studying superfluidity and many-body phenomena in this highly symmetric system, discussed in more detail in Chapter 8. The high loss-rates, however, make it difficult to create long-lived, strongly interacting three-component gases at these fields. More advanced preparation and cooling schemes will likely be required to further study ultracold gases of ^{6}Li atoms occupying the three lowest-energy Zeeman states in the high-field, strongly interacting regime.

It is interesting to compare the three-body parameters κ_* and η_* in the high-field region with those previously measured at lower fields. The regions are separated by a zero-crossing of all three scattering lengths near 560 G and it is therefore expected that the three-body parameters are not universally connected between these regions. We find, however, in comparing the measurements of the low-field parameters ($\kappa_*^{lf} \simeq 6.56 \times 10^{-3} a_0^{-1}$ and $\eta_*^{lf} \simeq 0.11$), calculated by E. Braaten and co-workers in Reference [3] with our calculations of the high-field parameters ($\kappa_*^{hf} = 6.9(2) \times 10^{-3} a_0^{-1}$ and $\eta_*^{hf} = 0.016^{+0.006}_{-0.010}$) that the values of κ_* are likely consistent within 1 σ. Remember that κ_* is only defined to within a multiplicative factor of the discrete scaling factor ($\simeq 22.7$), so that the observed resonances are not necessarily associated with the same Efimov state.

Although this agreement could be attributed to a coincidental tuning of the two-body parameters in these regimes, it suggests that the phase of the three-body wavefunction at short distances, which controls the spectrum of Efimov trimer states, is somehow unchanged by the presence of the broad Feshbach resonances that tune the scattering lengths. This interpretation has also been suggested in Reference [8], and similar apparently universal scalings of the three-body parameters have been observed in the earlier studies of ultracold ^{133}Cs gases exhibiting Efimov resonances on either side of a zero-crossing [35, 208, 209].

The inelasticity parameter η_*, on the other hand, varies between the low- and high-field regions by over an order of magnitude. This scaling may be directly related to the variation of the deeply-bound dimer states between these two regions, as was used to describe the variation of the widths of the two loss features at

approximately 125 and 500 G discussed in Section 6.3. Neither of the models used to explain this phenomena [5, 205] can be directly applied, however, as the binding energies of the most weakly-bound dimer states vary by approximately seven orders of magnitude between the low- and high-field regimes, whereas η_* varied by only a factor of 10 between these regions.

7.2.3 Efimov Physics in the High-Field Regime

In Figure 7.1, the tuning of the three scattering lengths a_{12}, a_{23}, and a_{13} with magnetic field is highlighted. For fields above 608 G (637 G), the magnitudes of all three scattering lengths exceed 125 $a_0 \sim 2l_{vdw}$ (2140 $a_0 \sim 34l_{vdw}$), where the atoms are in the universal (strongly universal) regime. The zero-range approximation should therefore be quite accurate throughout the high-field regime. Atoms prepared in this field region are expected to reveal novel few- and many-body phenomena attributed to the three overlapping Feshbach resonances in the $|1\rangle - |2\rangle$, $|2\rangle - |3\rangle$, and $|1\rangle - |3\rangle$ scattering channels at 834 G, 811 G, and 690 G respectively (vertical lines in Figure 7.1). Depending on the field of interest, any number of the scattering lengths can be positive, and 0, 1, 2, or 3 weakly-bound dimer states can exist. Three-component ^{6}Li gases prepared at these fields would therefore exhibit mutual coexistence and possibly competition of resonantly-enhanced attractive and repulsive pairwise interactions, the effects of which have not yet been demonstrated in any ultracold atomic system.

In Reference [8], E. Braaten *et al.* used our measurements of the high-field three-body parameters to make universal predictions about the spectrum of Efimov states and three-body loss rates throughout the high-field universal regime spanning 600 G $\leq B \leq$ 1200 G. Their calculations of the binding frequencies of the Efimov trimers ($E_T^{(n)}/(2\pi\hbar)$) in the high-field regime are shown in Figure 7.5. Only two trimer states exist with binding energies less than the van der Walls cutoff ($E_{vdw} = 2\pi\hbar \times 154$ MHz) in this region. The most weakly bound Efimov state ($E_T^{(1)}$) crosses the free-atom scattering threshold at the location of our observed loss resonance ($B = 895^{+4}_{-5}$ G). As the field is decreased, $E_T^{(1)}$ increases until the critical value $B_*^{(1)} = 672 \pm 2$ G, at which the Efimov trimer is predicted to come into resonance with the $|1\rangle + |23\rangle$ atom-dimer threshold. Here, the binding

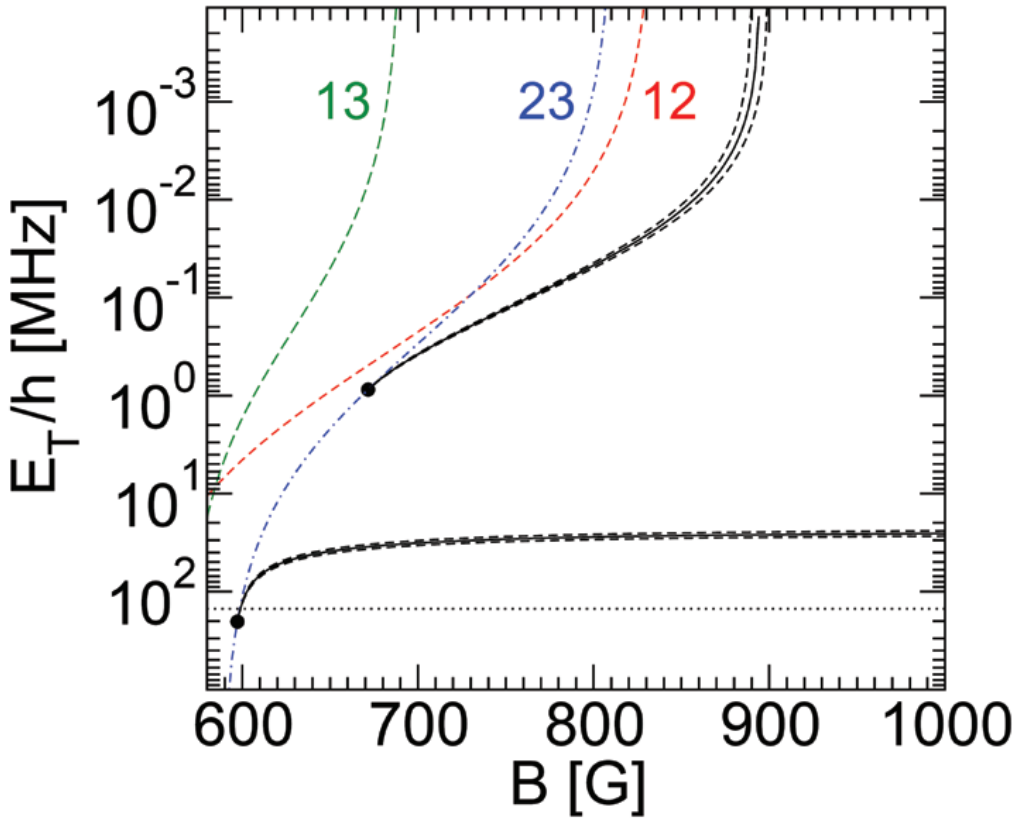

Figure 7.5. Energies of the Efimov trimer states as a function of the magnetic field over the region 600 G $\leq B \leq$ 1000 G. The solid curves are the calculated binding frequencies $E_T^{(n)}/(2\pi\hbar)$ based on our measurements of the high-field three-body parameters. The upper and lower error bounds are shown by the dashed curves. The colored curves labeled 12, 23, and 13 are the atom-dimer thresholds. The field locations where the trimers come into resonance with the $|1\rangle + |23\rangle$ atom-dimer threshold are indicated by the dots. For the ground-state trimer, the threshold crossing occurs at an energy exceeding the van der Waals energy, shown as the horizontal dotted line. Figure taken from [8].

frequency of the universal $|23\rangle$ dimer state with respect to the free-atom threshold is 871^{+43}_{-68} kHz. The maximum of the calculated frequency $\Gamma_T^{(1)}/(2\pi\hbar)$ associated with the width of the shallow trimer is 7.98 kHz, occurring at 692 G, and decreases to less than 1 kHz as the field approaches the free-atom and atom-dimer thresholds. The lifetime of the trimers occupying this state ranges from $\sim$ 20 to 160 μs, approximately three orders of magnitude longer than the lifetime of the low-field Efimov state.

The ground-state Efimov trimer has a binding frequency that decreases from $34.9^{+1.9}_{-1.9}$ Mhz at 672 G to $26.4^{+1.7}_{-1.6}$ MHz at 895 G. For $a < 0$, the critical scattering length for this state is calculated as $a'_* \simeq -292\ a_0$. Since all three scattering lengths converge to $aij \rightarrow -2140\ a_0$ at high fields, the binding energy of the ground-state Efimov trimer saturates as the field is increased, never crossing the free-atom threshold. For $a > 0$ their model predicts that the ground-state trimer crosses the $|1\rangle + |23\rangle$ atom-dimer threshold at $B_*^{(2)} = 597$ G, where the binding frequency relative to the three-atom threshold is 203 MHz. Here, the binding frequency is larger than the van der Waals frequency, and the smallest scattering length ($a_{23} = 54a_0$) is also smaller than the van der Waals length scale. E. Braaten and co-workers point out that the zero-range calculations are likely inaccurate for such large energies and small scattering lengths. The frequency associated with the width of the ground-state trimer state is approximately $\Gamma_T^{(0)}/(2\pi\hbar) = 1.7$ MHz at high fields, corresponding to a ~ 90 ns lifetime of the trimers occupying this state.

From the calculated spectrum of high-field Efimov trimer states, the authors of Reference [8] make further predictions of the three-body recombination rates in the field region 600 G $\leq B \leq$ 834 G, where all three scattering lengths are strongly tuned by the overlapping Feshbach resonances and one or more of the scattering lengths are positive. Their results are displayed here in Figure 7.6 for reference. Besides the resonant enhancement of K_3 we observed at 895 G, the only other expected peaks occur at the locations of the Feshbach resonances. These peaks simply arise from the a^4 scaling of K_3, where a is some form of the mean of the scattering lengths a_{12}, a_{23}, and a_{13}. Between the locations of the four loss peaks, three minima in the K_3 rates are expected. It is interesting to note, however, that the locations of the minima in the top (black) curves representing the total three-body loss rate into shallow and deeply-bound dimers significantly vary with respect to the lower curves (purple) representing the loss rates when only decay into the deeply bound dimer states is accounted for.

To get a better understanding of these features, E. Braaten and co-workers show the predictions for the three-body loss rates in the regions from 650 G to 850 G in more detail [8], presented here Figure 7.7. In addition to K_3 (black) and K_3^{deep} (purple), they show explicitly the contributions from recombination

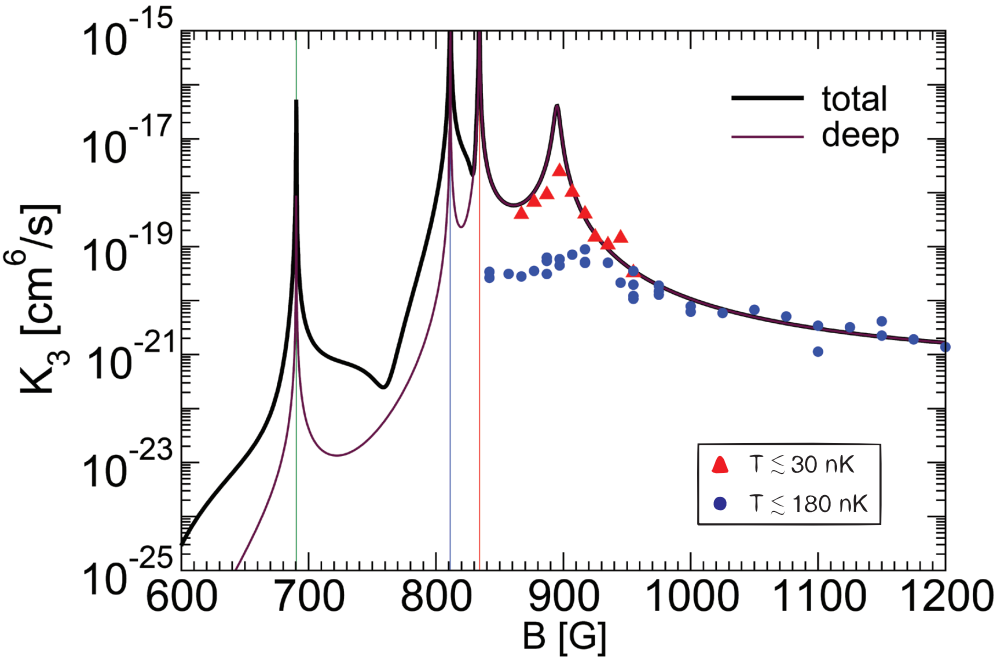

Figure 7.6. K_3 in three-component ^{6}Li gases over the field range 600 G $\leq B \leq$ 1200 G. The blue dots (red triangles) represent our high-field data taken in the large-volume trap I (II). The curve between 834 G and 1200 G is a fit to the data. In the region from 600 G to 834 G, the curves are predictions for the total three-body loss rates (black line) and the contribution from recombination into deeply bound dimer states (purple line) based on our measured three-body parameters in the high-field regime. The vertical lines mark the positions of the Feshbach resonances. Figure adapted from [8].

into the $|12\rangle$ (red), $|23\rangle$ (blue), and $|13\rangle$ (green) universal dimer states. This figure illustrates that at 830 G, a minima in the recombination rate into the $|12\rangle$ universal dimer (K_3^{12}) arises, attributed to a Stückelberg interference in the recombination pathways into the universal dimer state as discussed in Sections 3.2.2 and 3.3.1. Similar interference minima in the $|12\rangle$ and $|23\rangle$ scattering channels are observed at 757 G and 765 G respectively. There are also minima in the rates into the $|13\rangle$ dimer at 672 G and the $|23\rangle$ dimer state at 600 G, but their effects are not visible in the total recombination rate K_3.

A rich structure is predicted in the three-body loss of our three lowest-energy spin states of ^{6}Li in the vicinity of the three overlapping Feshbach resonances. It was quite surprising to see that resonant suppression of the three-body loss rates was predicted whenever any of the interactions were repulsive since this feature is highly dependent on the shape of the asymptotic three-body hyperspherical po-

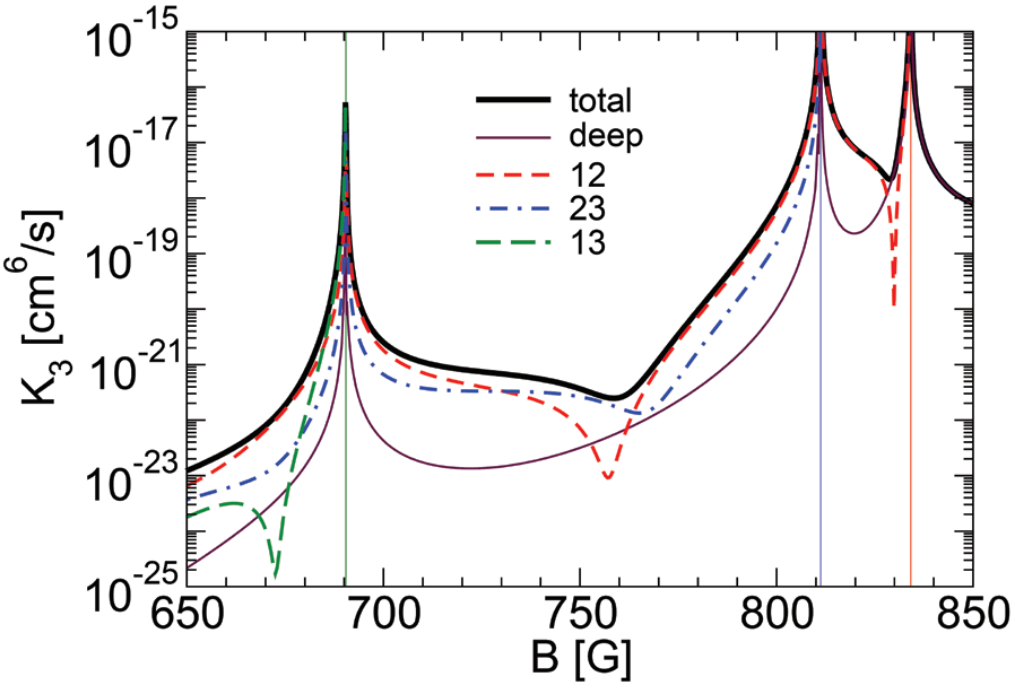

Figure 7.7. Detailed representation of the K_3 rate constant for three-component ^{6}Li atoms in the field range 650 G $\leq B \leq$ 850 G. The curves represent the predictions, based on our measurements of the high-field three-body parameters, for the total three-body recombination rate (black line), and the exclusive rate constants for recombination into only deeply-bound dimers (purple line), $|12\rangle$ dimers (red), $|23\rangle$ dimers (blue), and $|13\rangle$ dimers (green). Figure taken from [8].

tential as discussed in Chapter 3. We are currently exploring the three-body loss in the vicinity of the Feshbach resonances where these Stückelberg interference minima are predicted to occur. Deviation of the experimental results from the calculated three-body rates by E. Braaten and co-workers would suggest new physical mechanisms that cannot be explained in the zero-range universal theory.

7.3 SU(3) Symmetric Degenerate ^{6}Li Gas

We also note that despite the large rates of three-body loss in the high-field regime, we can produce quantum degenerate three-component Fermi gases at fields where the three scattering lengths are large, negative, and approximately equal. To demonstrate this, we initially prepared a two-state mixture in the large-volume trap I as described in Section 7.1, but extended the evaporation to cool the sample

to degeneracy with a reduced temperature $T \leq 0.25T_F$. Subsequently, the field was ramped to 1500 G within 10 ms and the three-component mixture was created with a 100 ms duration noisy RF pulse. After a 30 ms hold time at this field to assure thermal equilibrium, the population of the three-component gas was $N = 6(2)\times10^4$ atoms per spin state, yielding a Fermi temperature of $T_F = 180(20)$ nK. Impurity state thermometry was conducted by initially preparing the thermally equilibrated three-component Fermi gas in an identical manner. Subsequently, the population of atoms in state $|3\rangle$ was heated out of the gas using a pulse of on-resonance light at an intensity equal to 1/10 of the saturation intensity of the transition. As the light was detuned from the states $|1\rangle$ and $|2\rangle$ by more than $\delta = 2\pi \times 76$ MHz, off-resonant light scattering of atoms in these states was negligible. Subsequently, a minority component of state $|3\rangle$ atoms was repopulated from atoms in state $|2\rangle$ using a short, monochromatic RF pulse resonant with the $|2\rangle - |3\rangle$ transition. After an additional 20 ms hold time to allow for thermal equilibrium, the temperature and number of atoms in the minority component was probed.

By comparing the temperature of the minority component ($T = 50(10)$ nK) with the Fermi temperature previously recorded in the three-state sample, it was found that the three-component gas was degenerate with a reduced temperature $T/T_F = 0.28(6)$. Measurements of the population and temperature of the majority (state $|1\rangle$ atoms) component were consistent with the previous measurements in the balanced three-state mixture, assuring that the gas is not noticeably heated by the thermometry technique. At 1500 G, the difference in the mean field energies ($E_{ij}^{mf} = ng_{ij}$, where n is the density of atoms and $g_{ij} \propto a_{ij}$ is defined for a given pairwise interaction in Equation 2.18), is more than 1 order of magnitude smaller than any other energy scale in the system. In this way, we have demonstrated the viability of studying quantum physics in degenerate three-component Fermi gases which exhibit effective SU(3) symmetry. In Chapter 8, this system is explored in more detail, discussing the interesting many-body phases that are predicted to occur and the feasibility of using our system for many-body studies of strongly interacting three-component Fermi gases.

7.4 Recent Experiments in 3-State ^{6}Li Gases

As discussed in Section 3.2.1, enhanced loss in mixtures of atoms and dimers occur at the magnetic field values where an Efimov trimer state comes into resonance with the atom-dimer scattering threshold. In Figure 7.5, the calculated binding energies of the ground ($n = 0$) and first-excited ($n = 1$) high-field Efimov trimer states are shown in the vicinity of the atom-dimer threshold crossings [8]. These trimer states are predicted to come into resonance with the $|1\rangle - |23\rangle$ atom-dimer threshold at $B_*^{(1)} = 672 \pm 2$ G and $B_*^{(0)} = 597$ G respectively. In the magnetic field region below 730 G, the $|23\rangle$ dimer is the lowest-lying weakly bound dimer so that the only possible atom-dimer loss process for this mixture is relaxation into the deeply bound dimer states.

In Reference [8], E. Braaten and co-workers went on to make predictions of the magnetic-field dependent dimer relaxation rate constants, $\beta_{1(23)}$ as defined in Equation 3.31, for fields near the predicted crossing of the excited-state trimer with the $|1\rangle+|23\rangle$ atom-dimer threshold. Here, $\beta_{1(23)}$ is expected to be locally maximized at $B_*^{(1)}$, with a width that is set by the inelasticity parameter η_*. Assuming that the three-body parameters are constant throughout the high-field regime, which is one of the tenants of the universal theory, our measurements of κ_*^{hf} and η_*^{hf} should yield a peak in the $|1\rangle + |23\rangle$ atom-dimer loss rates at $B_*^{(1)} = 672 \pm 2$ G. The field dependence of the predicted atom-dimer resonance, calculated in Reference [8], is shown as the dashed line in Figure 7.8.

Two separate groups have recently published results for the inelastic atom-dimer decay rate coefficients in nearly-degenerate, ground-state ^{6}Li gases [210, 198]. In both References, the atom-dimer loss rate coefficients for mixtures of trapped atoms in state $|1\rangle$ and dimers associated from atoms occupying states $|2\rangle$ and $|3\rangle$ were measured over the range of fields 580 G $\lesssim B \lesssim$ 760 G. Their measurements both displayed resonant peaks in the measured atom-dimer loss coefficients $\beta_{1(23)}$ centered at 685 G and 602 G. Measurements made in our lab by Eric Hazlett of the $|1\rangle + |23\rangle$ atom-dimer loss rate coefficients near the upper resonance, shown as the red points in Figure 7.8, are in agreement with the published results. Although the peaks are likely associated with the $n = 1$ and $n = 0$ high-field Efimov trimer states crossing the $|1\rangle + |23\rangle$ atom-dimer threshold, the locations of the peaks vary

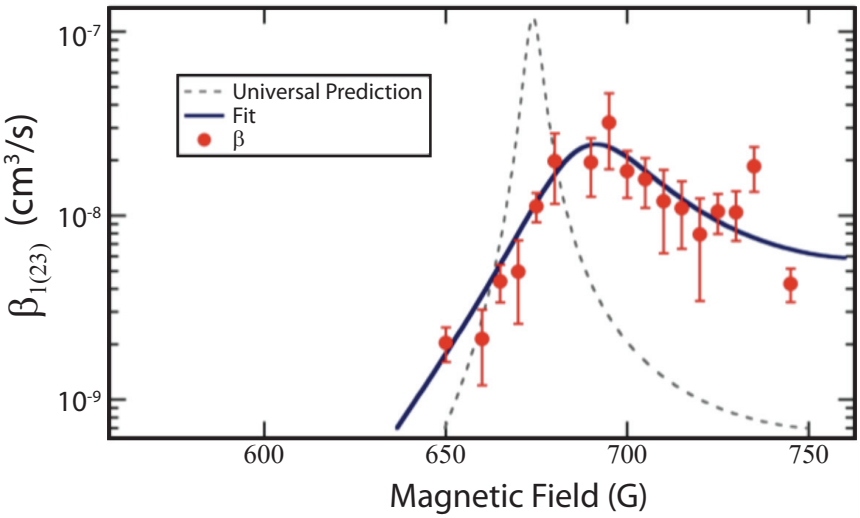

Figure 7.8. Dimer relaxation rate constant $\beta_{1(23)}$ for $|1\rangle + |23\rangle$ atom-dimer loss over the range of fields 650 G $\leq B \leq$ 750 G. The universal predictions, calculated in [8] based on our measurements of the high-field three-body parameters ($\kappa_{\simeq}6.9 \times 10^{-3} a_0^{-1}$ and $\eta_* \simeq 0.016$) (dashed line), are in disagreement with the experimental data (red dots) at these fields. A fit to the data using the universal calculations (solid curve) finds that the three-body parameters must be varied by approximately 30% to properly reproduce the measured atom-dimer loss rates which peak near 685 G.

significantly from those universal predictions in Reference [8].

T. Lompe *et al.* fit their measurements of the field-dependent atom-dimer loss rates to extract the three-body parameters using a formalism derived in Reference [8]. They find that the parameters must be varied by about 30% to properly fit the data near 685 G [198]. They point out that non-universal corrections are likely to play a role at these fields, as demonstrated by the fact that even at 685 G, the binding energy of the dimer deviates by $\sim 5\%$ from the universal predictions. The lower peak at 602 G also deviated from their fit, but this result is not surprising as the dimer state is no longer in the universal regime at this low field value.

S. Nakajima *et al.* went on to show that the locations of the atom-dimer loss peaks disagree with the universal theory predictions in a way that cannot be explained even with non-universal two-body corrections [210]. They used the STM formalism [8] to solve the three-body problem with zero-range interactions parameterized by energy-dependent scattering lengths. Even considering non-universal corrections to the two-body parameters $a(k)$, the predicted location of the second

resonance is unshifted at $\simeq$ 672 G unless the three-body parameters depend on energy as well, and possibly magnetic field. By including corrections to the short-range three-body parameters, however, they were able to obtain a good fit to their data, thereby making a first step at characterizing the non-universal three-body physics of ultracold, three-component ^{6}Li gases. Non-universal corrections near 685 G were not expected as all three scattering lengths are still resonantly enhanced near this field. The broad Feshbach resonances in ^{6}Li, however, allow for sensitive measurements of the limits of the universal theory, of which a great deal of work is left to be done.

In Reference [198], T. Lompe *et al.* also measured the loss rates in $|2\rangle + |13\rangle$ and $|3\rangle + |12\rangle$ atom-dimer mixtures. For these interactions, the measured decay rates $\beta_{A(BC)}$ includes loss events both into the deeply bound dimer states as well as in exchange processes of the form $|A\rangle + |BC\rangle \rightarrow |B\rangle + |AC\rangle$, where the free atom and one of the atoms constituting the weakly-bound dimer are exchanged in a small-energy exothermic process. They found two pronounced minima in $\beta_{3(12)}$ at 610 G and 695 G, where the loss rate was strongly suppressed. These features qualitatively agreed with the theoretical predictions by J. D'incao *et al.* that the existence of a trimer state can cause interference minima in the exchange reaction rates [142]. No distinct features were observed in $\beta_{2(13)}$.

The increase of the $|3\rangle + |12\rangle$ atom-dimer lifetime at the resonant fields may be useful for preparing samples in future experiments, and since all of the resonant features in the high-field regime should be universally connected, the locations of the $\beta_{3(12)}$ resonances may further shed light on the universality of the ^{6}Li gas in the vicinity of the three overlapping Feshbach resonances.

Finally, T. Lompe *et al.* recently published results of their RF spectroscopy measurements, in which they were able to directly observe the binding energies of the $n = 1$ Efimov state over the range of fields 670 G $\leq B \leq$ 740 G [211]. Here, the authors initially prepared mixtures of atoms in state $|2\rangle$ and $|12\rangle$ ($|23\rangle$) dimers at the field of interest. Subsequently, RF fields were applied to drive $|2\rangle \rightarrow |3\rangle$ ($|2\rangle \rightarrow |1\rangle$) transitions which, depending on the detuning of the pulse, can either (a) dissociate the dimer leading to three unbound atoms in states $|1\rangle$, $|2\rangle$, and $|3\rangle$; (b) flip the spin of the bare atom leading to $|3\rangle - |12\rangle$ ($|1\rangle - |23\rangle$) atom-dimer mixtures; or (c) associate the dimer and atom into a $|123\rangle$ Efimov trimer.

Their measurements constitute the first direct observation of the Efimov trimer state in any system, and yielded the binding energies of the Efimov trimer state throughout the range of fields studied. Their measurements of the trimer binding energies were also in good agreement with the predictions from the theoretical model discussed in Reference [210], which used the observed threshold crossings of the trimer states as inputs to calculate the trimer binding energies, including the necessary non-universal corrections to the three-body parameters. These RF association measurements have confirmed that within the range of measurements, the theory given in Reference [210] accurately describes the trimer binding energies in this system.

The rich spectrum of few-body phenomena that has been measured and predicted over the last few years have provided invaluable information relating to both the applicability of the universal theories to our system, and the behaviors of the gas in the vicinity of the three overlapping Feshbach resonances. The next logical step is to begin exploring the variety of many-body phases that emerge when the s-wave scattering lengths are unequal in magnitude and/or sign. In the next chapter, we discuss various theoretical investigations of the novel phenomena expected to emerge in this system. Further, based on our stability measurements of the gas, we can now consider the feasibility of realizing such many-body phenomena as superfluidity or magnetism in the high-field regime using our current experimental system. The inclusion of a third spin component to our ultracold Fermi gases has enabled the study of novel few-body interactions that are inaccessible in ultracold samples of identical bosons or two-component Fermi gases. In so doing, this system has revealed unique loss characteristics that shed light on previously unseen characteristics of the universal theory. It is to be expected that this will also be the case when exploring the many-body physics of three-component Fermi gases.

Chapter 8

Many-Body Physics in a Multi-Component Fermi Gas

This thesis was dedicated to studying few-body physics in three-component Fermi gases in the form of mapping out the spectrum of resonant Efimov features in ultracold ^{6}Li gases consisting of the three lowest-energy hyperfine spin states. Based on the recent experiments conducted with these systems and theoretical insights gained from interpreting the experimental results, discussed in Chapters 6 and 7, the few-body physics of ultracold multi-component gases is now becoming well understood. The next logical question relates to the feasibility of using our system to study some of the interesting many-body phenomena expected to arise in an ultracold gas of three distinguishable particles exhibiting three broad, overlapping Feshbach resonances.

This chapter begins with a brief overview of the superfluid phases that have been studied in ultracold two-component Fermi gases. A short review is then given of the various novel many-body phenomena that have been theoretically predicted to emerge when a third spin component is added to the system. The nature of the problem can change drastically whenever at least two interaction strengths are resonantly enhanced, allowing for effects which are generally forbidden in equal-population two-component Fermi gases. Such interactions include competition among various pairing states, phase separation, trimer formation, and even instability against collapse. Our previous measurements of the stability of the three-component ^{6}Li gas in the high-field regime can now be used to determine

the feasibility of experimentally studying some of these novel phenomena using ultracold ^{6}Li gases occupying the three states discussed in this thesis.

Then, a brief review of the physics of two- and three-component Fermi gases loaded into three-dimensional optical lattice potentials is discussed. The lattice breaks the effective translational symmetry of the system, causing the atoms to become more localized at the lattice sites and enhancing the strength of the interactions that give rise to many-body phenomena. For attractive pairwise interactions, lattice confinement has been shown to enhance the superfluid critical temperature [72], which is promising for observing multiple superfluid pairing states in three-component Fermi gases at high fields where the gas exhibits SU(3) symmetry. This *atomic color superfluid* phase would be particularly interesting due to a close analogy with the color superconducting phase in two-flavor quantum chromodynamics (QCD) [91], and may open the door to future quantum simulation of a simplified version of the QCD phase diagram with ultracold quantum gases.

In the repulsively interacting regime, quantum magnetism and possibly d-wave superfluidity is expected to emerge in lattice-confined two-component Fermi gases at sufficiently low temperatures. The behavior of the three-component Fermi gas in the regime where at least one of the scattering lengths is positive is currently an open question, both experimentally and theoretically. It can be expected, however, that for sufficiently long-lived samples at low temperatures, novel phases should emerge when the particles exhibit anisotropic, resonantly enhanced interactions where the ground-state of each pair tends toward magnetic ordering and/or Fermionic superfluid phases. Temperatures low enough to observe such exotic phases have yet to be achieved, however, in even two-component ultracold Fermi systems.

The chapter is concluded by discussing a cooling method that we proposed to prepare fermionic atoms in a three-dimensional optical lattice potential at unprecedentedly low temperatures and uniform filling factors. The method involves adiabatic loading of a degenerate two-component Fermi gas into a combined optical lattice and "box-like" trapping potential, followed by selective removal of atoms from all but the lowest energy band. Numerical calculations for sample sizes $\sim 10^5$ predict that temperatures $\sim 0.003\ T_F$, corresponding to an entropy per particle of $\sim 0.02\ k_B$ can be achieved. Two-component Fermi gases prepared in this manner

should be sufficiently cold to begin exploring quantum spin phases of fermionic atoms [72, 73, 74], which are currently inaccessible.

8.1 Superfluidity in 2-Component Fermi Gases

Superfluidity is one of the most spectacular properties associated with quantum degenerate systems. This phenomena, which is generally associated with condenstaion, is characterized by frictionless flow and persisting quantized vorticies. For degenerate Fermi gases, magnetically tuned Feshbach resonances in two-component gases have allowed the various regimes of fermion pairing and superfluidity to be experimentally realized. Multiple interacting spin components are required, however, to realize the superfluid phase as condensation is not allowed for single Fermi components by the exclusion principle.

Pairing on the BEC side of the resonance, where $a > 0$, can be understood in terms of condensed bosonic molecules consisting of one atom from each spin state. This case was considered in detail in Section 5.1.1, where we demonstrated that ultracold two-component Fermi gases can form long-lived, weakly-bound dimer states at magnetic fields where the pairwise interactions are resonantly enhanced. At sufficiently low temperatures, a molecular Bose-Einstein Condensate emerges, which has been shown to demonstrate superfluid behavior from the emergence of quantized vorticies in the time-of-flight images of rotated Fermi gases [22]. In a harmonically trapped sample, the critical temperature for molecular condensation scales with the Fermi energy as [108]

$$T_c^{BEC} \approx 0.22 T_F, \tag{8.1}$$

where T_F is defined as the Fermi energy in the non-interacting limit. The success of realizing the superfluid phase lies in the low inelastic loss rates of two-component Fermi gases, where the combined phase-space density and temperature of the gas define the required densities and interaction strengths to achieve stable molecular gases with sufficient degeneracy to Bose-condense.

For attractive pairwise interactions $a < 0$, no universal dimer state exists to allow for the formation of a molecular BEC. The pairing mechanism for these

fermions is a many-body effect, where the ground state of the system at zero temperature is a fermionic superfluid. In the weakly interacting regime, the pairing mechanism is described by Bardeen-Cooper-Schrieffer (BCS) theory, which was first derived to explain the phenomena of superconductivity [47, 48], but also accurately described the properties of superfluid ^{3}He. BCS theory predicts that the three-dimensional Fermi sea is unstable in the presence of arbitrarily small attractive interactions, preferring to form bound states (Cooper pairs) with exponentially small binding energies. The pairs can then Bose-condense at a critical temperature given by

$$T_c^{BCS} \approx 0.28\ T_F \exp\left(\frac{\pi}{2k_F a}\right), \tag{8.2}$$

where k_F is the Fermi wavevector, defined in terms of the Fermi energy as $E_F = \hbar^2 k_F^2/(2m)$. For temperatures below the critical temperature, the Fermi gas has been shown to exhibit superfluid behavior [22] due to the presence of a finite gap in the single-particle excitation spectrum ($\Delta_{gap} \approx 1.76\ k_B T_c^{BCS}$). For realistic values of $k_F a$ in ultracold Fermi gas experiments, the transition temperature quickly becomes prohibitively small, making observation of the true BCS state difficult.

It is now well understood that the pairing mechanisms in both limits (BEC and BCS) are smoothly connected by a crossover through the universal regime. The interaction regime is characterized by the dimensionless parameter $k_F a$, where $(k_F a)^{-1} \gg 1$ corresponds to the molecular BEC regime and for $(k_F a)^{-1} \ll -1$, the system is in the BCS regime. In between these extremes, the fermi gas is strongly interacting, allowing for a significant enhancement of the BCS critical temperature. It was discussed in Section 2.5 how the low-energy scattering properties of the gas scale in the unitarity regime, where the s-wave scattering length a greatly exceeds all other length scales in the problem. At unitarity, the critical superfluid temperature must also scale with the Fermi temperature as $T_c = \alpha T_F$, where α is a universal dimensionless parameter. Theoretical predictions [212, 213, 214] and experimental observations [59] of condensates at unitarity have placed $\alpha \approx 0.2$.

Recent experiments have also studied superfluidity in spin-imbalanced samples, in which the gas contains an unequal number of atoms in the two components. A breakdown of superfluidity was observed above a critical imbalance in addition to a spatial separation of a superfluid core surrounded by a partially-polarized

shell of thermal atoms [215, 216, 217, 218]. In this system of strongly-interacting polarized Fermi gases, a rich phase diagram has emerged, exhibiting two superfluid phases and a tricritical point, where the phase transitions can be either of first or second order. Additional phases associated with deformed Fermi surfaces (DFS) and spatially oscillating order parameters (FFLO) are predicted but have not yet been observed [219, 218].

The stability of two-component Fermi gases against two- and three-body inelastic loss was instrumental to the realization of superfluidity in both the spin-balanced and spin-polarized Fermi gas experiments. These experiments have revealed an extensive new body of knowledge to the many-body physics of strongly-interacting systems. The next section briefly reviews some of the novel many-body phenomena theoretically predicted to arise in an ultracold Fermi gas consisting of three mutually-interacting spin components. Further, based on our previous stability measurements, we discuss the feasibility of realizing fermionic superfluidity in a gas of ^{6}Li atoms equally occupying states $|1\rangle$, $|2\rangle$, and $|3\rangle$.

8.2 Many-Body Physics in 3-Component Fermi Gases

For a two-component Fermi gas in the universal regime, the system can be fully described by the scattering length a. The addition of the third spin component significantly changes the nature of the problem, where three distinct interaction strengths determine the ground state of the system. Further, a sample of three distinguishable fermions has a completely different symmetry, approaching SU(3) at high fields, compared to the SU(2) symmetry of two-component gases. SU(3) symmetry is also exhibited by the three different color of quarks in QCD. This analogy was recently noted by Nobel laureate F. Wilczek [92] as a potentially useful model system to explore the properties of low-temperature quark matter. Over the last 5 years, there has been a remarkable theoretical effort exploring these interacting three-body systems. Some of the interesting issues that have been considered include:

- Two component Fermi gases are stable against collapse even when the inter-

actions are tuned to infinity. Stability is no longer guaranteed if a third or fourth component is added [220], possibly leading to collapse analogous to the bosenova instability for trapped Bose gases with attractive interactions [221].

- At sufficiently low temperatures, two-component mixtures pair to form a superfluid. It is unknown how this phenomena translates for three mutually-interacting particles. Pairing competition may now emerge, in which two-components which would by themselves pair can now be cannibalized by a third component. This mechanism could determine the number of pairing states that will be mutually allowed. Further, first and second order phase transitions at finite temperatures between different paired states and the normal unpaired states have been predicted [84, 87, 85, 88, 222, 86, 203, 223].

- It is also questionable whether multiple paired phases can coexist in the same spatial region. In certain systems, depending on the anisotropy of the chemical potential, density, and strength of the pairwise interactions, the three-component Fermi gas is expected to form phase domains, shell structures, and/or breached pairing [224, 89, 222, 225, 226].

- It is predicted that in some instances, the critical temperature for the BCS superfluid transition can deviate from that predicted in a weakly interacting two-component system due to many-body contributions to the effective interaction between fermions in a three-component Fermi mixture [85, 227].

- It is unknown what the ground state of the system is when loaded into a one- or three-dimensional optical lattice. Dependent on the atomic density and the strength and anisotropy of the interactions, various density-waves and ordered states are expected [228, 229, 230]. Further, quantum phase transitions between superfluid and trion phases are predicted [84]. In response to a local perturbation in 1D, color-charge separation (analogous to spin-charge separation predicted by Luttinger Liquid theory [231]) may emerge [232]. It has also been proposed that strong three-body loss can be utilized to stabilize the paired superfluid phase in the optical lattice. [233]

- Under certain limits, the three scattering lengths for our three-component gas converge while still exhibiting resonantly enhanced interactions. In a 3D optical lattice, the system is well described by a SU(3) symmetric Hubbard Hamiltonian. Here, a color superfluid to trion phase transition may be applicable for simulating the physics of strongly interacting sub-atomic and fundamental particles such as the color superfluid to Baryon phase transition conjectured in QCD [90, 91, 92].

The similarity of these three-component Fermi gases to strongly interacting nuclear and quark matter, along with the extensive theoretical consideration of the system, demonstrates the potential impact that research with three-component Fermi gases could have on a broad range of physical disciplines. Experimental realization of these systems would shed light on the dependence of the above phenomena on such parameters as the chemical potential, mass ratio, temperature, and individual interaction strengths of the particles in the system.

8.2.1 Superfluidity vs. Stability in 3-State ^{6}Li Gases

Our measurements of the stability of the three-component ^{6}Li gas in the high-field regime can now be used to determine the feasibility of experimentally realizing superfluidity in this system to explore some of the novel phenomena discussed above. Essentially, superfluidity can be realized so long as at least two components of the gas have sufficient interaction strengths to support pairing. The strength of the interactions are parameterized by the density and pairwise interaction strengths as $k_F a$, where a is the s-wave scattering length for the pairing states and the Fermi wavevector is related to the peak density of the gas as $k_F^3 = 6\pi^2 n_0$. The temperature and density requirements to realize the BEC and BCS superfluid phases are constrained by Equations 8.1 and 8.2 respectively.

In contrast to the two-component experiments, where the gas is stable against two and three-body loss for fields above the 834 G Feshbach resonance, observing many-body effects in our three-component ^{6}Li gases is complicated by the significant three-body loss rates in this regime. Superfluidity cannot emerge unless the pair formation rate $\tau_{BCS} \propto (k_B T_c)/\hbar$ [109, 234] exceeds the rate of three-body loss $\tau_{K_3} = \dot{N}/N \simeq -K_3\langle n^2 \rangle$, given by Equation 6.2. Constraints on the temperature

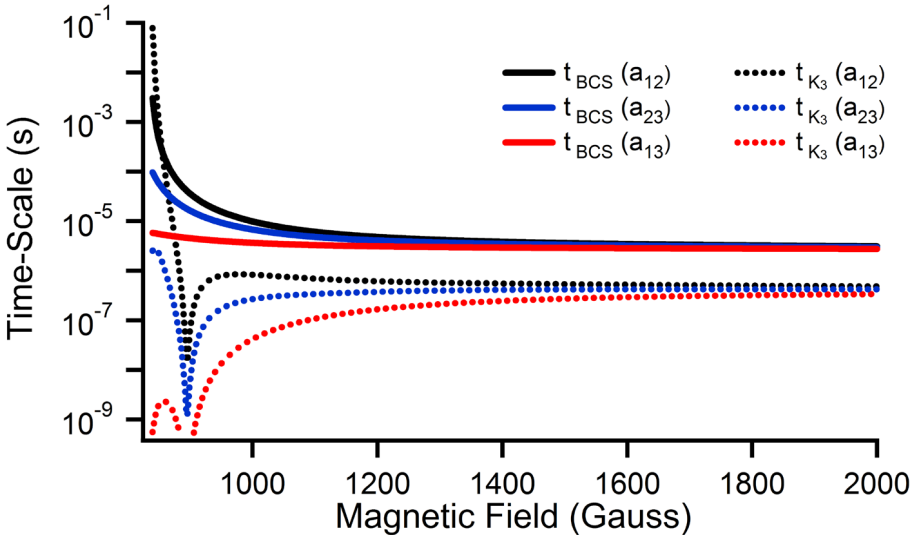

Figure 8.1. The calculated timescales for both BCS pairing (t_{BCS}, solid curves) and three-body loss (t_{k_3}, dotted curves) in the high-field BCS regime below $B \leq 2000$ G are shown. The atomic densities are varied so that the critical temperature is $T_c = 0.15T_F$ for each of the possible pairing states ($|1\rangle - |2\rangle$ (black), $|2\rangle - |3\rangle$ (blue), and $|1\rangle - |3\rangle$ (red)). Superfluid pairing is inhibited by rapid three-body loss for all pairing states throughout the BCS regime except for the $|1\rangle - |2\rangle$ pairing states near 834 Gauss.

and density of the gas are difficult to simultaneously satisfy. We have demonstrated long atomic lifetimes, even in the high three-body loss regimes near the 834 G Feshbach resonance, by expanding the gas to densities as low as $n_0 \leq 5 \times 10^9/\text{cm}^3$ in our large-volume traps. Even though the interactions are resonantly enhanced in this regime, however, the gas is still weakly interacting.

At 1500 G, for example, a gas at a density of even $n_0 = 3 \times 10^{11}/\text{cm}^3$ can survive for a time $t_{K_3} = \tau_{K_3}^{-1} \simeq 100$ ms, which is on the order of our three-state creation timescales. Here, the gas is in the SU(3) symmetric regime which is particularly interesting for studies of pairing competition and spontaneous symmetry breaking phenomena. At this density, $k_F a \simeq -0.39$ which translates to a critical BCS temperature of $T_c^{BCS} \simeq 4 \times 10^{-3} T_F$. It is inconceivable to cool our samples to such low temperatures, approximately an order of magnitude smaller than the current state-of-the-art reduced temperatures achieved with even two-component Fermi gases.

To further explore the possibility of observing superfluidity in three-component ^{6}Li gases in the high-field BCS regime ($B \geq 834$ G), we take as an assumption

that it is possible to create a degenerate three-state Fermi gas with reduced temperatures as low as $T/T_F = 0.15$. Equation 8.2 then requires that the gas must be sufficiently strongly interacting ($k_F a \simeq -2.5$) for superfluid pairing to emerge. In Figure 8.1, the calculated timescales for both BCS pairing ($t_{BCS} = \tau_{BCS}^{-1}$, solid curves) and three-body loss ($t_{k_3} = \tau_{K_3}^{-1}$, dotted curves) in the high-field BCS regime below $B \leq 2000$ G are shown. Here, the density of the gas was varied at each field so that the critical temperature remained constant at $T_c = 0.15 T_F$. The three-body loss rates used in this calculation were taken from the universal, zero-temperature fit to our high-field data, given by the dotted line in Figure 7.4. As the three scattering lengths were generally unequal, the density of the gas at each field determines whether one, two, or all three of the pairing states satisfy the temperature requirements for superfluidity to emerge. The BCS pairing and three-body loss timescales at which each of the possible pairing states, $|1\rangle - |2\rangle$ (black), $|2\rangle - |3\rangle$ (blue), and $|1\rangle - |3\rangle$ (red), has sufficient density for BCS pairing are therefore shown explicitly in Figure 8.1. Although BCS theory is not strictly justified in this strongly interacting regime, the temperature of the gas is still constrained below the critical temperature at unitarity $T_c \approx 0.2 T_F$, and should provide order-of-magnitude estimations of the relevant BEC formation and three-body loss timescales.

At high fields, the three-component Fermi gas is SU(3) symmetric, where the required densities to achieve BCS pairing for all three components converge. At the high critical temperatures we consider here, however, the three-body loss rates exceed the BCS pairing rates by nearly an order of magnitude so that the gas will decay before superfluidity can emerge. Superfluid pairing is in-fact inhibited by three-body loss for all pairing states throughout the BCS regime except for the $|1\rangle - |2\rangle$ pairing states below 856 Gauss. Here, the BCS pairing rate exceeds the K_3 loss rate since a_{12} is enhanced near the 834 G Feshbach resonance whereas the K_3 rates are dependent on all three interaction strengths.

At 840 G, a gas with a density of $n_0 \simeq 5 \times 10^9/\mathrm{cm}^3$ has a critical temperature of $T_c \simeq 0.15 T_F$ in the $|1\rangle - |2\rangle$ BCS pairing channel. In this case, the lifetime of the gas from three-body loss is $t_{k_3} \simeq 80$ ms, as compared to the BCS pairing timescale which is $t_{BCS}(a_{ij}) \simeq 3$ ms. It should be possible with our current apparatus to realize this BCS superfluid phase, however, the other components are normal

and very weakly interacting at this density and field. No pairing competition is expected, with a two-component superfluid and a superimposed weakly interacting gas of atoms in state $|3\rangle$ as the expected equilibrium states.

8.2.2 BECs and Phase Separation in 3-State ^{6}Li Gases

It is also interesting to consider the possibility of observing many-body phenomena and superfluidity in three-component ^{6}Li gases at fields below the 834 G Feshbach resonance, in which universal dimer states exist and mutual attractive and repulsive pairwise interactions can compete to define the ground state of the system. For equal populations in the three spin states, depending on the temperature and density of the gas, either a normal three-component Fermi gas, a Bose-Einstein condensate of dimers coexisting with a normal Fermi gas of the complementary atoms, multiple Bose-Einstein condensates of dimers, and even coexisting or competing BEC and BCS superfluid phases may exist. In all cases, interesting many-body effects can arise so long as the gas is sufficiently cold and long-lived.

A recent experiment with two-component ^{6}Li Fermi gases occupying states $|1\rangle$ and $|2\rangle$ has demonstrated that with sufficiently strong repulsive interactions, the spin-components of the gas separate to minimize the total energy of the system [235]. The phase-separation, referred to as *itenerant ferromagnetism*, is predicted to occur at a critical interaction strength $k_F a = \pi/2$, when the mean-field energy exceeds the kinetic energy cost for phase-separating. For our three-component Fermi gas, an itenerant ferromagnetic phase may emerge below the 834 G Feshbach resonance, but the inclusion of the third spin-state $|3\rangle$ may also significantly alter the ground-state of the system. Consider the gas at 670 G, where all three states are repulsively interacting with $a_{12} = +1086\ a_0$, $a_{23} = +807\ a_0$, and $a_{13} = +8576\ a_0$, and the three-body loss rates are predicted to be $K_3 \simeq 10^{-22}$ cm^6/s [8]. Here, it is expected that phase separation will occur as long as $k_F a \geq \pi/2$ for any two components, and all three components may phase separate when the pairwise interactions are sufficiently strongly interacting for all atoms in the gas. The critical densities required for $k_F a_{13} = \pi/2$ (all $k_F a_{ij} \geq \pi/2$) are $n_{crit} = 8.3 \times 10^{11}/\text{cm}^3$ ($10^{15}/\text{cm}^3$). At the lowest density considered, the expected lifetime of the gas is $t_{K_3} \simeq 75$ ms, which is reasonable with our current experimental methodology. When the densi-

ties are increased so that the gas satisfies the itenerant ferromagnetism criterion for at least two or three pairwise interactions, however, the lifetime of the gas drops below $t_{K_3} < 1$ μs.

At sufficiently low temperatures, one or multiple spin-components are expected to form a BEC of dimers. Here, we consider the many-body system at 731 G, where the gas is SU(2) symmetric with $a_{12} = a_{23} = +2500\ a_0$ and $a_{13} = -7100\ a_0$. If the gas is prepared with atoms of type $|1\rangle$ coexisting with a $|23\rangle$ dimer condensate, the mean-field energy of the atom is estimated by $E^{mf}_{1(23)} \simeq 2 \times 10^{-9}$ Hz cm^3 $\times(2\pi\hbar n_{(23)})$ [8]. The positive sign implies that the atoms are repelled by the $|23\rangle$ dimer condensate, possibly leading to phase separation. However, the $|23\rangle$ dimers are energetically degenerate with the $|12\rangle$ dimer states, so pairing competition may also come into play. The lifetime of the atom-dimer gas, given by Equation 3.31, is determined by the dimer relaxation rates $\beta_{1(23)} = \beta_{3(12)} \simeq 8 \times 10^9$ cm^3/s (see Figure 7.8), which are equal at this field by the SU(2) symmetry. At densities on the order of $n_0 \simeq 10^9/\text{cm}^3$, where the lifetime of the gas $t_{1(23)} = t_{3(12)} \simeq 100$ ms, the mean-field energy is $E^{mf}_{1(23)} \simeq k_B \times 0.12$nK, much smaller than the Fermi energy of the state $|1\rangle$ atoms ($E_F \simeq k_B \times 7nK$). Although phase separation is not likely at these densities and temperatures, pairing competition may lead to interesting many-body effects, justifying more experimental and theoretical study.

8.3 Many-Body Physics in Optical Lattices

We have seen previously that for our dilute three-component atomic Fermi gases, the gas must generally be in the regime where the Fermi momentum is small as compared to at least two of the scattering lengths ($k_F a_{ij} < 1$) for the atoms to have sufficient lifetime against three-body decay to enable creation and thermal equilibrium of the samples. In this regime, the superfluid critical temperature is prohibitively low in bulk, harmonically trapped samples to realize pairing in three-component gases with mutual superfluid components. On the other hand, if the atoms are confined in a periodic potential then the effects due to interactions, and hence the critical BCS temperatures, can be greatly enhanced.

Such potentials can be experimentally realized for cold atomic gases in one, two, or three dimensions from the interference pattern of multiple coherent laser beams.

Two-component Fermi gases loaded into these so-called optical lattice potentials are nearly-ideal quantum simulators for the Fermi Hubbard model [71], providing a testing ground for paradigm models of condensed matter physics [72, 73, 74]. By loading ultracold three-component Fermi gases into these periodic potentials, the existence of multiple pairing states and the inclusion of the trion, in which three atoms occupy the same quantum state, may be used to study phenomena beyond the well-established framework of condensed matter physics [91].

8.3.1 Optical Lattice Potentials for Ultracold Fermions

An optical lattice potential can most easily be created from the dipole trapping profile realized with superimposed counter-propagating laser beams. If the beams are derived from a single-longitudinal mode laser, the interference pattern results in a standing-wave intensity profile, where the atoms are attracted to or repulsed from the periodic intensity maxima dependent on whether the light is red or blue detuned with respect to the atomic transitions. Further, by focusing three mutually-perpendicular, retro-reflected lasers onto the atomic gas, a three-dimensional optical lattice can be formed, as illustrated in Figure 8.2(a). For identical lattice beams, so long as the interferences between standing waves are suppressed, the atoms at ultracold temperatures will experience a simple cubic lattice potential given of the form [236]

$$V(x_i) = V_0 \sum_{i=1}^{3} \sin^2(k_L x_i) + \frac{m}{2}\omega^2 x_i^2 \tag{8.3}$$

where k_L is the wave vector of the light and V_0 is the depth of the potential wells, typically expressed in units of the atomic recoil energy $E_R = \hbar^2 k_L^2/2m$, along each direction i. The ω^2 terms are the squares of the effective trapping frequencies of the external harmonic confinement due to the Gaussian profile of the lattice laser beams (see Section 4.6).

If the amplitudes of the lasers are sufficiently intense, then the ultracold atoms are localized to the minima of each of the optical potential wells and can only move by tunneling between the lowest lying states within each well. In this tight-binding limit, the atoms are effectively confined by an array of harmonic potentials

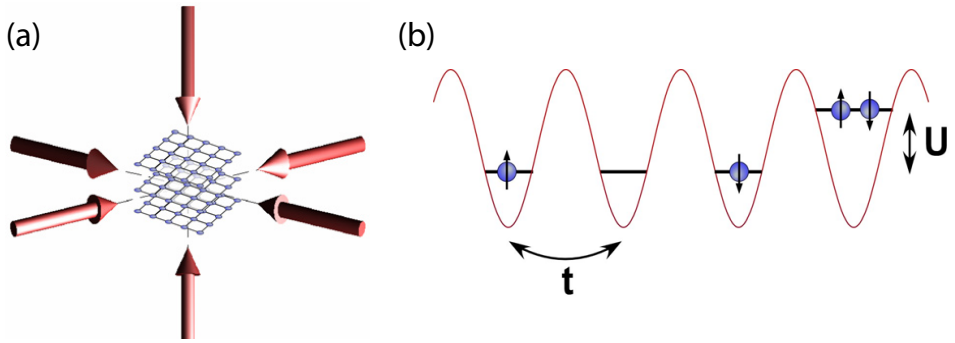

Figure 8.2. (a) Illustration of a 3D cubic lattice potential for the atoms, formed from the standing-wave interference patterns of three mutually-orthogonal pairs of counter-propagating laser beams. (b) A two-component Fermi gas with repulsive interactions loaded into an idealized lattice potential is shown along one dimension. The system is well-described by the Fermi Hubbard model, where t is the tunneling matrix element and U denotes the on-site interaction energy term.

with corresponding trapping frequencies at the center of each trap given by $\omega_L^2 = 2k_L^2\ V_0/m$. For retro-reflected beams, the lattice constant in each direction is directly related to the wavelength of the laser light (λ_L) from which the optical lattice is derived. Larger period lattices can also be realized by propagating the interfering lattice beams at small relative angles (θ), yielding lattice constants of $d(\theta) = \lambda_L/(2\sin(\theta/2))$ [237].

Further, if the atomic scattering lengths are smaller than the optical lattice constant, then the interactions are restricted to each lattice site. Correspondingly, for very cold atoms confined in a deep optical lattice ($k_BT, E_F \ll \hbar\omega_L$), and ignoring the effects of the confining potential in Equation 8.3, the system of interacting atoms is well described by the following Hamiltonian [91]

$$H = -t \sum_{\langle i,j\rangle,\alpha} \hat{c}_{i\alpha}^{+}\hat{c}_{j\alpha} + \sum_{\alpha\neq\beta}\sum_{i} \frac{U_{\alpha,\beta}}{2}(\hat{n}_{i\alpha}\hat{n}_{i\beta}), \tag{8.4}$$

where $\hat{c}_{i\alpha}^{+}$ is the creation operator of a fermionic atom in component α at site i, and $\hat{n}_{i\alpha} = \hat{c}_{i\alpha}^{+}\hat{c}_{i\alpha}$.

The first term in the Hamiltonian is the tunneling term, which describes the tunneling of atoms between neighboring potential wells, denoted by $\langle i, j\rangle$. The strength of the tunnel coupling is characterized by the tunneling matrix element

approximately given by [71, 72]

$$t \simeq \frac{2E_R}{\sqrt{\pi}} s^{3/4} e^{-2\sqrt{s}}, \tag{8.5}$$

where $s = V_0/E_R$. This kinetic energy term causes each atom in the ensemble to delocalize over the lattice.

The second term describes the interactions between spin-components α and β mutually occupying a single lattice site. The interaction term $U_{\alpha\beta}$ is related to the s-wave scattering length ($a_{\alpha\beta}$) as [71, 72]

$$U_{\alpha\beta} \simeq E_R a_{\alpha\beta} k_L \sqrt{8/\pi} s^{3/4}. \tag{8.6}$$

The interaction energy of the system is well described by this term, which generally tends to localize atoms on a given lattice site.

For a two-component gas, the Hamiltonian in Equation 8.4 corresponds to the Fermi Hubbard Hamiltonian, originally proposed as a phenomenological model for studying solid-state systems. In Figure 8.2(b), a two-component Fermi gas loaded into an idealized optical lattice is illustrated along one dimension. Here, the s-wave interactions are repulsive ($U > 0$) so that it is energetically unfavorable for multiple spin-components to occupy a given lattice site. Equations 8.5 and 8.6 demonstrate that by loading multi-component fermionic atoms into a deep optical lattice, a new degree of freedom is now available to vary the strength of the on-site interactions ($U_{\alpha\beta}$) and the magnitude of the tunneling matrix elements (t) through the depth of the optical lattice potential (s). Further, the on-site interaction energy can take on either positive or negative values depending on the sign of the s-wave scattering lengths to realize a range of many-body phases that may otherwise be prohibited in bulk Fermi gases.

8.3.2 BCS Superfluidity in a Lattice

It is the interplay of the terms t, U, and the filling factor ρ (defined as the average number of atoms per spin species per lattice cite) that define the ground state of the system. Consider first the case where $U < 0$. Previously, we discussed that attractive s-wave interactions ($a_{if} < 0$) can give rise to a BCS superfluid phase

for Fermi gases occupying multiple spin components. The exponential suppression of the critical temperature T_c^{BCS} for moderate values of $k_F a$ makes it extremely difficult to observe BCS pairing in bulk systems outside of the unitarity regime. In a periodic system, however, the effects due to interactions can be enhanced.

In Reference [72], W. Hofstetter *et al.* predicted that for attractively interacting two-component fermions in a shallow 3D optical lattice, where $t \gg |U|$, the BCS critical temperature scales as

$$T_c^{BCS} \approx t e^{-7t/|U|}. \tag{8.7}$$

As the depth of the optical potential is increased the atoms become more localized, with increased on-site interaction strength U and a decrease in the tunneling t. The combined effects lead to an exponential suppression of $t/|U|$, with a dramatic increase of T_c^{BCS}. As the on-site interactions become comparable with the tunneling energy, atom pairs are formed within a single lattice site with reduced mobility, leading to a decrease in T_c^{BCS}. At the crossover between the two regimes (where $U \sim 10t$), the critical temperature is maximized at

$$k_B T_c^{max} \simeq 0.3 E_F^{free} k_L |a_{ij}|, \tag{8.8}$$

where $E_F^{free} = (3/\pi)^{2/3} E_R$ at half-filling (approximately one atom per lattice site). T_c^{BCS} now scales linearly with the small parameter $k_L|a_{ij}|$, which is a dramatic improvement over the exponential suppression in bulk gases.

We propose using the enhancement of the BCS critical temperature to realize BCS pairing in a three-component gas of ^{6}Li atoms loaded at low densities into a weak cubic optical lattice potential. Consider a large-period optical lattice with lattice constant $d = 2$ μm. Loading a three-component ^{6}Li gas into the lattice with a filling factor of 1/3 (one atom on average per lattice cite) translates to a density of $n_0 = 1.25 \times 10^{11}/\text{cm}^3$. At high fields where the gas exhibits SU(3) symmetry and attractive pairwise interactions can support three distinct BCS superfluid phases, the lifetime is on the order of $t_{K_3} \simeq 200$ ms. If the lattice depth is raised to even $V_0 = 3E_R$, the BCS critical temperature is now increased to $T_c^{BCS} \simeq 0.2 T_F$, which is only slightly lower than the reduced temperatures that we previously achieved in our three-component samples at 1500 Gauss (see Section 7.3). Further,

the timescale for pair formation is expected to be on the order of $t_{BCS} \simeq 2$ ms, approximately two orders of magnitude shorter than the lifetime of the gas at this density. Such large-period optical lattices are readily available by designing the geometry of the lattice beams such that, for each interfering lattice beam pair, the lasers are propagated at a small relative angle [237], and BCS superfluidity has already been demonstrated with two-component Fermi gases loaded into a weak lattice potential [80]. It is anticipated that this proposed method should be directly experimentally realizable to study color superfluid phases in a degenerate, three-component ^{6}Li gas.

8.3.3 Magnetic Ordering of Ultracold Fermi Gases

Theoretical studies of two-component Fermi gases loaded into optical lattices with repulsive pairwise interactions ($U > 0$) have predicted that a number of exotic phases emerge at low temperatures [72, 73, 74]. The two most notable quantum phases predicted are:

Antiferromagnetic ordering is predicted near half-filling (one atom per lattice site). For sufficiently strong coupling (U/t), the lowest energy state is a two-sublattice spin ordering with a doubling of the unit cell as shown in Figure 8.3(b). Realization of this ordered phase would be an important first step towards quantum simulation of the low-temperature phase-diagram of the Fermi Hubbard model, as shown in a simplified version in Figure 8.3(a).

d-wave superfluidity is expected to emerge as the ground-state of the system when the filling factor is significantly decreased below 1/2, as shown in Figure 8.3(a). This phase is a suggested pairing mechanism responsible for high T_c superconductivity in the cuprates [238]. Therefore, quantum simulation of this exotic phase could be quite important for understanding doped Mott insulators in the strongly correlated regime.

However, temperatures low enough to observe such phases have yet to be attained in cold-atom-based Fermi systems. The lowest entropy per particle reported to date for two-component fermions in an optical lattice is $0.77k_B$ [239]. This exceeds the entropy at the antiferromagnetic (Néel) transition ($s_H \simeq ln(2)/2$) by more than a factor of two [74].

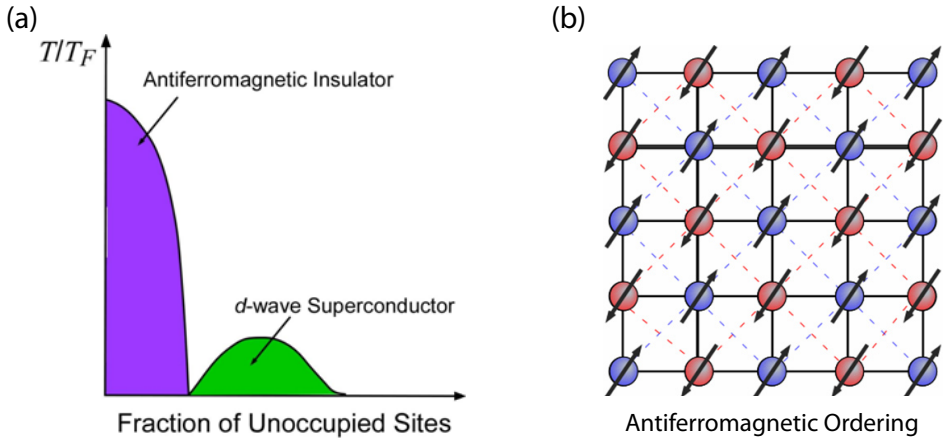

Figure 8.3. (a) Conjectured low-energy phase diagram of the Fermi Hubbard model. As the reduced temperature of the gas is decreased below a critical (Néel) temperature, antiferromagnetic ordering emerges at low unoccupied site fractions ($\rho \approx 1/2$). At lower filling fractions, a d-wave superfluid phase is expected to emerge at very low temperatures. (b) Antiferromagnetism is characterized by a spin ordering with alternating spins on neighboring lattice sites, leading to a bipartite lattice with a doubling of the unit cell (dashed lines).

It is not obvious what the ground state will be for a three-component ^{6}Li gas loaded into an optical lattice when at least one of the scattering lengths is positive. Recent theoretical investigations of fermionic alkaline earth atoms in optical lattice potentials, which exhibit SU(N) symmetry due to the lack of hyperfine coupling in the $N = 2I + 1$ nuclear spin states, have demonstrated that these systems can realize a variety of model correlated systems, many of which lack solid-state analogs [240, 241]. In contrast to the magnetic ordering expected in two-component Fermi gases, which exhibit SU(2) symmetry, it is found that for $N \geq 3$ there is a degeneracy of the classical ground states. These results suggest that for a repulsively interacting three-component Fermi gas with SU(3) symmetry, the magnetic order is underconstrained leading to geometric frustration even in a cubic lattice geometry.

For the three lowest hyperfine states of ^{6}Li at fields between 650 G $\leq B \leq$ 834 G, any number of the pairwise interactions can be repulsive and the three scattering lengths are resonantly enhanced leading to strong correlation in even moderately deep lattice potentials. The three overlapping Feshbach resonances, which yield widely varying strengths and anisotropies of the three pairwise interactions, provide a large parameter space for novel phases to emerge in our three-component system.

Here, SU(2) is the highest symmetry class at any field suggesting that magnetic ordering may again emerge at low temperatures. If all three interaction terms ($U_{\alpha,\beta}$) in Equation 8.4 are positive then magnetic ordering, frustrated magnetism, phase separation, and charge density states may emerge depending on the filling factor and anisotropy of the interactions. If, on the other hand, at least one of the interaction terms is negative, BCS pairing may also compete with magnetic ordering to define the ground state of the system.

Undoubtedly, two-component ^{6}Li atoms loaded into optical lattices will prove ideal for quantum simulation of the novel phases predicted by the Fermi Hubbard model. However, the observation of the antiferromagnetic phase in such two-component gases has remained elusive due to the low temperature/entropy requirements. By adding a third spin-component to the lattice, color superfluidity in a SU(3) symmetric gas should be realizable. The close analogy of this system with the color superconducting phase in two-flavor QCD [91] may open the door to future quantum simulation of a simplified version of the QCD phase diagram with ultracold quantum gases. Further, the magnetic ground state of three-component ^{6}Li gases in a lattice is currently unknown, but the system offers a promising foundation for realizing novel phases which may exhibit physics beyond the paradigms considered in condensed matter theory. It is likely, however, that very low temperature/entropy gases will be required to study the phase diagram of the system, and exploring new methods of cooling (removing entropy from) multi-component Fermi gases loaded into optical lattices is therefore of critical importance.

8.4 Preparing a Highly Degenerate Fermi Gas in an Optical Lattice

Previous to our findings with three-component Fermi gases, we began exploring methods of cooling two-component Fermi gases directly in a 3D optical lattice to begin mapping out the phase diagram of the Fermi Hubbard model. Methods for removing entropy considered elsewhere include defect filtering in a state-dependent optical lattice [242], compacting atoms in a site-addressable lattice [243], algorithmic filtering in a one-dimensional (1D) optical lattice in the presence of harmonic

confinement [244], and expelling excess entropy to the edges of a trapped system [245, 246, 82, 247]. Very recently, a proof-of-principle demonstration of entropy exchange between two atomic species was observed in a 1D lattice [248]. This section reviews our theoretical investigations of a cooling method we proposed to prepare fermionic atoms in a three-dimensional optical lattice potential at unprecedentedly low temperatures and uniform filling factors.

The method makes use of a "box-like" potential for external confinement and takes advantage of the Pauli exclusion principle to facilitate the selective removal of atoms from multiply-occupied lattice sites. We find that of critical importance is the use of a nonharmonic trapping potential to provide external confinement for the atoms. We assume that the box-like potential, which exhibits a central region of very small curvature surrounded by a steep repulsive barrier, is provided by the radial profile of a blue-detuned (repulsive), high-order Laguerre-Gaussian (LG) laser beam along each Cartesian axis. In this method, atoms are prepared via a two-step process involving (1) adiabatically loading atoms initially confined in the LG trap into a superimposed optical lattice, followed by (2) irreversibly filtering atoms from all but the lowest energy band (see Figure 8.4). We find that when the Fermi energy of the system is sufficiently large, such that atoms begin to significantly populate the first energy band prior to filtering, considerable cooling is achieved. For realistic experimental parameters, this procedure will produce a Fermi gas in a lattice with a reduced temperature of $T/T_F \sim 0.003$ and an entropy per particle of $s \sim 0.02 k_B$. The results of this investigation were recently published in Physical Review A, Rapid Communications [249].

8.4.1 Cooling in a Homogeneous Optical Lattice Potential

The energy spectrum of an ensemble of ultracold atoms is greatly affected by the addition of a 3D cubic optical lattice. We begin by describing the idealized cooling procedure as it would be implemented with a Fermi gas in a homogeneous 3D optical lattice potential (i.e., a uniform optical lattice confined over a finite range). Here, the lattice breaks the translational symmetry of the system, resulting in a series of discrete energy bands whose width and energy spacings are dependent on the intensity of the laser light. For a vanishing lattice depth, the band gaps

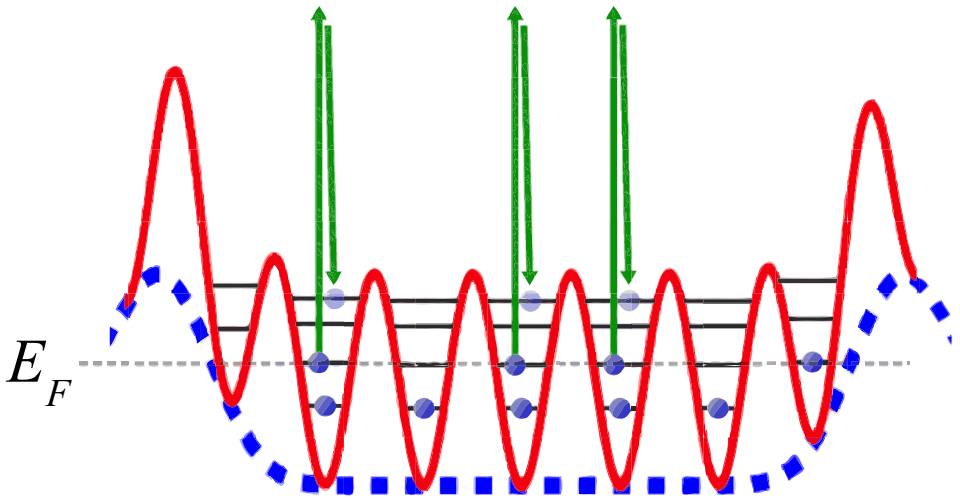

Figure 8.4. We filter atoms from a combined optical potential (red solid curve) consisting of a box-like trapping potential (blue dashed line) and optical lattice by selectively removing atoms from all but the lowest energy band. Amplitude modulation of the lattice potential can selectively transfer these atoms to high-lying bands via a two-photon transition (green arrows) where they can then tunnel out of the region. Dramatic cooling results when the Fermi energy (prior to filtering) lies within the first excited band.

disappear and the "bands" equal the free particle energy-momentum (dispersion) curves reduced to the first Brillouin zone. As the lattice depth is increased, the gaps between bands grow and the width of the bands is exponentially suppressed [250]. In Figure 8.5(a), the band structure for a $V_0 = 5E_R$ deep 1D sinusoidal optical lattice is shown. The eigenenergies are given in units of the lattice recoil energy E_R versus quasi momentum q within the first Brillouin zone ranging from $-\hbar k_L \leq q \leq \hbar k_L$.

Starting from a homogeneous degenerate Fermi gas, the depth of 3D optical lattice potential is adiabatically increased from zero. This results in adiabatic cooling (with no change in entropy) if the filling factor is greater than unity (i.e., more than one atom per spin species per lattice site on average) [251]. In this case, adiabatic cooling significantly diminishes the reduced temperature T/T_F since application of the lattice increases the Fermi energy $E_F = k_B T_F$, which lies within the first excited band at this density, and simultaneously reduces the width of the Fermi surface, which scales with the width of the first excited band, thereby reducing the temperature T. For sufficiently high final lattice depths, adiabatic cooling results in the ground ($n = 0$) band being uniformly filled with extremely

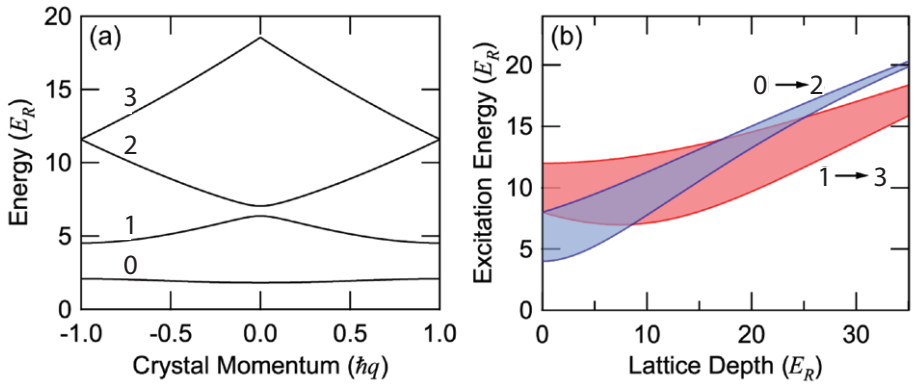

Figure 8.5. (a) Band structure for a 5 E_R deep lattice. (b) Atoms can be selectively excited from the n to $n+2$ energy bands by modulating the amplitude of the optical lattice light. The ranges of excitation energies between bands 0 and 2 (blue) and 1 and 3 (red) for fermions in all crystal momenta states are shown. As the depth of the optical lattice approaches 35 E_R, the overlap of these excitation energy ranges vanishes, thereby demonstrating the feasibility of performing the band selective excitations required in our filtering method.

high fidelity (because T/T_F is now very low) whereas the first excited ($n = 1$) band contains significant fluctuations in the occupation number. Entropy is removed in our method by selectively transferring population from the $n = 1$ to $n = 3$ band and subsequently reducing the depth of the confining potential to allow atoms in the high-lying bands ($n \geq 3$) to escape.

Atoms can be selectively transferred from the $n = 1$ to $n = 3$ energy band with no change in the crystal momentum q by modulating the intensity of the lattice beams [252]. In Figure 8.5(b), the band excitation energies are shown as a function of lattice depth for $n = 0 \rightarrow 2$ and $n = 1 \rightarrow 3$ transitions spanning all q within a Brillouin zone. By loading the sample into an optical lattice with a depth of $V_0 = 35\ E_R$, we find that these transitions are well resolved. It is therefore possible to apply a filtering process to selective transfer the atomic population from bands $n = 1 \rightarrow 3$ by adiabatic rapid passage. In this case, adiabatic rapid passage is implemented by sweeping the amplitude modulation frequency from below to above all $1 \rightarrow 3$ transition frequencies for different q within the Brillouin zone, while remaining below the lowest $0 \rightarrow 2$ transition frequency. The atoms now occupying the third and higher bands contain the majority of the entropy density in the system, and their removal via tunneling significantly reduces the entropy

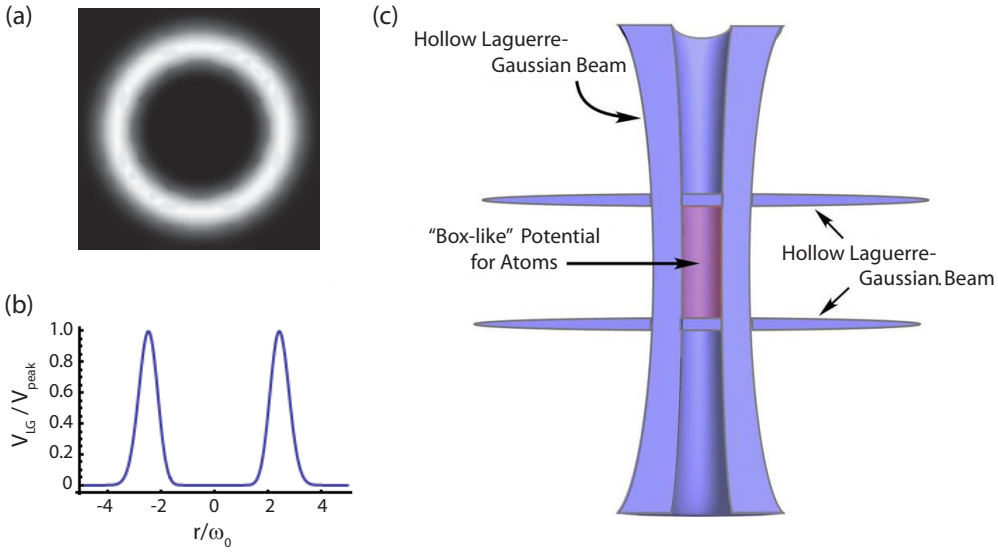

Figure 8.6. (a) Calculated 2D intensity profile of an $\ell = 12$ order LG beam. (b) Spatial profile along each axis of the confining potential ($V_{\rm LG}$ normalized to $V_{\rm peak}$) provided by a blue-detuned 12^{th} order LG beam. (c) Confinement is provided in 3D at the center of three elliptical blue-detuned LG beams with mutually orthogonal orientations. The third beam propagating out of the page is not shown.

per particle of the atoms remaining in the ground band, yielding a high fidelity system.

8.4.2 Cooling in an Experimentally Realizable System

It is currently unfeasible to experimentally realize the homogeneous trapping potential considered above. The majority of ultracold atomic gas experiments to-date have relied on the harmonic profile provided by either magnetic or optical fields to provide external confinement to the atoms. Later, it will be shown that our cooling scheme effectively breaks down if the atoms are purely confined in a combined optical lattice and harmonic trapping potential. Indeed, it has been theoretically predicted [75, 253] and experimentally observed [75] that fermi gases adiabatically loaded into an optical lattice with harmonic external confinement experience an increase of the reduced temperature T/T_F (reduced degeneracy) for all but very high initial temperatures and filling factors.

In order to experimentally approximate the homogenous lattice potential described above, we consider the addition of a box-like external potential which

can be produced by intersecting three elliptical, blue-detuned, ℓ^{th}-order Laguerre-Gaussian laser beams. Along each axis, these beams provide a potential $V_{\mathrm{LG}}(r) = V_{\mathrm{peak}} \left(\frac{2\,e\,r^2}{w_0^2\,\ell}\right)^{\ell} e^{-2r^2/w_0^2}$ at the beam waist w_0. For a given charge ℓ, the peak value V_{peak} of the potential occurs at $r_{\mathrm{max}} = w_0\sqrt{\ell/2}$ and the width of this peak decreases with decreasing w_0. Therefore, for a given trap size (r_{max}), the LG profile more closely approximates a box potential when ℓ is increased and w_0 is correspondingly reduced. Trapping of ultracold gases has been demonstrated in single or crossed beam configurations of LG beams up to $\ell = 16$ [254, 255, 256].

For the trap described above, the Hamiltonian along each cartesian axis is given by

$$H = \frac{-\hbar^2}{2m}\frac{d^2}{dx^2} + V_{\mathrm{LG}}(x) + V_0\cos^2(k_L x + \phi_x) + \frac{m\omega^2}{2}x^2, \tag{8.9}$$

where the third term represents a lattice potential of depth V_0 and phase offset ϕ_x. We also include a harmonic term that arises if red-detuned Gaussian beams are used to produce the lattice potential; in this case $\omega \propto \sqrt{V_0}$. The 1D eigenvalues ($\epsilon_i$) and eigenfunctions for a given depth of the optical lattice are calculated by numerically diagonalizing the Hamiltonian (Equation 8.9) using the Discrete Variable Representation (DVR) method described in [257]. This powerful method uses a grid-point representation in coordinate space to reduce the quantum eigenvalue calculation from an integral equation to a simple matrix representation. The Hamiltonian matrix can be quite sparse, requiring only five points per deBroglie wavelength to converge, where the potential energy is diagonal and the kinetic energy reduces to a sum of one-dimensional matrices. A copy of the *Mathematica* code written to diagonalize the 1D Hamiltonian (Equation 8.9) using this method is given in Appendix C.1.

For sufficiently shallow lattice depths, the low energy eigenstates are delocalized and closely approximate Bloch states in the lowest band of a homogeneous system. However, higher energy states are either localized at the edges of the trap (i.e. near $x = r_{\mathrm{max}}$) or delocalized and correspond to Bloch states in excited energy bands. The qualitative form of the eigenstates in the ground and first-excited energy bands for atoms in a combined LG and optical lattice potential at depths $V_{\mathrm{LG}}(x) = V_0 = 35\ E_R$ is illustrated for reference in Appendix C.1. Localization of the atoms occupying the edge states is clearly shown in the figures, whereas

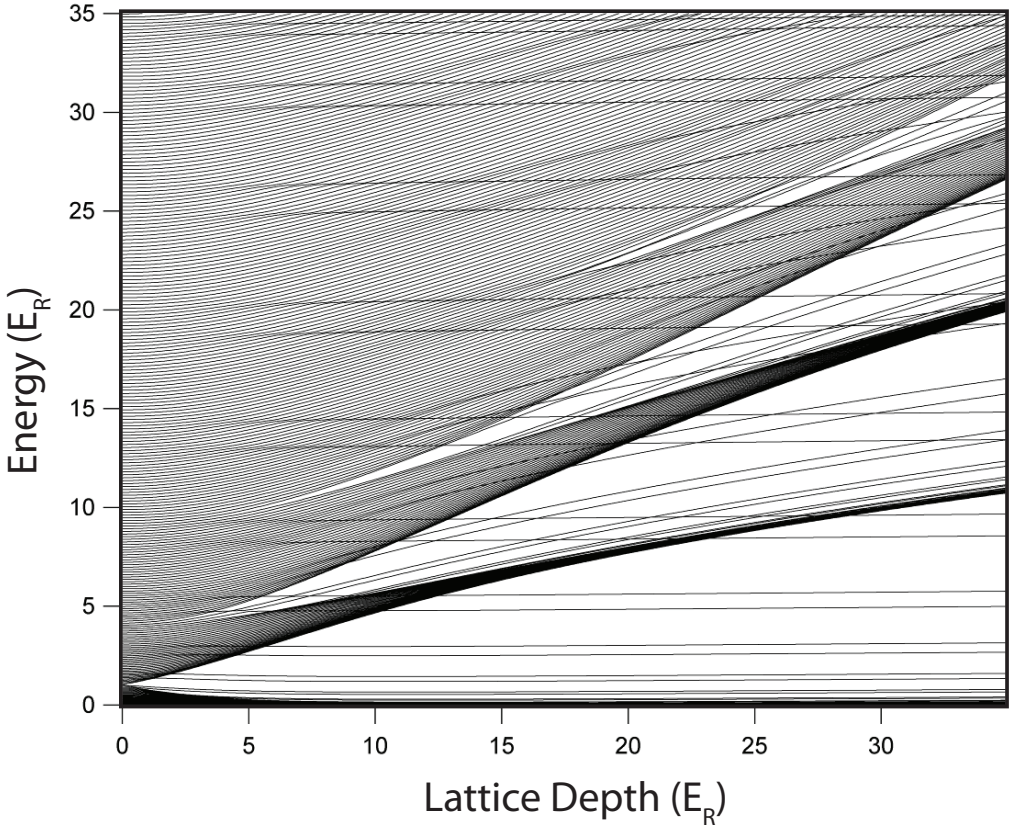

Figure 8.7. Energy level spectrum as a function of the optical lattice depth in units of the lattice photon recoil energy (E_R) for the 1D model Hamiltonian given in Equation 8.9. At higher lattice depths, the eigenvalues generally converge into a band structure. Deviations from the uniform band structure emerge from the existence of the edge states, which can trap atoms in lower vibrational levels at energies greatly exceeding the bandwidths and even the band-gaps characterizing the distributions of the central eigenstates.

the atoms near the center of the trap are still highly delocalized, even in the deep lattice potential. While a band structure picture is not strictly valid for this inhomogeneous system, we classify the set of eigenfunctions without nodes as constituting the lowest band.

A plot of the 1D eigenenergy spectrum for our model Hamiltonian with respect to the depth of the optical lattice V_0 is shown in Figure 8.7. As the lattice depth is adiabatically increased, the 1D eigenvalues generally separate into groups corresponding to a band structure. At higher energies and lattice depths, a series of avoided crossings are observed between the eigenvalues converging into one of the energy bands and a set of eigenvalues that evolve roughly in the same man-

ner as one of the lower-energy bands. These states that deviate in energy from the majority band structures are associated with lattice sites at the edges of the LG trapping potential. Atoms trapped in these edge states can become highly localized, and slow lattice ramps may be required to assure that adiabaticity and thermal equilibrium is maintained throughout the gas at all lattice depths.

We then extend our model to three dimensions, where the Hamiltonian $H_{3\mathrm{D}} = H(x) + H(y) + H(z)$. We further assume equal lattice depths in each direction. The 3D spectrum ($\mathcal{E}_m$) for a given depth of the optical lattice is then generated by calculating all possible combinations of the sum $\mathcal{E}_m = \epsilon_i + \epsilon_j + \epsilon_k$ for all values of the 1D eigenenergies (ϵ_p) in each spatial direction. The 3D energy spectrum for energy states in the lowest band of the optical lattice is calculated in a similar manner, where only the 1D eigenenergies associated with states in the lowest energy band are included.

In calculating thermodynamic quantities during the proposed cooling method, we assume thermal equilibrium before and after the selective removal of atoms from excited energy bands. Equilibrium is maintained by elastic collisions in a mixture of spin-1/2 fermions and changes in the trapping potential are adiabatic with respect to the rethermalization time scale. However, we also assume that the interactions can be tuned such that they are weak enough to not significantly modify the single-particle energy spectrum, $\mathcal{E}_m$. We therefore use $\mathcal{E}_m$ when calculating the following quantities:

$$\begin{aligned} N &= 2\sum_m \frac{1}{1+\exp[(\mathcal{E}_m-\mu)/k_BT]}, \\ E &= 2\sum_m \frac{\mathcal{E}_m}{1+\exp[(\mathcal{E}_m-\mu)/k_BT]}, \\ \frac{S}{k_B} &= 2\sum_m \ln[1+\exp[(\mu-\mathcal{E}_m)/k_BT]] + \frac{E}{k_BT} - \frac{\mu}{k_BT}N, \end{aligned} \tag{8.10}$$

where T is the temperature, μ is the chemical potential of an atom in either spin state, N is the total number of atoms, E is the total energy in the system, and S is the total entropy. The factor of two accounts for the fact we are considering a Fermi gas whose atoms occupy two spin-states.

Our method for cooling the atoms is comprised of (1) an adiabatic increase in

the lattice depth starting from zero, (2) an irreversible removal of atoms in excited bands, (3) rethermalization and (4) an optional adiabatic change to a final lattice depth. To model the thermodynamic changes that occur during adiabatic ramps of the potential, we calculate the change in the quantities μ and T using the multi-band energy spectrum, assuming that both N and S are conserved. In contrast, to model rethermalization after the selective filtering stage we initially calculate E and N (from Equation 8.10) for atoms *restricted to the lowest energy band* and subsequently solve for μ and T using the multi-band energy spectrum assuming that the system equilibrates with the calculated E and N after removing all of the atom from the excited bands. Section C.2 contains our main program, written in ANSI C, which calculates the energy-spectrum and thermodynamic evolution of the gas throughout the various stages of the cooling procedure.

8.4.3 Cooling Simulations

We consider a 50/50 spin mixture of ^{6}Li atoms initially trapped in a LG trapping potential with $\ell = 12$, $V_{\rm peak} = 35\,E_R$ and $r_{\rm max} = 13.5\,\mu$m. For reasonable lattice beam properties ($k_L = 2\pi/1064\,$nm and a Gaussian-beam waist of $w_{\rm Gauss} = 300\,\mu$m) we find $\omega = 2\pi\,(390{\rm Hz})$ for the final lattice depth $V_{0,\rm fin} = 35\,E_R$. At this depth, the final entropy per particle ($s_{\rm fin} \equiv S_{\rm fin}/k_B N_{\rm fin}$) after adiabatic loading, filtering and rethermalization, is shown in Fig. 8.8 for various initial reduced temperatures ($T_{\rm init}/T_F$) and sample sizes ($N_{\rm init}$). Fig. 8.8 also shows the final reduced temperature ($T_{\rm fin}/T_F$) and final atom number (N_f). In each case $\phi_x = \phi_y = \phi_z = 0$. This data shows that the thermodynamic properties of the system are highly dependent on the initial filling factor and can be separated into two distinct regions A and B. The vertical dashed line separating the regions represents the number of atoms at which the Fermi energy enters the first excited band.

In region A, the Fermi energy before filtering lies below the first excited energy band. For very low initial filling factors, the filtering/cooling procedure does not reduce the atom number or the entropy per particle since there is negligible population in excited bands. This is indicated in Fig. 8.8 by the fact that for low $N_{\rm init}$, $N_{\rm fin} = N_{\rm init}$ and $s_{\rm fin}$ remains constant at a value determined by the initial entropy

per particle (which $\simeq \frac{\pi^2}{2}\frac{T_{\rm init}}{T_F}$, the entropy of a homogeneous Fermi gas). Initially, as $N_{\rm init}$ is increased, T/T_F increases while the entropy per particle remains constant. As the Fermi energy before filtering approaches the first-excited band, both the reduced temperature and the entropy per particle begin to decrease.

In region B, the density is such that the Fermi energy before filtering lies within the first excited band. In this region the adiabatic cooling and filtering procedure can result in a dramatic reduction of both T/T_F and s and produces a sample with a precisely defined atom number. We find that significant cooling is achieved for initial temperatures in the vicinity of $T_{\rm init} = 0.1\,T_F$ or below. In this case, the final entropy per particle $s_{\rm fin} \lesssim 0.02\,k_B$ and reduced temperature $T_{\rm fin}/T_F \lesssim 0.004$ over a range of initial atom numbers which varies by 20%. For initial temperatures $T_{\rm init} \leq 0.05\,T_F$, the final entropy per particle and reduced temperature saturate at $s_{\rm fin} \sim 0.01\,k_B$ and $T_{\rm fin}/T_F \sim 0.002$ respectively each having been reduced by more than an order of magnitude. This lower limit on the achievable reduced temperature and entropy is set by the residual harmonic confinement from the Gaussian lattice beams and the steepness of the walls of the box-like potential. We also note that, as shown in Fig. 8.8(b), $N_{\rm fin}$ is insensitive to fluctuations in $N_{\rm init}$ for low initial temperatures. For example, at $T_{\rm init} = 0.05\,T_F$, a variation of $\pm 10\%$ around $N_{\rm init} = 1.6 \times 10^5$ yields a variation of only $+0.09\%/-0.2\%$ in $N_{\rm fin}$.

The cooling efficiency and number filtering are dependent on the choice of the relative phases between the optical lattice and the center of the LG trapping potential along each axis (e.g. ϕ_x in Equation 8.9) due to the sensitive effect these phases have on the location of localized edge state eigenenergies relative to the Fermi energy. To study this effect, we modeled the system allowing the phase in each direction to be independently selected from the set $\phi_\alpha = (0, \pi/10, ..., \pi/2)$. We considered samples with $T_{\rm init} = 0.05\,T_F$ and $N_{\rm init} = 1.5 \times 10^5$ atoms, parameters close to optimal for cooling. From the set of all possible phase combinations, we find an average final entropy per particle $s_{\rm fin} = 0.014\,k_B$ with a standard deviation of $0.004\,k_B$ and an average final temperature $T_{\rm fin} = 0.003\,T_F$ with a standard deviation of $0.001\,T_F$. From this same set, we find an average final number $N_{\rm fin} = 1.20 \times 10^5$ with a standard deviation of 1.6×10^3.

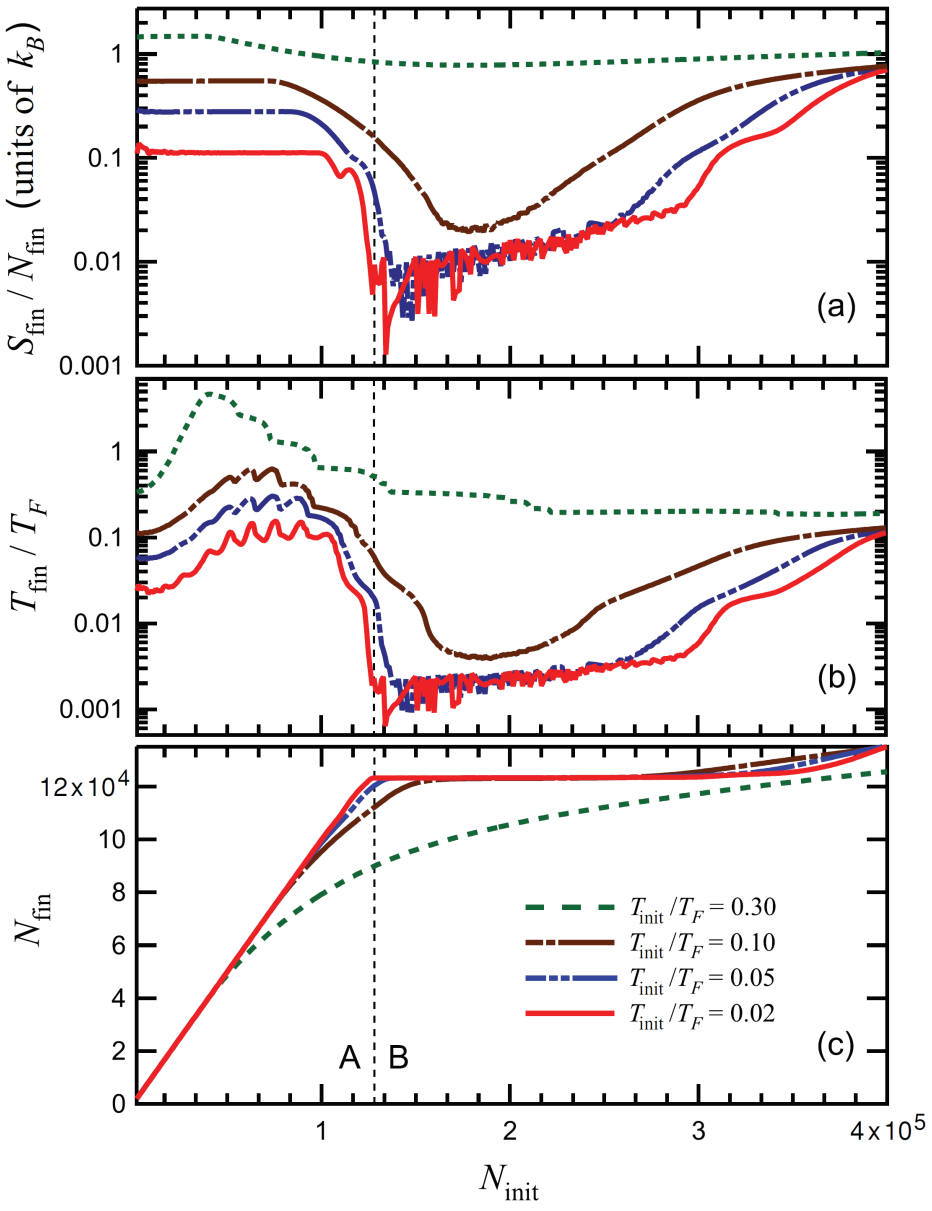

Figure 8.8. (Color online) As a function of initial atom number we report (a) the final entropy per particle in units of k_B, (b) the final reduced temperature and (c) the final atom number after filtering for various initial temperatures between 0.02 and $0.3\,T_F$. The vertical dashed line represents the number of atoms for which the Fermi energy enters the first excited band. The trap and lattice parameters are as described in the text.

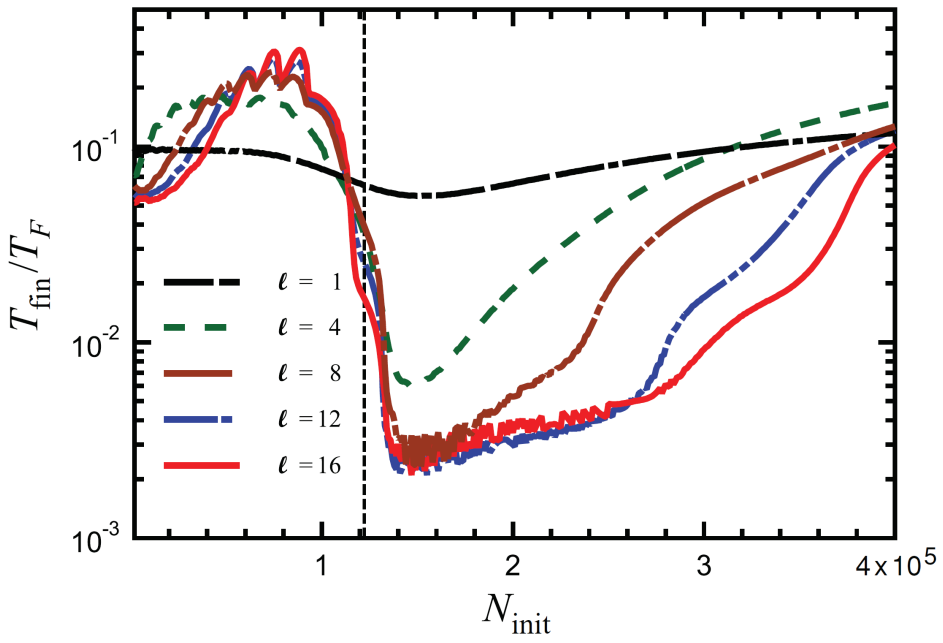

Figure 8.9. (Color online) The effects of the charge ℓ of the Laguerre - Gaussian trapping potential on the efficiency of our proposed cooling and filtering method. For each data set, the initial temperature $T_{\rm init} = 0.05\,T_F$ and the phases $\phi_x = \phi_y = \phi_z = 0$. For all ℓ values, the number of atoms at which the Fermi energy enters the first excited band (vertical dashed line) is held constant.

8.4.4 Technical Limitations of the Cooling Method

Two technical challenges for implementing this technique are (1) maintaining thermal equilibrium when increasing the depth of the optical lattice and (2) maximizing the fidelity with which atoms are filtered from excited energy bands. Here, we describe what is required to achieve $s_{\rm fin} \leq 0.028\,k_B$ (i.e. a quantity within a factor of 2 of the average value of the phase-averaged data).

To study the effects of nonadiabatic ramps of the optical lattice, we consider the possibility that thermal equilibrium is maintained only up to a lattice depth $V_{\rm adiab}$. For $V_0 > V_{\rm adiab}$, we assume that changes are performed diabatically with respect to collisions, however, single particle band excitations are not induced. Thus, the occupation number distribution found in the single-particle states at a depth of $V_{\rm adiab}$ is simply mapped on to the corresponding single-particle states for the final lattice depth $V_{0,\rm fin} = 35\,E_R$ where filtering is performed. After filtering, the depth is returned to $V_0 = V_{\rm adiab}$ (again without band excitation) where the system is

assumed to then be able to rethermalize via collisions. We consider samples with $N_{\rm init} = 1.5 \times 10^5$, $T_{\rm init}/T_F = 0.05$, and phases $\phi_x = \phi_y = \phi_z = 0$. We find that if thermal equilibrium can be maintained up to a lattice depth of $V_{\rm adiab} \geq 15.5\, E_R$, the final entropy per particle $s_{\rm fin} \leq 0.028\, k_B$. It seems reasonable to expect the high tunneling rate in the first-excited band will help to maintain thermal equilibrium as the lattice depth is increased to $V_{\rm adiab} = 15.5\, E_R$. For example, for $V_0 < 15.5\, E_R$, the tunneling time between lattice sites in the first-excited band is $\lesssim 74\, \mu$s for ^{6}Li atoms in a lattice with $k = 2\pi/(1064\,{\rm nm})$. For comparison, the inverse of the photon scattering rate $R_{\rm sc}^{-1} \sim 10\,{\rm s}$, which sets the timescale for heating, is always more than five orders of magnitude larger. A detailed analysis to determine the timescale for adiabatic loading, however, is beyond the scope of this thesis.

Further, to study the effects of incomplete filtering, we modeled the cooling method with fully adiabatic ramps, but randomly allow a small percentage of the occupation number distribution for atoms in excited energy bands to remain after filtering. We find that for the system described above, entropies per particle below $0.028\, k_B$ are achieved if the atoms are removed with a fidelity better than 98.5%. The constraint on the inadvertent loss of atoms from the ground band is more stringent, requiring that the occupation number in the ground band must be maintained with a fidelity $> 99.99\%$ in order to achieve $s_f < 0.028\, k_B$.

8.4.5 Effects of Varying the Confining Potential

Finally, we consider the effect of the charge ℓ of the LG beams for samples with $T_{\rm init} = 0.05\, T_F$, phase $\phi_x = \phi_y = \phi_z = 0$, final lattice depth of $35\, E_R$, and various initial atom numbers (see Fig. 8.9). For this data, the waists of the Gaussian lattice beams are assumed to be $w_{\rm Gauss} = 200\, \mu$m, somewhat smaller than before. For each ℓ-value, the waist of the LG beam is adjusted such that the number of states below the first excited energy band is held constant at 1.22×10^5. As seen in Fig. 8.9, the cooling efficiency of this procedure is highly dependent on the charge. For $\ell = 1$, which approximates harmonic external confinement, only a modest reduction in $T_{\rm fin}/T_F$ is observed. For $\ell \geq 8$ a reduction by a factor $\simeq 20$ is achieved. For $\ell \gtrsim 8$, the minimum reduced temperature saturates to $T_{\rm fin}/T_F \lesssim 0.003$. For higher values of ℓ, the extent of the saturation regime grows.

The efficiency of the cooling scheme proposed is highly dependent on both the charge ℓ of the LG trapping potential (defining the "steepness" of the walls of the box-like potential) and the magnitude of the harmonic confinement provided by the optical lattice beams (defining the "flatness" of the central region of the confining potential). We have checked that as the waist of the Gaussian lattice beams grows, the absolute minimum of $T_{\rm fin}/T_F$ decreases. In fact, when considering a true box potential ($w_{\rm Gauss}, \ell \to \infty$), for samples with $T_{\rm init} = 0.05\,T_F$, phase $\phi_x = \phi_y = \phi_z = 0$, and final lattice depth of $35\,E_R$, the final $T_{\rm fin}/T_F$ and s_{fin} are too low for us to accurately determine with the limited grid-size used in the simulation. However, both the optical lattice and the high-ℓ LG confining potentials simulated in this proposal are currently experimentally accessible, and our cooling scheme should be directly implementable using the current of the state-of-the-art technology to cool two-component degenerate Fermi gases to unprecedented low temperatures and entropies per particle with very little variation in the final atom number.

8.4.6 Applicability of the Cooling Method for Two- and Three-Component Fermi Gases

In this section we have discussed a method for preparing a sample of highly degenerate two-component Fermi gases by adiabatic loading into a combined optical lattice and "box-like" trapping potential followed by selective removal of atoms from all but the lowest energy band. Numerical calculations for sample sizes $\sim 10^5$ predict that temperatures $\sim 0.003\,T_F$ corresponding to an entropy per particle $\sim 0.02\,k_B$ can be prepared in this manner. This method is robust against initial number and temperature fluctuations for a sufficiently degenerate initial sample of atoms and yields samples with little variance in the final number. While the selective removal of atoms must occur in a deep lattice (in order to spectrally resolve the band excitations), subsequent reduction of the lattice depth, if desired, will maintain the extremely low entropy per particle if changes are made adiabatically. Two-component gases prepared in this manner should be sufficiently cold to explore quantum spin phases of fermionic atoms [72, 73, 74], including antiferromagnetic ordering and possibly d-wave superfluidity, which are currently inaccessible. This method could also provide a physical realization of an essentially perfect quantum

register.

It is further conceivable that two-component Fermi gases prepared in this manner could provide an initial low-temperature basis for producing highly-uniform three-component Fermi gases confined in the same optical lattice and LG trapping potentials. Applying state-driving broadband RF pulses to the pre-cooled 50-50 mixture of ^{6}Li atoms in the presence of a magnetic field will cause the atoms in the lattice to equally occupy the lowest three Zeeman sublevels. Particular attention to the field value, field gradient, and hold time after the RF pulse will be required to assure decoherence while maintaining uniform filling of the gas at two atoms per lattice site. The decreased density of the spin states, however, leads to a decrease of the Fermi energy and hence an increase of the reduced temperature so that very little, if any, cooling is achieved in this manner. Further, by blowing away one of the two spin components before applying the state-driving RF pulses, three-component gases with almost perfect filling of one atom per lattice cite can be realized in the combined trapping potentials. Using these methods, the uniform atomic filling may be maintained at effectively one or two atoms per lattice site. It is also conceivable to preform the cooling technique with three distinguishable components loaded into each lattice site. Very weak interactions will be required, however, at such high densities to achieve any cooling of the gas.

Chapter 9

Conclusions and Outlook

Efimov's theory considered the few-body interactions of identical bosons with resonantly-enhanced interactions. Ultracold gases consisting of ^{6}Li atoms equally occupying the three lowest-energy hyperfine spin states have proven to be a nearly ideal test-bed for studying the validity of Efimov physics for more complicated systems consisting of three distinguishable but resonantly interacting particles. Further, numerous theoretical studies have recently predicted that a host of new many-body phenomena are expected to emerge in these systems. The wide range of phenomena available for study with these gases are attributed to the rich structure of their pairwise interactions. Three overlapping Feshbach resonances and a zero-energy resonance in the triplet potential provide a wide variety of interaction strengths and imbalances. These range from SU(3) symmetric interactions at high-fields, to three large and characteristically unequal scattering lengths near the Feshbach resonances, to regions where the scattering lengths go to zero and pairs of particles are non-interacting. Further, the gas exhibits regions where any number of the scattering lengths can be positive and between 0 and 3 universal dimer states exist.

The ultracold nature of the gas and the short-range of the two-body potentials make these systems ideal for universal studies of the spectrum of weakly-bound trimer states that can emerge and the various many-body phases that are expected to arise for such three-component systems. Based on the impact that few- and many-body studies of ultracold Fermi gases have had to-date on a range of physical disciplines, it is anticipated that future studies with both two- and

three-component Fermi gases will reveal a host of new knowledge to expand our understanding of the universal physics of a variety of interacting Fermi systems.

9.1 Few-Body Studies

Starting with the low-field K_3 measurements, we already saw that Efimov trimer states can exist even when the gas is characterized by three unique s-wave scattering lengths. Fortuitously, the low-field trimer came into resonance with the free-atom threshold at two field locations, as shown by the white arrows in Figure 9.1 [145, 144]. The locations and widths of the two resonant loss features subsequently provided the necessary information both to extract the low-field three-body parameters describing the properties of the Efimov state in this region [4, 28, 8], and to derive new models explaining how the inelasticity parameter (η_*) varies with the binding energies of the most weakly-bound dimer states [5, 205]. The red curve in Figure 9.1(a) was obtained by fitting our low-field data using the Heidelberg model [5], yielding an excellent agreement between the data and the universal predictions calculated in the zero-range approximation for field values between 16 G $< B <$ 600 G.

Throughout the great majority of the high-field regime, all three scattering lengths exceed the van der Waals length scale by well over an order of magnitude. This region is therefore interesting because universal calculations based on the zero-range approximations should be highly accurate, with non-universal corrections of $l_{vdw}/a \leq 3\%$. We therefore conducted a series of experiments measuring the magnetic field dependent three-body recombination rate for a three-state Fermi gas of ^{6}Li atoms over the range of fields $834 \leq B \leq 1500$ G. Particular attention to the temperature and density of the gas was required for these experiments, due to the extremely large scattering lengths and loss rates at these fields, to assure that the K_3 measurements were immune to unitarity and thermal averaging effects. Novel hybrid optical and magnetic traps were specially developed for this experiment, allowing for the measurement of three-body recombination rates which varied by over eight orders of magnitude.

The high-field data, which was taken at low sample temperatures ($T \leq 30$ nK and $T \leq 180$ nK) for comparison with the zero-temperature theory, is rep-

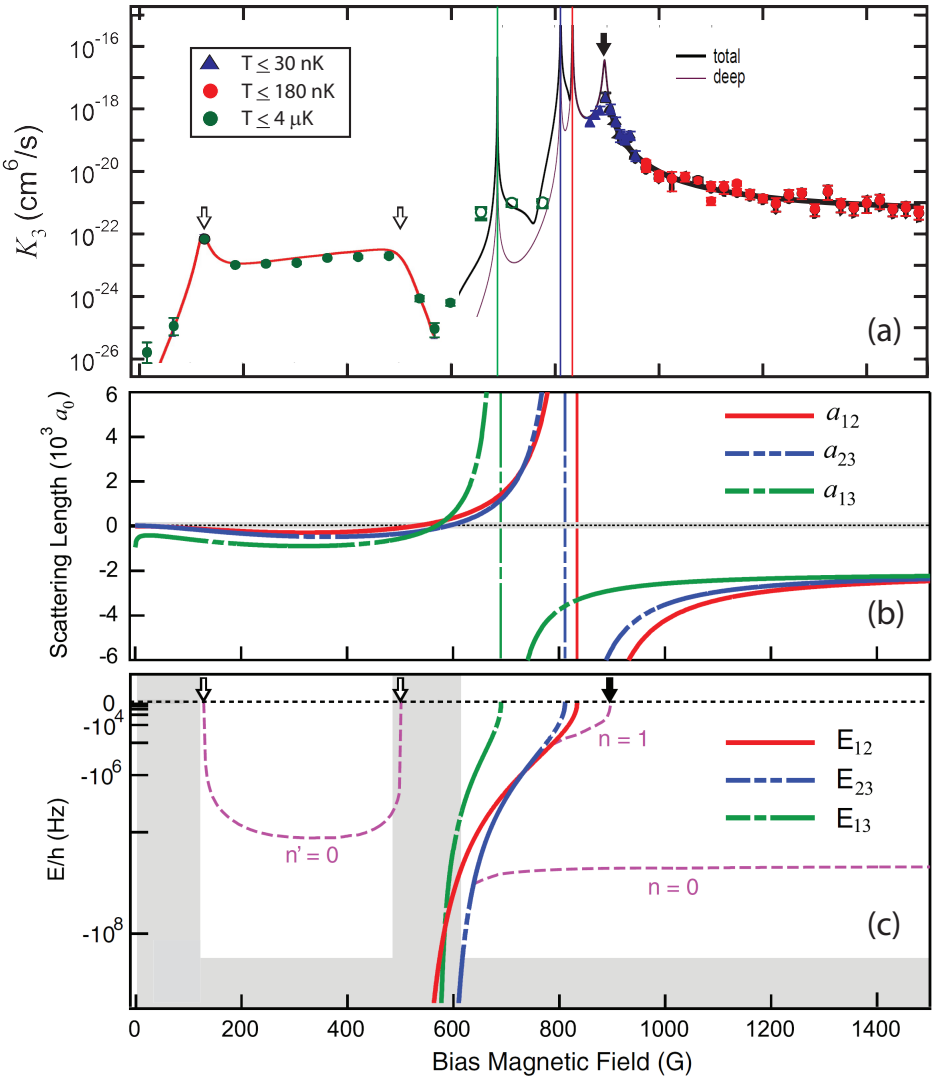

Figure 9.1. (a) Our entire data set containing both the low-field (green) and high-field (blue and red) measurements of K_3 along with universal fits to the data using the Heidelberg model (red curve) and a numerical solution of the STM equations (black and purple curves, adapted from Reference [8]). Resonant three-body loss was observed (arrows) when an Efimov trimer intersected the three-atom scattering threshold. (b) Three overlapping s-wave Feshbach resonances in ^{6}Li for states $|1\rangle$, $|2\rangle$, and $|3\rangle$. (c) The binding energies (E_{12}, E_{23}, and E_{13}) of the universal dimer states associated with the Feshbach resonances. The dashed lines (n and n') depict the binding energies of the Efimov trimer states [8]. The grey shaded areas identify non-universal regions where $E < E_{vdw}$ or $|a_{ij}| < 2l_{vdw}$.

resented by the blue triangles and red circles respectively in Figure 9.1(a). Our measurements exhibited enhanced loss attributed to an Efimov trimer state crossing threshold near 895 G [147] (black arrows in Figure 9.1). A numerical fit of our high-field K_3 measurements using the model provided by D. Kang and E. Braaten, which explicitly accounted for the variation of the scattering lengths [6], was used to extract the three-body parameters in the high-field regime. These parameters also predicted the locations of the loss features previously observed at lower magnetic field values, which was unexpected as these features are separated by a range of scattering lengths which are not universally connected in Efimovs theory.

Our measurements constituted the first observation of multiple Efimov features in any fermionic system and provided the three-body parameters that were subsequently used to map out the entire spectrum of Efimov states throughout the high-field universal regime [8]. In Figure 9.1(c), the calculated binding energies of the ground ($n = 0$) and first-excited ($n = 1$) high-field Efimov trimer states are shown. E. Braaten and co-workers found that the ground (first-excited) trimer state is predicted to come into resonance with the $|1\rangle - |23\rangle$ atom-dimer threshold at $B_*^{(1)} = 672 \pm 2$ G ($B_*^{(0)} = 597$ G). They went on to use our measurements of the high-field three-body parameters to calculate the three-body loss rate coefficients for free ^{6}Li atoms throughout the high-field regime. Their calculations are included in Figure 9.1(a), where the black (purple) curves represent the loss-rates to both weakly- and deeply-bound (deeply-bound only) dimer states. Their model predicts multiple minima in the three-body loss rates attributed to Stückelberg interferences, demonstrating that these loss features can occur whenever at least one of the scattering lengths are positive.

Recent experiments have begun to explore some of the predicted features at high fields, including measuring the enhancement of the atom-dimer loss rates near where the Efimov trimer states crosses the $|1\rangle + |23\rangle$ atom-dimer thresholds [210, 198]. Measurements of the atom-dimer resonance at 685 G and the free-atom resonance at 895 G effectively complete the observation of the spectrum of Efimov states in ^{6}Li. The disagreement of the atom-dimer loss measurement with the theoretical prediction based on the high-field three-body parameters, however, has required the inclusion of non-universal scalings of the three-body parameters to properly fit all of the loss data [210]. Experiments directly measuring the binding

energies of the Efimov trimer states using RF photoassociation techniques [198] may be the key to solving this mystery.

The spectrum of Efimov trimer states and resonant loss features in ultracold ^{6}Li atoms occupying the three lowest Zeeman sublevels ($|1\rangle$, $|2\rangle$, and $|3\rangle$) are now becoming well understood. However, the source and field-dependence of the non-universal corrections, that apparently emerge with the inclusion of the weakly-bound dimer states, is not yet fully known and further data may be required to shed light on this phenomena. Measurements of the locations and widths of the Stückelberg interference minima in the three-body loss rates for free atoms, predicted in Reference [8], could be enlightening since universal predictions characterizing these features already exist and the non-universal theories [210] can be directly applied to calculate these features based on the pre-existing free-atom and atom-dimer loss measurements.

Studies of the universal three-body physics in ultracold ^{6}Li gases are therefore far from exhausted. A natural question also arises as to the possibility of observing universal four-body physics in these systems. In a recent experiment F. Ferlaino *et al.* found evidence for the existence of universal four-body (tetramer) bound states in a ^{133}Cs gas [258]. These states, which were theoretically predicted by J. von Stecher *et al.* [259], exhibit unique universal properties. It turns out that the tetramer states are related to Efimov physics since the four-body potential is only attractive enough to support two universal tetramer states in the close proximity of a trimer state, and therefore the universal relations do not require any four-body parameters. In ultracold ^{7}Li gases, two sets of tetramers have been observed corresponding to two Efimov trimer states [38]. Further, there are theoretical predictions that even higher N-body universal states may exist [260], but their experimental observation becomes exceedingly difficult.

The Pauli exclusion principle, however, prohibits four-body interactions in a Fermi gas consisting of only three distinguishable states. These studies already suggest that new effects are expected to arise by adding a fourth distinguishable state to the system. Although for different reasons, we have begun exploring the interactions of atoms occupying state $|4\rangle$ with our multi-component gases.

The recently reported RF photoassociation spectroscopy technique [211] provides a powerful new tool to explore the spectrum of Efimov states in a range of

three-body system. Associating Efimov trimers from two-component Fermi gases is limited, however, because three particles are prohibited from occupying the same spatial region due to Pauli exclusion. Further, the RF-transition drives the atoms between states in a coherent way so that the addressed atoms remain identical, prohibiting the formation of trimers [211]. This problem was circumvented by probing an atom-dimer mixture in which the free and bound atoms occupying the same internal states were distinguishable, with resonant RF frequencies differing by the binding energy of the dimer.

Using this method, the authors made the first direct measurement of the binding energies of an Efimov trimer state. However, RF spectroscopy could only be preformed using this technique at fields significantly below the Feshbach resonance. We have been exploring the possibility of preforming RF photoassociation spectroscopy to associate the $|123\rangle$ Efimov trimer from ^{6}Li gases consisting of either $|4\rangle$ atoms and $|12\rangle$ molecules or $|1\rangle$, $|2\rangle$, and $|4\rangle$ coexisting free-atom states. Three distinct atomic states would now exist in this system, avoiding the limitations associated with Pauli-exclusion and distinguishability. Further, preliminary results for the calculated s-wave scattering lengths and spin-exchange decay rates at low fields [261] suggest that in the absence of RF addressing, these mixtures should be relatively long-lived.

It is conceivable that, by using this method, RF photoassociation could be used to map out the binding energies of the entire spectrum of Efimov states in the system. These measurements would provide valuable information for testing both the continuity of the trimer states across the Feshbach resonances and the scaling of the trimer binding energies E_T^0/E_T^1. With high resolution measurements it should also be possible to use this technique for precision tests of non-universal corrections to the few-body theories and to directly measure the lifetime of the Efimov trimers from the width of the association peaks.

9.2 Outlook for Many-body Studies

To date, all of the experiments with ultracold three-component Fermi gases have concentrated on the few-body properties of the system. However, now that the stability of the gas is known throughout the high-field, strongly universal regime,

the field is primed to begin studying some of the novel many-body phenomena that are predicted to emerge with the inclusion of a third spin component to the gas. In general, collective effects emerge in degenerate gases exhibiting strong pairwise interactions. Although we have demonstrated quantum degeneracy of a three-component Fermi gas in the high-field, SU(3) symmetric, regime the gas was too weakly interacting to realize the atomic color superfluid phase at these fields.

In Chapter 8, the density and lifetime requirements of the gas were considered for realizing a variety of predicted phenomena in both bulk and lattice confined three-component Fermi systems. It was found that in bulk samples, the lifetime of the ^{6}Li gas was generally too short to create gases with more than one pair of components in the strongly interacting regime. It is therefore not possible to create bulk three-component ^{6}Li gases with multiple coexisting BCS superfluid components. Various initial studied are available, however, to demonstrate many-body effects in this system.

A relatively simple first experiment, which was previously discussed, would be to create a BCS superfluid of $|1\rangle - |2\rangle$ atoms coexisting with a weakly-interacting gas of atoms in state $|3\rangle$ near the 834 G Feshbach resonance. Demonstration of this phase mixture would in fact be a first realization of an atomic color superfluid, where two of the components form a superfluid while the third component remains as a spectator. Another interesting scenario was recently considered by T. Ottenstein [175] to probe the mean-field energy between atoms and dimers. Here, an initial mixture of atoms in state $|2\rangle$ and $|23\rangle$ molecules are considered. As the molecules are cooled below the BEC critical temperature, the sample is shown to phase separate to form a superfluid core surrounded by a shell of the free atoms. The atoms can then be rapidly transferred to state $|1\rangle$ with a resonant RF pulse. So long as the atom-dimer scattering length is sufficiently large and positive the system should remain phase separated, minimizing the atom-dimer loss rates and demonstrating a mean-field dominated phase in a three-component gas. This experiment can be further generalized to study the collapse of the gas as the field is reduced toward 731 Gauss, where pairing competition emerges due to the degeneracy of the binding energies of the $|12\rangle$ and $|23\rangle$ dimer states.

The greatest opportunity for realizing exotic many-body phases in two- and three-component Fermi gases, however, will likely come from loading the atoms

into a lattice potential. For three-component ^{6}Li gases at high fields, the lattice may act to significantly increases the BCS critical temperature. Depending on the strength of the pairwise interactions, the ground state of the system is then characterized by either a color superfluid phase or a phase of trions consisting of one atom from each spin component [84, 90, 91, 92].

In the high-field SU(3) symmetric regime, the atomic color superfluid phase may provide a useful analog for studying the color superconducting phase in two-flavor quantum chromodynamics (QCD) [91]. The high loss rates of the gas, however, suggest that the trion phase will be highly unstable, especially for the case where three distinguishable ^{6}Li atoms are highly localized at a single lattice site. Counterintuitively, it is conjectured that strong three-body loss can be useful for stabilizing the color superfluid phase [233]. This phenomena is due to a Quantum-Zeno like effect where the immediate loss of a trion is analogous to continuous interrogation of the quantum system as the atoms tunnel among nearest-neighbor lattice sites.

Although our experiments to-date have concentrated on the three-component systems, the original goal of the lab was dedicated to studying the exotic phases that are predicted to emerge for repulsively interacting two-component Fermi gases confined in a three-dimensional optical lattice potential. These gases provide a nearly ideal model system for studying the low-temperature phase diagram of the Fermi Hubbard model, which predicts a phase transition to an antiferromagnetically ordered state and possibly even a d-wave superfluid phase at extremely low temperatures.

To this end, we theoretically investigated the cooling efficiency of a method that we developed to prepare a highly-degenerate Fermi gas in a deep three-dimensional optical lattice with a box-like external confining potential. The method involves adiabatic loading of a two-component gas into the lattice with sufficiently high density that the Fermi energy lies within the second energy band, followed by a filtering procedure which removes all of the atoms in the excited energy bands. Our investigations found that weakly-interacting Fermi gases prepared in this manner can be cooled to reduced temperatures on the order of $T/T_F \sim 10^{-3}$, sufficiently low for possible studies of quantum magnetic ordering in multi-component Fermi gases, with very little variance of the final number of atoms per lattice site.

We further found that the cooling procedure breaks down as the profile of the confining potential is transformed from box-like to harmonic. In fact, the ground-state properties of the lattice-confined gas are significantly unique for the boxlike potential. Even in a relatively deep trap, a large portion of the eigenstates are characterized by delocalized "Bloch wave" like states in the central region surrounded by highly localized states at the edges of the potential. Atoms prepared by our cooling method are expected to form a band insulator in the central region with a population in the localized edge states exhibiting suppressed tunneling rates into the central region as compared to the rates of tunneling to neighboring edge states. This scenario is reminiscent of the central insulator and conducting edge states characterizing a topological insulator.

The boxlike potential we considered can be realized by intersecting three mutually orthogonal, elliptical 12^{th} order Laguerre-Gaussian (LG) laser beams which are blue detuned from the atomic resonance. Eric Hazlett and Yi Zhang in our lab have both made a great deal of progress in designing the LG trapping beams, which will soon be installed on our apparatus, and the next upgrade of our system is dedicated to installing a three-dimensional lattice potential which will enable a host of new experiments aimed at studying quantum magnetism and exotic many-body phenomena using ultracold multi-component ^{6}Li gases.

Appendix A

Reference Data

A.1 Fundamental Constants and ^{6}Li Properties

Symbol	Value	Definition
h	$6.62606896 \times 10^{-34}$ Js	Planck's constant
$\hbar$	$1.05457162 \times 10^{-34}$ Js	Planck's constant/2π
c	2.99792458×10^{8} ms^{-1}	Speed of light in vacuum
μ_0	$12.5663706 \times 10^{-7}$ NA^{-2}	Magnetic permeability in freespace
ϵ_0	$8.854187812 \times 10^{-12}$ Fm^{-1}	Electric constant
k_B	$1.3806504 \times 10^{-23}$ JK^{-1}	Boltzmann's constant
μ_B	$927.400915 \times 10^{-26}$ JT^{-1}	Bohr's magneton
a_0	$0.529177209 \times 10^{-10}$ m	Bohr's radius
Properties of ^{6}Li		
m_{Li}	$9.988341146 \times 10^{-27}$ kg	Mass of a ^{6}Li atom
λ_{D_2}	670.977338 nm	Wavelength of the D_2 line in vacuum
Γ_{D_2}	5.8724 MHz	Natural linewidth of the D_2 transition
$\mathrm{I}_{sat}(D_2)$	2.54 mW/cm^2	Saturation intensity of the D_2 transition
$\sigma_0(D_2)$	2.1495972 m^2	Optical cross-section of the D_2 transition
E_R(671 nm)	$k_B \times 3.535$ μK	Photon recoil energy (671 nm light)
E_R(1064 nm)	$k_B \times 1.405$ μK	Photon recoil energy (1064 nm light)

Table A.1. Fundamental constants used in this thesis, values taken from Reference [10]. The properties of ^{6}Li are calculated or taken from Reference [11].

A.2 Magnetic Field Tuning of D_2 Transitions

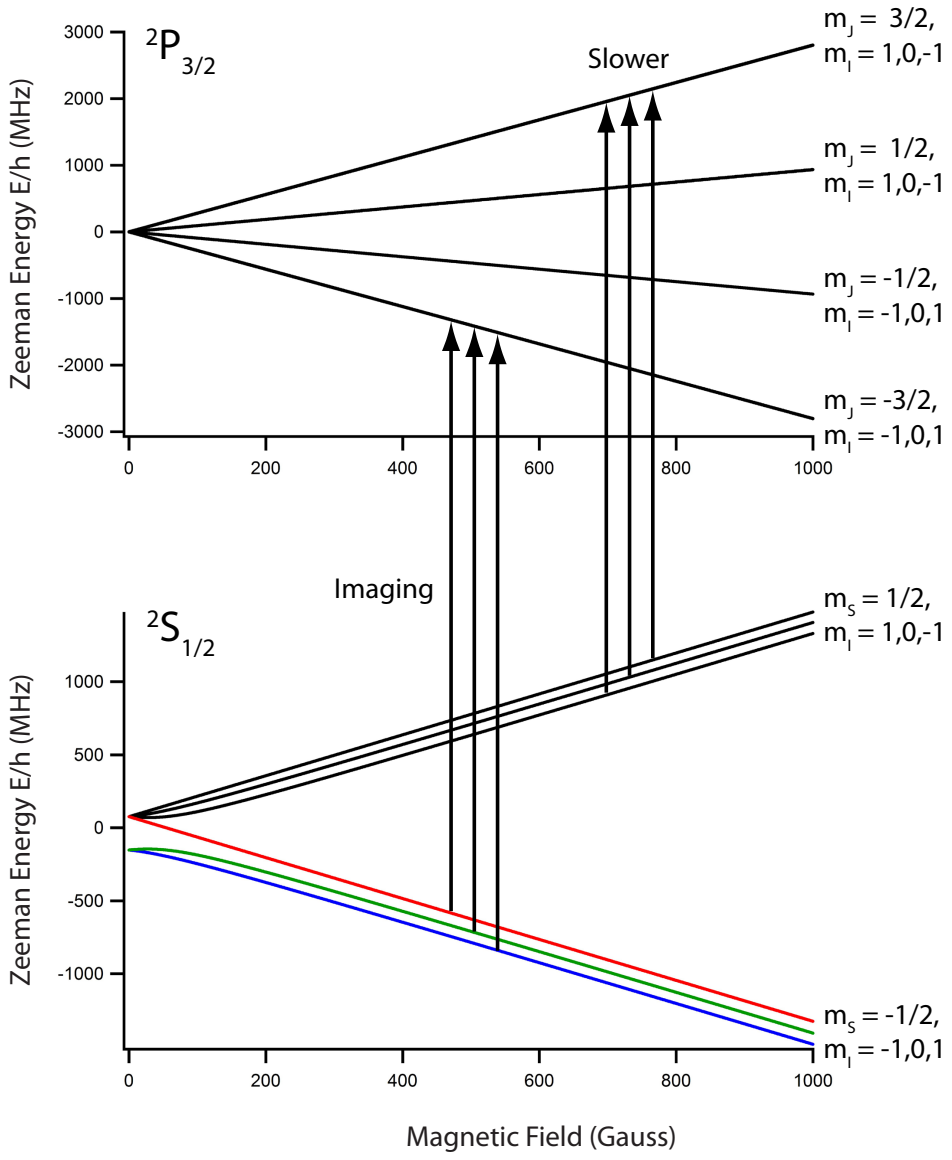

Figure A.1. Energy tuning of the $^2S_{1/2}$ (ground) and $^2P_{3/2}$ (excited) Zeeman hyperfine levels in a magnetic field. The arrows indicate the slower cooling transitions (at $\sim B_{max}$) and the energy-resolved imaging transitions near $\sim$ 500 Gauss.

Appendix B

Supplementary Experimental Data

This appendix includes supplementary data related to the "qualitative" stability measurements of the three-component ^{6}Li gas described in Section 6.1.2. In Figure 6.1(a) of the main text, the ratio $N_{201\text{ms}}/N_{1\text{ms}}$ is reported, which is the ratio of the populations remaining after spending either 201 ms or 1 ms in the primary optical trap at the field of interest B_{hold}. We report this ratio to account for the fact that atoms are lost during the field sweeps to and from the various fields of interest and that the number of atoms lost depends in a smoothly varying way on the particular field of interest. The entire data set containing the number of atoms remaining in each state after spending either 1 ms ($N_{1\text{ms}}$) or 201 ms ($N_{201\text{ms}}$) at the field of interest is provided here for reference in Figure B.1. This data set represents the raw data used to generate Figure 6.1(a).

We have also observed the low-field resonant loss features near 130 G and 500 G in a somewhat different trapping configuration and at an initial temperature twice that reported in the main text. For the data shown in Figure B.2, the trap oscillation frequencies are comparable to those reported for the primary trap in Section 6.1.2. However, the axis of the crossed-beam trap was oriented along the $\hat{x} - \hat{z}$ axis (i.e. orthogonal to the direction of gravity) at an angle of 34° with respect to the $\hat{z}$ (magnetic bias field) axis. For this data, the initial temperature of the cloud was 4 μK.

The experimental sequence for measuring the population remaining in the trap was nearly identical to that described in Section 6.1.2. The notable differences are that the data presented in Figure B.2 is not normalized by a measurement of $N_{1\text{ms}}$,

and therefore does not account for the atom loss during the field sweeps. Additionally, the calibration of the magnetic field is shifted by several hundred milliGauss between the two data set. This shift explains the absence of the narrow p-wave resonance at 228 G from this data set. Figures B.2 and 6.1(a) are qualitatively consistent, both exhibiting the anomalous resonant loss features near 130 G and 500 G. Additionally, the resonant loss feature near 500 G results in a larger loss of atoms from states $|1\rangle$ and $|2\rangle$ in both data sets. The state-selective loss is not in agreement with the data presented in Reference [145].

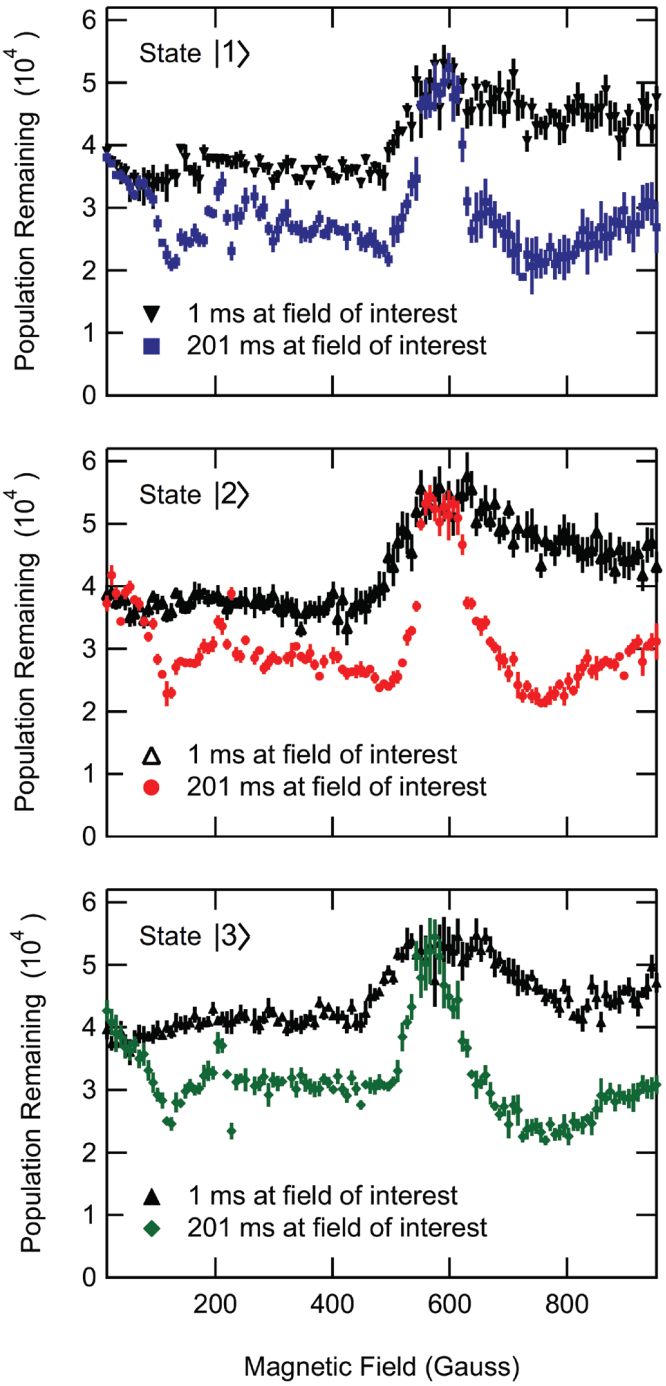

Figure B.1. The number of atoms remaining in the primary optical trap in each of the three spin states ($|1\rangle$, $|2\rangle$, and $|3\rangle$) after spending either 1 ms or 201 ms at the field of interest B_{hold}. The data reported in Figure 6.1(a) is produced by computing the ratio $N_{201\text{ms}}/N_{1\text{ms}}$. Here, the values for $N_{201\text{ms}}$ (colored data sets) and $N_{1\text{ms}}$ (black data sets) are shown explicitly for each field of interest.

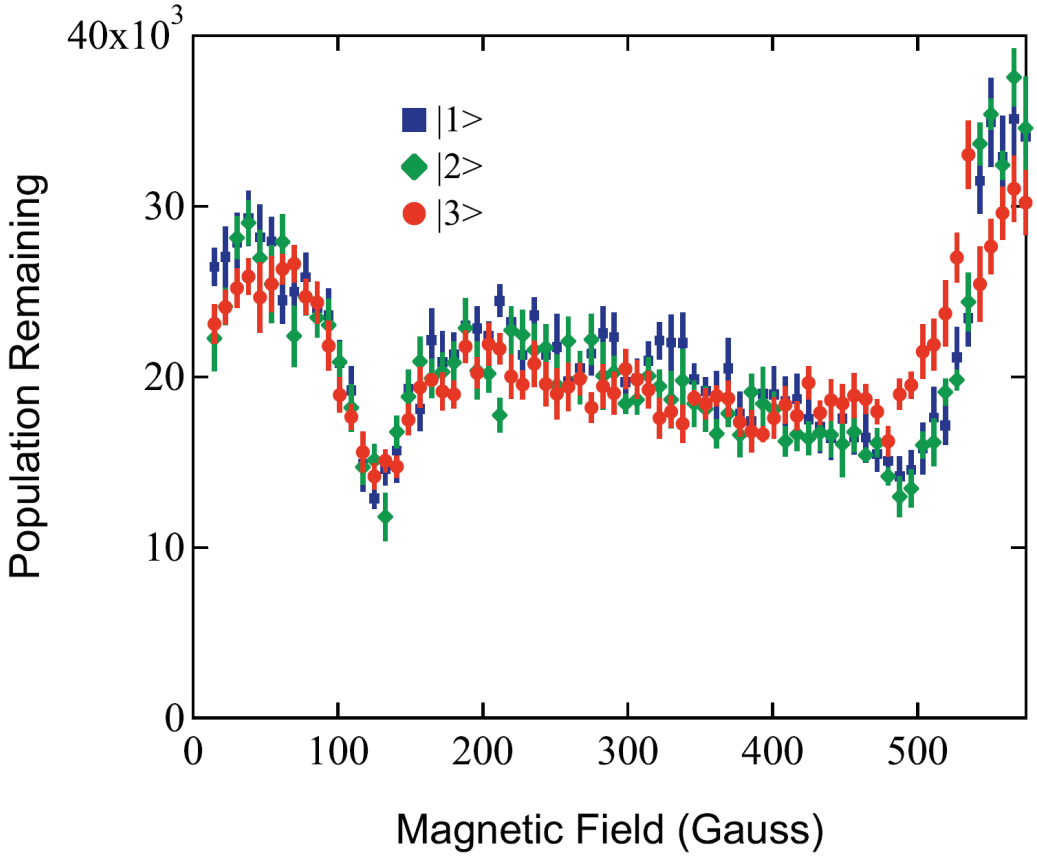

Figure B.2. The number of atoms remaining in an optical dipole trap in each of the three spin states ($|1\rangle$, $|2\rangle$, and $|3\rangle$) after spending 200 ms at the field of interest B_{hold}. The samples are prepared in a manner similar to that described in Section 6.1.2. For the data reported here, the trap had a similar geometry and trap frequencies as the final primary trap geometry used for the collisional stability measurements shown in Figure 6.1(a), but was rotated so that the trap-axis was orthogonal to gravity, and the initial temperature of the cloud was now 4 μK. Resonant loss features are again observed near 130 and 500 G. The loss which occurs near 500 G also leads to a population imbalance.

Appendix C

Lattice Cooling Simulator

This appendix includes the code used to numerically simulate the thermodynamic evolution of a Fermi gas throughout the various stages of the cooling method that we proposed, discussed in Chapter 8. The codes presented here are a template which can be easily altered for various simulations. In their current form, the programs are generally applicable for ultracold fermions trapped in a combined 12^{th} order Laguerre-Gaussian and optical lattice trapping potential. Numerical diagonalization of the Hamiltonian is simplified by using a Discrete Variable Representation (DVR) method to obtain a simple kinetic energy matrix in the position basis [257], which allows us to accurately calculate the energy-spectrum at various depths of the 3D optical lattice.

Section C.1 contains *Mathematica* code that calculates and plots the 1D eignevalues and eigenfunctions for a given Hamiltonian. When changing either the external or optical lattice trapping potentials, the user-defined set of 1D eigenfunctions in the lowest-energy band can be graphically determined from this program, consisting of all of the eigenstates without nodes. Section C.2 contains our main program, written in ANSI C, which calculates the energy-spectrum and thermodynamic evolution of the gas throughout the cooling procedure. Analogous programs were used to calculate all of the data in Figures 8.7, 8.8, and 8.9 in Section 8.4.

C.1 Eigenfunction/Eigenvalue Calculator

■ **Definition of Constants**

In[4]:=
```
μm = 10^-6;
nm = 10^-9;
kB := 1.38 × 10^(-23);
h := 2 π 1.0545 × 10^(-34);
hbar := h / (2 π);
k := 2. * π / (1064 nm)
```

■ **Definition of Laguerre - Gaussian Beam and optical lattice wavelength**

```
LGRad[r_, ℓ_, w0_] := (2 e)^ℓ / ℓ^ℓ Exp[-2 r^2 / w0^2] (r / w0)^(2 ℓ)
λOL := 1064 nm
```

■ **Define the grid size and the kinetic energy matrix for the x and y directions**

In[13]:=
```
gridsize = 1500;
gridstart = - 26 π;
gridend = - gridstart;
δgrid = (gridend - gridstart) / (gridsize - 1.);
T_{x,y} = 1 / (gridend - gridstart)^2 π^2 / 2
   Table[N[If[i == j, (2. (gridsize + 1.)^2 + 1.) / 3. - Sin[π i / (gridsize + 1.)]^-2, (-1)^(i-j)
       (Sin[(i - j) π / (2 (gridsize + 1.))]^-2 - Sin[(i + j) π / (2 (gridsize + 1.))]^-2)]],
         {i, 1, gridsize}, {j, 1, gridsize}];
```

■ **Diagonalize the Hamiltonian**

```
W = 1;
l = 12;
potential_{x,y} = Table[35. Cos[x]^2 + 35 LGRad[x / k, l, 5.5 μm * W] + .0001 x^2,
   {x, gridstart, gridend, δgrid}]; (* Make the potential *)
h = DiagonalMatrix[potential_{x,y}] + T_{x,y}; (*Hamiltonian = V+T*)
A = Eigensystem[h]; (* diagonalize the hamiltonian*)
ival = Ordering[A[[1]], All, Less]; (* find the coefficients of the ordered eigenvals *)
OrderedIValList_{x,y} = Table[A[[1]][[ival[[i]]]], {i, 1, gridsize}];
VC = 35;

OneDEigenVals_{x,y} = 0;
If[OrderedIValList_{x,y}[[1]] < VC,
  OneDEigenVals_{x,y} = Table[OrderedIValList_{x,y}[[i]], {i, 1, 1}]];
Do[If[OrderedIValList_{x,y}[[i]] < VC, OneDEigenVals_{x,y} =
   Append[OneDEigenVals_{x,y}, OrderedIValList_{x,y}[[i]]]], {i, 2, gridsize}]
L_{x,y} = Length[OneDEigenVals_{x,y}]
```

Out[30]= 160

■ **Combined Optical Lattice and Laguerre-Gaussian Trapping Potential**

```
ListPlot[{potential0, potentialx,y}, PlotRange → All, Joined → True, Axes → True,
 AxesOrigin → {0, -10}, PlotStyle -> {Thick, Directive[Thin, Opacity[0.5]]}]
```

Out[50]=

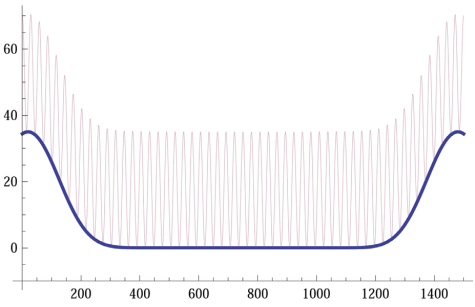

■ **Ground-Band Edge State**

```
ListPlot[A[[2]][[ival[[40]]]], PlotRange → All, PlotJoined → True]
```

Out[32]=

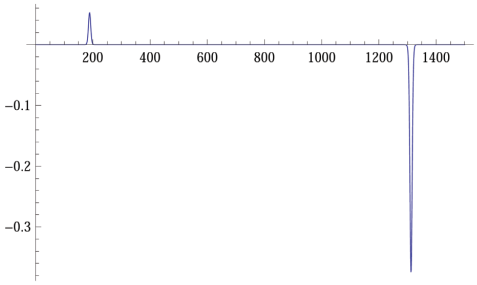

■ **First-Excited Band Central State**

```
ListPlot[A[[2]][[ival[[42]]]], PlotRange → All, PlotJoined → True]
```

Out[33]=

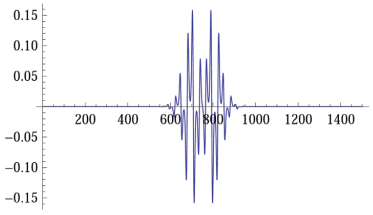

■ **First-Excited Band Edge State**

```
ListPlot[A[[2]][[ival[[76]]]], PlotRange → All, PlotJoined → True]
```

Out[34]=

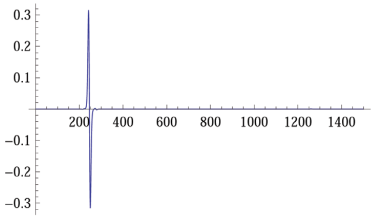

■ **Central and Edge States in the Ground- (Purple) and First-Excited (Blue) Energy Bands**

In[51]:=
```
ListPlot[{50 * A[[2]][[ival[[77]]]] + potential0, 50 * A[[2]][[ival[[78]]]] + potential0 ,
  50 * A[[2]][[ival[[76]]]] + potential0 + E2, 50 * A[[2]][[ival[[75]]]] + potential0 + E2,
  50 * A[[2]][[ival[[43]]]] + potential0 + E2, 50 * A[[2]][[ival[[3]]]] + potential0},
 PlotRange → All, Joined → True, Axes → True, AxesOrigin → {0, -10}, PlotStyle → Thick]
```

Out[51]=

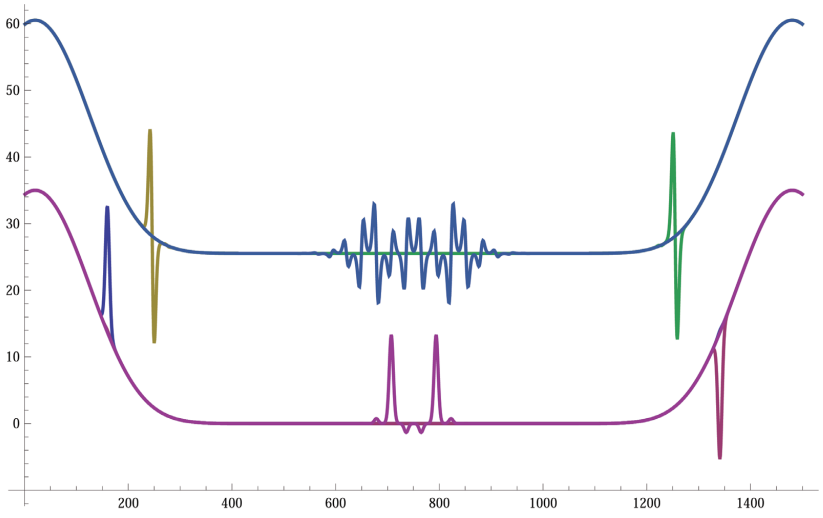

C.2 Main Cooling Program

```
/*****************************************************************
*                                                                *
*   Thermodynamic Simulator for Adiabatic loading of fermions into a   *
*   3D Optical lattice and filtering the atoms from all excited bands  *
*                                                                *
*****************************************************************/


#include "spectrum.h"
#include <stdio.h>
#include <math.h>

/*  User-defined parameters */

#define GRDSZ  3500
#define GRDSTRT -26*PI
#define GRDEND 26*PI
#define dGRD ((GRDEND-GRDSTRT)/(GRDSZ - 1.0))
/*#define SSTRT  0
#define SEND  35
#define NSVALS 8
#define dS  (SEND-SSTRT)/(NSVALS - 1.0)*/
#define TAU_STRT 0.005
#define TAU_END 6.0
#define TAU_NPTS 250
#define TAUSTEP 2
#define dTAU  (TAU_END-TAU_STRT)/(TAU_NPTS-1.0)
#define MUSTEP 1.0
#define NEIGSOUT 300
/*#define NUM 100000*/
#define MAX_ITRS 150
#define EIGVAL_CUTOFF 35.0
#define Min_Atom_Nums 1000
#define Max_Atom_Nums 100500
#define dAtom_Nums 500
#define Num_Atom_Nums ((Max_Atom_Nums-Min_Atom_Nums)/(dAtom_Nums))+1
#define InitTemp .1
#define phase PI/8.0


int NUM_EIGS3D;
int NUM_EIGS1D;
int NUM_EIGS_1BAND3D;
int NUM_EIGS_1BAND1D;
int NUM;

long double Entropy_0, Energy_0;
```

```
/* Function to find number of eigenvalues with energies below cutoff */

int GetNum1DEigVals(float *EigVals)
{
  int i;
  for(i=1;i<GRDSZ+1;i++)
    {
      if(EigVals[i] > EIGVAL_CUTOFF)
            {
             return(((int) i-1));
            }
    }
  return(GRDSZ);
}

/* Entropy evaluator function  */

float EvalEntropy(float mu,float tau,float *EigVals3D)
{
  int i;
  long double logZ;
  long double Energy;
  long double Factor;
  long double PosExpFactor;
  long double NegExpFactor;
  long double Entropy;
  logZ = 0.0;
  Energy = 0.0;

  for(i=1;i<NUM+1;i++)
    {
      Factor = ((long double) EigVals3D[i]- (long double) mu)/((long double) tau);
      PosExpFactor = (long double) exp((long double) Factor);
      logZ += (long double) log((long double) PosExpFactor + (long double) 1.0) - Factor;
      Energy += (long double) EigVals3D[i]/((long double) PosExpFactor + 1.0);
    }

  for(i=NUM+1;i<NUM_EIGS3D+1;i++)
    {
      Factor = ((long double) EigVals3D[i]- (long double) mu)/((long double) tau);
      PosExpFactor = (long double) exp((long double) Factor);
      NegExpFactor = (long double) exp(-(long double) Factor);
      logZ += (long double) log((long double) 1.0 + (long double) NegExpFactor);
      Energy += (long double) EigVals3D[i]/((long double) PosExpFactor + 1.0);
    }
  Entropy = logZ + Energy/((long double) tau) - (long double) mu*NUM/((long double) tau);
  return((float) Entropy);
}
```

```
/*  Energy evaluator function  */

float EvalEnergy(float mu,float tau,float *EigVals3D)
{
  int i;
  long double Energy;
  long double Factor;
  long double PosExpFactor;
  Energy = 0.0;


  for(i=1;i<NUM_EIGS3D+1;i++)
    {
     Factor = ((long double) EigVals3D[i]- (long double) mu)/((long double) tau);
     PosExpFactor = (long double) exp((long double) Factor);
     Energy += (long double) EigVals3D[i]/((long double) PosExpFactor + 1.0);
    }
  return((float) Energy);
}


/*  Function to determine approprite range of chemical potential for iterators  */

float BracketMu(float (*NConstraint)(float,float,float *),float mu_plus,float delta_mu,float
tau,float *EigVals3D)
{
  int i;
  float mu_neg;

  mu_neg = mu_plus - delta_mu;

  for(i=1;i<MAX_ITRS+1;i++)
    {
     if(NConstraint(mu_neg,tau,EigVals3D) < 0.0)
           {
            return(mu_neg);
           }
     mu_neg -=  delta_mu;
    }
  printf("Error: Max iterations reached in function BracketMu");
  exit(1);
  return(1);
}


/*  Define functional form of external trapping potential  */

float LGRad(float x,float w0,int l)
{
  return(pow(2.0*E,l)*exp(-2.0*x*x/(w0*w0))*pow(x/w0,2.0*l)/pow(l,l));
}
```

```
/*  Another function for determining approprite range of chemical potential for iterators  */

float BracketMuPlus(float (*NConstraint)(float,float,float *),float mu_plus,float delta_mu,float
tau,float *EigVals3D)
{

  int i;
  float mu_plus_test;
  mu_plus_test = mu_plus;
  for(i=1;i<MAX_ITRS+1;i++)
    {
     if(NConstraint(mu_plus_test,tau,EigVals3D) > 0.0)
           {
            return(mu_plus_test);
           }
     mu_plus_test +=  delta_mu;
    }
  printf("Error: Max iterations reached in function BracketMu");
  exit(1);
  return(1);
}


/*  Function for calculating 1D eigenvalues */

void MakeIValList(float s,float *EigVals, float **T, float **V, float **H)
{
  int i;
  int j;
  float x;
  x = GRDSTRT;
  for(i=1;i<GRDSZ+1;i++)
    {
     V[i][i] = s*pow(cos(x+(phase)),2.0)+35.0*LGRad(x,32.4789,12)+(s/35.0)*0.0001*x*x;
     x += dGRD;
    }
  for(i=1;i<GRDSZ+1;i++)
    {
     for(j=1;j<GRDSZ+1;j++)
           {
            H[i][j] = T[i][j] + V[i][j];
           }
    }
  call_eval_solver(GRDSZ,H,EigVals);
  for(i=2;i<GRDSZ+1;i++)
    {
     EigVals[i] -= EigVals[1];
    }
  EigVals[1] = 0.0;
```

```
}


/*  Function to express Kinetic Energy in position space                    *
*   Based on D. T. Colbert and W. H. Miller, J. Chem. Phys.  96, 1982 (1991).      */


void InitTMatrix(float **T)
{
  int i,j;
  float TFactor;
  TFactor = PI*PI/(2.0*(GRDEND-GRDSTRT)*(GRDEND-GRDSTRT));
  for(i=1;i<GRDSZ+1;i++)
    {
     for(j=1;j<GRDSZ+1;j++)
           {
            if(i == j)
              {
                T[i][i] = TFactor*(0.66666667*(GRDSZ+1.0)*(GRDSZ+1.0)+0.3333333 -
pow(sin(PI*i/(GRDSZ+1.0)),-2.0));
              }
            else
              {
                T[i][j] = TFactor*(pow(-1.0,i-j)*(pow(sin((i-j)*PI/(2.0*(GRDSZ+1.0))),-2.0) -
pow(sin((i+j)*PI/(2.0*(GRDSZ+1.0))),-2.0)));
              }
           }
    }
}

/* Function to initialize matrix for Potential */

void ZeroVMatrix(float **V)
{
  int i,j;
  for(i=1;i<GRDSZ+1;i++)
    {
     for(j=1;j<GRDSZ+1;j++)
           {
            V[i][j] = 0.0;
           }
    }
}

/*  Function to build 3D list of eigenenergies from list of 1D eigenenergies  */

void Build3DIValList(float *EigVals,float *EigVals3D,int NUM_EIG1D,int NUM_EIG3D)
{
  int j,k,m;
  for(j=1;j<NUM_EIG1D+1;j++)
    {
```

```
    for(k=1;k<NUM_EIG1D+1;k++)
          {
           for(m=1;m<NUM_EIG1D+1;m++)
             {
              EigVals3D[j+NUM_EIG1D*(k-1)+NUM_EIG1D*NUM_EIG1D*(m-1)] =
EigVals[j] + EigVals[k] + EigVals[m];
             }
          }
   }
  sort(NUM_EIG3D,EigVals3D);
}


/*  Function to calculate Number of particles from chem. potential, tau, and 3D eigenenergies  */

float NConstraint(float mu,float tau,float *EigVals3D)
{
  int i;

  long double NSum;
  NSum = 0.0;
  for(i=1;i<NUM_EIGS3D+1;i++)
    {
     NSum += 1.0/(exp(((long double)EigVals3D[i]-(long double)mu)/(long double)tau)+1.0);
    }
  return((float)NSum-NUM);
}

/* Function to Calculate Number of doubly occupied sites from chem. potential, tau, and 3D
eigenenergies  */

float NumDouble(float mu,float tau,float *EigVals3D)
{
  int i;
  long double N2Sum;
  N2Sum = 0.0;
  for(i=1;i<NUM_EIGS3D+1;i++)
    {
     N2Sum += pow(1.0/(exp(((long double)EigVals3D[i]-(long double)mu)/(long
double)tau)+1.0), 2);
    }

  return((float)N2Sum);
}


/*  Function to compare calculated entropy to known entropy for adiabatic operations */

float EntropyConstraint(float mu,float delta_mu,float tau,float *EigVals3D)
{
  int i;
```

```
  float Entropy_test, MUNEG, MUPLUS;
  Entropy_test = 0.0;
  MUPLUS= mu+1.0;
  MUNEG = BracketMu(NConstraint,mu,delta_mu,tau,EigVals3D);
  MUPLUS = MUNEG + delta_mu;
  mu = zbrent(NConstraint,MUPLUS,MUNEG,tau,EigVals3D,0.0000000001);
  Entropy_test = EvalEntropy(mu,tau,EigVals3D);
  return(Entropy_test - Entropy_0);
}


/*****************************
*   Main body of the program  *
*****************************/

main(int argc, char **argv)
{
  int i,j,k;
  int N0;
  FILE *fileptr;
  float x, s, mu, tau;
  long double mu_plus, mu_neg;
  long double tau_plus, tau_neg, tau_0;
  float EFermi[Num_Atom_Nums+1],RethEFermi[Num_Atom_Nums+1];
  float TTF[Num_Atom_Nums+1],RethTTF[Num_Atom_Nums+1];
  float **Entropy;
  long double Entropy_Test, Energy_Test;
  float EigVals[GRDSZ+1];
  float *EigVals3D;
  float OneBand_EigVals[52];
  float *OneBand_EigVals3D;
  long double Energy_OneBand[Num_Atom_Nums+1];
  long double NUM_OneBand[Num_Atom_Nums+1];
  long double NUM_35ER, N2;
  float **T;
  float **H;
  float **V;

  Entropy = matrix(1,2,1,Num_Atom_Nums);

  H = matrix(1,GRDSZ,1,GRDSZ);
  T = matrix(1,GRDSZ,1,GRDSZ);
  V = matrix(1,GRDSZ,1,GRDSZ);

  InitTMatrix(T);
  ZeroVMatrix(V);

  /*for(i=1;i<NSVALS+1;i++)
    {*/
  i=1;
  printf("Calculate entropy at zero lattice depth for various atom numbers \n" );
```

```
s = 0;

        MakeIValList(s,EigVals,T,V,H);
    NUM_EIGS1D = GetNum1DEigVals(EigVals);
    NUM_EIGS3D = NUM_EIGS1D*NUM_EIGS1D*NUM_EIGS1D;
    EigVals3D = vector(1,NUM_EIGS3D);
    Build3DIValList(EigVals,EigVals3D,NUM_EIGS1D,NUM_EIGS3D);
    NUM = Min_Atom_Nums;

        for(j=1;j<Num_Atom_Nums+1;j++)
        {
                mu = (EigVals3D[NUM]+EigVals3D[NUM+1])/2;
                EFermi[j] = mu;
                tau = InitTemp*EFermi[j];
                mu_plus = mu*2.5;
                mu_neg = BracketMu(NConstraint,mu,MUSTEP,tau,EigVals3D);
/*              mu_plus = mu_neg + MUSTEP;

                mu_plus = BracketMuPlus(NConstraint,mu,MUSTEP,tau,EigVals3D);*/
                mu = zbrent(NConstraint,mu_plus,mu_neg,tau,EigVals3D,0.0000000001);
                Entropy[i][j] = EvalEntropy(mu,tau,EigVals3D);
/*              printf("\t NUM: %f\t EFermi: %f\t TTF: %f\t Entropy:
%f\n",NUM,EFermi[j],tau/EFermi[j],Entropy[i][j]);*/
                NUM += dAtom_Nums;
        }

    free_vector(EigVals3D,1,NUM_EIGS3D);


/*  Build 3-D Eigenvector list for atoms in 35 Er lattice depth potential*/

        s = 35;
        MakeIValList(s,EigVals,T,V,H);
    NUM_EIGS1D = GetNum1DEigVals(EigVals);
    NUM_EIGS3D = NUM_EIGS1D*NUM_EIGS1D*NUM_EIGS1D;
    EigVals3D = vector(1,NUM_EIGS3D);
    Build3DIValList(EigVals,EigVals3D,NUM_EIGS1D,NUM_EIGS3D);

/*  Build 3-D Eigenvector list for atoms in first E-Band at 35 Er lattice depth (user-defined)*/

        for(i=1; i<41; i++)
        {
        OneBand_EigVals[i] = EigVals[i];
        }
        OneBand_EigVals[41]=EigVals[76];
        OneBand_EigVals[42]=EigVals[78];
        OneBand_EigVals[43]=EigVals[81];
        OneBand_EigVals[44]=EigVals[115];
        OneBand_EigVals[45]=EigVals[123];
        OneBand_EigVals[46]=EigVals[131];
        OneBand_EigVals[47]=EigVals[165];
```

```
            OneBand_EigVals[48]=EigVals[169];
            OneBand_EigVals[49]=EigVals[188];
            OneBand_EigVals[50]=EigVals[193];
            OneBand_EigVals[51]=EigVals[GRDSZ];


          NUM_EIGS_1BAND1D = GetNum1DEigVals(OneBand_EigVals);
     NUM_EIGS_1BAND3D =
NUM_EIGS_1BAND1D*NUM_EIGS_1BAND1D*NUM_EIGS_1BAND1D;
     OneBand_EigVals3D = vector(1,NUM_EIGS_1BAND3D);

Build3DIValList(OneBand_EigVals,OneBand_EigVals3D,NUM_EIGS_1BAND1D,NUM_EIGS
_1BAND3D);

            if((fileptr = fopen("Laguerre_pi_8_1_1.dat","w")) == NULL)
    {
     printf("Can't open output file\n");
     return(1);
    }


/*  Begin Adiabatic Cooling Iterator */

 NUM = Min_Atom_Nums;
            for(j=1;j<Num_Atom_Nums+1;j++)
            {
                        printf("Starting Blakie Cooling with %i %s \n \n", NUM, " Atoms");
                        Entropy_0 = Entropy[1][j];
                        mu = (EigVals3D[NUM]+EigVals3D[NUM+1])/2.0;
                        EFermi[j] = mu;
                        tau_0 = .05*EFermi[j];
                        tau_neg = .0001*EFermi[j];
                        tau_plus = EFermi[j];

                        for(i=1;i<MAX_ITRS+1;i++)
                                    {
                                    mu = (EigVals3D[NUM]+EigVals3D[NUM+1])/2.0;
                                    mu_plus = mu*2.5;
                                    mu_neg = BracketMu(NConstraint,mu,MUSTEP,tau_0,EigVals3D);
/*                                  mu_plus =
BracketMuPlus(NConstraint,mu,MUSTEP,tau,EigVals3D);*/
                                    mu =
zbrent(NConstraint,mu_plus,mu_neg,tau_0,EigVals3D,0.0000000001);
                                    Entropy_Test = EvalEntropy(mu,tau_0,EigVals3D);
                                    printf("Tau_0/EF = %Lf %s %Lf %s %Lf %s %Lf %s %i
\n",tau_0/EFermi[j]," Entropy_0 = ",Entropy_0," Entropy_Test = ",Entropy_Test, " Entropy_Test
- Entropy_0 = ",Entropy_Test - Entropy_0,"  i = ",i);

                                    if(fabs(Entropy_Test - Entropy_0) > .001 && tau_plus - tau_neg >
tau_0/100000.)
                                    {
```

```
                                        if(Entropy_Test > Entropy_0)
                                        {
                                                tau_plus = tau_0;
                                                tau_0 = (tau_plus + tau_neg)/2;
                                        }
                                        else
                                        {
                                                tau_neg = tau_0;
                                                tau_0 = (tau_plus + tau_neg)/2;
                                        }
                                }
                                else
                                {
                                        break;
                                }
                                if(i == MAX_ITRS)
                                {
                                printf("Error: Max iterations reached in Blakie Cooling");
                                return(1);
                                }
                        }
/* fprintf(fileptr,"\t%f\n",tau_neg);

                        tau =
zbrent_tau(EntropyConstraint,tau_plus,tau_neg,mu,MUSTEP,EigVals3D,0.0000000001);
*/
                tau = tau_0;
                TTF[j] = tau/EFermi[j];
                NUM_OneBand[j] = 0;
                NUM_35ER = 0;
                N2 = 0;
                Energy_OneBand[j] = 0;
                for(i=1;i< NUM_EIGS_1BAND3D + 1;i++)
                {
                NUM_OneBand[j] += 1.0/(exp(((long double)OneBand_EigVals3D[i]-(long
double)mu)/(long double)tau)+1.0);
                Energy_OneBand[j] += (long double)OneBand_EigVals3D[i]/(exp(((long
double)OneBand_EigVals3D[i]-(long double)mu)/(long double)tau)+1.0);
                }
                NUM_35ER = 1.0/(exp(((long double)OneBand_EigVals3D[NUM_EIGS_1BAND3D]-
(long double)mu)/(long double)tau)+1.0);
                N2 = NumDouble(mu, tau, EigVals3D);
               printf("%i %s %i %s %Lf %s %Lf \n \n", NUM," ", NUM_EIGS_1BAND3D, " ",
NUM_OneBand[j], " ",Energy_OneBand[j] );

               fprintf(fileptr,"%i \t %f \t %Lf \t %Lf \t %f \t %Lf \t %Lf \t %f \t %f \t %LE \t %LE
\n",NUM,TTF[j],Entropy_0,Entropy_Test -
Entropy_0,EFermi[j],NUM_OneBand[j],Energy_OneBand[j],mu,tau, NUM_35ER, N2);
                        NUM += dAtom_Nums;
                }
        fprintf(fileptr,"\n \n");
```

```
/*  Rethermalization after filtering iterator */

   for(j=1;j<Num_Atom_Nums+1;j++)
   {
    N0 = Min_Atom_Nums;
    Energy_0 = Energy_OneBand[j];
    NUM = NUM_OneBand[j];
    mu = (EigVals3D[NUM]+EigVals3D[NUM+1])/2.0;
    RethEFermi[j] = mu;
    tau_0 = .05*RethEFermi[j];
    tau_neg = .00001*RethEFermi[j];
    tau_plus = RethEFermi[j];

    printf("Starting rethermalization with %i %s \n \n", NUM, " Atoms");


    for(i=1;i<MAX_ITRS+1;i++)
    {
                        mu = (EigVals3D[NUM]+EigVals3D[NUM+1])/2.0;
                        mu_plus = mu*2.5;
                        mu_neg = BracketMu(NConstraint,mu,MUSTEP,tau_0,EigVals3D);
/*                      mu_plus =
BracketMuPlus(NConstraint,mu,MUSTEP,tau,EigVals3D);*/

                        mu =
zbrent(NConstraint,mu_plus,mu_neg,tau_0,EigVals3D,0.0000000001);
                        Energy_Test = EvalEnergy(mu,tau_0,EigVals3D);
                        printf("Tau_0/RethEF = %Lf %s %Lf %s %Lf %s %Lf %s %i
\n",tau_0/RethEFermi[j]," Energy_0 = ",Energy_0," Energy_Test = ",Energy_Test, "
Energy_Test - Energy_0 = ",Energy_Test - Energy_0,"  i = ",i);

        if(fabs(Energy_Test - Energy_0) > .001 && tau_plus - tau_neg > tau_0/100000.)
        {
                        if(Energy_Test > Energy_0)
                        {
                                tau_plus = tau_0;
                                tau_0 = (tau_plus + tau_neg)/2;
                        }
                        else
                        {
                                tau_neg = tau_0;
                                tau_0 = (tau_plus + tau_neg)/2;
                        }
                }
                else
                {
                        break;
                }
```

```
        if(i == MAX_ITRS)
                                {

                                printf("Error: Max iterations reached in Blakie Cooling");
                                return(1);
                                }
        }

          tau = tau_0;
          RethTTF[j] = tau/RethEFermi[j];
          NUM_OneBand[j] = 0;
          NUM_35ER = 0;
          N2 = 0;
          Energy_OneBand[j] = 0;
          for(i=1;i< NUM_EIGS_1BAND3D + 1;i++)
          {
          NUM_OneBand[j] += 1.0/(exp(((long double)OneBand_EigVals3D[i]-(long
double)mu)/(long double)tau)+1.0);
          Energy_OneBand[j] += (long double)OneBand_EigVals3D[i]/(exp(((long
double)OneBand_EigVals3D[i]-(long double)mu)/(long double)tau)+1.0);
          }

          NUM_35ER = 1.0/(exp(((long double)OneBand_EigVals3D[NUM_EIGS_1BAND3D]-
(long double)mu)/(long double)tau)+1.0);
          N2 = NumDouble(mu, tau, EigVals3D);

                                printf("Tau_0/EF = %Lf %s %Lf %s %Lf %s %LE %s %i
\n",tau_0/RethEFermi[j]," Energy_0 = ",Energy_0," Energy_Test = ",Energy_Test, "
Energy_Test - Energy_0 = ",Energy_Test - Energy_0,"  i = ",i);
                        fprintf(fileptr,"%i \t %i \t %f \t %Lf \t %LE \t %f \t %Lf \t %Lf \t %f \t %f \t
%LE \t %LE \n",N0,NUM,RethTTF[j],Energy_0,Energy_Test -
Energy_0,RethEFermi[j],NUM_OneBand[j],Energy_OneBand[j],mu,tau, NUM_35ER, N2);
                    N0 += dAtom_Nums;
        }
    free_vector(EigVals3D,1,NUM_EIGS3D);
    free_vector(OneBand_EigVals3D,1,NUM_EIGS_1BAND3D);


/*      NUM = Min_Atom_Nums;
    fprintf("\t NUM; %f\t TTF; %f\t Entropy; %f\t EFermi");
           for(i=1;i<Num_Atom_Nums+1;i++)
   {
           j=1;*/
           /*NUM += dAtom_Nums;*/

  fclose(fileptr);
  free_matrix(Entropy,1,2,1,Num_Atom_Nums);
  free_matrix(H,1,GRDSZ,1,GRDSZ);
  free_matrix(T,1,GRDSZ,1,GRDSZ);
  free_matrix(V,1,GRDSZ,1,GRDSZ);
  return(1);}
```

Bibliography

[1] Braaten, E. and H. W. Hammer (2006) "Universality in few-body systems with large scattering length," *Phys. Rep.*, **428**(5), p. 259.

[2] Greene, C. H., B. D. Esry, and H. Suno (2010) "Universal insights from few-body land," *Physics Today*, **63**, p. 40.

[3] Braaten, E., H. W. Hammer, D. Kang, and L. Platter (2009) "Three-Body Recombination of ^{6}Li Atoms with Large Negative Scattering Lengths," *Phys. Rev. Lett.*, **103**, p. 073202.

[4] Naidon, P. and M. Ueda (2009) "Possible Efimov Trimer State in a Three-Hyperfine-Component Lithium-6 Mixture," *Phys. Rev. Lett.*, **103**, p. 073203.

[5] Wenz, A. N., T. Lompe, T. B. Ottenstein, F. Serwane, G. Zürn, and S. Jochim (2009) "A Universal Trimer in a Three-Component Fermi Gas," *Phys. Rev. A*, **80**, p. 040702.

[6] Kang, D. and E. Braaten, Private communication, Ohio State University OH.

[7] Greene, C. H., B. D. Esry, and H. Suno (2004) "A revised formula for 3-body recombination that cannot exceed the unitarity limit," *Nucl. Phys.*, **A737**, p. 119.

[8] Braaten, E., H. W. Hammer, D. Kang, and L. Platter (2009) "Efimov Physics in 6Li Atoms," *Phys. Rev. A*, **81**, p. 013605.

[9] Chin, C., R. Grimm, P. Julienne, and E. Tiesinga (2010) "Feshbach resonances in ultracold gases," *Rev. Mod. Phys*, **82**, p. 1225.

[10] "The NIST Reference on Constants, Units, and Uncertainty," Published online at http://physics.nist.gov/cuu/Constants/.

[11] Gehm, M. E. (2003) *Preparation of an Optically-Trapped Degenerate Fermi Gas of ^{6}Li: Finding the Route to Degeneracy*, Ph.D. thesis, Duke University, Department of Physics.

[12] Heiselberg, H. (2001) "Fermi systems with long scattering lengths," *Phys. Rev. A*, **63**, p. 043606.

[13] Ho, T. L. (2004) "Universal Thermodynamics of Degenerate Quantum Gases in the Unitarity Limit," *Phys. Rev. Lett.*, **92**, p. 090402.

[14] Thomas, J. E. (2009) "Is an Ultra-Cold Strongly Interacting Fermi Gas a Perfect Fluid?" *Nucl. Phys. A*, **830**, p. 665c.

[15] ——— (2010) "The nearly perfect Fermi gas," *Physics Today*, **63**, p. 34.

[16] Baker, G. A. (1999) "Neutron matter model," *Phys. Rev. C*, **60**, p. 054311.

[17] Heiselberg, H., C. J. Pethick, H. Smith, and L. Viverit (2000) "Influence of Induced Interactions on the Superfluid Transition in Dilute Fermi Gases," *Phys. Rev. Lett.*, **85**, p. 2418.

[18] Hammer, H. W. and L. Platter (2010) "Efimov States in Nuclear and Particle Physics," *ArXiv*, p. 1001.1981.

[19] Shuryak, E. (2004) "Why does the Quark-Gluon Plasma at RHIC behave as a nearly ideal fluid ?" *Prog. Part. Nucl. Phys.*, **53**, p. 273.

[20] O'Hara, K. M., S. L. Hemmer, M. E. Gehm, S. R. Granade, and J. E. Thomas (2002) "Observation of a strongly-interacting degenerate Fermi gas of atoms," *Science*, **298**, p. 2179.

[21] Bartenstein, M., A. Altmeyer, S. Riedl, S. Jochim, C. Chin, J. H. Denschlag, and R. Grimm (2004) "Crossover from a molecular Bose-Einstein condensate to a Degenerate Fermi Gas," *Phys. Rev. Lett.*, **92**, p. 120401.

[22] Zwierlein, M. W., J. R. Abo-Shaeer, A. Schirotze, C. H. Schunck, and W. Ketterle (2005) "Vortices and superfluidity in a strongly interacting Fermi gas," *Nature*, **435**, p. 1047.

[23] Greiner, M., C. A. Regal, and D. S. Jin (2003) "Emergence of a molecular Bose-Einstein condensate from a Fermi gas," *Nature*, **426**, p. 537.

[24] Jochim, S. (2004) *Bose-Einstein Condensation of Molecules*, Ph.D. thesis, Universität Innsbruck.

[25] Clancy, B. E. (2008) *Hydrodynamics of a Rotating Strongly Interacting Fermi Gas*, Ph.D. thesis, Duke University, Department of Physics.

[26] Luo, L. (2008) *Entropy and Superfluid Critical Parameters of a Strongly Interacting Fermi gas*, Ph.D. thesis, Duke University, Department of Physics.

[27] Regal, C. A. (2006) *Experimental realization of BCS-BEC crossover physics with a Fermi gas of atoms*, Ph.D. thesis, University of Colorado.

[28] Schunck, C. H. (2008) *Pairing and Superfuidity in Strongly Interacting Fermi Gases*, Ph.D. thesis, Massachusetts Institute of Technology, Department of Physics.

[29] Stewart, J. (2004) *Probing a strongly interacting Fermi gas*, Ph.D. thesis, University of Colorado.

[30] Efimov, V. (1970) "Energy levels arising from resonant two-body forces in a three-body system," *Physics Letters B*, **33**, p. 563.

[31] ——— (1971) "Weakly-bound States of Three Resonantly-Interacting Particles," *Sov. J. Nucl. Phys.*, **12**, p. 589.

[32] ——— (1979) "Low-energy Properties of Three Resonantly-interacting Particles," *Sov. J. Nucl. Phys.*, **29**, p. 546.

[33] Lim, T. K., S. K. Duffy, and W. C. Damer (1977) "Efimov State in the ^{4}He Trimer," *Phys. Rev. Lett.*, **38**, p. 341.

[34] Schöllkopf, W. and J. P. Tönnies (1996) "The nondestructive detection of the helium dimer and trimer," *J. Chem. Phys.*, **104**, p. 1155.

[35] Kraemer, T., M. Mark, P. Waldburger, J. G. Danzl, C. Chin, B. Engeser, A. D. Lange, K. Pilch, A. Jaakkola, H.-C. Nagerl, and R. Grimm (2006) "Evidence for Efimov quantum states in an ultracold gas of caesium atoms," *Nature*, **440**, p. 315.

[36] Gross, N., Z. Shotan, S. Kokkelmans, and L. Khaykovich (2009) "Observation of universality in ultracold 7Li three-body recombination," *Phys. Rev. Lett.*, **103**, p. 163202.

[37] Zaccanti, M., B. Deissler, C. DErrico, M. Fattori, M. Jona-Lasinio, S. Mueller, G. Roati, M. Inguscio, and G. Modugno (2009) "Observation of an Efimov spectrum in an atomic system," *Nature Phys.*, **5**, p. 586.

[38] Pollack, S., D. Dries, and R. Hulet (2009) "Universality in Three- and Four-Body Bound States of Ultracold Atoms," *Science*, **326**, p. 1683.

[39] Barontini, G., C. Weber, F. Rabatti, J. Catani, G. Thalhammer, M. Inguscio, and F. Minardi (2009) "Observation of Heteronuclear Atomic Efimov Resonances," *Phys. Rev. Lett.*, **103**, p. 043201.

[40] Knoop, S., F. Ferlaino, M. Mark, M. Berninger, H. Schoebel, H.-C. Naegerl, and R. Grimm (2009) "Observation of an Efimov-like trimer resonance in ultracold atom-dimer scattering," *Nature Phys.*, **5**, p. 227.

[41] Leanhardt, A. E., T. A. Pasquin, M. Saba, A. Schirotzek, Y. Shin, D. Kielpinski, D. E. Pritchard, and W. Ketterle (2003) "Adiabatic and Evaporative Cooling of Bose-Einstein Condensates below 500 Picokelvin," *Science*, **301**, p. 1513.

[42] Metcalf, H. J. and van der Stratten (1999) *Laser Cooling and Trapping*, Springer-Verlag, New York.

[43] Ketterle, W. and N. van Druten (1996) "Evaporative cooling of atoms," *Advances in Atomic, Molecular, and Optical Physics*, **37**, p. 181.

[44] Anderson, M. H., J. R. Ensher, M. R. Matthews, C. E. Wieman, and E. A. Cornell (1995) "Observation of Bose-Einstein condensation in a Dilute Atomic Vapor," *Science*, **269**, p. 198.

[45] Davis, K. B., M. O. Mewes, M. R. Andrews, N. J. van Druten, D. S. Durfee, D. M. Kurn, and W. Ketterle (1995) "Bose-Einstein condensation in a gas of sodium atoms," *Phys. Rev. Lett*, **75**, p. 3969.

[46] Bradley, C. C., C. A. Sackett, J. J. Tollett, and R. G. Hulet (1995) "Evidence of Bose-Einstein Condensation in an Atomic Gas with Attractive Interactions," *Phys. Rev. Lett.*, **75**, p. 1687.

[47] Bardeen, J., L. N. Cooper, and J. R. Schrieffer (1957) "Microscopic theory of superconductivity," *Phys. Rev.*, **106**, p. 162.

[48] ——— (1957) "Theory of superconductivity," *Phys. Rev.*, **108**, p. 1175.

[49] DeMarco, B. and D. S. Jin (1999) "Onset of Fermi degeneracy in a trapped atomic gas," *Science*, **285**, p. 1703.

[50] Truscott, A. G., K. E. Strecker, W. I. McAlexander, G. B. Partridge, and R. G. Hulet (2001) "Observation of Fermi Pressure in a Gas of Trapped Atoms," *Science*, **291**, p. 2570.

[51] Roati, G., F. Riboli, G. Modugno, and M. Inguscio (2002) "Fermi-Bose Quantum Degenerate 40K-87Rb Mixture with Attractive Interaction," *Phys. Rev. Lett.*, **89**, p. 150403.

[52] Hadzibabic, Z., C. A. Stan, K. Dieckmann, S. Gupta, M. Zwierlein, A. Gorlitz, and W. Ketterle (2002) "Two-Species Mixture of Quantum Degenerate Bose and Fermi Gases," *Phys. Rev. Lett.*, **88**, p. 160401.

[53] Granade, S. R., M. E. Gehm, K. M. O'Hara, and J. E. Thomas (2002) "All-Optical Production of a Degenerate Fermi Gas," *Phys. Rev. Lett.*, **88**, p. 120405.

[54] Jochim, S., M. Bartenstein, G. Hendl, J. H. Denschlag, R. Grimm, A. Mosk, and M. Weidemuller (2002) "Magnetic field control of elastic scattering in a cold gas of fermionic lithium atoms," *Phys. Rev. Lett.*, **89**, p. 273202.

[55] Jochim, S., M. Bartenstein, A. Altmeyer, G. Hendl, S. Reidl, C. Chin, J. H. Denschlag, and R. Grimm (2003) "Bose-Einstein condensation of molecules," *Science*, **302**, p. 5653.

[56] Zwierlein, M. W., C. A. Stan, C. H. Schunck, S. M. F. Raupach, S. Gupta, Z. Hadzibabic, and W. Ketterle (2003) "Observation of Bose-Einstein Condensation of Molecules," *Phys. Rev. Lett.*, **91**, p. 250401.

[57] Regal, C. A., M. Greiner, and D. S. Jin (2004) "Observation of Resonance Condensation of Fermionic Atom Pairs," *Phys. Rev. Lett*, **92**, p. 040403.

[58] Bourdel, T., L. Khaykovich, J. Cubizolles, J. Zhang, F. Chevy, M. Teichmann, L. Tarruell, S. J. J. M. F. Kokkelmans, and C. Salomon (2004) "Experimental Study of the BEC-BCS Crossover Region in Lithium 6," *Phys. Rev. Lett.*, **93**, p. 050401.

[59] Zwierlein, M. W., C. A. Stan, C. H. Schunck, S. M. F. Raupach, A. J. Kerman, and W. Ketterle (2004) "Condensation of pairs of fermionic atoms near a feshbach resonance," *Phys. Rev. Lett.*, **92**, p. 120403.

[60] Kinast, J., S. L. Hemmer, M. Gehm, A. Turlapov, and J. E. Thomas (2004) "Evidence for superfluidity in a resonantly interacting Fermi gas," *Phys. Rev. Lett.*, **92**, p. 150402.

[61] Altmeyer, A., C. Kohstall, E. R. Sanchez-Guajardo, J. H. Denschlag, R. Grimm, M. J.Wright, and S. Ried (2007) "Finite-temperature collective dynamics of a fermi gas in the bec-bcs crossover," *Phys. Rev. Lett.*, **99**, p. 150403.

[62] Wright, M., C. Kohstall, J. H. D. abd R. Grimm, A. Altmeyer, and S. Riedl (2007) "Dynamics of a strongly interacting fermi gas: the radial quadrupole mode," *Phys. Rev. A*, **76**, p. 033610.

[63] Stewart, J. T., J. P. Gaebler, and D. S. Jin (2008) "Using photoemission spectroscopy to probe a strongly interacting Fermi gas," *Nature*, **454**, p. 744.

[64] Chin, C., M. Bartenstein, A. Altmeyer, S. Riedl, S. Jochim, J. H. Denschlag, and R. Grimm (2004) "Observation of the Pairing Gap in a Strongly Interacting Fermi Gas," *Science*, **305**, p. 1128.

[65] Gaebler, J. P., J. T. Stewart, T. E. Drake, D. S. Jin, A. Perali, P. Pieri, and G. C. Strinati (2010) "Observation of pseudogap behavior in a strongly interacting Fermi gas," *arXiv*, p. 1003.1147v1.

[66] Lou, L. and J. E. Thomas (2009) "Thermodynamic Measurements in a Strongly Interacting Fermi Gas," *J. Low Temp. Phys.*, **154**, p. 1.

[67] Stewart, J. T., J. P. Gaebler, C. A. Regal, and D. S. Jin (2006) "The potential energy of a ^{40}K Fermi gas in the BCS-BEC crossover," *Phys. Rev. Lett.*, **97**, p. 220406.

[68] Clancy, B., L. Luo, and J. E. Thomas (2007) "Observation of Nearly Perfect Irrotational Flow in Normal and Superfluid Strongly Interacting Fermi Gases," *Phys. Rev. Lett*, **99**, p. 140401.

[69] Kolb, P. F. and U. Heinz (2003) *Hydrodynamic Description of Ultrarelativistic Heavy Ion Collisions*, Quark-Gluon Plasma, World Scientific.

[70] Stewart, J. T., J. P. Gaebler, T. E. Drake, and D. S. Jin (2010) "Verification of universal relations in a strongly interacting Fermi gas," *arXiv*, p. 1002.1987.

[71] Jaksch, D., C. Bruder, J. I. Cirac, C. W. Gardiner, and P. Zoller (1998) "Cold Bosonic Atoms in Optical Lattices," *Phys. Rev. Lett.*, **81**, p. 3108.

[72] Hofstetter, W., J. I. Cirac, P. Zoller, E. Demler, and M. D. Lukin (2002) "High-Temperature Superfluidity of Fermionic Atoms in Optical Lattices," *Phys. Rev. Lett.*, **89**, p. 220407.

[73] Jaksch, D. and P. Zoller (2005) "The cold atom Hubbard toolbox," *Ann. Phys.*, **315**, p. 52.

[74] Werner, F., O. Parcollet, A. Georges, and S. R. Hassan (2005) "Interaction-Induced Adiabatic Cooling and Antiferromagnetism of Cold Fermions in Optical Lattices," *Phys. Rev. Lett.*, **95**, p. 056401.

[75] Kohl, M., H. Moritz, T. Stoferle, K. Gunter, and T. Esslinger (2005) "Fermionic Atoms in a Three Dimensional Optical Lattice: Observing Fermi Surfaces, Dynamics, and Interactions," *Phys. Rev. Lett.*, **94**, p. 080403.

[76] Strohmaier, N., Y. Takasu, K. Günter, R. Jördens, M. Köhl, H. Moritz, and T. Esslinger (2007) "Interaction-Controlled Transport of an Ultracold Fermi Gas," *Phys. Rev. Lett.*, **99**, p. 220601.

[77] Pezzé, L., L. Pitaevskii, A. Smerzi, S. Stringari, G. Modugno, E. de Mirandes, F. Ferlaino, H. Ott, G. Roati, and M. Inguscio (2004) "Insulating Behavior of a Trapped Ideal Fermi Gas," *Phys. Rev. Lett.*, **93**, p. 120401.

[78] Jordens, R., N. Strohmaier, K. Gunter, H. Moritz, and T. Esslinger (2008) "A Mott insulator of fermionic atoms in an optical lattice," *Nature*, **455**, p. 204.

[79] Schneider, U., L. Hackermuller, S. Will, T. Best, I. Bloch, T. A. Costi, R. W. Helmes, D. Rasch, and A. Rosch (2008) "Metallic and Insulating Phases of Repulsively Interacting Fermions in a 3D Optical Lattice," *Science*, **322**, p. 1520.

[80] Chin, J. K., D. E. Miller, Y. Liu, C. Stan, W. Setiawan, C. Sanner, K. Xu, and W. Ketterle (2006) "Evidence for superfluidity of ultracold fermions in an optical lattice," *Nature*, **443**, p. 961.

[81] Rom, T., T. Best, D. V. Oosten, U. Schneider, S. Fölling, B. Paredes, and I. Bloch (2006) "Free fermion antibunching in a degenerate atomic Fermi gas released from an optical lattice," *Nature*, **444**, p. 733.

[82] Bernier, J.-S., C. Kollath, A. Georges, L. D. Leo, F. Gerbier, C. Salomon, and M. Kohl (2009) "Cooling fermionic atoms in optical lattices by shaping the confinement," *Phys. Rev. A*, **79**, p. 061601.

[83] Luu, T. and A. Schwenk (2007) "Three-Fermion Problems in Optical Lattices," *Phys. Rev. Lett.*, **98**, p. 103202.

[84] Honerkamp, C. and W. Hofstetter (2004) "BCS pairing in Fermi systems with N different hyperfine states," *Phys. Rev. B*, **70**, p. 094521.

[85] Paananen, T., J. P. Martikainen, and P. Torma (2006) "Pairing in a three-component Fermi gas," *Phys. Rev. A*, **73**, p. 053606.

[86] Bedaque, P. and J. P. D'Incao (2009) "Superfluid phases of the three-species fermion gas," *Ann. Phys.*, **324**, p. 1763.

[87] He, L., M. Jin, and P. Zhuang (2006) "Superfluidity in a three-flavor Fermi gas with SU(3) symmetry," *Phys. Rev. A*, **74**, p. 033604.

[88] Zhai, H. (2007) "Superfluidity in three-species mixtures of Fermi gases across Feshbach resonances," *Phys. Rev. A*, **75**, p. 031603(R).

[89] Cherng, R., G. Refael, and E. Demler (2007) "Superfluidity and Magnetism in Multicomponent Ultracold Fermions," *Phys. Rev. Lett.*, **99**, p. 130406.

[90] Rapp, A., G. Zarand, C. Honerkamp, and W. Hofstetter (2007) "Color Superfluidity and Baryon Formation in Ultracold Fermions," *Phys. Rev. Lett*, **98**, p. 160405.

[91] Rapp, A., W. Hofstetter, and G. Zarand (2008) "Trionic phase of ultracold fermions in an optical lattice: A variational study," *Phys. Rev. B*, **77**, p. 144520.

[92] Wilczek, F. (2007) "Quantum chromodynamics: Lifestyles of the small and simple," *Nature Physics*, **3**, p. 375.

[93] Arimondo, E., M. Inguscio, and P. Violino (1977) "Experimental Determinations of the Hyperfine Structure in the Alkali Atoms," *Rev. Mod. Phys.*, **49**, p. 31.

[94] Corney, A. (1977) *Atomic and Laser Spectroscopy*, Clarendon Press.

[95] O'Hara, K. M. (2000) *Optical Trapping and Evaporative Cooling of Fermionic Atoms*, Ph.D. thesis, Duke University, Department of Physics.

[96] Gribakin, G. F. and V. V. Flambaum (1993) "Calculation of the scattering length in atomic collisions using the semiclasical approximation," *Phys. Rev. A*, **48**, p. 546.

[97] Griffiths, D. J. (1995) *Introduction to Quantum Mechanics*, Prentice Hall, Upper Saddle, NJ.

[98] Shankar, R. (1994) *Principles of Quantum Mechanics*, 2nd edition ed., Plenum, New York.

[99] Sakurai, J. J. (1994) *Modern Quantum Mechanics*, revised edition ed., Addison-Wesley, New York.

[100] Cohen-Tannoudji, C., B. Diu, and F. Laloé (1977) *Quantum Mechanics*, vol. Volume Two, John Wiley & Sons, New York.

[101] Landau, R. H. (1996) *Quantum Mechanics II, A second Course in Quantum Theory*, second edition ed., Wiley-Interscience.

[102] Mahan, G. D. (2009) *Quantum Mechanics in a Nutshell*, Princeton University Press, Princeton, NJ.

[103] Joachain, C. J. (1975) *Quantum Collision Theory*, North-Holland Publishing, Amsterdam · Oxford.

[104] Julienne, P., A. Smith, and K. Burnett (1992) *Theory of Collisions between Laser Cooled Atoms*, vol. Volume 30 of *Advances in Atomic, Molecular, and Optical Physics*, Academic Press.

[105] DeMarco, D., J. L. Bohn, J. P. Burke, M. Holland, and D. S. Jin (1999) "Measurement of p-wave threshold law using evaporatively cooled Fermionic atoms," *Phys. Rev. Lett.*, **82**, p. 4208.

[106] Schwinger, J. (1947) "A Variational Principle for Scattering Problems," *Phys. Rev.*, **72**, p. 742.

[107] Dalibard, J. (1999) *Collisional dynamics of ultra-cold atomic gases*, Proceedings of the International School of Physics - Enrico Fermi, IOS Press.

[108] Pethic, C. and H. Smith (2002) *Bose-Einstein condensation in dilute gases*, Cambridge University Press.

[109] Houbiers, M., R. Ferwerda, T. C. Stoof, W. I. McAlexander, C. A. Sackett, and R. G. Hulet (1997) "Superfluid state of atomic ^{6}Li in a magnetic trap," *Phys. Rev. A*, **56**, p. 4864.

[110] Stoof, H. T. C., J. M. V. A. Koelman, and B. J. Verhaar (1988) "Spin-exchange and dipole relaxation rates in atomic hydrogen: Rigorous and simplified calculations," *Phys. Rev. B*, **38**, p. 4688.

[111] O'Hara, K. M., M. E. Gehm, S. R. Granade, S. Bali, and J. E. Thomas (2000) "Stable, Strongly Attractive, Two-State Mixture of Lithium Fermions in an Optical Trap," *Phys. Rev. Lett.*, **85**, p. 2092.

[112] Feshbach, H. (1958) "A Unified Theory of Nuclear Reactions," *Ann. Phys.*, **5**, p. 337.

[113] Fano, U. (1961) "Effects of configuration interaction on inten-sities and phase shifts," *Phys. Rev. A*, **124**, p. 1866.

[114] Moerdijk, B. J. V., A. J. and A. Axelsson (1995) "Resonances in ultracold collisions of ^{6}Li, ^{7}Li, and ^{23}Na," *Phys. Rev. A*, **51**, p. 4852.

[115] Bartenstein, M., A. Altmeyer, S. Riedl, R. Geursen, S. Jochim, C. Chin, J. H. Denschlag, R. Grimm, A. Simoni, E. Tiesinga, C. J. Williams, and P. S. Julienne (2005) "Precise determination of 6Li cold collision parameters by radio-frequency spectroscopy on weakly bound molecules," *Phys. Rev. Lett.*, **94**, p. 103201.

[116] Julienne, P., Private communications, NIST, University of Maryland, Gaithersburg, MD.

[117] Strecker, K. E., G. B. Partridge, and R. G. Hulet (2003) "Conversion of an atomic Fermi gas to a long-lived molecular Bose gas," *Phys. Rev. Lett.*, **91**, p. 080406.

[118] Schunck, C. H., M. W. Zwierlein, C. A. Stan, S. M. F. Raupach, W. Ketterle, A. Simoni, E. Tiesinga, C. J. Williams, and P. S. Julienne (2005) "Feshbach resonances in fermionic ^{6}Li," *Phys. Rev. A*, **71**, p. 045601.

[119] Zhang, J., E. G. M. van Kempen, T. Bourdel, L. Khaykovich, J. Cubizolles, F. Chevy, M. Teichmann, L. Taruell, S. J. J. M. F. Kokkelmans, and C. Salomon (2004) "P-wave Feshbach resonances of ultracold ^{6}Li," *Phys. Rev. A*, **70**, p. 030702(R).

[120] Grimm, R. (2007) *Ultracold Fermi gases in the BEC-BCS crossover: a review from the Innsbruck perspective*, Ultracold Fermi Gases, Procs. of the Int. School of Physics "Enrico Fermi", Course CLXIV, Varenna, 20 - 30 June 2006, IOS Press.

[121] Efimov, V. (1973) "Energy levels of three resonantly interacting particles," *Nucl. Phys. A*, **201**, p. 157.

[122] Bethe, H. A. and E. E. Salpeter (1957) *Quantum Mechanics of One- and Two-electron Atoms*, Springer Verlag, New York.

[123] Nielsen, E., D. Fedorov, A. Jensen, and E. Garrido (2001) "The three-body problem with short-range interactions," *Phys. Rep.*, **347**(5), p. 373.

[124] Delves, L. (1960) "Tertiary and general-order collisions (II)," *Nucl. Phys.*, **20**, p. 275.

[125] Faddeev, L. and S. Merkuriev (1993) *Quantum Scattering Theory for Several Particle Systems*, no. 11 in Mathematical Physics and Applied Mathematics, Kluwer, Dordrecht, The Netherlands.

[126] Faddeev, L. (1961) "Scattering Theory For A Three Particle System," *Sov. Phys. JETP*, **12**, p. 1014.

[127] Braaten, E. and H. W. Hammer (2007) "Efimov Physics in Cold Atoms," *Annals. Phy.*, **322**, p. 120.

[128] D'Incao, J. P., C. H. Greene, and B. D. Esry (2009) "The short-range three-body phase and other issues impacting the observation of Efimov physics in ultracold quantum gases," *J. Phys. B: At. Mol. Opt. Phys.*, **42**, p. 044016.

[129] Platter, L., C. Ji, and D. R. Phillips (2009) "Range corrections to three-body observables near a Feshbach resonance," *Phys. Rev. A*, **79**, p. 022702.

[130] Thøgersen, M. (2009) *Universality in Ultra-Cold Few- and Many-Boson Systems*, Ph.D. thesis, Århus University, Department of Physics, Denmark.

[131] Gogolin, A. O., C. Mora, and R. Egger (2008) "Analytical solution of the bosonic three-body problem," *Phys. Rev. Lett.*, **100**, p. 140404.

[132] Esry, B. D. and J. P. D'Incao (2007) "Efimov physics in ultracold three-body collisions," *Journal of Physics: Conference Series*, **88**, p. 012040.

[133] Braaten, E. and H. W. Hammer (2004) "Enhanced Dimer Relaxation in an Atomic and Molecular BEC," *Phys. Rev. A*, **70**(5), p. 042706.

[134] Nielsen, E. and J. Macek (1999) "Low-energy Recombination of Identical Bosons by Three-Body Collisions," *Phys. Rev. Lett.*, **83**, p. 1566.

[135] Esry, B., C. Greene, and J. Burke (1999) "Recombination of Three Atoms in the Ultracold Limit," *Phys. Rev. Lett.*, **83**, p. 1751.

[136] Bedaque, P., E. Braaten, and H. W. Hammer (2000) "Three-body recombination in Bose gases with large scattering length," *Phys. Rev. Lett.*, **85**, p. 908.

[137] Mott, N. F. and H. S. W. Massey (1965) *The Theory of Atomic Collisions*, 3rd edition ed., Clarendon Press, Oxford.

[138] D'Incao, J. P. and B. D. Esry (2005) "Scattering Length Scaling Laws for Ultracold Three-Body Collisions," *Phys. Rev. Lett.*, **94**, p. 213201.

[139] Amado, R. and J. Noble (1972) "Efimovs Effect: A New Pathology of Three-Particle Systems. II," *Phys. Rev. D*, **5**, p. 1992.

[140] Efimov, V. (1972) "Level Spectrum of Three Resonantly Interacting Particles," *Sov. Phys. JETP Lett.*, **16**, p. 34.

[141] Ovchinnikov, Y. and I. Sigal (1979) "Number of Bound States of Three-Body Systems and Efimovs Effect," *Ann. Phys.*, **123**, p. 274.

[142] D'Incao, J. P. and B. D. Esry (2009) "Ultracold three-body collisions near overlapping Feshbach resonances," *ArXiv*, p. 0905.0772.

[143] D'Incao, J., Private communications, JILA, University of Colorado, Greene Group.

[144] Huckans, J. H., J. R. Williams, E. L. Hazlett, R. W. Stites, and K. M. OHara (2009) "Three-Body Recombination in a Three-State Fermi Gas with Widely Tunable Interactions," *Phys. Rev. Lett.*, **102**, p. 165302.

[145] Ottenstein, T. B., T. Lompe, M. Kohnen, A. N. Wenz, and S. Jochim (2008) "Collisional Stability of a Three-Component Degenerate Fermi Gas," *Phys. Rev. Lett*, **101**, p. 203202.

[146] Braaten, E., H. W. Hammer, D. Kang, and L. Platter (2009) "Three-body Recombination of Lithium-6 Atoms with Large Negative Scattering Lengths," *Phy. Rev. Lett*, **103**, p. 073202.

[147] Wille, E. (2009) *Preparation of an Optically Trapped Fermi-Fermi Mixture of Li6 and K40 Atoms and Characterization of the Interspecies Interactions by Feshbach Spectroscopy*, Ph.D. thesis, Universität Innsbruck.

[148] Braaten, E., H. W. Hammer, and T. Mehen (2002) "The Dilute Bose-Einstein Condensate with Large Scattering Length," *Phys. Rev. Lett.*, **88**, p. 040401.

[149] Hammer, H. W., T. A. Lahde, and L. Platter (2007) "Effective Range Corrections to Three-Body Recombination for Atoms with Large Scattering Length," *Phys. Rev. A*, **75**, p. 032715.

[150] Braaten, E., H. W. Hammer, D. Kang, and L. Platter (2008) "Three-Body Recombination of Identical Bosons with a Large Positive Scattering Length at Nonzero Temperature," *Phy. Rev. A*, **78**, p. 043605.

[151] D'Incao, J. P., H. Suno, and B. D. Esry (2004) "Limits on Universality in Ultracold Three-Boson Recombination," *Phys. Rev. Lett.*, **93**, p. 123201.

[152] Esry, B., C. Greene, and H. Suno (2001) "Threshold laws for three-body recombination," *Phys. Rev. A*, **65**, p. 010705.

[153] Moore, J., C. Davis, M. Coplan, and S. Greer (2003) *Building Scientific Apparatus*, Westview Press.

[154] Chambers, A. (2005) *Modern Vacuum Physics*, Chapman & Hall/CRC.

[155] Bali, S., K. M. O'Hara, M. E. Gehm, S. R. Granade, and J. E. Thomas (1999) "Quantum-diffractive background gas collisions in atom-trap heating and loss," *Phys. Rev. A*, **60**, p. 29(R).

[156] Stan, C. A. (2005) *Experiments with Interacting Bose and Fermi Gases*, Ph.D. thesis, Massachusetts Institute of Technology, Department of Physics.

[157] Stowe, K. (1984) *Introduction to Statistical Mechanics and Theromdynamics*, John Wiley & Sons.

[158] Scoles, G. (1988) *Atomic and molecular beam methods*, Oxford University Press.

[159] Hitchcock, J., Private communication, Rice University TX, Hulet Group.

[160] Serwane, F. (2007), "The setup of a Magneto Optical Trap for the Preparation of a Mesoscopic Degenerate Fermi Gas," Diploma thesis, university of Heidelberg, Department of Physics.

[161] Hadzibabic, Z. (2003) *Studies of a Quantum Degenerate Fermionic Lithium Gas*, Ph.D. thesis, Massachusetts Institute of Technology, Department of Physics.

[162] Hänsch, T. W. (1981) *High Resolution Laser Spectroscopy*, vol. 95 of *Advances in laser spectroscopy*, Plenum Press, New York.

[163] Gerstenkorn, S. and P. Luc *Atlas du Spectre D'absorption de la Molëcule D'Iode, Complement 14800–20000*, CNRSll.

[164] Chen, L. (2002) *High-Precision Spectroscopy of Molecular Iodine: From Optical Frequency Standards to Global Descriptions of Hyperfine Interactions and Associated Electronic Structure*, Ph.D. thesis, University of Colorado, Department of Physics.

[165] Horowitz, P. and W. Hill (1980) *The Art of Electronics*, Cambridge University Press.

[166] Appel, J., A. MacRae, and A. I. Lvovsyk (2009) "A versatile digital GHz phase lock for external cavity diode lasers," *Meas. Sci. Technol.*, **20**, p. 055302.

[167] Meyrath, T. P. and F. Schreck (2004), "Digital RF Synthesizer: DC to 135 MHz," Published online at http://iqoqi006.uibk.ac.at/users/c704250/, atom Optics Laboratory and the Center for Nonlinear Dynamics, University of Texas at Austin.

[168] Jonathan, D. (2004) *Eliminating Parasitic Oscillation between Parallel MOSFETs*, *Application Note APT-0402 RevA*, Advanced Power Technology.

[169] DeMarco, B. (2001) *Quantum Behavior of an Atomic Fermi Gas*, Ph.D. thesis, University of Colorado, Department of Physics.

[170] Foot, C. J. (2005) *Atomic Physics*, Oxford University Press.

[171] Savard, T. (1998) *Raman Induced Resonance Imaging of Trapped Atoms*, Ph.D. thesis, Duke University, Department of Physics.

[172] Chu, S., L. Hollberg, J. Bjorkholm, A. Cable, and A. Ashkin (1985) *Laser Spectroscopy VII*, chap. Three Dimensional Viscous Confinement and cooling of Atoms by Resonance Radiation Pressure, Springer-Verlag.

[173] Chu, S., L. Hollberg, J. E. Bjorkholm, A. Cable, and A. Ashkin (1985) "Laser Cooling and Viscous Confinement of Sodium Atoms," *Phys. Rev. Lett*, **55**, p. 48.

[174] Cohen-Tannoudji, C., J. Dupont-Roc, and G. Grynberg (1992) *Atom-Photon Interactions, Basic Processes and Applications*, John Wiley & Sons.

[175] Ottenstein, T. (2010) *Few-body physics in ultracold Fermi gases*, Ph.D. thesis, University of Heidelberg.

[176] Grimm, R., W. M., and Y. B. Ovchinnikov (2000) "Optical dipole traps for neutral atoms," *Advances in Atomic, Molecular, and Optical Physics*, **42**, p. 95.

[177] Huckans, J. H. (2006) *Optical Lattices and Quantum Degenerate ^{87}Rb in Reduced Dimensions*, Ph.D. thesis, University of Maryland, Department of Physics.

[178] Gehm, M. E., K. M. OHara, T. A. Savard, and J. E. Thomas (1998) "Dynamics of noise-induced heating in atom traps," *Phys. Rev. A*, **58**, p. 3914.

[179] Grimm, R., Private communications, Institute for Experimental Physics, University of Innsbruck, Austria.

[180] Chin, C., Private communications, James Franck Institute, University of Chicago, IL.

[181] Friebel, S., C. D. Andrea, J. Walz, M. Weitz, and T. W. Hansch (1998) "CO_2-laser optical lattice with cold rubidium atoms," *Phys. Rev. A*, **57**, p. R20.

[182] Petrov, D. S. (2003) "Three-body problem in Fermi gases with short-range interparticle interaction," *Phys. Rev. A*, **67**, p. 010703.

[183] O'Hara, K. M., M. E. Gehm, S. R. Granade, and J. E. Thomas (2001) "Scaling laws for evaporative cooling in time-dependent optical traps," *Phys. Rev. A*, **64**, p. 051403.

[184] Petrov, D. S., C. Salomon, and G. V. Shlyapnikov (2005) "Scattering properties of weakly bound dimers of fermionic atoms," *Phys. Rev. A*, **71**, p. 012708.

[185] Jochim, S., M. Bartenstein, A. Altmeyer, G. Hendl, C. Chin, J. H. Denschlag, and R. Grimm (2003) "Pure Gas of Optically Trapped Molecules Created from Fermionic Atoms," *Phys. Rev. Lett.*, **91**, p. 240402.

[186] Cubizolles, J., T. Bourdel, S. J. J. M. F. Kokkelmans, G. V. Shlyapnikov, and C. Salomon (2003) "Production of Long-Lived Ultracold Li2 Molecules from a Fermi Gas," *Phys. Rev. Lett*, **91**, p. 240401.

[187] Regal, C. A., M. Greiner, and D. S. Jin (2004) "Lifetime of Molecule-Atom Mixtures near a Feshbach Resonance in 40K," *Phys. Rev. Lett*, **92**, p. 083201.

[188] Chin, C. and R. Grimm (2004) "Thermal equilibrium and efficient evaporation of an ultracold atom-molecule mixture," *Phys. Rev. A*, **69**, p. 033612.

[189] Petrov, D., C. Salomon, and G. Shlyapnikov (2004) "Weakly bound dimers of fermionic atoms," *Phys. Rev. Lett.*, **93**, p. 090404.

[190] Wenz, A. N. (2008), "Few-Body Physics in a Three-Component Fermi Gas," Diploma thesis, university of Heidelberg, Department of Physics.

[191] Weisbluth, M. (1989) *Photon Atom Interactions*, Academic Press.

[192] Gupta, S., Z. Hadzibabic, M. W. Zwierlein, C. A. Stan, K. Dieckmann, C. H. Schunck, E. G. M. van Kempen, B. J. Verhaar, and W. Ketterle (2003) "Radio-Frequency Spectroscopy of Ultracold Fermions," *Science*, **300**, p. 1723.

[193] Zwierlein, M., Z. Hadzibabic, S. Gupta, and W. Ketterle (2003) "Absence of clock shifts in fermionic gases," *Phys. Rev. Lett.*, **91**, p. 250404.

[194] Campbell, G. K., M. M. Boyd, J. W. Thomsen, M. J. Martin, S. Blatt, M. Swallows, T. L. Nicholson, T. Fortier, C. W. Oates, S. A. Diddams, N. D. Lemke, P. Naidon, P. Julienne, J. Ye, and A. D. Ludlow (2009) "Probing interactions between ultracold fermions," *Science*, **324**, p. 360.

[195] Butts, D. A. and D. S. Rokhsar (1997) "Trapped Fermi gases," *Phys. Rev. A*, **5**, p. 4346.

[196] Kinoshita, T., T. Wenger, and D. S. Weiss (2005) "All-optical Bose-Einstein condensation using a compressible crossed dipole trap," *Phys. Rev. A*, **71**, p. 011602.

[197] Kraemer, T., J. Herbig, M. Mark, T. Weber, C. Chin, H.-C. Nagerl, and R. Grimm (2004) "Optimized production of a cesium Bose-Einstein condensate," *Appl. Phys. B*, **79**, p. 1013.

[198] Lompe, T., T. B. Ottenstein, F. Serwane, K. Viering, A. N. Wenz, G. Zürn, and S. Jochim (2010) "Atom-Dimer Scattering in a Three-Component Fermi Gas," *arXiv*, p. 1003.0600.

[199] Weber, T. (2003) *Bose-Einstein Condensation of Optically Trapped Cesium*, Ph.D. thesis, Universität Innsbruck.

[200] Weber, T., J. Herbig, M. Mark, H.-C. Nägerl, and R. Grimm (2003) "Three-Body Recombination at Large Scattering Lengths in an Ultracold Atomic Gas," *Phys. Rev. Lett.*, **91**, p. 123201.

[201] Bevington, P. R. and D. K. Robinson (1992) *Data Reduction and Error Analysis for the Physical Sciences*, second edition ed., McGraw-Hill.

[202] Press, W. H., B. P. Flannery, S. A. Teukolsky, and W. T. Vetterling (1986) *Numerical Recipes, The Art of Scientific Computing*, Cambridge University Press.

[203] Floerchinger, S., R. Schmidt, and C. Wetterich (2009) "Three-body loss in lithium from functional renormalization," *Phys. Rev. A*, **79**, p. 053633.

[204] Braaten, E. and H. W. Hammer (2001) "Three-Body Recombination into Deep Bound States in a Bose Gas with Large Scattering Length," *Phys. Rev. Lett*, **87**(16), p. 160407.

[205] Rittenhouse, S. T. (2010) "Magnetic Field Dependence and Efimov Resonance Broadening in Ultracold Three-Body Recombination," *ArXiv*, p. 1002.4891.

[206] Luo, L., B. Clancy, J. Joseph, J. Kinast, A. Turlapov, and J. E. Thomas (2006) "Evaporative cooling of unitary Fermi gas mixtures in optical traps," *New J. Phys.*, **8**, p. 213.

[207] Abraham, E. R. I., W. I. McAlexander, J. M. Gerton, R. G. Hulet, R. Cote, and A. Dalgarno (1997) "Triplet s-wave resonance in ^{6}Li collisions and scattering lengths of ^{6}Li and ^{7}Li," *Phys. Rev. A*, **55**, p. R3299.

[208] Massignan, P. and H. T. C. Stoof (2008) "Efimov states near a Feshbach resonance," *Phys. Rev. A*, **78**, p. 030701 (R).

[209] Jona-Lasinio, M. and L. Pricoupenko (2003) "Three Resonant Ultracold Bosons: Off-Resonance Effects," *Phys. Rev. Lett.*, **104**, p. 023201.

[210] Nakajima, S., M. Horikoshi, T. Mukaiyama, P. Naidon, and M. Ueda (2010) "Nonuniversal Efimov Atom-Dimer Resonances in a Three-Component Mixture of ^{6}Li," *Phys. Rev. Lett.*, **105**, p. 023201.

[211] Lompe, T., T. B. Ottenstein, F. Serwane, A. N. Wenz, G. Zürn, and S. Jochim (2010) "Radio Frequency Association of Efimov Trimers," *arXiv*, p. 1006.2241.

[212] Stajic, J., J. N. Milstein, Q. Chen, M. L. Chiofalo, M. J. Holland, and K. Levin (2004) "Nature of superfluidity in ultracold Fermi gases near Feshbach resonances," *Phys. Rev. A*, **69**, p. 063610.

[213] Stoof, H. T. C., M. Houbiers, C. A. Sackett, and R. G. Hulet (1996) "Superfluidity of Spin-Polarized ^{6}Li," *Phys. Rev. Lett.*, **75**, p. 10.

[214] Combescot, R. (1999) "Trapped ^{6}Li: A High T_c Superfluid?" *Phys. Rev. Lett*, **83**, p. 19.

[215] Partridge, G. B., W. Li, Y. A. Liao, R. G. Hulet, M. Haque, and H. T. C. Stoof (2006) "Deformation of a Trapped Fermi Gas with Unequal Spin Populations," *Phys. Rev. Lett.*, **97**, p. 190407.

[216] Shin, Y., M. W. Zwierlein, C. H. Schunck, A. Schirotzek, and W. Ketterle (2006) "Observation of Phase Separation in a Strongly Interacting Imbalanced Fermi Gas," *Phys. Rev. Lett.*, **97**, p. 030401.

[217] il Shin, Y. (2008) "Determination of the equation of state of a polarized Fermi gas at unitarity," *Phys. Rev. A*, **77**, p. 041603.

[218] Shin, Y., C. H. Schunck, A. Schirotzek, and W. Ketterle (2008) "Phase diagram of a two-component Fermi gas with resonant interactions," *Nature*, **451**, p. 689.

[219] Hulet, R. G., G. B. Partridge, W. Li, and Y. A. Liao (2008) *Coherence and Quantum Optics IX*, chap. Fermion Pairing with Unequal Spin Populations, Optical Society of America, p. 110.

[220] Blume, D., S. T. Rittenhouse, J. von Stecher, and C. H. Greene (2008) "Stability of inhomogeneous multicomponent Fermi gases," *Phys. Rev. A*, **77**, p. 033627.

[221] Donley, E. A., N. R. Claussen, S. L. Cornish, J. L. Roberts, E. A. Cornell, and C. E. Wieman (2001) "Dynamics of collapsing and exploding Bose-Einstein condensates," *Nature*, **412**, p. 295.

[222] Catelani, G. and E. A. Yuzbashyan (2008) "Phase diagram, extended domain walls, and soft collective modes in a three-component fermionic superfluid," *Phys. Rev. A*, **78**, p. 033615.

[223] Silva, T. N. D. (2009) "Three-component fermion pairing in two dimensions," *Phys. Rev. A*, **80**, p. 013620.

[224] Paananen, T., P. Torma, and J. P. Martikainen (2007) "Coexistence and shell structures of several superfluids in trapped three-component Fermi mixtures," *Phys. Rev. A*, **75**, p. 023622.

[225] Errea, B., J. Dukelsky, and G. Ortiz (2009) "Breached pairing in trapped three-color atomic Fermi gases," *Phys. Rev. A*, **79**, p. 051603.

[226] Silva, T. N. D. (2010) "Density profiles and density oscillations of an interacting three-component normal Fermi gas," *J. Phys. B*, **43**, p. 035301.

[227] Martikainen, J. P., J. J. Kinnunen, P. Torma, and C. J. Pethick (2009) "Induced Interactions and the Superfluid Transition Temperature in a Three-Component Fermi Gas," *Phys. Rev. Lett*, **103**, p. 260403.

[228] Azaria, P., S. Capponi, and P. Lecheminant (2009) "Three-Component Fermi Gas in a one-dimensional Optical Lattice," *Phys. Rev. A*, **80**, p. 041604(R).

[229] Molina, R. A., J. Dukelsky, and P. Schmitteckert (2009) "Crystallization of trions in SU(3) cold-atom gases trapped in optical lattices," *Phys. Rev. A*, **80**, p. 013606.

[230] Miyatake, S., K. Inaba, and S. Suga (2010) "Three-component fermionic atoms with repulsive interaction in optical lattices," *Phys. Rev. A*, **81**, p. 021603(R).

[231] Recati, A., P. O. Fedichev, W. Zwerger, and P. Zoller (2003) "Fermi one-dimensional quantum gas: Luttinger liquid approach and spin-charge separation," *J. Opt. B*, **5**, p. S55.

[232] Ulbricht, T., R. A. Molina, R. Thomale, and P. Schmitteckert (2010) "Color-charge separation in trapped SU(3) fermionic atoms," *Phys. Rev. A*, **82**, p. 011603.

[233] Kantian, A., M. Dalmonte, S. Diehl, W. Hofstetter, P. Zoller, and A. J. Daley (2009) "An atomic colour superfluid via three-body loss," *Phys. Rev. Lett.*, **103**, p. 240401.

[234] Zwierlein, M., C. H. Schunck, C. A. Stan, S. M. F. Raupach, and W. Ketterle (2005) "Formation Dynamics of a Fermion Pair Condensate," *Phys. Rev. Lett*, **94**, p. 180401.

[235] Jo, G., Y. Lee, J. Choi, C. Christensen, T. Kim, J. Thywissen, D. Pritchard, and W. Ketterle (2009) "Itinerant ferromagnetism in a Fermi gas of ultracold atoms," *Science*, **325**, p. 1521.

[236] Greiner, M. (2003) *Ultracold quantum gases in three-dimensional optical lattice potentials*, Ph.D. thesis, Ludwig-Maximilians-Universitat Munchen.

[237] Nelson, K. D., X. Li, and D. S. Weiss (2007) "Imaging single atoms in a three-dimensional array," *Nature Phys.*, **3**, p. 556.

[238] Lee, P. A., N. Nagaosa, and X. G. Wen (2006) "Doping a Mott insulator: Physics of high-temperature superconductivity," *Rev. Mod. Phys.*, **78**, p. 17.

[239] Jordens, R., L. Tarruell, D. Greif, T. Uehlinger, N. Strohmaier, H. Moritz, T. Esslinger, L. D. Leo, C. Kollath, A. Georges, V. Scarola, L. Pollet, E. Burovski, E. Kozik, and M. Troyer (2010) "Quantitative Determination of Temperature in the Approach to Magnetic Order of Ultracold Fermions in an Optical Lattice," *Phys. Rev. Lett*, **104**, p. 180401.

[240] Hermele, M., V. Gurarie, and A. M. Rey (2009) "Mott Insulators of Ultracold Fermionic Alkaline Earth Atoms: Underconstrained Magnetism and Chiral Spin Liquid," *Phys. Rev. Lett.*, **103**, p. 135301.

[241] Gorshkov, A. V., M. Hermele, V. Gurarie, C. Xu, P. S. Julienne, J. Ye, P. Zoller, E. Demler, M. D. Lukin, and A. M. Rey (2010) "Two-orbital SU(N) magnetism with ultracold alkaline-earth atoms," *Nature Phys.*, **6**, p. 289.

[242] Rabl, P., A. J. Daley, P. O. Fedichev, J. I. Cirac, and P. Zoller (2003) "Defect-Suppressed Atomic Crystals in an Optical Lattice," *Phys. Rev. Lett.*, **91**, p. 110403.

[243] Weiss, D. S., J. Vala, A. V. Thapliyal, S. Myrgren, U. Vazirani, and K. B. Whaley (2004) "Another way to approach zero entropy for a finite system of atoms," *Phys. Rev. A*, **70**, p. 040302.

[244] Popp, M., J. J. Garcia-Ripoll, K. G. H. Vollbrecht, and J. I. Cirac (2006) "Cooling toolbox for atoms in optical lattices," *New J. Phys.*, **8**, p. 164.

[245] Ho, T. L. and Q. Zhou (2009) "Squeezing out the entropy of fermions in optical lattices," *Proc. Natl. Acad. Sci. USA*, **106**, p. 6916.

[246] Heidrich-Meisner, F., S. R. Manmana, M. Rigol, A. Muramatsu, A. E. Feiguin, and E. Dagotto (2009) "Quantum distillation: Dynamical generation of low-entropy states of strongly correlated fermions in an optical lattice," *Phys. Rev. A*, **80**, p. 041603 (R).

[247] Ho, T. L. and Q. Zhou (2009) "Universal Cooling Scheme for Quantum Simulation," *arXiv*, p. 0911.5506v1.

[248] Catani, J., G. Barontini, G. Lamporesi, F. Rabatti, G. Thalhammer, F. Minardi, S. Stringari, and M. Inguscio (2009) "Entropy Exchange in a Mixture of Ultracold Atoms," *Phys. Rev. Lett.*, **103**, p. 140401.

[249] Williams, J. R., J. H. Huckans, R. W. Stites, E. L. Hazlett, and K. M. OHara (2010) "Preparing a highly degenerate Fermi gas in an optical lattice," *Phys. Rev. A*, **82**, p. 011610(R).

[250] Bloch, I., M. Greiner, and T. W. Hansch (2009) *Cold Atoms and Molecules*, chap. Bose-Einstein Condensates in Optical Lattices, Wiley-VCH, p. 315.

[251] Blakie, P. B. and A. Bezett (2005) "Adiabatic cooling of fermions in an optical lattice," *Phys. Rev. A*, **71**, p. 033616.

[252] Denschlag, J. H., J. E. Simsarian, H. Haffner, C. McKenzie, A. Browaeys, D. Cho, K. Helmerson, S. L. Rolston, and W. D. Phillips (2002) "A Bose-Einstein condensate in an optical lattice," *J. Phys. B*, **35**, p. 3095.

[253] Blakie, P. B., A. Bezett, and P. Buonsante (2007) "Degenerate Fermi gas in a combined harmonic-lattice potential," *Phys. Rev. A*, **75**, p. 063609.

[254] Fatemi, F. K., M. Bashkansky, and Z. Dutton (2007) "Dynamic high-speed spatial manipulation of cold atoms using acousto-optic and spatial light," *Optics Express*, **15**, p. 3589.

[255] Rhodes, D. P., D. M. Gherardi, J. Livesey, D. McGloin, H. Melville, T. Freegarde, and K. Dholakia (2006) "Atom guiding along high order LaguerreGaussian light beams formed by spatial light modulation," *J. Mod. Opt.*, **53**, p. 547.

[256] Fatemi, F. K. and M. Bashkansky (2006) "Cold atom guidance using a binary spatial light modulator," *Optics Express*, **14**, p. 1368.

[257] Colbert, D. T. and W. H. Miller (1992) "A novel discrete variable representation for quantum mechanical reactive scattering via the S-matrix Kohn method," *J. Chem. Phys.*, **96**, p. 1982.

[258] Ferlaino, F., S. Knoop, M. Berninger, W. Harm, J. P. DIncao, H.-C. Nagerl, and R. Grimm (2009) "Evidence for Universal Four-Body States Tied to an Efimov Trimer," *Phys. Rev. Lett.*, **102**, p. 140401.

[259] von Stecher, J., J. DIncao, and C. H. Greene (2009) "Signatures of universal four-body phenomena and their relation to the Efimov effect," *Nature Phys.*, **5**, p. 417.

[260] von Stecher, J. (2010) "Weakly Bound Cluster States of Efimov Character," *J. Phys. B*, **43**, p. 101002.

[261] Hanna, T., Private communications, NIST, University of Maryland, Gaithersburg, MD.

Vita

Jason Reid Williams

Education:	**Ph.D. in Physics**, The Pennsylvania State University, University Park, PA (2010) **M.S. in Physics**, Idaho State University, Pocatello, ID (2004) **B.S. in Physics**, Idaho State University, Pocatello, ID (2002)
Employment:	**Graduate Research Assistant**, The Pennsylvania State University, University Park, PA (2004 - 2010) **Graduate Teaching Assistant**, The Pennsylvania State University, University Park, PA (2004 - 2005) **Graduate Research Assistant**, Idaho State University, Pocatello, ID (2002 - 2004) **Teaching Assistant**, Idaho State University, Pocatello, ID (2000 - 2003) **Accelerator Technician** The Idaho Accelerator Center, Idaho State University, Pocatello, ID (1999 - 2002)
Honors :	Downsbrough Student appointment (2004 - 2010) Dean's List, Idaho State University (2000 - 2004)
Fellowships:	David C. Duncan Graduate Fellowship (2004, 2006, 2008) Downsbrough Graduate Fellowship (2004) W. Donald Miller Graduate Fellowship (2004)

Selected Publications:

- Williams J. R., J. H. Huckans, R. W. Stites, E. L. Hazlett, and K. M. O'Hara (2010) "Preparing a highly degenerate Fermi gas in an optical lattice", *Phys. Rev. A*, **82**, p. 011610(R).
- Williams J. R., E. L. Hazlett, J. H. Huckans, R. W. Stites, Y. Zhang, and K. M. O'Hara (2009), "Evidence for an excited-state Efimov trimer in a three-component Fermi Gas", *Phys. Rev. Lett.*, **103**, p. 130404.
- Huckans J. H., J. R. Williams, E. L. Hazlett, R. W. Stites, and K. M. O'Hara (2009) "Three-Body Recombination in a Three-State Fermi Gas with Widely Tunable Interactions", *Phys. Rev. Lett.*, **102**, p. 165302.